A Structural, Electrochemical and Thermal Study of New Mono- and Bimetallic Long Chain Carboxylates

Submitted in fulfilment of the requirements in respect of the Doctoral degree qualification

Philosophiae Doctor

In the

Department of Chemistry

In the Faculty of Natural and Agricultural Sciences

At the

University of the Free State

Date

July 2015

By

Ebrahiem Botha

Supervisor

Dr. Elizabeth Erasmus

Table of Contents

List of Abbreviations

Å	angstrom
CH_3CN	acetonitrile
CH_3OH	methanol
CO	carbon monoxide
Cp	cyclopentadienyl $(C_5H_5)^-$
δ	chemical shift
Δ_{Shift}	**$(C\overline{\overline{\cdots}}O)^{anti}$ - $(C=O)^{free\ acid}$** i.e. the anti-symmetric carbonyl stretching wavenumber for the metal carboxylatido complex subtracted from the carbonyl stretching wavenumber for the free carboxylic acid
$\Delta_{Difference}$	**$(C\overline{\overline{\cdots}}O)^{anti}$ - $(C\overline{\overline{\cdots}}O)^{sym}$** i.e. anti-symmetric stretching wavenumber subtracted from the symmetric stretching wavenumber within the same molecule.
DCM	dichloromethane
DSC	differential scanning calorimetry
CV	cyclic voltammetry
OYSW	Osteryoung square wave voltammetry
LSV	linear sweep voltammetry
$E^{\circ\prime}$	formal reduction potential
E_{pa}	peak anodic potential
E_{pc}	peak cathodic potential
ΔE_p	separation of peak anodic and peak cathodic potentials
i_{pa}	peak anodic current
i_{pc}	peak cathodic current
exo	exothermic
endo	endothermic
Fc	ferrocene
Fc*	Decamethyl ferrocene
ATR-FTIR	Attenuated Total Reflectance Fourier Transform Infrared Spectroscopy
ΔH	change in enthalpy
M	metal atom
m.p.	melting point
MS	mass spectrometry
m/z	mass ion current
^{1}H NMR	proton nuclear magnetic resonance spectroscopy
ppm	parts per million

SCE	standard calomel electrode
Anti-sym	Anti-symmetric
sym	symmetric
T	temperature
TGA	thermal gravimetric analysis
TGA-MS	thermal gravimetric analysis coupled with mass spectrometry
py	Pyridine
salen	[H_2salen = *N*,*N*'–ethylenedi(salicylaldimine)]
TOF	Turn over frequency
PdO	Palladium oxide
MO	Metal oxide

List of Structures

The number system, ONLY applies from chapter 3, onwards.

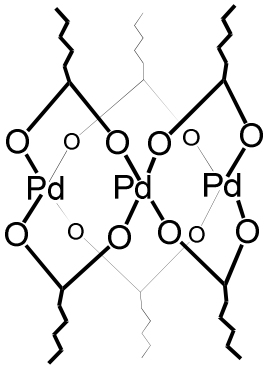

[1]

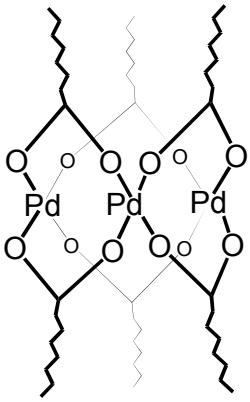

[2]

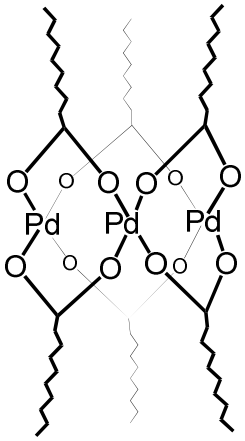

[3]

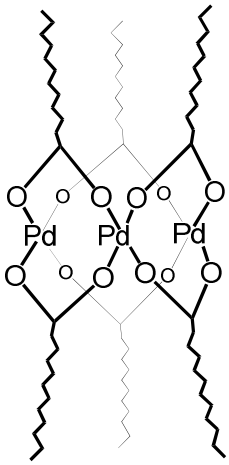

[4]

$K[OOC(CH_2)_4CH_3]$ $K[OOC(CH_2)_6CH_3]$ $K[OOC(CH_2)_8CH_3]$ $K[OOC(CH_2)_{10}CH_3]$

[5] **[6]** **[7]** **[8]**

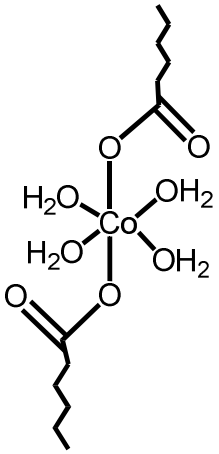

[9]

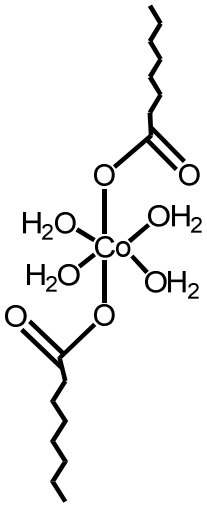

[10]

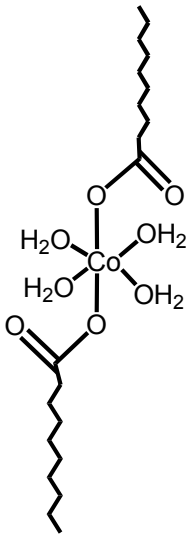

[11]

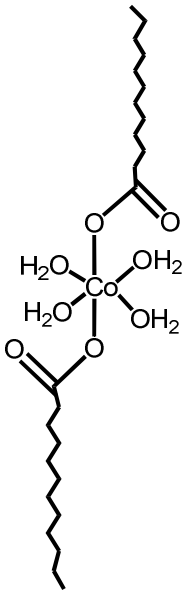

[12]

$[Ni^{II}(OOC(CH_2)_8CH_3)_2]\bullet 4H_2O$ **[13]**

$[Mn^{II}(OOC(CH_2)_8CH_3)_2]$ **[14]**

$[Zn^{II}(OOC(CH_2)_8CH_3)_2]$ **[15]**

$[Ca^{II}(OOC(CH_2)_8CH_3)_2]\bullet H_2O$ **[16]**

$[Sr^{II}(OOC(CH_2)_8CH_3)_2]$ **[17]**

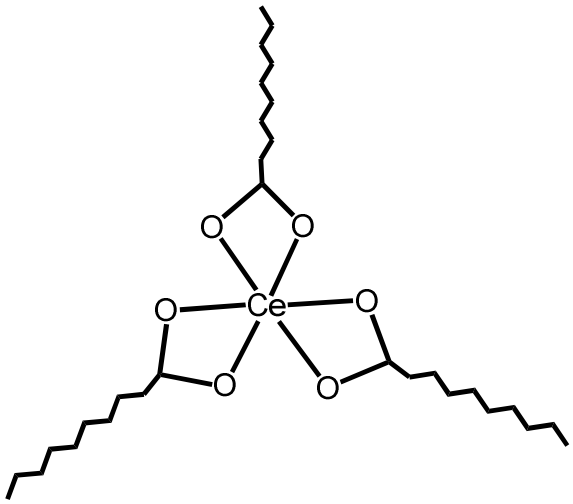

[18]

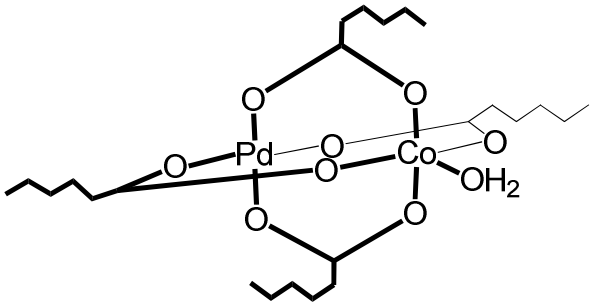

[19]

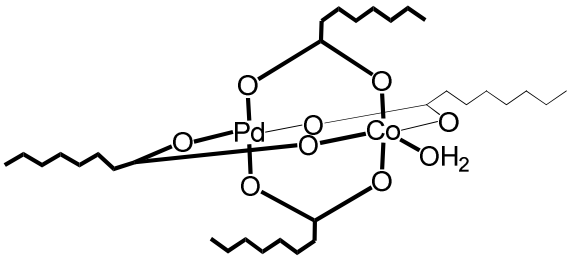

[20]

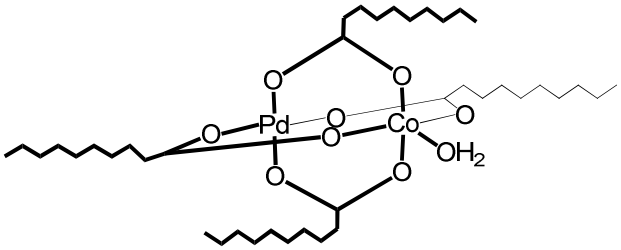

[21]

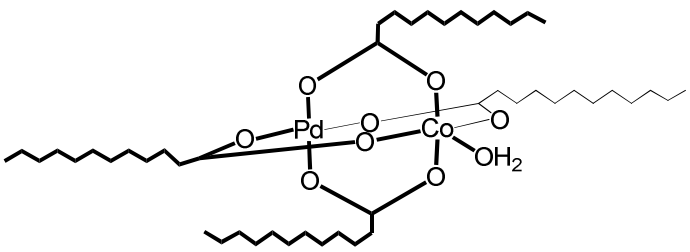

[22]

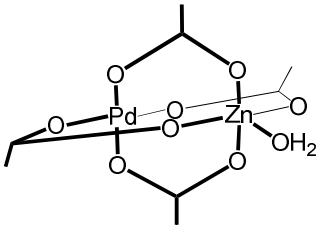

[23]

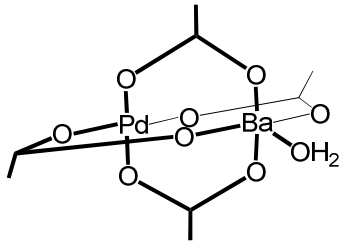

[24]

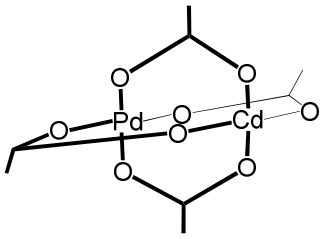

[25]

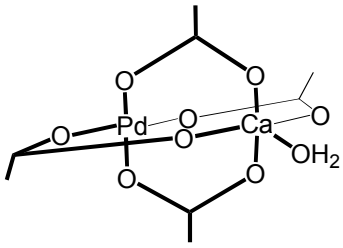

[26]

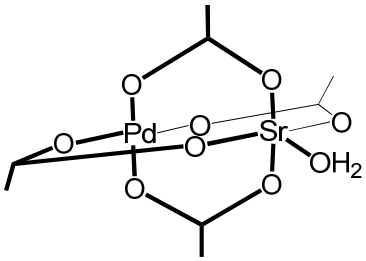

[27]

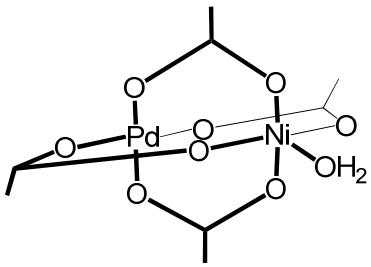

[28]

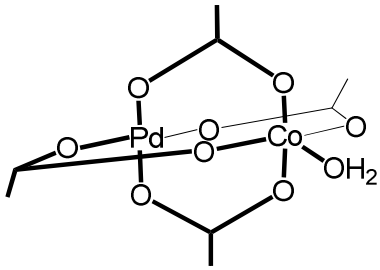

[29]

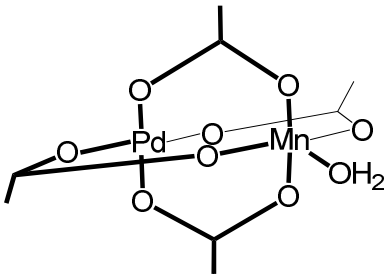

[30]

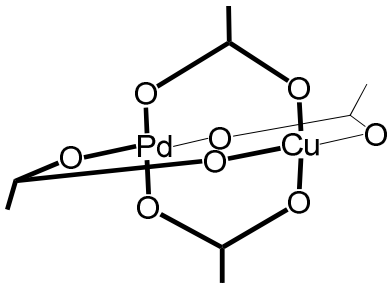

[31]

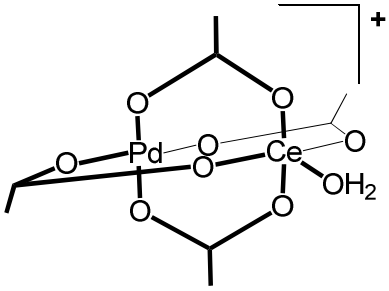

[32]

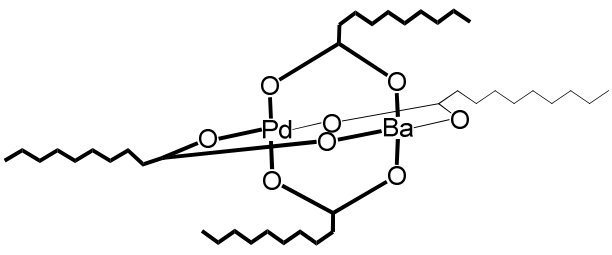

[33]

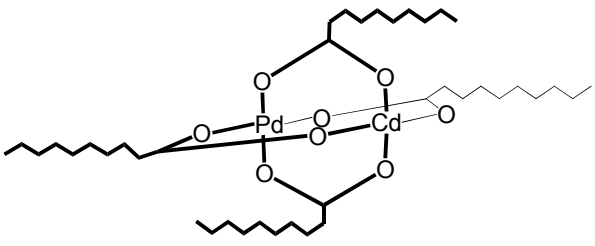

[34]

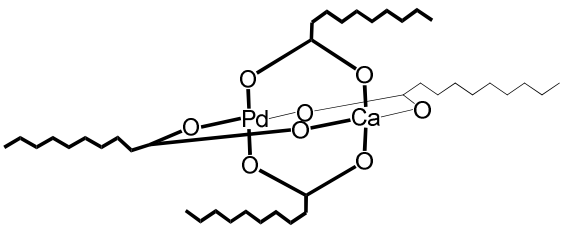

[35]

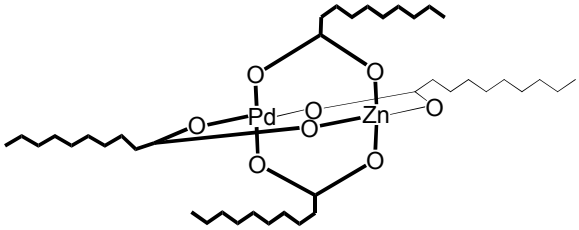

[36]

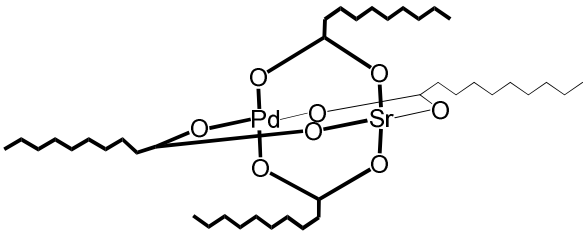

[37]

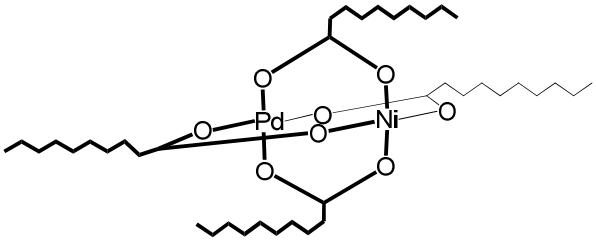

[38]

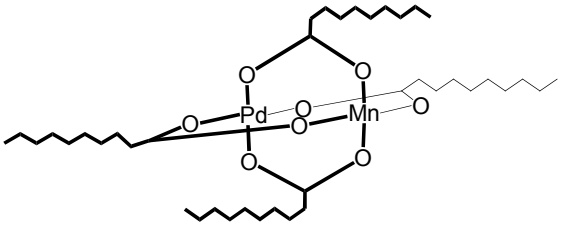

[39]

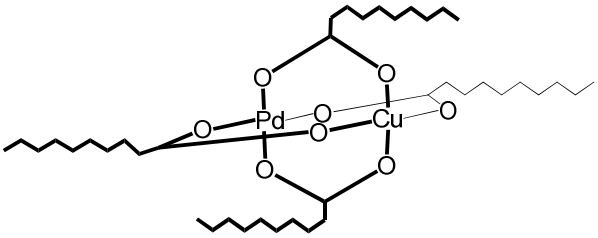

[40]

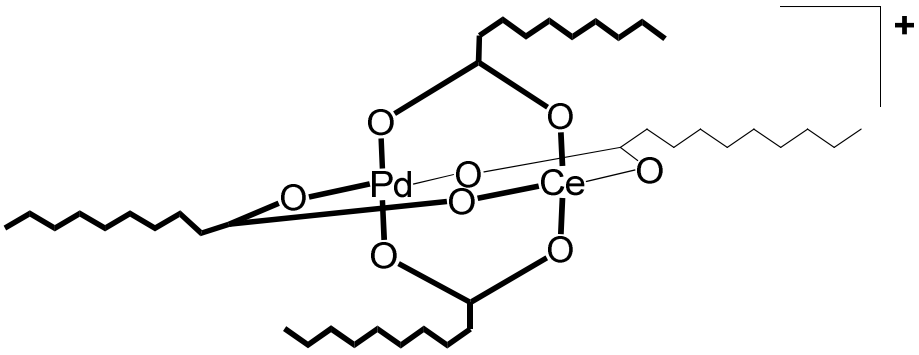

[41]

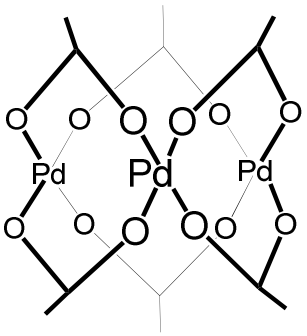

[42]

$[Zn^{II}(OOCCH_3)_2]$

[43]

$[Ba^{II}(OOCCH_3)_2]$

[44]

$[Cd^{II}(OOCCH_3)_2]$

[45]

$[Ca^{II}(OOCCH_3)_2]$

[46]

$[Sr^{II}(OOCCH_3)_2]$

[47]

$[Ni^{II}(OOCCH_3)_2]$

[48]

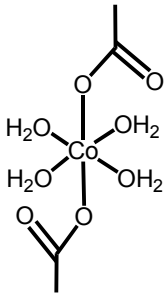

[49]

$[Mn^{II}(OOCCH_3)_2]$

[50]

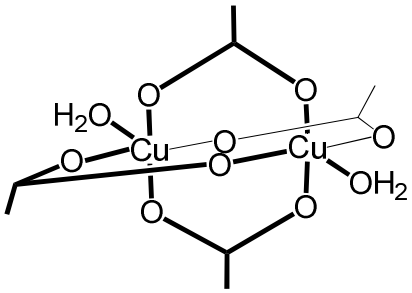

[51]

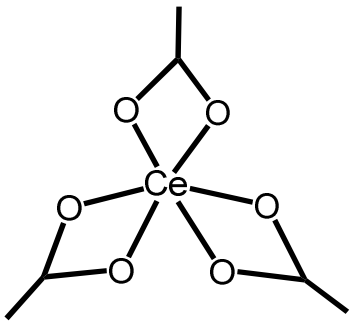

[52]

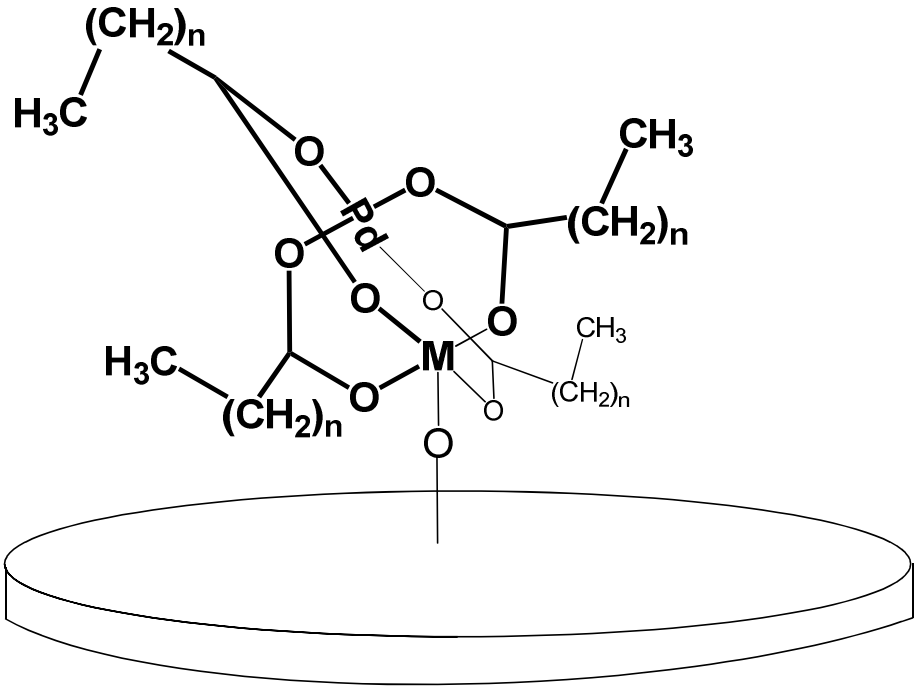

[53]: M = Zn, n = 0 **[60]:** M = Co, n = 4, **[61]:** M = Co, n = 6
[54]: M = Ba, n = 0 **[62]:** M = Co, n = 8, **[63]:** M = Co, n =10
[55]: M = Cd, n = 0 **[64]:** M = Ba, n = 8, **[65]:** M = Cd, n = 8
[56]: M = Sr, n = 0 **[66]:** M = Ca, n = 8, **[67]:** M = Zn, n = 8
[57]: M = Ni, n = 0 **[68]:** M = Sr, n = 8, **[69]:** M = Ni, n = 8
[58]: M = Co, n = 0 **[70]:** M = Mn, n = 8, **[71]:** M = Cu, n = 8
[59]: M = Mn, n = 0 **[72]:** M = Ce, n = 8

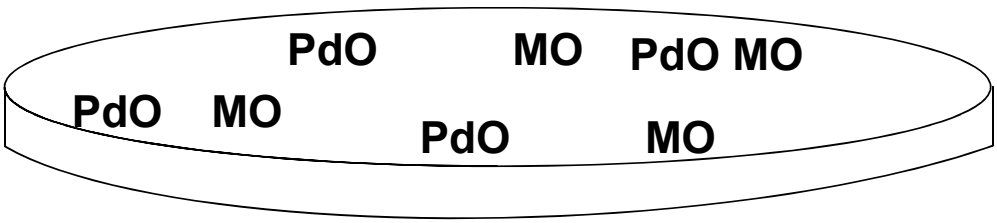

[73]: M = Zn, n = 0 **[80]:** M = Co, n = 4, **[81]:** M = Co, n = 6
[74]: M = Ba, n = 0 **[82]:** M = Co, n = 8, **[82]:** M = Co, n =10
[75]: M = Cd, n = 0 **[84]:** M = Ba, n = 8, **[85]:** M = Cd, n = 8
[76]: M = Sr, n = 0 **[86]:** M = Ca, n = 8, **[77]:** M = Zn, n = 8
[77]: M = Ni, n = 0 **[88]:** M = Sr, n = 8, **[89]:** M = Ni, n = 8
[78]: M = Co, n = 0 **[91]:** M = Mn, n = 8, **[91]:** M = Cu, n = 8
[79]: M = Mn, n = 0 **[92]:** M = Ce, n = 8

Acknowledgements

Dr. Elizabeth Erasmus, my promoter for all the help and support during my Ph.D. studies.

Prof. Jannie Swarts and the physical chemistry group for the Friday afternoon group meetings, it really helped me grow as a chemist.

My parents, Gilbert and Yvonne, and my brothers, Leonard and Christopher, for the prayers and only seeing me once every year during Christmas time.

My family (from both my Mom and Dad's side) for the support during my studies.

Everyone from the Pentecostal Protestant Church, in South Africa, especially the Calvary congregation in George.

My primary schools: The Crags (The Crags, a little town outside Plettenberg Bay), Bergsig (Oudtshoorn), my secondary schools: Morestêr (Oudtshoorn), P.W. Botha (George) and Knysna Senior Secondary School Hornlee (Knysna).

The NRF (National Research Foundation) for financial support.

Abstract

Two methods were used for the synthesis of the mixed-metal carboxylatido complexes. The first method involves the reaction of one equivalent of $[Pd_3^{II}(\mu\text{-}OOC(CH_2)_nCH_3)_6]$ where n = 4, 6, 8, or 10 with three equivalents of the relevant $[M^{II}(OOC(CH_2)_nCH_3)_2]$ where n = 4, 6, 8, or 10 or $[Ce^{III}(OOC(CH_2)_8CH_3)_3]$, which results in $[Pd^{II}M^{II}(\mu\text{-}OOC(CH_2)_nCH_3)_4]$ where n = 4, 6, 8, or 10 or $[Pd^{II}Ce^{III}(\mu\text{-}OOC(CH_2)_8CH_3)_4]^+$ with yields between 56 to 95 %.

The second method involves a ligand exchange type of reaction where $[Pd^{II}M^{II}(\mu\text{-}OOCH_3)_4]$ or $[Pd^{II}Ce^{III}(\mu\text{-}OOCH_3)_4]^+$ is reacted with the desired long chain carboxylic acid. This results in $[Pd^{II}M^{II}(\mu\text{-}OOC(CH_2)_nCH_3)_4]$ where n = 4, 6, 8, or 10 or $[Pd^{II}Ce^{III}(\mu\text{-}OOC(CH_2)_8CH_3)_4]^+$, with yields between 66 to 99 %.

The mono-metal and mixed-metal complexes were characterised using ATR-FTIR. This study indicated that the mixed-metal complexes have more than one binding mode, namely the unidentate, bidentate, tridendate, bridging (*syn-syn*) binding mode and ionic binding mode.

The single crystal X-ray structures of $[Pd^{II}Co^{II}(\mu\text{-}OOC(CH_2)_8CH_3)_4]$ **[21]** (Z = 2, space group $P2_1/c$), $[Pd^{II}Zn^{II}(\mu\text{-}OOC(CH_2)_8CH_3)_4]$ **[36]** (Z = 4, space group $P2_1/c$), and $[Pd^{II}Ni^{II}(\mu\text{-}OOC(CH_2)_8CH_3)_4]$ **[38]** (Z = 2, space group *P*-1) were solved and confirmed the binding modes observed in the ATR-FTIR studies.

Selected complexes were subjected to thermal analysis using DSC and TGA-MS. Liquid crystal properties was observed for $PdCo(C_8)_4$ **[20]**, $PdCo(C_{10})_4$ **[21]** and $PdZn(C_{10})_4$ **[36]**. Polymorphism was observed for $PdCd(C_{10})_4$ **[34]**, $PdMn(C_{10})_4$ **[39]** and $PdCu(C_{10})_4$ **[40]**. Variable temperature polarized light microscopy studies was used to shed light on the processes observed using DSC. TGA-MS analysis indicated volatile decomposition products were methane, hydroxide ions, water, carbon monoxide, oxygen, methanol, propyne, carbon dioxide and other products. Non-volatile decomposition product residues obtained were metal oxides.

Cyclic Voltammetry, Osteryoung Square Wave Voltammetry and Linear sweep voltammetry was performed on selected complexes and electronic communication between the metals was observed. The length of the carbon chain had an influence on the position of the oxidation wave of the palladium cerium paddlewheel carboxylatido complexes.

By increasing the carboxylatido carbon chain length from two to ten, the E_{pa} decreased from **514 mV** for $[Pd^{II}Ce^{III}(\mu\text{-}OOCCH_3)_4]^+$ **[32]**, to **297 mV** for $[Pd^{II}Ce^{III}(\mu\text{-}OOC(CH_2)_8CH_3)_4]^+$ **[41]**.

Selected mixed-metal paddlewheel complexes were spin coated onto modified silicon wafers using either acetone or DCM as solvent. The pre-catalyst was activated by oxidation in a stream of oxygen at 450 °C. This results in palladium oxide and metal oxide being deposited on the modified silicon wafer surface.

The catalysts were tested in the solvent-free aerobic oxidation of 1-octadecanol to 1-octadecanoic acid. The reaction was monitored by following the appearance of the carbonyl stretching frequencies at 1730 and 1710 cm^{-1} using ATR-FTIR.

Turn over frequencies (TOF) between 0.8 to 2 molecules s^{-1} were obtained for catalysts prepared from short-chain mixed-metal complexes. TOF's between 4 to 7 molecules s^{-1} were obtained for catalysts prepared from long-chain mixed-metal complexes. XPS analysis of the catalysts revealed that the PdO and MO (metal oxide) ratio was close to 1:1 and also 1:1.5.

Keywords: mixed-metal carboxylatido complexes, long-chain carboxylatido complexes, electrochemistry, DSC, TGA, catalyst, Silicon wafer.

Uittreksel

Twee metodes is gebruik vir die sintese van gemengde-metaal karboksilatido komplekse. Die eerste metode behels die reaksie tussen een ekwivalent van $[Pd_3^{II}(\mu\text{-}OOC(CH_2)_nCH_3)_6]$ waar n = 4, 6, 8 of 10 en drie ekwivalente van die relevante $[M^{II}(OOC(CH_2)_nCH_3)_2]$ waar n = 4, 6, 8 of 10 of $[Ce^{III}(OOC(CH_2)_8CH_3)_3]$, wat $[Pd^{II}M^{II}(\mu\text{-}OOC(CH_2)_nCH_3)_4]$ waar n = 4, 6, 8 of 10 of $[Pd^{II}Ce^{III}(\mu\text{-}OOC(CH_2)_8CH_3)_4]^+$ met n opbrengs tussen 56 en 95 % gee.

Die tweede metode behels ‘n liganduitruilreaksie waar $[Pd^{II}M^{II}(\mu\text{-}OOCH_3)_4]$ of $[Pd^{II}Ce^{III}(\mu\text{-}OOCH_3)_4]^+$ gereageer word met die gekose langketting karbosielsuur. Dit lei tot die vorming van $[Pd^{II}M^{II}(\mu\text{-}OOC(CH_2)_nCH_3)_4]$ waar n = 4, 6, 8 of 10 of $[Pd^{II}Ce^{III}(\mu\text{-}OOC(CH_2)_8CH_3)_4]^+$ met opbrengste tussen 66 en 99 %.

Die mono-metaal en gemengde-metaal komplekse is gekarakteriseer met ATR-FTIR. Die studie het aangedui dat die gemengde-metaal komplekse meer as een bindingsmodus besit, naamlik unidentaat, bidentaat, tridentaat, gebrugde (*syn-syn*) en ioniese bindings.

Die enkelkristal X-straal strukture van $[Pd^{II}Co^{II}(\mu\text{-}OOC(CH_2)_8CH_3)_4]$ **[21]** (Z = 2, ruimte groep $P2_1/c$), $[Pd^{II}Zn^{II}(\mu\text{-}OOC(CH_2)_8CH_3)_4]$ **[36]** (Z = 4, ruimte groep $P2_1/c$), en $[Pd^{II}Ni^{II}(\mu\text{-}OOC(CH_2)_8CH_3)_4]$ **[38]** (Z = 2, ruimte groep *P*-1) is bepaal en het die bindingsmodusse soos deur ATR-FTIR waargeneem, bevestig.

DSC en TGA-MS is gebruik om termiese analise van geselekteerde komplekse te doen. Vloeikristal eienskappe is waargeneem vir $PdCo(C_8)_4$ **[20]**, $PdCo(C_{10})_4$ **[21]** en $PdZn(C_{10})_4$ **[36]**. Polimorfisme is waargeneem vir $PdCd(C_{10})_4$ **[34]**, $PdMn(C_{10})_4$ **[39]** en $PdCu(C_{10})_4$ **[40]**.

Verstelbare temperatuur, gepolariseerde lig mikroskoopstudies is gebruik om lig te werp op die prosesse waargeneem tydens DSC. TGA-MS analise het vlugtige ontbindings produkte aangetoon: metaan, hidroksied ione, water, koolstofmonoksied, suurstof, metanol, propyn, koolstofdioksied en ander produkte. Nie-vlugtige ontbindingsprodukte wat verkry is, is metaal oksiede.

Sikliese voltammetrie, Osteryoung vierkant golf voltammetrie en lineêre skanderings voltammetrie van geselekteerde komplekse het elektroniese komunikasie tussen die verskillende metale aangetoon. Die lengte van die koolstofketting het ‘n invloed op die posisie van oksidasie koppel van die palladium cerium skepwiel karboksilatido komplekse.

As die kettinglengte van die karboksilatido ligand van twee na tien vermeerder word, neem E_{pa} af van **514 mV** vir $[Pd^{II}Ce^{III}(\mu\text{-}OOCCH_3)_4]^+$ **[32]** na **297 mV** vir $[Pd^{II}Ce^{III}(\mu\text{-}OOC(CH_2)_8CH_3)_4]^+$ **[41]**.

Lagies van geselekteerde gemengde-metaal komplekse is op aangepaste silikonplaatjies gespin met behulp van asetoon of dichlorometaan as oplosmiddel. Die voor-katalisator is geaktiveer deur oksidasie in ‘n suurstofstroom by 450 °C. Dit het gelei tot palladiumoksied en metaaloksied op die aangepaste silikonplaatjie se oppervlakte. Die kataliste is getoets vir die oplosmiddel-vrye aerobiese oksidasie van 1-oktadekanol na 1-oktadekanoësuur. Die reaksie is gemoniteer deur die verskuiwing van karboniel strekkingsfrekwensies by 1730 en 1710 cm^{-1} te volg, met behulp van ATR-FTIR. Omskakelingsfrekwensies tussen 0.8 en 2 molekules s^{-1} is verkry vir kataliste wat vanaf kort-ketting gemengde-metaal komplekse berei is. Omskakelings-frekwensies tussen 4 en 7 molekules s^{-1} is vir kataliste verkry wat vanaf lang-ketting gemengde-metaal komplekse berei is. XPS analise van die kataliste het getoon dat die PdO en MO (metaaloksied) verhouding ongeveer 1:1 en ook 1:1.5 is.

Sleutelwoorde: gemengde-metaal karboksilatido komplekse, lang-ketting karboksilatido komplekse, elektrochemie, DSC, TGA, katalise, Silikonplaatjie.

1. Introduction

1.1 Introduction

Metal carboxylatido complexes are well known in the chemical industry, especially the long-chain mono-metal non-paddlewheel complexes.[1,2,3] Metal carboxylatido complexes offer a large variety of industrial applications including uses as disinfectants, additives, liquid crystals, reducing agents, cosmetics, paint coatings and even catalysis.[1,2,3,4]

To get particles evenly dispersed on a solid support to create a mixed-metal heterogeneous catalyst is very difficult. The methodology to obtain a homogeneous dispersion of metal particles on the support surface plays an important role for the metals on the solid support.[5,6] Successive or co-impregnation of two metals onto a solid support is the most common method to prepare bi-metallic heterogeneous catalysts.[7,8,9] To ensure that the metal particles stay as close to each other as possible on the solid support, without aggregating, these catalysts can be prepared from a mixed-metal complex.[10]

Brandon[11] in 1968 published the first paper on short-chain mixed-metal paddlewheel carboxylatido complexes. Kozitsyna, *et al.*[12] (2006) and Akhmadullina, *et al.*[13] (2009), also published papers on mixed-metal paddlewheel complexes, proving that these complexes can be easily crystallised from acetic acid.

Mono-metal non-paddlewheel carboxylate/carboxylatido complexes are notoriously difficult to analyse, most probably due to the difficulty to grow crystals from these complexes, because of their insolubility at room temperature in suitable solvents.[14,15] This causes problems when attempting to record NMR spectra of these complexes. Also, NMR does not give structural information of the mono-metal carboxylate/carboxylatido complexes. Due to these difficulties, the best method of

[1] K. Binnemans, Chem. Rev. 2005, **105**, 4148
[2] R. D. Dworkin, *J. Vinyl technology*, 1989, **11**, 15
[3] S. Mauchauffee, E. Meux and M. Schneider, *Ind. Eng. Chem. Res.*, 2008, **47**, 7533
[4] P. N. Nelson and R. A. Taylor, *Appl. Petrochem Res.*, 2014, **4**, 253
[5] A. Borgna, B. G. Anderson, A. M. Saib, H. Bluhm, M. Havecker, A. Knop-Gericke, A. E. T. Kuiper, Y. Tamminga and J. W. Niemantsverdriet, *J. Phys. Chem. B*, 2004, **108**, 17905
[6] B. Delmon, *J. Thermal. Anal. Cal.*, 2007, **90**, 49
[7] I. Dodoucje, D. P. Barbosa, M. do Carmo Rangel and F. Epron, *Appl. Catal. B: Envir.*, 2009, **93**, 50
[8] B. J. Auten, H. Lang and B. D. Chandler, *Appl. Catal. B: Enviro.*, 2008, **81**, 225
[9] O. S. Alexeev and B. C. Gates, *Ind. Eng. Chem. Res.*, 2003, **42**, 1571
[10] B. Cog and F. Figueras, *J. Mol. Catal. A: Chem.*, 2001, **173**, 117
[11] R.W. Brandon and D.V. Claridge, *Chem. Commun.* 1968, 677
[12] N. Y. Kozitsyna, S. E. Nefedov, F. M. Dolgushin, N. V. Cherkashina, M. N. Vergaftik and I. I. Moiseev, *Inorganica Chimica Acta*, 2006, **359**, 2072
[13] N. S. Akhmadullina, N. V. Cherkashina, N. Kozisyna, I. P. Stolarov, E. V. Perova, A. E. Gekhman, S. E. Nefedov, M. N. Vargaftik, I. I. Moiseev, *Inorg. Chim. Acta*, 2009, **362**, 1943
[14] E. F. Marques, H. D. Burrows and M. da Graca Miguel, *J. Chem. Soc., Faraday Trans.*, 1998, **94**, 1729
[15] L. Jongen, K. Binnemans, D. Hinz and G. Meyer, *Material Science and Engineering C*, 2001, **18**, 199

analysis of these carboxylatido and carboxylate complexes is ATR-FTIR. This method is extensively used internationally in carboxylatido/carboxylate chemistry.[16,17]

Nakamoto[16] and Deacon and Phillips[17] showed that infrared, after single crystal structure determination, is the most powerful tool to obtain structure information or binding modes using the difference between the anti-symmetric and symmetric stretching frequencies of the complexes. Because different binding modes lead to small but noticeable changes in frequencies of symmetric and anti-symmetric vibrations of the carbonyl group, FTIR is often by necessity (due to poor solubility etc.) the preferred instrumental technique to obtain structural information.

It may be hypothesised that by increasing the number of carbons in the short-chain mixed-metal paddlewheel carboxylatido complexes to create long-chain mixed-metal aliphatic carboxylatido paddlewheel complexes. This will lead to catalysts being designed that have a high surface area i.e. little to no aggregation of metals.

The group II metals in this study Ca, Sr and Ba are known as promoters in the Fischer-Tropsch reactions. The catalytic activity of group VII, IX and X, metals for example Mn, Co, Ni and Pd are well documented and form also the basis of catalysis in this study. Group XI and XII metals for example Cu, Zn and Cd are frequently found in industrial piping and have an influence in industrial catalysis and are therefore included in this study. The choice for the mixed-metal complexes for catalytic studies was also based on our interest in the catalytic activity between catalysts that were prepared from short-chain complexes vs long-chain complexes. Turn over frequency (TOF) for all tested catalysts will be used to determine if any changes in catalytic activity were observed under the specified conditions. All the long-chain mixed-metal complexes of this study are completely new. This study also addresses preparative and characterisation issues of the novel complexes.

For this specific reason this research project was undertaken to synthesise long-chain mixed-metal aliphatic bridged paddlewheel carboxylatido complexes which are soluble in chlorinated solvents at room temperature. Developing a new reaction procedure to synthesise these long-chain mixed-metal aliphatic paddlewheel carboxylatido complexes, may result in a purer compound, with high yields. The paddlewheel complexes can be studied using Attenuated Total Reflectance Fourier Transform Infrared Spectroscopy (ATR-FTIR) to identify different binding modes in the complexes. Obtaining crystal structures of the paddlewheel complexes would confirm the binding modes predicted by the ATR-FTIR studies. Thermal analysis of the paddlewheel complexes can provide further insight into the physical properties of these complexes. This might include polymorphism, liquid crystalline mesophase behaviour and decomposition profiles of the complexes. Electrochemistry might give insight to identify any intramolecular communication between the coordinating metal centres of the mixed-metal paddlewheel carboxylatido complexes.

[16] K. Nakamoto, *Infrared and Raman Spectra of Inorganic and Coordination Compounds,* John Wiley & Sons, Inc., 231 - 233 (1997).
[17] G.B. Deacon and R. J. Phillips, *J. Coord. Chem. Rev*., 1980, **33**, 227.

Coating modified silicon wafers with these short- and long-chain mixed-metal aliphatic paddlewheel complexes and testing for catalytic activity, will give an indication to the catalytic activity of these catalysts.

1.2 Objectives

With this background, the following objectives were set for this research project.

Objective 1, Synthesis

Synthesis of long-chain mono-metal aliphatic non-paddlewheel carboxylatido complexes $[Pd_3^{II}(\mu\text{-}OOC(CH_2)_nCH_3)_6]$ where n = 4, 6, 8 or 10 (novel), $K[OOC(CH_2)_nCH_3]$ where n = 4, 6, 8 or 10, $[Co^{II}(OOC(CH_2)_nCH_3)_2]$ where n = 4, 6, 8 or 10, $[M^{II}(OOC(CH_2)_8CH_3)_2]$ where M = Ni, Mn, Zn, Ca or Sr as well as $[Ce^{III}(OOC(CH_2)_8CH_3)_3]$.

Synthesis of short- and long-chain mixed-metal aliphatic paddlewheel carboxylatido complexes $[Pd^{II}Co^{II}(\mu\text{-}OOC(CH_2)_nCH_3)_4]$ where n = 4, 6, 8 or 10 (novel), $[Pd^{II}M^{II}(\mu\text{-}OOCCH_3)_4]$, $[Pd^{II}M^{II}(\mu\text{-}OOC(CH_2)_8CH_3)_4]$ where M = Ba, Cd, Ca, Zn, Sr, Ni, Mn or Cu as well as $[Pd^{II}Ce^{III}(\mu\text{-}OOCCH_3)_4]^+$ and $[Pd^{II}Ce^{III}(\mu\text{-}OOC(CH_2)_8CH_3)_4]^+$ (novel).

Objective 2, Spectroscopy

All synthesised complexes will be characterised *via* Attenuated Total Reflectance Fourier Transform Infrared Spectroscopy (ATR-FTIR). These measurements will give insight into binding modes, frequency shifts and the influence of the aliphatic chain length. ^1H NMR will be employed for the circular palladium carboxylatido complexes. Elemental analysis will be utilised to determine the carbon and hydrogen content of all new complexes synthesised.

Objective 3, X-ray Crystallography

Single crystal X-ray crystallography will be used to determine the molecular structure of selected long-chain mixed-metal aliphatic carboxylatido compounds. Obtaining these structures will confirm the binding modes observed using ATR-FTIR.

Objective 4, Differential scanning calorimetry (DSC)

The thermal properties of the selected compounds listed in objective 1 will be determined using Differential Scanning Calorimetry (DSC) with temperature limits between -50 °C and 450 °C. Solid state transitions, polymorphism, liquid crystal mesophases, melting points and decomposition temperatures will be investigated.

Objective 5, Variable temperature polarised light microscopy

Selected carboxylatido compounds will be subjected to variable temperature polarised light microscopy to confirm thermal events detected by the DSC studies.

Objective 6, Thermogravimetric analysis coupled with mass spectroscopy (TGA-MS)

Thermogravimetric analysis (TGA) will be used to determine the continuous mass loss curves of selected compounds listed in objective 1 with temperature limits between 30 to 700 °C, to identify the volatile and non-volatile products formed during the thermal decomposition. Mass spectroscopy coupled with TGA will be used to identify gases liberated while heating the circular palladium complexes and palladium cobalt paddlewheel complexes, to obtain the decomposition profiles.

Objective 7, Electrochemistry

An electrochemical study will be performed on selected mixed-metal paddlewheel complexes in DCM. From the cyclic voltammagrams the oxidation and reduction potentials of the redox active centres can be determined and an attempt will be made to establish if there is any intra-molecular communication between the metal centres.

Objective 8, Catalysis and XPS

All mixed-metal complexes that are soluble (in suitable solvents) will be coated onto hydroxylated silicon wafers using spin coating. These pre-catalysts will be thermally activated and its catalytic activity will be tested using the model reaction of the aerobic solvent-free oxidation of 1-octadecanol to 1-octadecanoic acid. X-ray Photoelectron Spectroscopy (XPS) will be used to characterize these modified silicon wafer surfaces.

2. Literature Survey

2.1. Introduction

The literature survey has its own numbering system as is customary at UFS. A survey of mixed-metal paddlewheel and mono-metal non-paddlewheel aliphatic carboxylatido complexes is presented in this chapter. Published methods that were used to synthesise these compounds are reviewed. Related published crystal structures, thermal studies (DSC and TGA), surface chemistry of modified silicon wafers (XPS) and FTIR spectroscopy are illustrated and discussed. The electrochemistry of palladium acetatido complex will also be discussed. Coating of the complexes onto modified silicon wafers and the catalytic activity of these catalysts will also be reviewed.

2.2. Carboxylic acids

Carboxylic acids are organic compounds containing the –COOH functionality, which consist of a carbonyl and hydroxyl group. When the hydrogen atom is removed from the carboxylic acid a carboxylate anion ($-COO^-$) is produced. This anion is relatively stable due to the delocalization of the electron cloud over the C-O and C=O bonds (see **Figure 2.1**). Carboxylic acids have a relatively low pK_a in comparison to e.g. alcohols, due to this resonance stabilisation.[1,2]

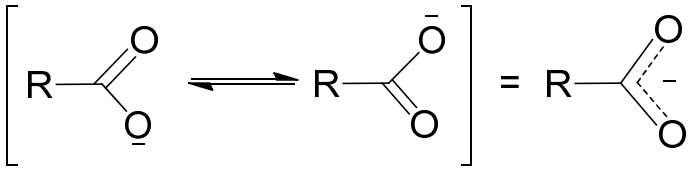

Figure 2.1: Resonance stabilisation of the carboxylate anion.

Carboxylic acids occurring in nature include fatty acid (a carboxylic acid containing a long aliphatic chain), hydroxy acids (a class of carboxylic acids containing an extra hydroxyl group e.g. citric acid from citrus fruits and glucolic acid from sugar cane), keto acids (a class of carboxylic acid containing a ketone group) and important life sustaining amino acids (a class of carboxylic acids containing an amine group).

Many other derivatives of carboxylic acids, have a wide variety of applications. Some of these include acyl halides, acid anhydrides, esters and amides. Esters for example are an important class of glycerides and are commonly found in essential oils, and are thus used in the fragrance industry.[1,2]

[1] J. McMurry, *Organic Chemistry*, Brooks/Cole Publishing Company Pacific Grove, California, 1996, 4th, 775.

Even though carboxylic acids can be prepared by a number of reactions it is, however, mainly prepared by the oxidation of different functional groups (see **Figure 2.2**). These include the oxidation[1,2] of an alcohol (**II**) using an oxidant like $KMnO_4$ or Jones's reagent (CrO_3, H_2O, H_2SO_4), or the oxidation of an aldehyde group (**III**) with either Tollen's reagent (basic Ag_2O) or the already named Jones's reagent to produce the desired carboxylic acid (**I**). The reaction of an alkene with $KMnO_4$ (**IV**) or the oxidation of Grignard's reagents (**V**) with CO_2 also produces carboxylic acids.[1,2]

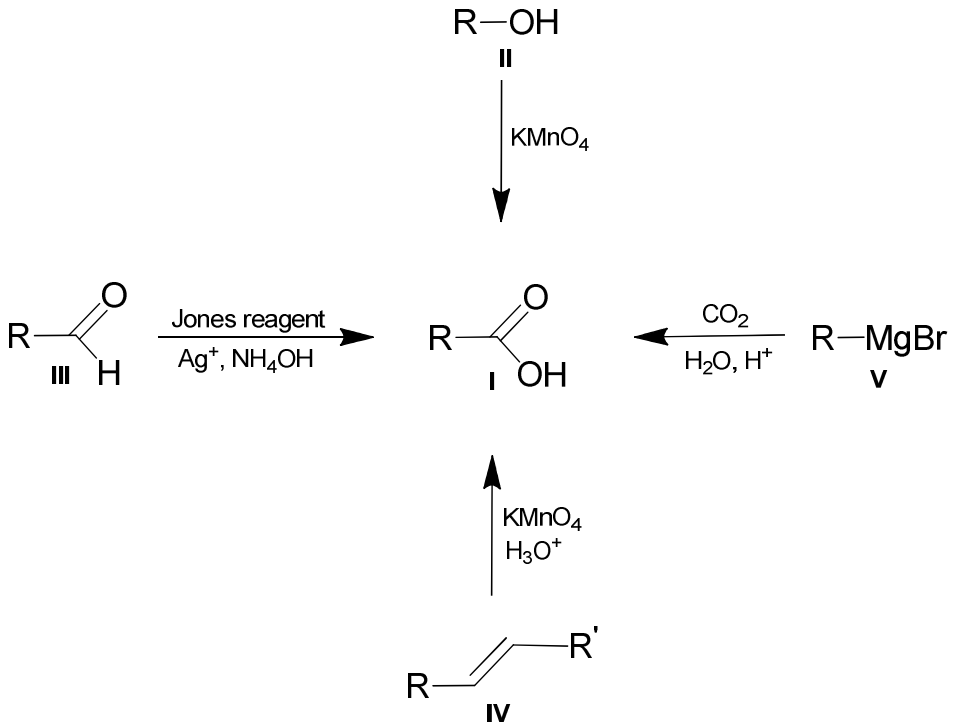

Figure 2.2: The preparation of carboxylic acids by oxidation of different functional groups.[1,2]

The hydrolysis[1] of a variety of different functional groups, including acid halides (**VI**), anhydrides (**VII**), esters (**VIII**), amides (**IX**), and nitriles (**X**), with acid and heat can also be used to produce carboxylic acids (see **Figure 2.3**).

[2] R. J. Fessenden and J. S. Fessenden, *Organic Chemistry*, Brooks/Cole Publishing Company Pacific Grove, California, 1990, 4th, 498.

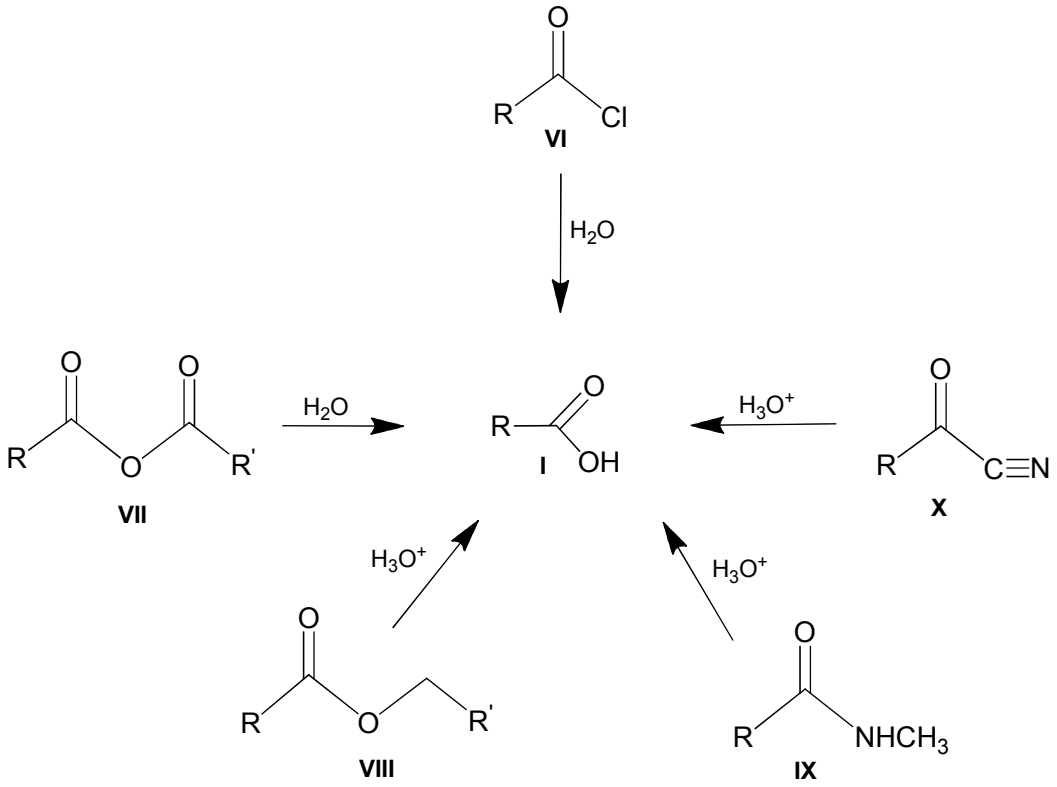

Figure 2.3: The preparation of carboxylic acids by hydrolysis of different functional groups.[1,2]

2.3. Metal carboxylate and carboxylatido complexes*

To simplify the writing process, the following short hand system will be used. The circular tripalladium hexaacetatido complex, $Pd_3(\mu\text{-}OOCCH_3)_6$, **[1]**, will be abbreviated as follows: $Pd_3(C_2)_6$, where the Pd_3, refers to the three palladium atoms arranged in a triangle, the C_2, indicates the number of carbons in the carboxylatido ligand and $(C_2)_6$ indicates that there are six acetatido ligands coordinated to the three palladium atoms in a bridged type structure. Non-paddlewheel $Mn(OOCCH_3)_2$ **[2]**, complexes will be abbreviated as follows: $Mn(C_2)_2$, where Mn refers to the manganese atom in the complex, C_2 indicates the number of carbons in the carboxylatido ligand and $(C_2)_2$ indicates that there are two acetatido ligands coordinated to the manganese atom. Paddlewheel, $PdMn(\mu\text{-}OOCCH_3)_4$ **[3]**, complexes will be abbreviated as follows: $PdMn(C_2)_4$, where PdMn refers to the palladium and manganese atoms in the complex, C_2 indicates the number of carbons in the carboxylatido ligand and $(C_2)_4$ indicates that there are four acetatido ligands coordinated to the palladium and manganese atoms. See **Figure 2.4** for the paddlewheel type structures.

*According to IUPAC, the term "carboxylate" implies that the anionic carboxylate ligand is ionically bound (i.e. electrostatically) to the K^+ cation, e.g. $K[OOCCH_3]$. The term "carboxylatido" implies that the anionic ligand is covalently coordinated to a metal, e.g. $[Pd_3(\mu\text{-}OOCCH_3)_6]$.

These abbreviations will also apply to the long-chain aliphatic mono-metal carboxylatido complexes.

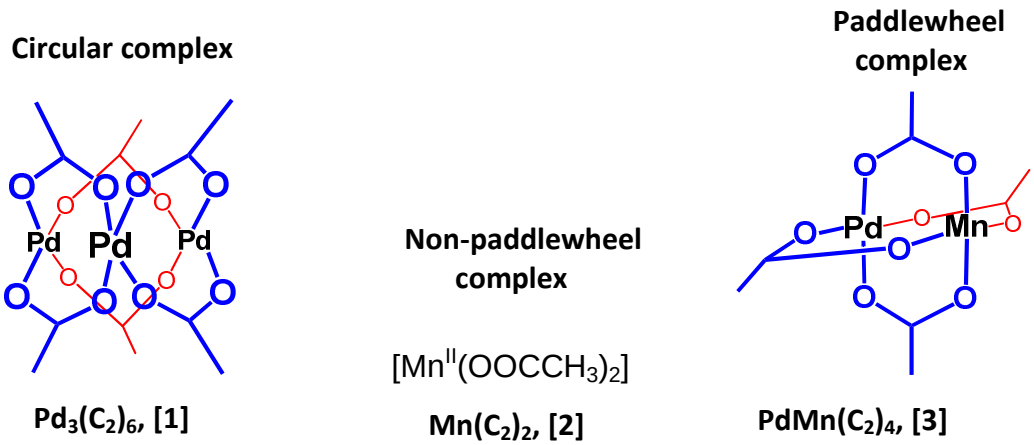

Figure 2.4: Shows the circular hexaacetatidotripalladium(II) complex, $Pd_3(\mu\text{-}OOCCH_3)_6$, $Pd_3(C_2)_6$, **[1] (left)**, non-paddlewheel $Mn(OOCCH_3)_2$, $Mn(C_2)_2$, **[2]**, **(middle)**, and tetraacetatidopalladium(II)manganese(II), $PdMn(\mu\text{-}OOCCH_3)_4$, $PdMn(C_2)_4$, **[3]** mixed-metal paddlewheel complex. The red carboxylatido ligands are behind the page plane while the blue ones are in the front.

With the onset of the industrial revolution of the 1800's, rapid progress was made in the field of metal carboxylates and carboxylatido* complexes and since this time, their use in a variety of different industries increased. Some of the uses includes: drying agents for paints and printing, accelerators in unsaturated polyesters, curing agents for polyurethane, additives for lubricating oils and greases, catalysts in organic reactions, fungicides and wood preservatives and as steel cord-rubber adhesion promoters.[3,4,5]

[3] R. D. Dworkin, *J. Vinyl technology*, 1989, **11**, 15
[4] S. Mauchauffee, E. Meux and M. Schneider, *Ind. Eng. Chem. Res.*, 2008, **47**, 7533
*According to IUPAC, the term "carboxylate" implies that the anionic carboxylate ligand is ionically bound (i.e. electrostatically) to the K^+ cation, e.g. $K[OOCCH_3]$. The term "carboxylatido" implies that the anionic ligand is covalently coordinated to a metal, e.g. $[Pd_3(\mu\text{-}OOCCH_3)_6]$.
[5] P. N. Nelson and R. A. Taylor, *Appl. Petrochem Res.*, 2014, **4**, 253

2.3.1. Synthesis of non-paddlewheel carboxylate and carboxylatido complexes

Researchers have synthesised a variety of long-chain mono-metal aliphatic non-paddlewheel carboxylates and carboxylatido complexes. Including alkali metals[6,7,8,9] (Na, K), alkaline earth metals[10] (Ca), transition metals[11] (Co, Ni, Cu, Zn, Cd) and lanthanide metals[12,13,14] (La-Lu), via either a one pot or a two-step metathesis process. The synthesis involves neutralising the carboxylic acid (fatty acid) in an alcoholic and/or aqueous medium by using KOH or NaOH and then slowly adding the metal nitrate/halide/acetate dissolved in an alcohol/aqueous medium to the K/Na carboxylate solution. These carboxylatido complexes are generally insoluble in alcohols and aromatic solvents at room temperature, but can be recrystallised from these solvents at elevated temperatures. Hexanol was found to be the best recrystallisation solvent at temperatures between 60-80 °C for the lanthanide complexes[15,16] Valor *et al*.[17] synthesised short- and long-chain aliphatic calcium carboxylatido/carboxylate complexes by mixing calcium hydroxide powder with an excess of the liquid acids in an agate mortar. Solid carboxylic acids were heated to 85 ˚C in distilled water. To this was then added an aqueous solution of calcium hydroxide, with constant stirring. Subsequently the target complexes were filtered and washed with distilled water and dried at room temperature. The powders were then furthermore washed with chloroform and again dried at room temperature.

Stephenson *et al*. [18] synthesised a variety of nobel metal carboxylatido complexes (Pd, Pt and Rh), of which particular interest was the circular tripalladium hexaacetatido complex. Interaction between palladium black/sponge, concentrated nitric acid and acetic acid yielded the circular tripalladium hexaacetatido complex, $Pd_3(C_2)_6$, **[1]**, while NO_x gases are liberated see **Figure 2.5**.

---

[6] T. R. Lomer *Acta Cryst.*, 1952, **5**, 11
[7] T. R. Lomer and J. H. Dumbleton, *Acta Cryst.*, 1965, **19**, 301
[8] T. Ishioka, H. Wakisaka, T. Saito, and I Kanesaka, *J. Phys. Chem. B*, 1998, **102**, 5239
[9] B. Zacharie, A. Ezzitouni, J. Duceppe and C. Penney, *Org. Process Res Dev*, 2009, **13**, 581.
[10] R. F. P. Pereira, A. J. M. Valente, M. Fernandes and H. D. Burrows. *Phys. Chem. Chem. Phys.*, 2012, **14**, 7517
[11] A. Mesbah, C. Juers, M. Francois, E. Rocca and J. Steinmetz, *Z. Kristallogr. Suppl*, 2007, **26**, 593
[12] S. N. Misra, T. N. Misra and R. C. Mehrotra, *J. Inorg. Nucl. Chem.*, 1963, **25**, 195
[13] E. F. Marques, H. D. Burrows and M. da Graca Miguel, *J. Chem. Soc, Faraday Trans.*, 1998, **94**, 1729
[14] K. Binnemans, L. Jongen, C. Gorller-Walrand, W. D'Olieslager, D. Hinz and G. Meyer, *Eur. J. Inorg. Chem.* 2000, 1429
[15] E. F. Marques, H. D. Burrows and M. da Graca Miguel, *J. Chem. Soc., Faraday Trans.*, 1998, **94**, 1729
[16] L. Jongen, K. Binnemans, D. Hinz and G. Meyer, *Material Science and Engineering C*, 2001, **18**, 199
[17] A. Valor, E. Reguera, E. Torres-García, S. Mendoza and F. Sanchez-Sinencio, *Thermochimica Acta*, 2002, **389**, 133
[18] T. A. Stephenson, S. M. Morehouse, A**.** R. Powell, J. P. Heffer, and G. Wilkinson, *J. Chem. Soc.*, 1965, 3632

Benzoatido-, trifluoroacetatido-, and pentafluoropropionatidopalladium(II) derivatives can also be obtained through exchange reactions.

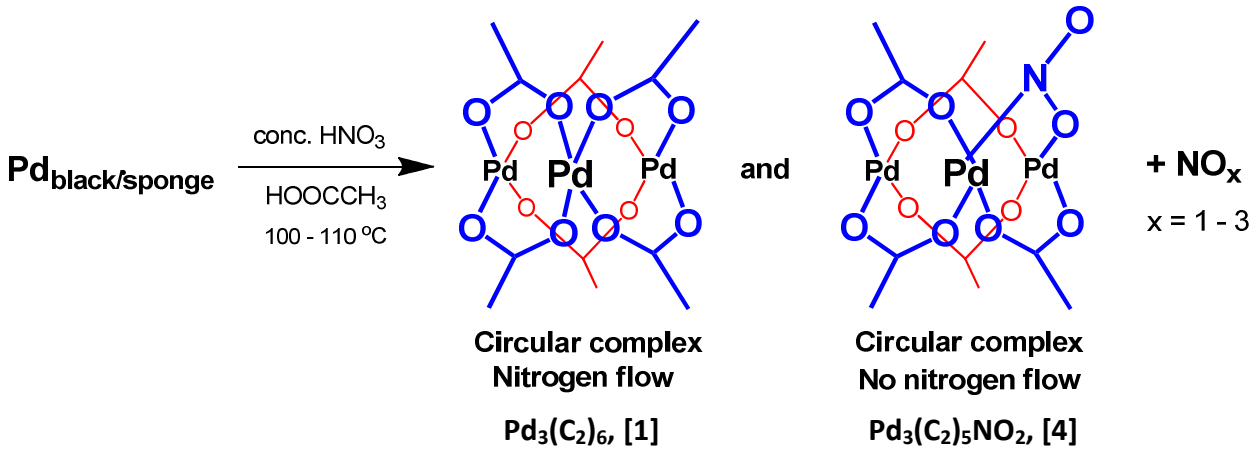

Figure 2.5: The synthesis of circular hexaacetatidotripalladium(II) complex, $Pd_3(\mu\text{-}OOCCH_3)_6$, $Pd_3(C_2)_6$ **[1]**, and the circular pentaacetatidotripalladium(II) nitrate complex, $Pd_3(\mu\text{-}OOCCH_3)_5(NO_2)$, $Pd_3(C_2)_5NO_2$ **[4]**. The red carboxylatido ligands are behind the page plane while the blue ones are in the front.

Using a similar method to that of Stephenson *et al*[19] Bakhmutov *et al.*[20] prepared a compound where one of the acetatido ligands of the circular paddlewheel complex $Pd_3(C_2)_6$, **[1]**, are replaced with a nitrogen dioxide, to produce the circular tripalladium pentaacetatido nitrate, $Pd_3(C_2)_5(NO_2)$, **[4]**, complex. In this complex, the nitrogen atom of the nitrite group is coordinated to one of the palladium atoms, while the adjacent palladium atom is coordinated to one of the oxygen atoms. This was achieved by reducing palladium(II) chloride with sodium hydroxide and sodium formate to form palladium black. The palladium black was then allowed to react with concentrated nitric acid and acetic acid. With no nitrogen flow a mixture of the circular $Pd_3(C_2)_6$, **[1]** and circular $Pd_3(C_2)_5(NO_2)$, **[4]**, complexes was obtained, see **Figure 2.5**. With a nitrogen flow, only the circular $Pd_3(C_2)_6$, **[1]**, complex was obtained.

2.3.2. Synthesis of mixed-metal paddlewheel acetatido complexes

Palladium based mixed-metal carboxylatido complexes were synthesised by Brandon and Claridge[21] by adding equimolar amounts of the circular $Pd_3(C_2)_6$, **[1]**, complex and another bivalent metal such as ($Mn(C_2)_2$, **[2]**, $Ba(C_2)_2$, **[5]**, $Sr(C_2)_2$, **[6]**, $Ca(C_2)_2$, **[7]**, $Zn(C_2)_2$, **[8]**, $Co(C_2)_2$, **[9]**, $Ni(C_2)_2$, **[10]**, $Cu(C_2)_2$,**[11]**, or $Cd(C_2)_2$,**[12]**) acetatido complexes, usually the hydrate, in acetic acid. Heating resulted in the target complexes $PdMn(C_2)_4$, **[3]**, $PdBa(C_2)_4$, **[13]**, $PdSr(C_2)_4$, **[14]**,

[19] T. A. Stephenson, S. M. Morehouse, A**.** R. Powell, J. P. Heffer, and G. Wilkinson, *J. Chem. Soc.*, 1965, 3632
[20] V. I. Bakhmutov, J. F. Berry, F. A. Cotton, S. Ibragimov and C. A. Murillo, *Dalton Trans.*, 2005, 1989
[21] R.W. Brandon and D.V. Claridge, *Chem. Commun*. 1968, 677

$PdCa(C_2)_4$, **[15]**, $PdZn(C_2)_4$, **[16]**, $PdCo(C_2)_4$, **[17]**, $PdNi(C_2)_4$, **[18]**, $PdCd(C_2)_4$, **[19]** or $PdCu(C_2)_4$, **[20]** see **Figure 2.6**.

Kozitsyna, *et al.*[22] and Akhmadullina, *et al.*[23] also prepared short-chain mixed-metal paddlewheel acetatido complexes, including $PdMn(C_2)_4$, **[3]**, $PdZn(C_2)_4$, **[16]**, $PdCo(C_2)_4$, **[17]**, $PdNi(C_2)_4$, **[18]**, $PdCu(C_2)_4$, **[20]**, and $PdCe(C_2)_4$, **[22]**, according to a similar method, as illustrated in **Figure 2.6**. Yields for the crystals obtained range between 75 % to 93 %.

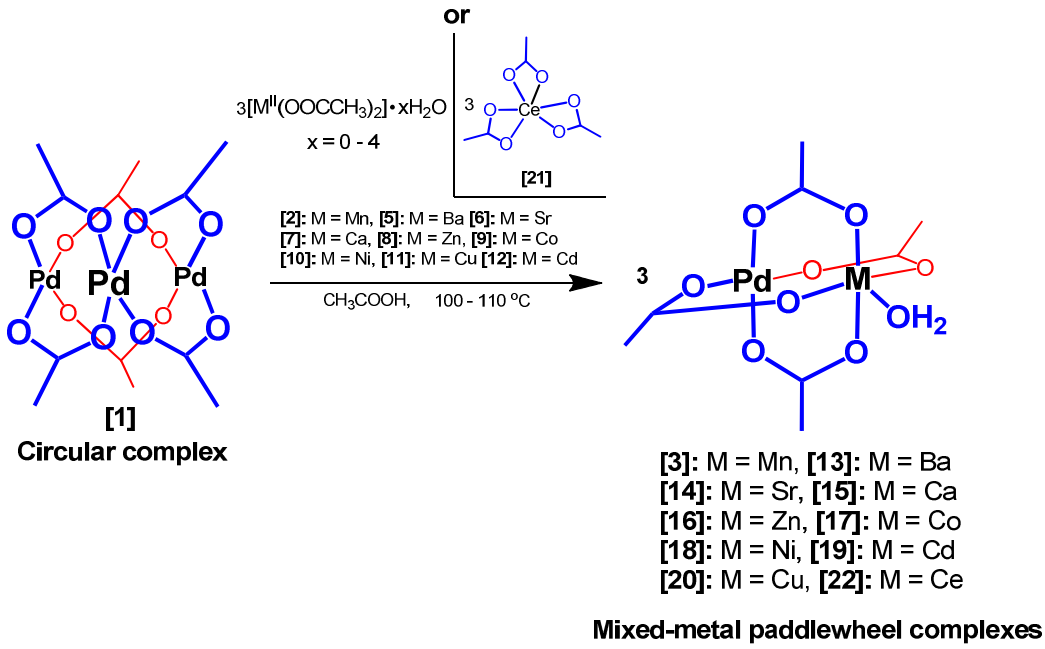

Figure 2.6: The synthesis of tetracarboxylatidopalladium(II)metal(II) and tetracarboxylatidopalladium(II)cerium(III) mixed-metal paddlewheel complexes **[3]**, **[13-20]** or **[22]**. The red carboxylatido ligands are behind the page plane while the blue ones are in the front.

Li *et al.*[24], synthesised deca(trifluoroacetatido)dipalladium(II)dibismuth(III) di(trifluoroacetic acid), $[Bi_2Pd_2(O_2CCF_3)_{10}(HO_2CCF_3)_2]$, by sealing a stoichiometric mixture of $[Bi(O_2CCF_3)_3(HO_2CCF_3)]$ and $[Pd_3(O_2CCF_3)_6]$ in an evacuated glass ampule. Yellow-brown block crystals were obtained (3 days) after placing the ampule in an electric furnace. Depending on the experiment, the furnace was kept between 120-130 ˚C. Crystals were collected in the cold section of the ampule where the temperature was 6 ˚C lower. These crystals were grafted onto functionalised carbon supports and activated by placing it in an oven at 500 ˚C under nitrogen flow. The resulted palladium/bismuth supported on the carbon catalysts were then tested by oxidising D-glucose into gluconic acid.

[22] N. Y. Kozitsyna, S. E. Nefedov, F. M. Dolgushin, N. V. Cherkashina, M. N. Vergaftik and I. I. Moiseev, *Inorg. Chim. Acta*, 2006, **359**, 2072

[23] N. S. Akhmadullina, N. V. Cherkashina, N. Kozisyna, I. P. Stolarov, E. V. Perova, A. E. Gekhman, S. E. Nefedov, M. N. Vargaftik, I. I. Moiseev, *Inorg. Chim. Acta*, 2009, **362**, 1943

[24] B. Li, H. Zhang, L. Huynh, C. Diverchy, S. Hermans, M. Devilliers and E. V. Dikarev, *Inorg. Chem.*, 2009, **48**, 6152

Li *et al.*[25] also synthesised tetra(trifluoroacetatido)rhodium(II)molybdenum(II), [$MoRh(O_2CCF_3)_4$], using the same method as described in the previous paragraph. A stoichiometric mixture of [$Mo_2(O_2CCF_3)_4$] and [$Rh_2(O_2CCF_3)_4$] was sealed in an evacuated glass ampule resulting in [$MoRh(O_2CCF_3)_4$]. The furnace temperature was 150 ˚C and the greenish crystals were obtained after 7 days. These crystals had 50 % molybdenum and 50 % rhodium in the crystal structure.

2.4. Binding modes and crystal structures

2.4.1. Binding modes of coordination

Carboxylatido complexes are able to form a variety of stable coordination complexes by using a number of different binding modes. The cationic metal centre is responsible for the binding mode of the carboxylatido group.[26] Four binding modes of carboxylatido oxygen-metal centre have been identified, i.e. ionic, unidentate, bidentate and bridging, see **Table 2.1** and **Table 2.2**.[27]

Following the synthesis of circular tripalladium hexacarboxylatido complex **[1]** the carbonyl stretching frequency (C=O, at *c.a.* 1700 cm^{-1}) of the free acid (acetic acid) is replaced by the coordinated carboxylatido stretching frequencies at *ca.* 1600 cm^{-1} and 1427 cm^{-1}.
The stretching frequency at *ca.* 1600 cm^{-1} is associated with the anti-symmetric carboxylatido stretching frequency, while the stretching frequency at *ca.* 1427 cm^{-1} is associated with the symmetric carboxylatido stretching frequency of the circular tripalladium hexacarboxylatido complex **[1]**. By calculating the difference between the anti-symmetric and symmetric frequencies the binding mode of the complex may be determined.[18]

[25] B. Li, H. Zhang, L. Huynh, M. Shatruk and E. V. Dikarev, *Inorg. Chem.*, 2007, **46**, 9155
[26] R. K. Hocking and T. W. Hambley, *Inorg. Chem.*,2003, **42**, 2833.

Table 2.1: Ionic, unidentate, bidentate and bridging carboxylatido binding modes.

Type	Description	Example
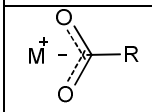	Ionic	$[Co(imidazole)_6](O_2CMe)_2H_2O$[28] $K(O_2CMe)MeCO_2H$[29]
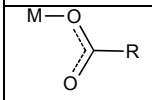	Unidentate	$B(O_2CMe)_2(acac)$[30] $Li(OOCCH_3)\bullet 2H_2O$[31]
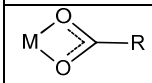	Bidentate	$Zn(O_2CMe)_2\bullet(H_2O)_2$[32]
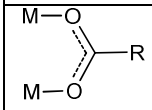	Bridging	Several types exist see table 2.2

Deacon and Philips[33] performed a detailed study on eighty-four acetatido and trifluoroacetatido complexes, seventy acetatido and fourteen trifluoroacetatido complexes.

The difference between the carboxylatido stretching anti-symmetric and symmetric frequencies is calculated as follows:

$$\Delta_{Difference} = \mathbf{(C\overline{\cdots}O)^{anti} - (C\overline{\cdots}O)^{sym}}$$

In the above equation, $\mathbf{(C\overline{\cdots}O)^{anti}}$ is the wavenumber of the anti-symmetric frequencies and $\mathbf{(C\overline{\cdots}O)^{sym}}$ is the wavenumber of the symmetric frequencies. For a $\Delta_{Difference} > 200$ cm^{-1}, the carboxylatido binding mode to the metal is considered to be unidentate while for a $\Delta_{Difference} < 120$ cm^{-1}, the binding mode is considered to be bidentate. When a series of symmetric and anti-symmetric stretching frequencies are observed that results in a $\Delta_{Difference} = 120 - 200$ cm^{-1}, the binding mode is considered to be bridging. For a $\Delta_{Difference} = 150 - 200$ cm^{-1}, (mostly closer to 150 cm^{-1}), the binding mode is considered to be ionic. This latter range overlaps with the $\Delta_{Difference}$ region of the bridging binding mode, making it sometimes difficult to distinguish between the bridging and ionic complexes. The bidentate and unidentate complexes can however be clearly identified from their $\Delta_{Difference}$ values.[33]

---

[27] G. Wilkinson, R.D. Gillard and J.A. McCleverty, *Comprehensive Coordination Chemistry,* Pergamon Press, Oxford, 1987, **2**, 435
[28] A. Gadet and O. L. Soubeyran, *Acta Crystallogr. Sect. B*, 1974, **30**, 716
[29] M. Currie, *J. Chem. Soc., Perkin Trans II*, 1972, 832
[30] F. A. Cotton and W. H. Ilsley, *Inorg. Chem.*, 1982, **21**, 300
[31] A. Amirthalingham and V. M. Padmanabhan, *Acta. Cryst.*, 1985, **11**, 896
[32] J. N. van Niekerk, F. R. L. Schoening and J. H. Talbot, *Acta Crystallogr.*, 1953, **6**, 720
[33] G.B. Deacon and R. J. Phillips, *J. Coord. Chem. Rev*., 1980, **33**, 227

Table 2.2: Different binding modes of carboxylatido oxygen-metal bridging coordination.

Type	Description	Example
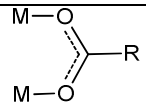	*Syn-syn*	$(Os(O_2CCH_3)(CO)_3)_2$[34] $(Rh(O_2CCH_3)_2py)_2$[35]
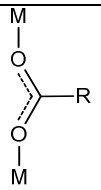	*Ant-anti*	$Mn(O_2CCH_3)_2(H_2O)_4$[36] $Mn(O_2CCH_3)(salen)$[37]
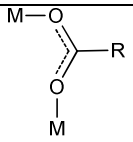	*Syn-anti*	$Cu(O_2CH)_2$[38] $(CH_3)_3Sn(O_2CCH_3)$[39]
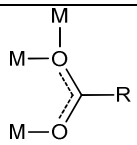	Tridentate	$Cu(O_2CCH_3)$[40]

Table 2.3: Comparison of $\Delta_{Difference}$ values between the anti-symmetric and symmetric carbonyl stretching frequencies.

	Brandon 1968[21]			**Kozitsyna 2006[22]**		
Complex	**$(C\overline{\cdots}O)^{anti\text{-}sym}$**	**$(C{=}O)^{sym}$**	**$\Delta_{Difference}$**	**$(C\overline{\cdots}O)^{anti\text{-}sym}$**	**$(C{=}O)^{sym}$**	**$\Delta_{Difference}$**
$PdMn(C_2)_4$, **[2]**	1600	1410	190 Bridging	1605	1422	183 Bridging
$PdBa(C_2)_4$, **[13]**	1631	1412	219 Unidenate	-	-	-
$PdSr(C_2)_4$, **[14]**	1626	1412	214 Unidentate	-	-	-
$PdCa(C_2)_4$, **[15]**	1629	1435	194 Bridging	-	-	-
$PdZn(C_2)_4$, **[16]**	1626	1395	231 Unidentate	1595	1397	198 Bridging
$PdCo(C_2)_4$, **[17]**	1616	1400	216 Unidentate	1610	1406	201 Unidentate
$PdNi(C_2)_4$, **[18]**	1600	1400	200 Unidentate	1611	1387	224 Unidentate
$PdCd(C_2)_4$, **[19]**	1600	1410	190 Bridging	-	-	-
$PdCu(C_2)_4$, **[20]**	1608	1449	159 Bridging	1607	1429	178 Bridging
$PdCe(C_2)_4$, **[22]**	-	-	-	1559	1445	114 Bidentate

[34] J. G. Bullit and F. A. Cotton, *Inorg. Chim. Acta*, 1971, **5**, 406 and refs. therein
[35] Y. B. Koh, G. G. Christoph, Inorg. Chem., 1978, **17**, 2590
[36] E. F. Bertaut, Tran Qui Duc, P. Burlet, P. Burlet, M. Thomas and J. M. Moreau, *Acta Crystallogr. Sect. B*, 1974, **30**, 2234
[37] J. E. Davies, B. M. Gatehouse and K. S. Murray, *J. Chem. Soc., Dalton Trans.*, 1973, 2523
[38] G. A. Barclay and C. H. L. Kennard, *J. Chem. Soc.*, 1961, 3289
[39] H. Chih and B. R. Penfold, *J. Cryst. Mol. Struct.*, 1973, **3**, 285

Table 2.3 contains the carbonyl stretching frequencies obtained from IR values determined by Brandon *et al.*[21] and Kozitsyna *et al.*[22] From the table it is clear that the complexes have a mixture of unidentate and bridging binding modes across the two metals. Brandon *et al.*[21] obtained bridging binding modes for **[2]**, **[15]**, **[19]** and **[20]** as well as a unidentate binding mode for **[13]**, **[14]** and **[16-18]**. Kozitsyna *et al.*[22] obtained a bridging binding mode for **[2]**, **[16]** and **[20]**, as well as unidentate binding mode for **[17]** and **[18]**. Furthermore, Kozitsyna *et al.*[22] assigned a bidentate binding mode for **[22]**.

Table 2.4: : The anti-symmetric and symmetric carbonyl stretching as well as the $\Delta_{Difference}$ values obtained from IR data of mono-metal aliphatic complexes indicating their mode of coordination.[13]

Complex		n=8	n=10	n=12	n=14	n=16	n=18
$Na[OOC(CH_2)_nCH_3]$	$(C\overline{\cdots}O)^{anti-sym}$	1565	-	1563	-	1563	1563
	$(C=O)^{sym}$	1427	-	1427	-	1425	1425
	$\Delta_{Difference}$	138 Ionic	-	136 Ionic	-	138 Ionic	138 Ionic
$[Ce(OOC(CH_2)_nCH_3)_3]$	$(C\overline{\cdots}O)^{anti-sym}$	1532	1530	1537	1545	1541	1543
	$(C=O)^{sym}$	1406	1410	1412	1412	1412	1414
	$\Delta_{Difference}$	126 Bidentate	120 Bidentate	125 Bidentate	133 Bidentate	129 Bidentate	129 Bidentate
$[Cu_2(OOC(CH_2)_nCH_3)_4]$	$(C\overline{\cdots}O)^{anti-sym}$	1587	1586	1587	-	1585	-
	$(C=O)^{sym}$	1416	1416	1417	-	1416	-
	$\Delta_{Difference}$	171 Bridging	170 Bridging	170 Bridging	-	169 Bridging	-
$[Zn(OOC(CH_2)_nCH_3)_2]$	$(C\overline{\cdots}O)^{anti-sym}$	1541	1543	1543	1542	1541	1544
	$(C=O)^{sym}$	1400	1400	1401	1400	1400	1400
	$\Delta_{Difference}$	141 Bidentate	142 Bidentate	143 Bidentate	141 Bidentate	141 Bidentate	144 Bidentate

Table 2.4 contains the anti-symmetric and symmetric carbonyl stretching frequencies as well as the $\Delta_{Difference}$ values obtained from IR data of a series of three mono-metal and one dicopper[41,42] paddlewheel carboxylatido complexes.[13] Marques *et al.* argued that zinc carboxylatido complexes have bidentate binding modes and, because their $\Delta_{Difference}$ values are comparable to those of the cerium carboxylatido complexes, they have assigned the binding mode of the cerium carboxylatido complexes as bidentate. The sodium carboxylates were assigned an ionic binding mode and the copper carboxylatido complexes were assigned a bridging binding mode.[13]

[40] R. D. Mounts, T. Ogura and Q. Fernando, *Inorg. Chem*., 1974, **13**, 802
[41] T.R. Lomer and K. Perera, *Acta Cryst.*, 1974, **B30**, 2912
[42] T.R. Lomer and K. Perera, *Acta Cryst.*, 1974, **B30**, 2913

2.4.2. Mixed-metal paddlewheel acetatido molecular structures

Kozitsyna, *et al.*[22] obtained crystals for $PdZn(C_2)_4$, **[16]**, $PdCo(C_2)_4$, **[17]** and $PdNi(C_2)_4$, **[18]** see **Figure 2.7**.

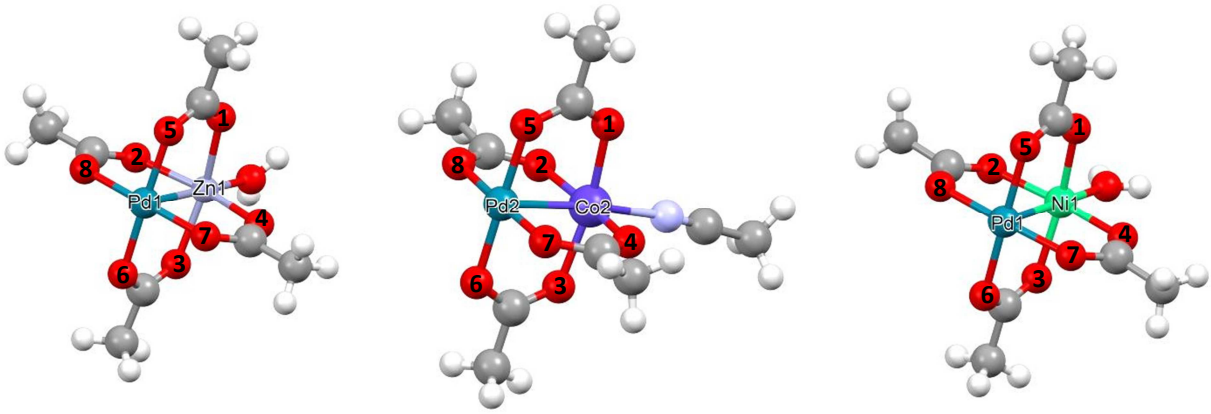

$PdZn(C_2)_4$ **[16]** $PdCo(C_2)_4$ **[17]** $PdNi(C_2)_4$ **[18]**

Figure 2.7: Three mixed-metal paddlewheel carboxylatido molecular structures of $PdZn(C_2)_4$ **[16] (left)**, $PdCo(C_2)_4$ **[17] (middle)** and $PdNi(C_2)_4$ **[18] (right)**.[22]

The complexes in **Figure 2.7** are described as being a mixed-metal paddlewheel tetraacetatido bridged unit. The Zn/Co/Ni metal atoms have an unusual distorted tetragonal-pyramidal environment because of the O atoms belonging to the acetatido adducts and the O/N atom of the Co/Zn/Ni coordinated acetonitrile/water molecule. **Table 2.5** contains selected bond lengths (Å) and angles (°) of $PdZn(C_2)_4$, **[16]**, $PdCo(C_2)_4$, **[17]** and $PdNi(C_2)_4$ **[18]**. The Pd-M bond length in each crystal is 2.5811(6) Å, 2.5304(8) Å and 2.483(2) Å for $PdZn(C_2)_4$, **[16]**, $PdCo(C_2)_4$, **[17]** and $PdNi(C_2)_4$ **[18]** respectively. The Pd-O bond lengths, for $PdNi(C_2)_4$, are in general longer than that of $PdCo(C_2)_4$ and $PdZn(C_2)_4$, while the M-O bond lengths are in general the same distance, with the exception of Zn-O(4) which has a much longer bond length with a distance of 2.135(3) Å. Complexes with dimetal (M-M) bridging coordinating units for example Mo-Mo and Rh-Rh where the bond lengths are 2.1036(4) Å and 2.3813(8) Å respectively, have significantly shorter metal-metal bonds than the mixed-metal carboxylatido complexes **[16-18]**. Shorter bond length means a stronger bond between the bridged complexes.[25]

Table 2.5: Selected bond lengths (Å) and angles (˚) for $PdZn(C_2)_4$ **[16]**, $PdCo(C_2)_4$ **[17]** and $PdNi(C_2)_4$ **[18]**.[22]

$PdZn(C_2)_4$ [16]				**$PdCo(C_2)_4$ [17]**			
Atoms	**length (Å)**	**Atoms**	**Angles (°)**	**Atoms**	**length (Å)**	**Atoms**	**Angles (°)**
Pd-Zn	2.5811(6)	Zn-Pd-O(5)	88.93(8)	Pd-Co	2.5304(8)	O(7)-Pd-O(5)	88.97(16)
Zn-O(1)	2.049(3)	Zn-Pd-O(8)	89.52(7)	Co-O(1)	2.061(4)	O(8)-Pd-O(5)	90.33(16)
Zn-O(2)	2.068(3)	Zn-Pd-O(7)	91.25(7)	Co-O(2)	2.085(4)	O(8)-Pd-O(6)	89.43(17)
Zn-O(3)	2.064(2)	Zn-Pd-O(6)	90.56(7)	Co-O(3)	2.037(4)	O(6)-Pd-O(7)	91.29(17)
Zn-O(4)	2.135(3)	O(8)-Pd-O(6)	89.83(11)	Co-O(4)	2.061(4)	Co-Pd-O(7)	90.96(10)
Pd-O(5)	2.003(3)	O(7)-Pd-O(5)	89.94(11)	Pd-O(5)	2.006(4)	Co-Pd-O(5)	89.77(11)
Pd-O(6)	1.999(3)	O(6)-Pd-O(7)	90.02(11)	Pd-O(6)	1.996(4)	Co-Pd-O(8)	90.24(11)
Pd-O(7)	1.998(3)	O(8)-Pd-O(5)	90.21(11)	Pd-O(7)	2.000(4)	Co-Pd-O(7)	89.26(11)
Pd-O(8)	1.998(3)	-	-	Pd-O(8)	1.994(4)	-	-
$PdNi(C_2)_4$ [18]				-	-	-	-
Atoms	**length (Å)**	**Atoms**	**Angles (°)**	-	-	-	-
Pd-Ni	2.483(2)	O(5)-Pd-O(7)	90.82(18)	-	-	-	-
Ni-O(1)	2.028(6)	O(8)-Pd-O(5)	89.53(19)	-	-	-	-
Ni-O(2)	2.055(6)	O(7)-Pd-O(6)	88.85(18)	-	-	-	-
Ni-O(3)	2.076(6)	O(4)-Pd-O(6)	90.56(18)	-	-	-	-
Ni-O(4)	2.040(6)	O(3)-Ni-Pd	80.83(12)	-	-	-	-
Pd-O(5)	2.027(4)	O(1)-Ni-Pd	82.34(13)	-	-	-	-
Pd-O(6)	2.036(4)	O(2)-Ni-Pd	82.31(12)	-	-	-	-
Pd-O(7)	2.034(5)	O(4)-Ni-Pd	81.03(12)	-	-	-	-
Pd-O(8)	2.020(5)	-	-	-	-	-	-

In some instances a phenomenon occurs in crystallography that cannot always be explained. An example of this is when two metals are in a crystal structure and only 50 % of the metal is "seen" by the X-ray machine. Li *et al.*[25] synthesised a complex which shows this type of phenomenon, namely a tetra(trifluoroacetatido)rhodium(II)molybdenum(II), $[MoRh(O_2CCF_3)_4]$, crystal with 50 % molybdenum and 50 % rhodium in the structure, see **Figure 2.8**.

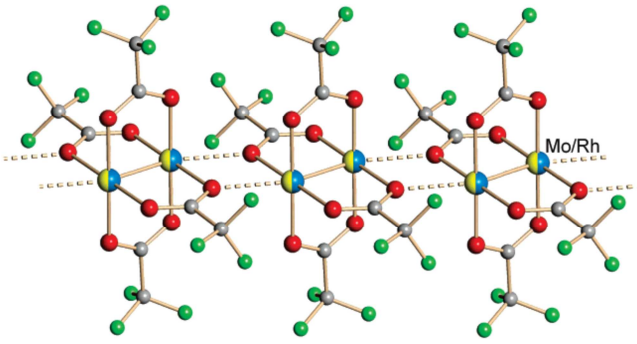

Figure 2.8: ORTEP view of tetra(trifluoroacetatido)rhodium(II)molybdenum(II), $[MoRh(O_2CCF_3)_4]$, crystal with 50 % molybdenum and 50 % rhodium. "Reprinted (adapted) with permission from (B. Li, H. Zhang, L. Huynh, M. Shatruk and E. V. Dikarev, *Inorg. Chem.*, 2007, **46**, 9155). Copyright (2007) American Chemical Society."

The paddlewheel complexes are combined in a series of 1D infinite chains connected via axial M-O interactions of 2.439(3) Å. The two crystal structures of $MoCr(O_2CCH_3)_4$[43] and $MoW(O_2C^tBu)_4$[44] show the exact same phenomenon, where both crystal structures exhibit 50 % of each atom in the structure.

2.5. Thermal Studies

2.5.1. Definitions

The following definitions apply to polymorphism, DSC (Differential Scanning Calorimetry) and TGA-MS (Thermogravimetric analysis coupled with mass spectroscopy) thermal techniques.

2.5.2. Polymorphism

A polymorph is a material that can exist in different structural forms and is a phenomenon which can occur in any crystalline material including polymers, minerals and metals. DSC is the ideal analytical instrument to probe the polymorphic nature of these materials by measuring the enthalpy change and temperature associated with solid state transition.[45]

2.5.3. DSC (Differential Scanning Calorimetry)

Differential scanning calorimetry (DSC) is a popular thermal analysis method, because of its simplicity, speed and availability. In the DSC experiment the heat flow to and from the sample is measured relative to a reference in a controlled atmosphere, for example nitrogen.

DSC has many applications in the characterisation of materials, for example studying phase transitions, such as melting, glass transitions, liquid crystal mesophase, polymorphism or decompositions. The energy changes that are involved in these transitions can be detected by DSC with great sensitivity.[46]

---

[43] C. D. Garner, R. G. Senior and T. J. King, *J. Am. Chem. Soc.* 1976, **98**, 3526

[44] (a) V. Katovic, J. L. Templeton, R. J. Hoxmeier, R. E. McCarley, *J. Am. Chem. Soc.* 1975, **97**, 5300. (b) V. Katovic, R. E. McCarley, *J. Am. Chem. Soc.* 1978, **100**, 5586. (c) M. H. Chisholm, J. S. D'Acchioli, B. D. Pate, N. J. Patmore, N. S. Dalal, D. J. Zipse, *Inorg.Chem.* 2005, **44**, 1061

[45] T. Hatakeyama and F. X. Quinn, *Thermal Analysis, Fundementals and Applications to Polymer Science*, John Wiley and Sons, England, 1999, 2nd, 107

[46] D. A. Skoog, F. J. Holler and S. R. Crouch, *Principles of Instrumental Analysis*, Thomson Brooks/Cole, USA, 2007, 900-904

2.5.4. TGA-MS (Thermogravimetric analysis coupled with mass spectroscopy)

With thermogravimetric analysis (TGA) the sample is heated linearly, while the mass loss is recorded continuously as a function of time or temperature in a controlled atmosphere for example argon or medical air. The TGA method has a wide array of applications since the information obtained is quantitative. This however limits the method to oxidation and decomposition reactions and to physical processes such as sublimation, vaporization and desorption. Decomposition profiles of multicomponent systems and compositional analysis are considered as two of the most important applications of TGA.[47] The TGA instrument can be used as a stand-alone instrument or a mass spectrometer can be coupled to the TGA instrument to identify the liberated gases. The gases or volatile components liberated from heating the sample in the TGA instrument is detected by the mass spectrometer and separates the gases according to their mass-to-charge ratios, *m/z*. From this the fragments liberated by heating the sample can be accurately identified.[48]

2.5.5. Liquid crystal mesophases

Metal carboxylate/carboxylatido complexes have the ability to undergo mesomorphic phase transitions.[5] This means, having a metal containing liquid crystal also referred to as metallomesogens. Most Liquid crystals are composed of rod-like molecules and are classified as nematic, smectic or cholesteric (not shown) mesophases see **Figure 2.9**. Metal carboxylate/carboxylatido complexes exhibit liquid crystal phases of the type A and C, SmA and SmC and many other smectic types.[49] The nematic phase is usually characterised with thread like liquid crystals. Smectic phases form well defined layers that can slide over each other. Smectic liquid crystal mesophases also occur at a smaller temperature range than other types of liquid crystals. Metal carboxylatido and carboxylate complexes mostly exhibit smectic mesophase behaviour. This is due to the fact that metal carboxylatido complexes have layered structures in the crystalline state which is maintained upon heating. Smectic mesophases have more order than nematic phases. The reason is smectic mesophases is an example of calamitic liquid crystal phase.[5]

[47] D. A. Skoog, F. J. Holler and S. R. Crouch, *Principles of Instrumental Analysis*, Thomson Brooks/Cole, USA, 2007, 894-896
[48] D. A. Skoog, F. J. Holler and S. R. Crouch, *Principles of Instrumental Analysis*, Thomson Brooks/Cole, USA, 2007, 281-301
[49] M. S. Akanni, E. K. Okoh, H. D. Burrows and H. A. Ellis, *Thermocim. Acta.*, 1992, **208**, 1

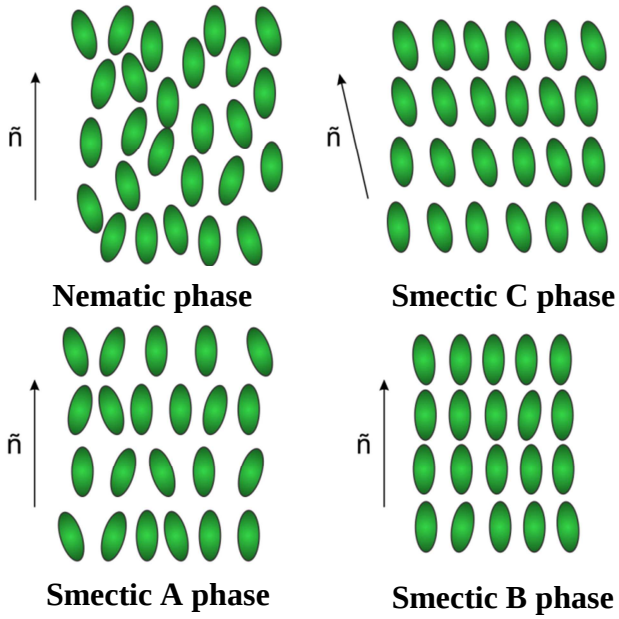

Figure 2.9: Nematic (N) and smectic (SmA, SmB and SmC) liquid crystal phases. The figure was stylistically changed.[5]

Having a metal covalently or electrostatically interacting with the carboxylate/carboxylatido ligand upon heating will maintain the rod-like structure of the complex. This allows for the small core (comprised of the oxygen atoms and metal atom/s) with the peripheral parts (comprised of carbon and hydrogen atoms) to give the layered packing upon heating in the liquid crystal. The packing structure relies on three factors a) associated coordination geometry and nature of the metal, b) binding mode of the complex and lastly c) substituents on the carboxylate/carboxylatido ligand (chain length, branched hydrocarbon chain etc.).[50,51] Varying the chain length can induce mesomorphism of the carboxylate/carboxylatido complexes.[49]

2.5.5.1. Thermal analysis of nickel acetatido complex

The thermal decomposition of $Ni(C_2)_2$, **[10]** in H_2, He and air,[52] proceeds in three stages (**Figure 2.10**). These three stages of decomposition observed are labelled I-III, where I is associated with dehydration, II is the major decomposition of the dehydrated intermediate, while III is only observed for the He atmosphere and is pressure dependant.

[50] M. S. Akanni, H. D. Burrows, H. A. Ellis, D. N. Asongwed, H. B. Babalola and P. O. Ojo, *J. Chem. Technol. Biotechnol.*, 1984, **34A**, 127
[51] K. Binnemans, *Chem. Rev.*, 2005, **105**, 4148
[52] J. C. De Jesus, I. Gonzáles, A. Quevedo and T. Puerta, *J. Mol. Catal. A: Chem*, 2005, **228**, 283

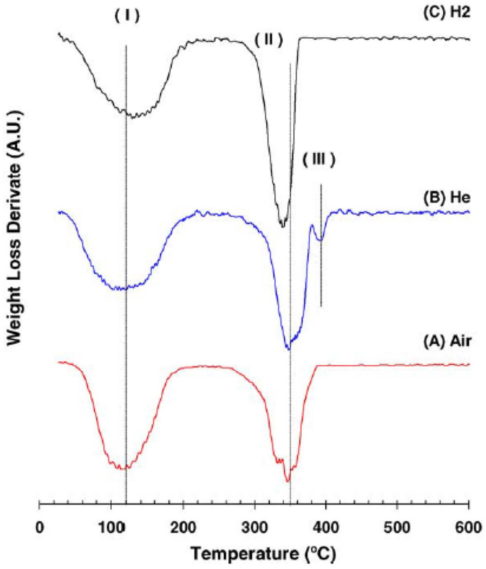

Figure 2.10: DGA (first derivative of the TGA) of tetraacetidonickel(II), $Ni(C_2)_2$ **[10]**, under H_2, He and air atmospheres. "Reprinted from The Lancet, 228, J. C. De Jesus, I. Gonzáles, A. Quevedo and T. Puerta, Thermal decomposition of nickel acetate tetrahydrate: an integrated study by TGA, QMS and XPS techniques, 283-291, Copyright (2005), with permission from Elsevier."

Stage I, is also associated with the release of acetic acid and also small amounts of additional products. For stage II, a weight retention of 24% under H_2 is consistent with the formation of Ni^0 (theoretical amount 23.6%), while under air, a weight retention of 30.7 % is consistent with NiO (theoretical amount 30.0%) formation. Some of the products detected with a mass quadrupole (QMS) include: hydrogen, methane, water, carbon monoxide, ethanol, formic acid, acetone and acetic acid.

2.5.5.2. Thermal analysis of aliphatic cerium carboxylatido complexes

Marques *et al.*[13] synthesised and studied the thermal behaviour of a series of cerium(III) carboxylatido complexes, $Ce(C_m)_3$, where m = 8, 10, 12, 14, 16, 17 or 18. **Figure 2.11** depicts the TG (thermogravimetry) of $Ce(C_{10})_3$ and $Ce(C_{18})_3$. This research revealed that $Ce(C_8)_3$ and $Ce(C_{10})_3$ has one coordinated molecule of water each. Complex $Ce(C_{12})_3$ adsorbed an equivalent amount of water (one molecule of water for each molecule of $Ce(C_{12})_3$) while the longer chain lengths $Ce(C_m)_3$, where m = 14, 16, 17 or 18 adsorbed less than the equivalent amount of water.

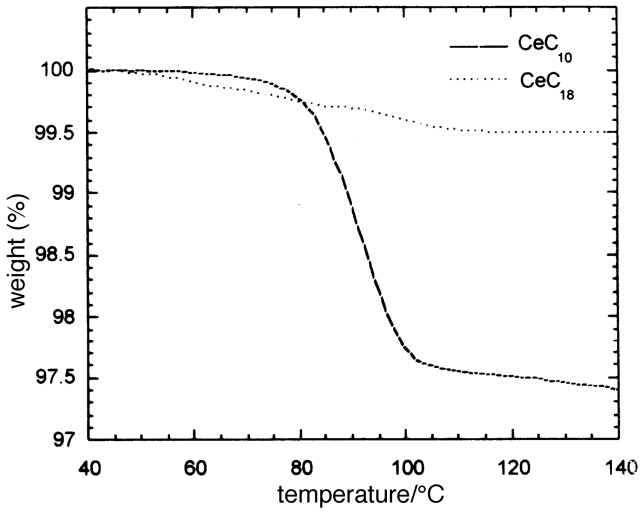

Figure 2.11: TG curves for trioctadecanoatidocerium(III) complex, $Ce(C_{18})_3$ and tridecanoatidocerium(III) complex $Ce(C_{10})_3$. Reproduced ("Adapted" or "in part") from Ref 13 with permission of The Royal Society of Chemistry.

Lanthanides and divalent transition metal long-chain carboxylatido complexes exhibit mesophase behaviour in one or more steps upon heating before transition to the isotropic liquid. There are clear thermal differences between the short chain $Ce(C_8)_3$, $Ce(C_{10})_3$ and $Ce(C_{12})_3$ and longer chain $Ce(C_{14})_3$, $Ce(C_{16})_3$, $Ce(C_{17})_3$ and $Ce(C_{18})_3$ carboxylatido complexes. The short-chain complexes have higher melting points than the long-chain complexes. This is a typical trend in aliphatic metal carboxylatido complexes which is indicative of the ionic character of the cerium(III) carboxylatido complexes.

Figure 2.12 depicts the DSC curves for cerium(III) carboxylatido complexes, which shows dehydration in (a) at 344.2 K (71.05 ˚C) and a solid state transition in (b).

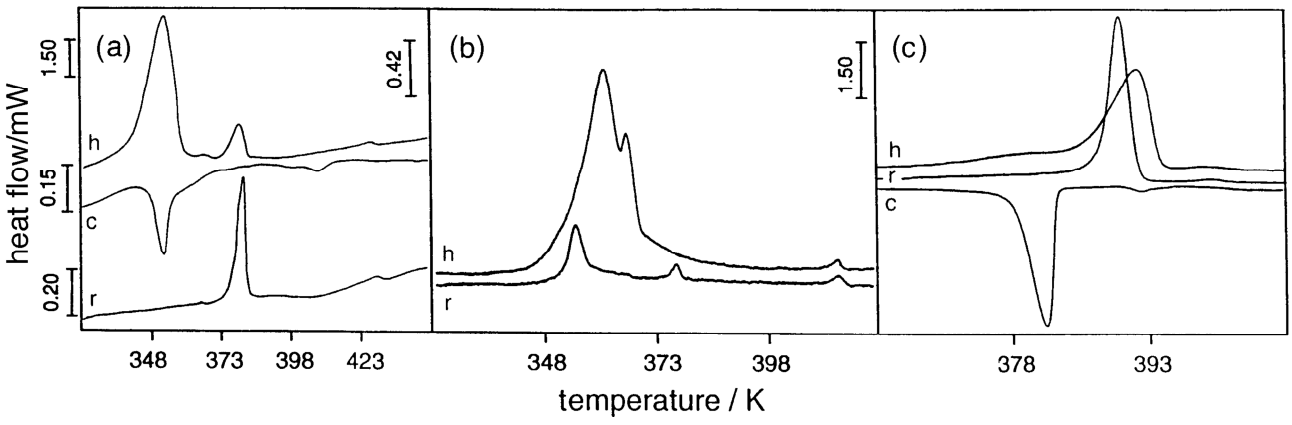

Figure 2.12: DSC curves for cerium(III) carboxylatido complex, where (h) heating, (c) cooling and (r) reheating are depicted: (a) cerium octanoatido complex, (b) cerium decanoatido complex and (c) cerium octadecanoatido complex. Reproduced ("Adapted" or "in part") from Ref 13 with permission of The Royal Society of Chemistry.

Jongen *et al.*[16] also synthesised a series of cerium(III) carboxylatido complexes $Ce(C_m)_3$ where m = 5, 6, 7, 8, 9, 10, 11, 12, 13, 14, 15, 16 or 17 in order to investigate the thermal behaviour of these complexes. The shorter cerium(III) carboxylatido complexes loses their water molecules

before the melting point, while the hydrated longer cerium carboxylatido complexes loses their water molecules at the melting point. **Figure 2.13** illustrates the TG curve and DSC curve of cerium(III) dodecanoatido complex showing the intense peak of the DSC which is associated with the loss of water and the melting point. The second smaller peak is a result of the smectic A phase to isotropic liquid transition.

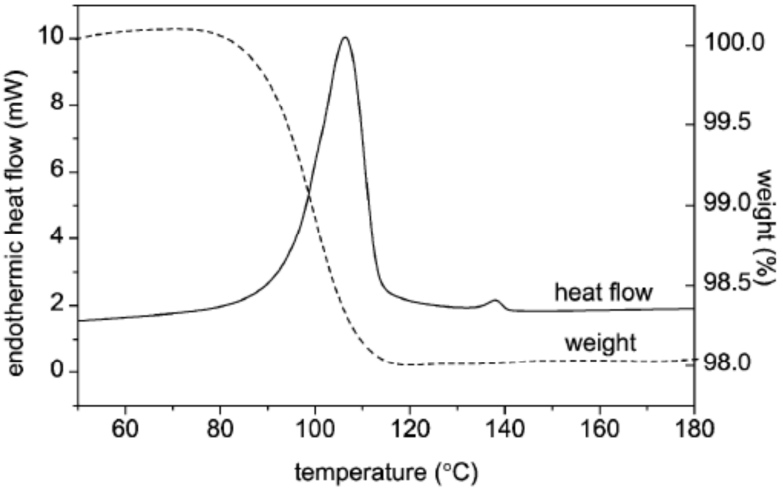

Figure 2.13: TG (thermogravimetry) curve (dotted line) and DSC curve (first heating run) of cerium(III) dodecanoatido complex. Heating rate 5 ˚C min^{-1}. "Reprinted from The Lancet, 18, L. Jongen, K. Binnemans, D. Hinz and G. Meyer, Mesomorphic behavior of cerium(III) alkanoates, 199-204, Copyright (2001), with permission from Elsevier."

Figure 2.14 depicts the first heating and cooling cycle of cerium(III) pentadecanoatido complex. The melting peak and the clearing peak is well resolved, showing the mesophase properties of the complex. In the cooling segment, super-cooling is observed and this is due to the ionic nature of the complexes.

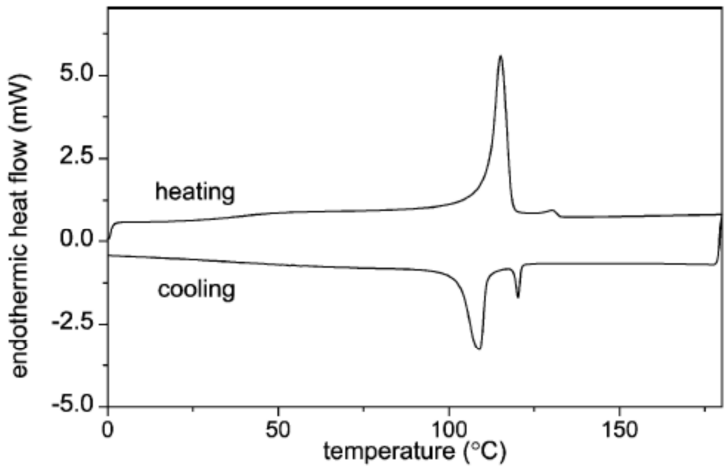

Figure 2.14: DSC heating cycle of cerium(III) pentadecanoate. "Reprinted from The Lancet, 18, L. Jongen, K. Binnemans, D. Hinz and G. Meyer, Mesomorphic behavior of cerium(III) alkanoates, 199-204, Copyright (2001), with permission from Elsevier."

2.5.5.3. Thermal analysis of calcium carboxylatido complexes

Valor *et al*.[17] studied the thermal decomposition of several calcium carboxylatido complexes. From **Figure 2.15**, which depicts the TG curves of different chain lengths, two distinct decomposition steps are observed. The first is the loss of crystal water at temperatures between 110 – 120 ˚C. From this it was deduced that the complexes were monohydrates, meaning a loss of one molecule of water per one molecule of calcium carboxylatido complex. When dehydration is complete a second step is observed, which is dependent on the chain length. The calcium carboxylatido complexes with shorter chain lengths are more stable toward thermal decomposition than the longer chain calcium carboxylatido complexes. This is evident from **Figure 2.15**. For example, calcium propanoatido complex has a decomposition onset temperature of 312 ˚C while for calcium dodecanoatido complex, the onset temperature is 170 ˚C.

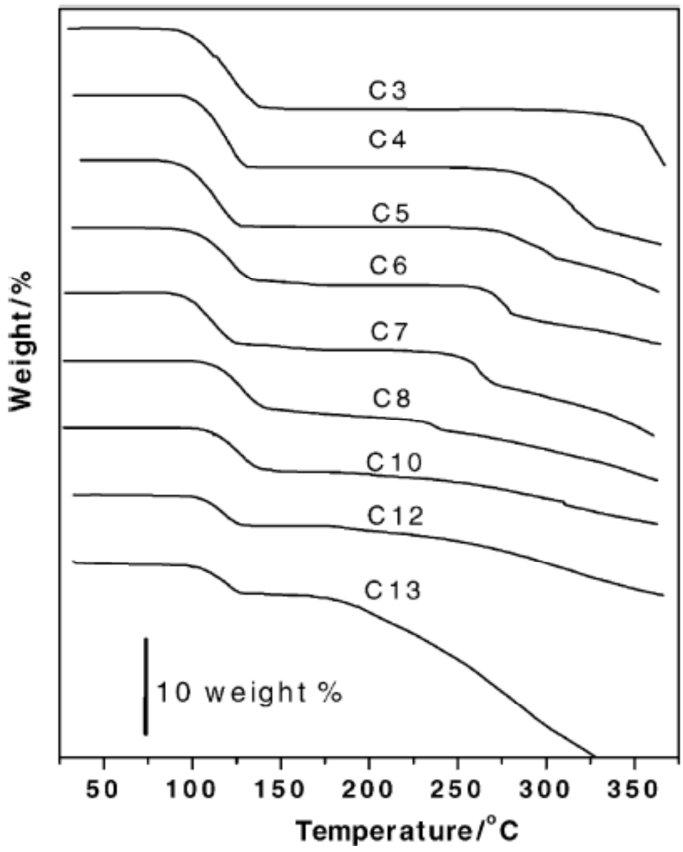

Figure 2.15: Thermograms of short and long chain calcium carboxylatido complexes. Mass loss at around 100 ˚C is associated with dehydration. The second step is decomposition, the samples were heated at 10 ˚C min^{-1} in dry air. "Reprinted from The Lancet, 389, A. Valor, E. Reguera, E. Torres-García, S. Mendoza and F. Sanchez-Sinencio, Thermal decomposition of the calcium salts of several carboxylic acids, 133-139, Copyright (2002), with permission from Elsevier."

Figure 2.16 depicts the DSC heating curves of a series of short- and long-chain calcium carboxylatido complexes. All the DSC curves have one endothermic peak between 100 and 150 ˚C which is assigned to dehydration. For the calcium propanoatido complex and calcium butanoatido complex, an exothermic peak is observed which indicates a recrystallisation process. The calcium pentanoatido complex, calcium hexanoatido complex, calcium heptanoatido complex and calcium decanoatido complexes all have a reversible endothermic peak that corresponds to the melting of the complexes.

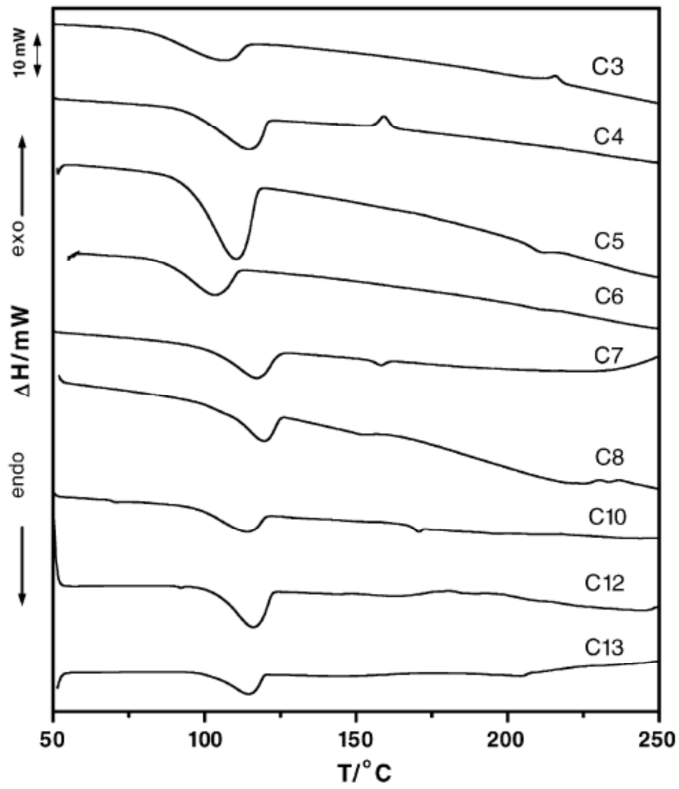

Figure 2.16: DSC curves of short- and long-chain calcium(II) carboxylatido complexes with a heating rate of 10˚C min^{-1} in dry air. "Reprinted from The Lancet, 389, A. Valor, E. Reguera, E. Torres-García, S. Mendoza and F. Sanchez-Sinencio, Thermal decomposition of the calcium salts of several carboxylic acids, 133-139, Copyright (2002), with permission from Elsevier."

2.6. Electrochemistry

Cyclic voltammetry[53,54] (CV) is by far the most effective electroanalytical technique for the study of electroactive species. Because of its versatility and ease of measurement, CV's have been extensively used in the field of electrochemistry, organic chemistry, inorganic chemistry, and biochemistry. CV's are effective in its capability for quickly observing redox behaviour of molecules over a wide potential range. Cyclic voltammetry comprises of cycling the potential of the working electrode, which is submerged in an unstirred solution containing the sample, and determining the resulting current.

The potential of the working electrode is controlled with a reference electrode such as a saturated calomel electrode (SCE) or a silver/silverchloride electrode (Ag/AgCl) and referenced against an internal standard such as FcH/FcH^+ as recommended by IUPAC.[55,56] The potential applied across the two electrodes can be considered as an excitation signal. **Figure 2.17** shows the excitation signal that causes the potential to first scan forward from -0.2 V to 0.4 V vs. SCE where the scan direction is reversed, creating a backward scan to the original potential of -0.2 V. The scan rate, as reflected by the slope, is 100 mV s^{-1}. A second cycle is indicated by the broken line. With modern instruments the switching of potentials and scan rates can easily be varied. By measuring the current at the working electrode during the potential scan a cyclic voltammogram is obtained (**Figure 2.17**) as the sample is oxidised or reduced. The current can be considered as the response signal to the potential excitation signal. The voltammogram has a vertical axis (current) vs. a horizontal axis (potential). The potential varies linearly with time and the horizontal axis can then be considered as a time axis.

Two important parameters[57] of cyclic voltammetry exist and that is the peak separation and the current ratios. The peak separation, i.e. $\Delta E_p = E_{pa}-E_{pc}$, where E_{pa} and E_{pc} are the peak potentials of the anodic and cathodic scans respectively, see **Figure 2.18**, associated with an electrochemical process. Current ratio, i_{pc}/i_{pa}, is associated with a chemical process. The formal reduction potential is defined as $E^0 = (E_{pa}+E_{pc})/2$. A redox couple is said to be electrochemically reversible if the difference in peak potential (ΔE_p) is 59 mV at 25 °C for a one electron transfer process. Because of slow transfer kinetics at the electrode surface, over potentials and high solvent resistance, the peak separation increases to above 59 mV. A redox couple is said to be chemically reversible if i_{pc}/i_{pa} is equal to unity.

---

[53] P. T. Kissinger and W. R. Heineman, *J. Chem. Ed.*, 1983, **60**, 702
[54] D. H. Evans, K. M. O'Connell, R. A. Peterson and M. J. Kelly, *J. Chem. Ed.*, **1983**, 60, 290
[55] G. Gritzner and J. Kuta, *Pure Appl. Chem.*, 1984, **56**, 461
[56] R. R. Gagné, C. A. Koval and G. C. Lisensky, *Inorg. Chem.*, 1980, **19**, 2855
[57] P. A. Christensen and A. Hamnett, *Techniques and Mechanisms in Electrochemistry*, Blackie Academic & Professional, London, 1994, 55, 170

The redox couple is said to be electrochemically quasi-reversible or irreversible, when both the oxidation and reduction process take place, but there is slow electron exchange between the electrode and the molecule in solution. A peak separation of 90 mV $\leq \Delta E_p \leq$ 150 mV is considered quasi-reversible, while $\Delta E_p >$ 150 mV indicates electrochemically irreversible behaviour. A complete chemically irreversible system is where only reduction or oxidation can occur.

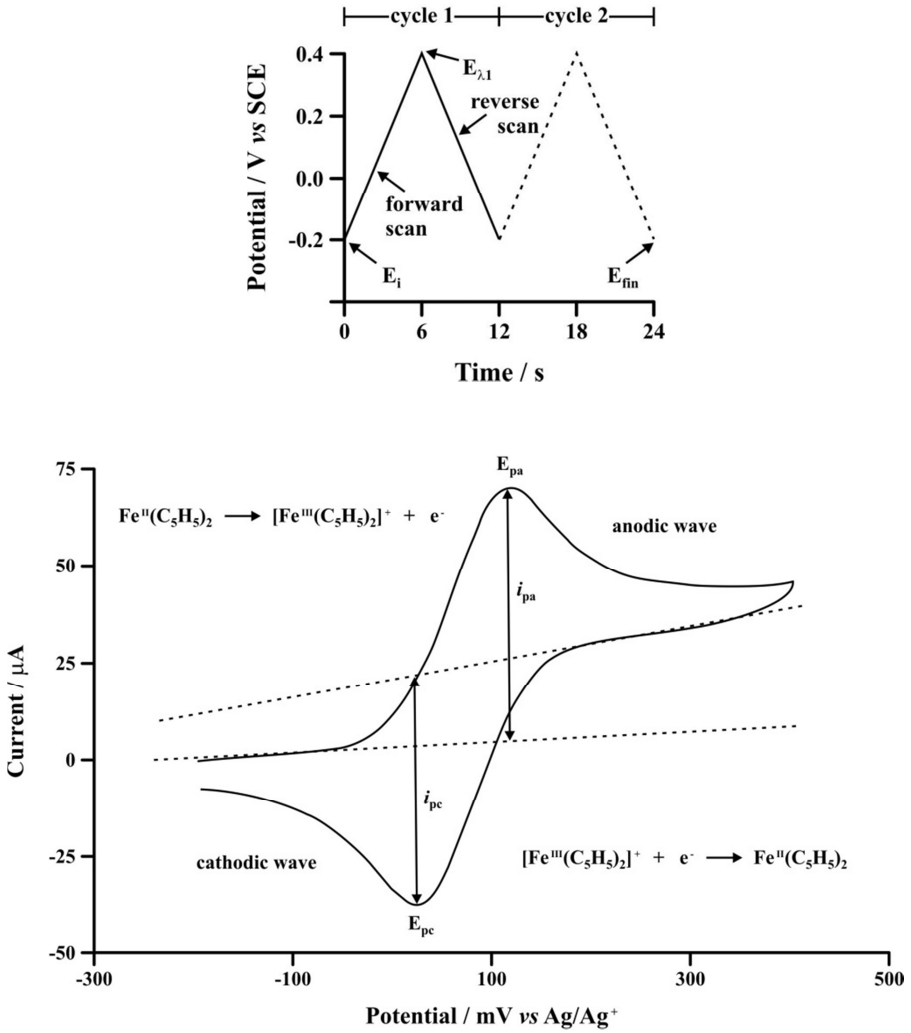

Figure 2.17: Triangular waveform (top) with switching potentials at -0.2 V and 0.4 V vs SCE. Cyclic voltammogram (bottom) of 3.0 mM Fc (ferrocene) measured in 0.1 mM tetrabutylammonium hexafluorophosphate/acetonitrile at a scan rate of 100 mV s^{-1} with a glassy carbon working electrode at 25 °C.

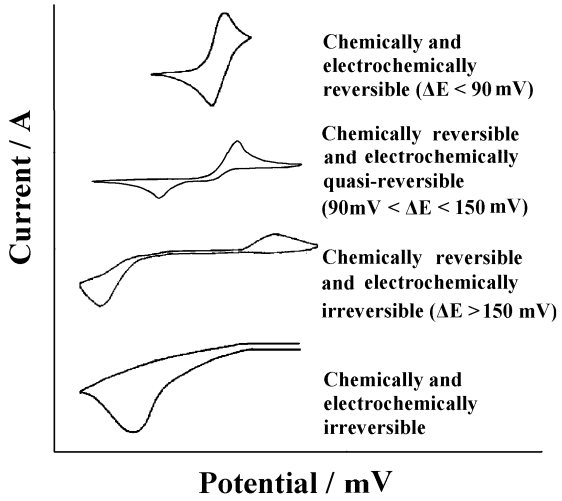

Figure 2.18: A schematic representation of the cyclic voltammogram expected from an electrochemical reversible, an electrochemical irreversible and a chemical irreversible system.

2.6.1.1. Electrochemistry of hexaacetatidotripalladium(II), $Pd_3(C_2)_6$, [1]

Amatore *et al.*[58] studied the in situ formation of a zero-valent diacetatidopalladium(0) triphenylphosphine complex from $Pd(C_2)_2$, ($Pd_3(C_2)_6$, **[1]**) and two equivalents of triphenylphosphine in THF or DMF. The resultant complex was characterised by its reduction wave, -1380 mV vs SCE in THF and -1180 mV in DMF see **Figure 2.19a**.

$$Pd(OOCCH_3)_2 + 2PPh_3 \longrightarrow Pd(OOCCH_3)_2(PPh_3)_2$$

This mixture was however observed to be unstable and it spontaneously but slowly gave rise to a species that was characterised by its oxidation wave, 225 mV in THF and 30 mV in DMF see **Figure 2.19b**. The oxidation wave increased with time as the reduction wave of palladium acetatido triphenylphosphine decreased see **Figure 2.19**. Starting directly from the original palladium acetatido triphenylphosphine complex gave the same result.

[58] C. Amatore, A. Jutand and M. A. M'Barki, *Organometallics*, 1992, **11**, 3009

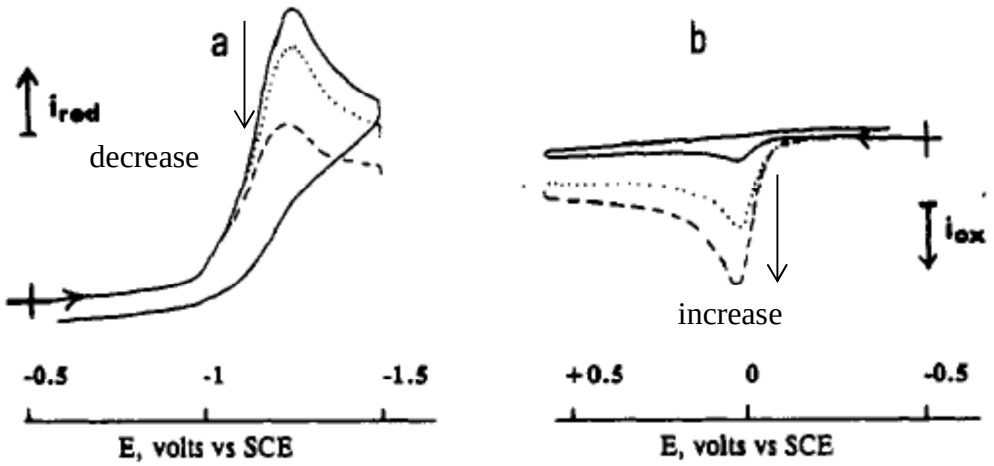

Figure 2.19: (a) CV of $Pd(C_2)_2$ **[1]** and triphenylphosphine in DMF with nBu_4NBF_4 as electrolyte using a gold disk electrode and a scan rate of 200 mV s^{-1}, from -500 mV to -1500 mV. The CV was performed as a function of time: solid line 4 min, dotted line 14 min and dashed line 33 min. (b) CV of the zero-valent palladium complex which was generated in situ from palladium acetate and triphenylphosphine in DMF with nBu_4NBF_4 as electrolyte using a gold disk electrode and a scan rate of 200 mV s^{-1}, from -500 mV to 500 mV. The CV was performed as a function of time: solid line 7 min, dotted line 17 min and dashed line 31 min. "Reprinted (adapted) with permission from (C. Amatore, A. Jutand and M. A. M'Barki, *Organometallics*, 1992, **11**, 3009). Copyright (1992) American Chemical Society."

In another study, circular hexaacetatidotripalladium(II), $Pd_3(C_2)_6$, **[1]** was reduced with hydrazine in the presence of a surfactant, which resulted in a solution of 80 % palladium metal and 20 % $Pd_3(C_2)_6$, **[1]**. The suspended palladium particles produced an anodic wave, 1720 mV and a cathodic wave, -320 mV. The anodic wave is assigned to the oxidation of $Pd^0 \rightarrow Pd^{II}$ and the cathodic wave is assigned to the reduction of the palladium acetatido moiety to palladium metal see **Figure 2.20**.[59]

[59] K. Aoki, Y. Zhao and J. Chen, *Electrochimica Acta*, 2007, **52**, 2485

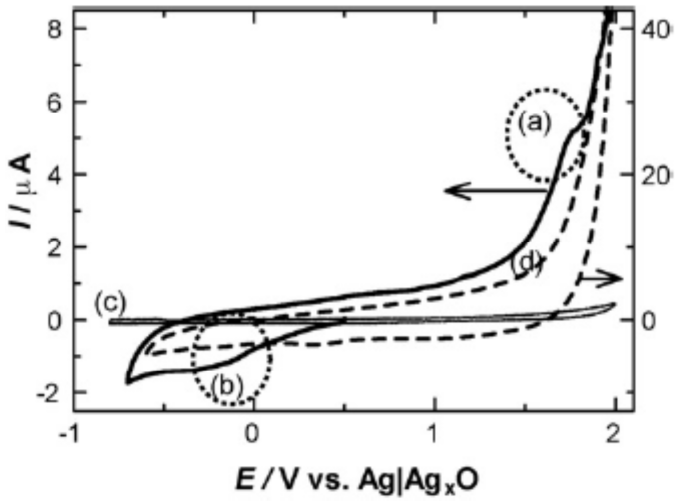

Figure 2.20: CV's of the suspended palladium particles in acetonitrile with $TBAPF_6$ as electrolyte and a platinum electrode. Scan speed 150 mV/s. "Reprinted from The Lancet, 52, K. Aoki, Y. Zhao and J. Chen, Colloidal submicron-palladium particles stabilised with acetate, 2485-2491, Copyright (2007), with permission from Elsevier."

2.7. Surface Chemistry

2.7.1. Wafer preparation

Two-dimensional silicon wafers can be used as a support on which to model heterogeneous catalysts, which in turn can anchor a variety of complexes. The procedure for the preparation of a silver supported model catalyst is shown in **Figure 2.21**.[60]

[60] E. Erasmus, P. C. Thune, M. W. G. M. (Tiny) Verhoeven, J. W. (Hans) Niemandtsverdriet, J. C. Swarts, *Catal. Commun*, 2012, **27**, 193

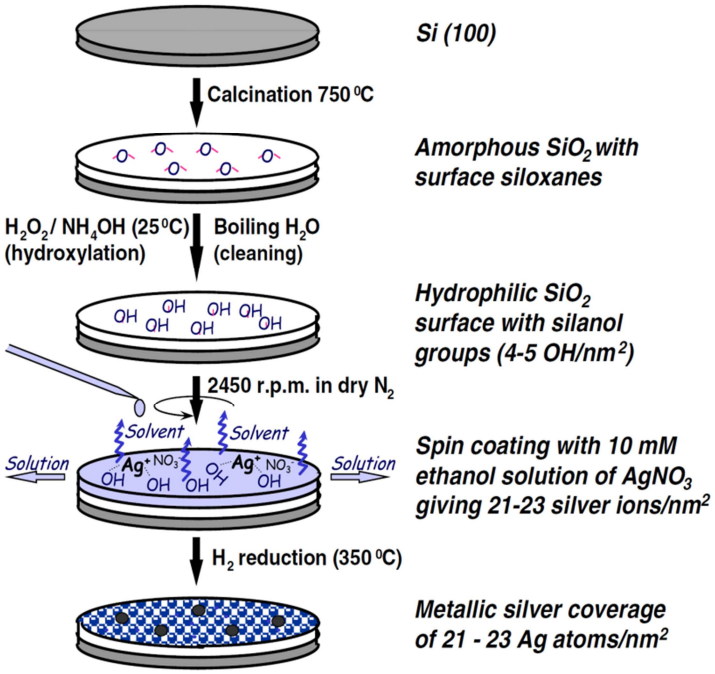

Figure 2.21: The above illustration demonstrates the preparation of silicon wafers by calcination and by spin coating $AgNO_3$ dissolved in ethanol onto it. "Reprinted from The Lancet, **27**, E. Erasmus, P. C. Thune, M. W. G. M. Verhoeven, J. W. Niemantsverdriet and J. C. Swarts, A new approach to silver-catalysed aerobic oxidation of octadecanol: Probing catalysts utilising a flat, two-dimensional silicon-based model support system, 193-199, Copyright (2012), with permission from Elsevier."

The procedure for preparing a hydroxylated silicon wafer capable of anchoring complexes by means of either spin coating or grafting can be described as follows: The Si(100) is calcined at 750 °C in air to form a thin layer of –O-Si-O-, 90 nm thick. The calcined wafer is then etched/cleaned with a hydrogen peroxide/ammonium hydroxide mixture and then hydrolysed by boiling it in distilled water to form a hydrophilic –Si-OH layer. The dissolved complex can now be anchored onto the modified wafer.

The pre-catalyst can be activated by oxidation or reduction using oxygen or hydrogen respectively which results in metal oxide or metal particles on the modified wafer.[60]

2.7.2. Catalytic and XPS studies

Li *et. al.*[24] used a palladium(II) bismuth(III) tetra(trifluoroacetatido) precursor to design a mixed-metal Pd^{II}-Bi^{III} carbon-supported catalyst. The catalysts were tested for the oxidation of glucose to gluconoic acid. The procedure proved to be more effective than to prepare the catalysts from

multisource mononuclear Pd^{II} and Bi^{III} precursors. Erasmus *et al.*[61] synthesised and coated a mixed-metal ($PdCo(C_2)_4$) complex onto a flat model silicon wafer using grafting and spin-coating.

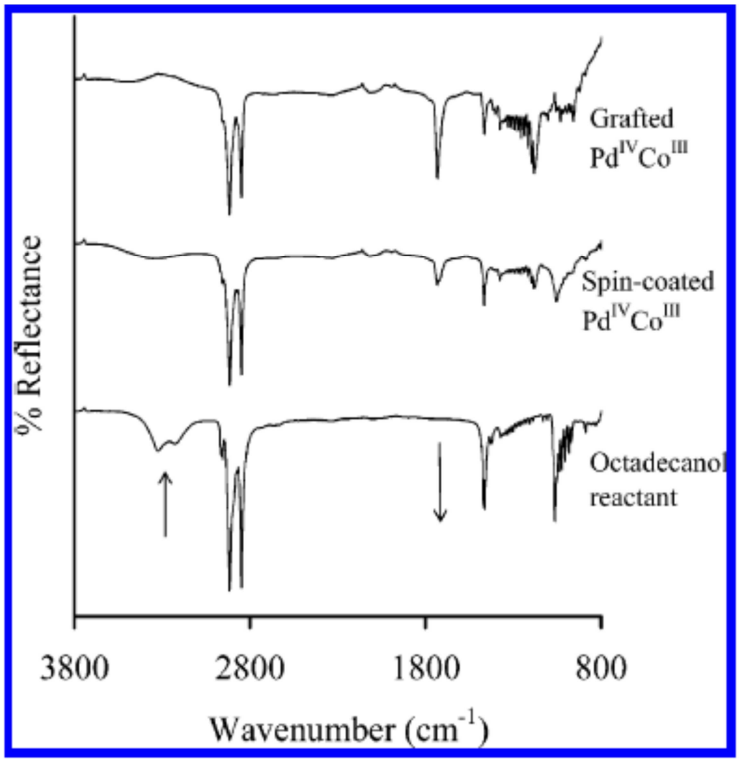

Figure 2.22: ATR FTIR spectra of the catalytic testing of 1-octadecanol (top) grafted $Pd^{IV}C^{III}$/Si(OH)/SiO_2/Si(100), (middle) spin-coated $Pd^{IV}Co^{III}$/Si(OH)/SiO_2/Si(100) and (bottom) pure 1-octadecanol. "Reprinted (adapted) with permission from (E. Erasmus, J. W. (Hans) Niemantsverdriet and J. C. Swarts, *Langmuir*, 2012, **28**, 16477). Copyright (2012) American Chemical Society."

Erasmus *et al.*[61] tested the catalytic activity of this $Pd^{IV}O_2Co^{III}{}_2O_3$ mixed-metal model catalyst for the aerobic and solvent-free oxidation of 1-octadecanol to 1-octadecanoic acid. From the catalyst testing a turn over frequency of 9 molecules per second was obtained for the reaction.

As the reaction progressed the disappearance of the OH peak at 3340 cm^{-1} and the appearance of the CO peak at 1718 and 1734 cm^{-1} was monitored using FTIR. Both the spin-coated and grafted catalysts were tested see **Figure 2.22**.

The results obtained in this study proved that using a single source mixed-metal catalyst precursor to prepare a mixed-metal catalyst to oxidise an alcohol is better than using a physical mixture of two different metals to prepare a mixed-metal catalyst. This research also proved that using a 2D catalyst is useful to study the catalytic reactions of organic compounds.

[61]E. Erasmus, J. W. (Hans) Niemantsverdriet and J. C. Swarts, *Langmuir*, 2012, **28**, 16477

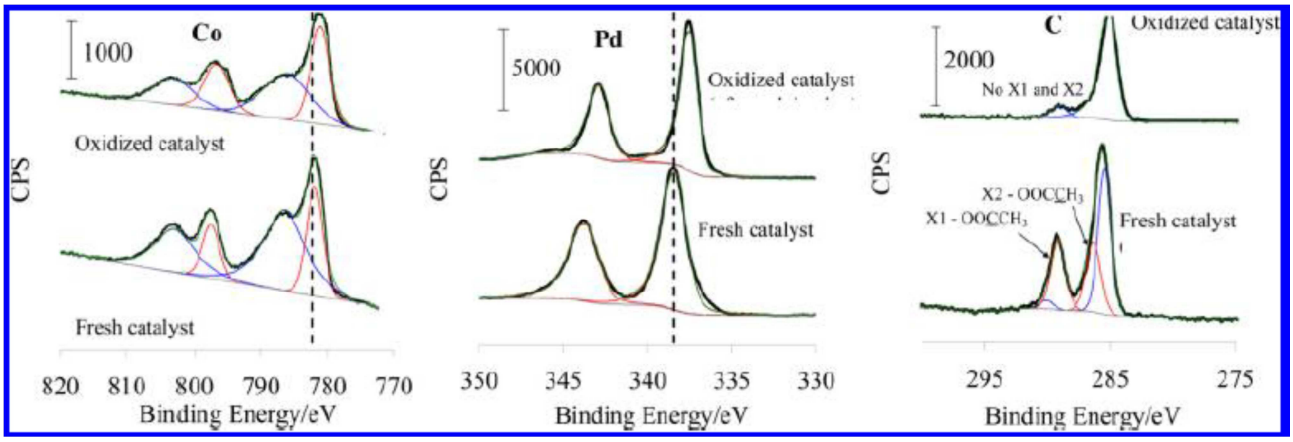

Figure 2.23: XPS spectra of silicon wafers for cobalt, palladium and carbon, (left), (middle) and (right) respectively. "Reprinted (adapted) with permission from (E. Erasmus, J. W. (Hans) Niemantsverdriet and J. C. Swarts, *Langmuir*, 2012, **28**, 16477). Copyright (2012) American Chemical Society."

XPS spectra of the $Pd^{IV}Co^{III}$ mixed-metal catalyst are shown in **Figure 2.23**. The XPS studies is consistent with the observation that one of the four acetate ligands was replaced by a Si-O-Co covalent bond during the grafting preparation method. The spin-coated complex is coordinated onto the silicon surface via a hydrogen bond. XPS results show that peak $3d_{5/2}$ for $Pd^{IV}O_2$ was observed at 337.5 eV and the $2p_{3/2}$ peak for $Co^{III}{}_2O_3$ was observed at 781.1 eV.[61]

This concludes the literature survey for this study.

3. Results and Discussion

3.1. Introduction

The results and discussion section has its own numbering system as is customary at UFS and will be the same as the synthesis chapter. This chapter presents results of the research performed by the author. The synthesis and characterisation of a selection of short- and long-chain mono- and mixed-metal aliphatic paddlewheel carboxylate and carboxylatido* complexes are presented. A general schematic, representing the synthesis of the mono- and mixed-metal paddlewheel aliphatic complexes are shown in **Scheme 3.1** and **Scheme 3.2**. These carboxylate and carboxylatido complexes are of the type:

a) $[Pd_3^{II}(\mu\text{-}OOC(CH_2)_nCH_3)_6]$ where n = 4 for **[1]**, 6 for **[2]**, 8 for **[3]** and 10 for **[4] (novel)**

b) $K[OOC(CH_2)_nCH_3)]$ where n = 4 for **[5]**, 6 for **[6]**, 8 for **[7]** and10 for **[8]** these published complexes will be used as precursors for the synthesis of the novel complexes.

c) $[Co^{II}(OOC(CH_2)_nCH_3)_2]$ where n = 4 for **[9]**, 6 for **[10]**, 8 for **[11]** and 10 for **[12]** these published complexes will be used as precursors for the synthesis of the novel complexes.

d) $[M^{II}(OOC(CH_2)_8CH_3)_2]$ where M = Ni for **[13]**, Mn for **[14]**, Zn for **[15]**, Ca for **[16]** and Sr for **[17]** as well as $[Ce^{III}(OOC(CH_2)_8CH_3)_3]$ **[18]** these published complexes will be used as precursors for the synthesis of the novel complexes.

e) $[Pd^{II}Co^{II}(\mu\text{-}OOC(CH_2)_nCH_3)_4]$ where n = 4 for **[19]**, 6 for **[20]**, 8 for **[21]** and 10 for **[22] (novel)**

f) $[Pd^{II}M^{II}(\mu\text{-}OOCCH_3)_4]$ where M = Zn for **[23]**, Ba for **[24]**, Cd for **[25]**, Ca for **[26]**, Sr for **[27]**, Ni for **[28]**, Co for **[29]**, Mn for **[30]** and Cu for **[31]** as well as $[Pd^{II}Ce^{III}(\mu\text{-}OOCCH_3)_4]^+$ **[32]** these published complexes will be used as precursors for the synthesis of the novel complexes.

g) $[Pd^{II}M^{II}(\mu\text{-}OOC(CH_2)_8CH_3)_4]$ where M = Ba for **[33]**, Cd for **[34]**, Ca for **[35]**, Zn for **[36]**, Sr for **[37]**, Ni for **[38]**, Mn for **[39]** and Cu for **[40]** as well as $[Pd^{II}Ce^{III}(\mu\text{-}OOC(CH_2)_8CH_3)_4]^+$ **[41] (novel)**

Spectroscopic analysis of the complexes was performed by Attenuated Total Reflectance Fourier Transform Infrared Spectroscopy (ATR-FTIR) and Nuclear Magnetic Resonance Spectroscopy (NMR). Where possible all new carboxylatido complexes were subjected to elemental analysis. Crystal structures of $Pd^{II}Co^{II}(\mu\text{-}OOC(CH_2)_8CH_3)_4$ **[21]**, $Pd^{II}Zn^{II}(\mu\text{-}OOC(CH_2)_8CH_3)_4$ **[36]** and $Pd^{II}Ni^{II}(\mu\text{-}OOC(CH_2)_8CH_3)_4$ **[38]** are presented.

*According to IUPAC, the term "carboxylate" implies that the anionic carboxylate ligand is ionically bound (i.e. electrostatically) to the K^+ cation, e.g. $K[OOC(CH_2)_4CH_3]$. The term "carboxylatido" implies that the anionic ligand is coordinatively (covalently) bound to a metal, e.g. $[Pd_3^{II}(\mu\text{-}OOC(CH_2)_4CH_3)_6]$.

Results from thermal analysis of selected synthesised complexes in the form of Differential Scanning Calorimetry (DSC), Thermal Gravimetric Analysis coupled with Mass Spectroscopy (TGA-MS) and variable temperature polarised light microscopic (PLM) studies are also presented.

Results from an electrochemical analysis were used to identify any intramolecular communication between the coordinating metal centres of the mixed-metal paddlewheel carboxylatido complexes.

Finally, spin coating was used to coat modified two-dimensional silicon wafers with the synthesised mixed-metal paddlewheel carboxylatido complexes. X-ray Photoelectron Spectroscopy (XPS) investigations were used to characterise these modified silicon wafer surfaces. The pre-catalyst was activated by oxidation in a stream of oxygen at 450 °C. This resulted in palladium oxide and metal oxide on the modified silicon wafer surface. The catalysts were tested in a model reaction for their catalytic activity for the aerobic solvent-free oxidation of alcohols using 1-octadecanol as reagent.

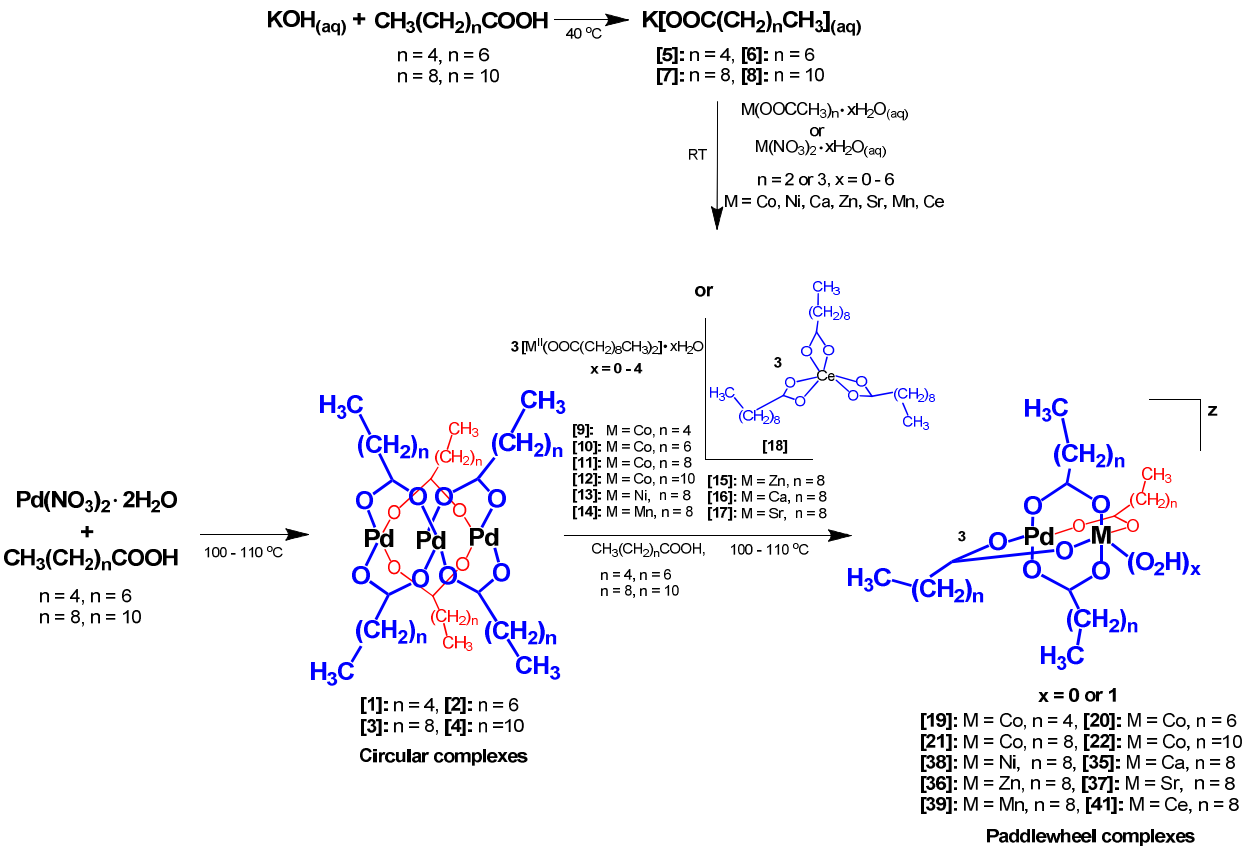

Scheme 3.1: Synthetic procedure for the long-chain mono- and mixed-metal aliphatic paddlewheel and non-paddlewheel complexes using method 1. The charge, z = 0 for all the mixed-metal paddlewheel complexes, except for **[41]** where z = +1, counter ion: decanoate. The red carboxylatido ligands are behind the page plane while the blue ones are in the front.

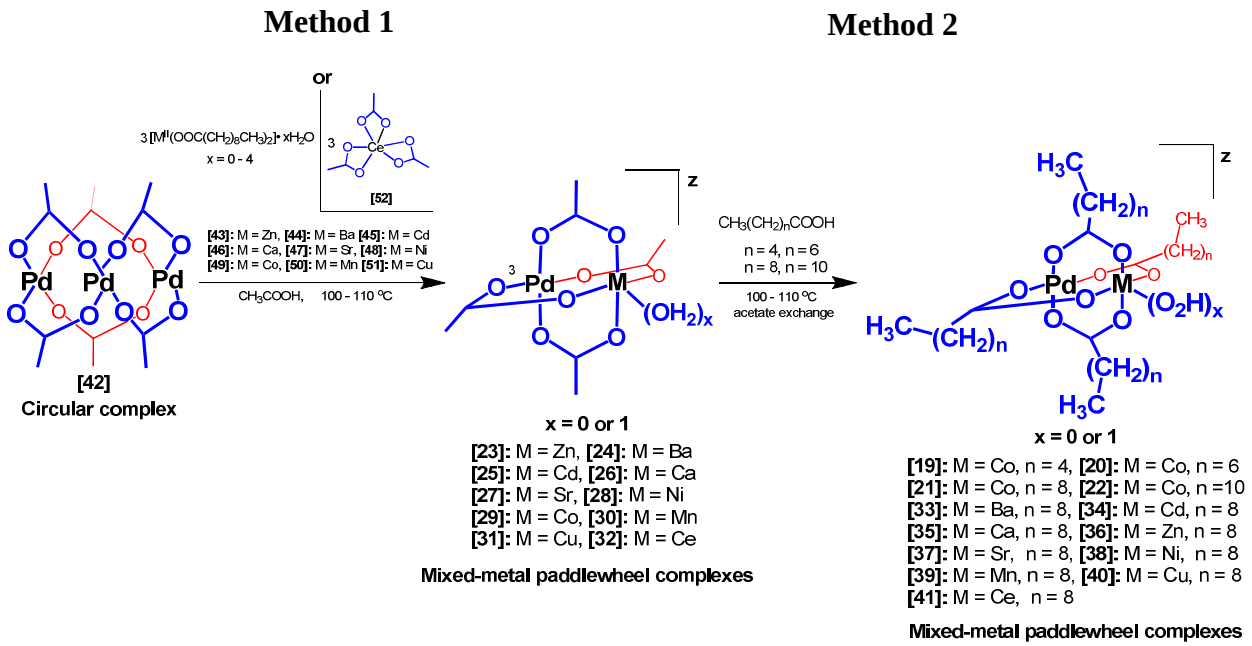

Scheme 3.2: Synthetic procedure for short- (method 1) and long-chain mixed-metal aliphatic paddlewheel carboxylatido complexes using method 2. The charge, z = 0 for all the mixed-metal paddlewheel complexes except for **[32]** and for **[41]** where z = +1, counter ion: decanoate. The red carboxylatido ligands are behind the page plane while the blue ones are in the front.

3.2. Synthesis

3.2.1. Synthesis of circular hexacarboxylatidotripalladium(II) complexes

A series of long-chain circular aliphatic hexacarboxylatidotripalladium(II) complexes, $[Pd_3^{II}(\mu\text{-}OOC(CH_2)_nCH_3)_6]$, where n = 4 for **[1]**, 6 for **[2]**, 8 for **[3]** or 10 for **[4]** were synthesised following the reaction procedure in **Scheme 3.3**, with yields in excess of 70%. For simplicity $[Pd_3^{II}(\mu\text{-}OOC(CH_2)_nCH_3)_6]$ complexes **[1-4]** will be abbreviated as $Pd_3(C_m)_6$ where m = 6 for **[1]**, 8 for **[2]**, 10 for **[3]** or 12 for **[4]**. Here m represents the number of carbon atoms in the even numbered carboxylatido backbone, while n represents the number of $-CH_2-$ groups in the even numbered carboxylatido backbone therefore m is always n+2. This abbreviation will be used throughout the chapter and will also apply to the short- and long-chain mono- and mixed-metal paddlewheel and non-paddlewheel complexes.

Palladium(II) nitrate was allowed to react with the appropriate long chain carboxylic acid (hexanoic-, octanoic-, decanoic-, or dodecanoic acid), to liberate the long-chain circular aliphatic hexacarboxylatidotripalladium(II) complexes, $Pd_3(C_6)_6$ **[1]**, $Pd_3(C_8)_6$ **[2]**, $Pd_3(C_{10})_6$ **[3]** or $Pd_3(C_{12})_6$ **[4]**.

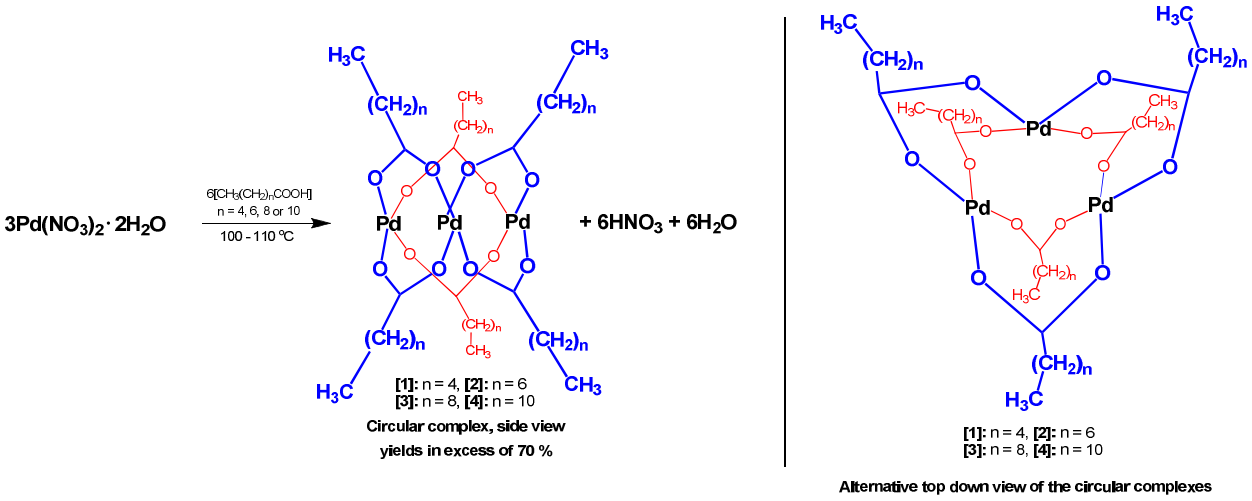

Scheme 3.3. Synthesis of long-chain circular aliphatic hexacarboxylatidotripalladium(II) complexes **[1-4]** using the scheme shown. The complexes **[1-4]** are synthesised by reacting palladium(II) nitrate with the appropriate free long chain carboxylic acid. Side view (left) and alternative top down view (right) of **[1-4]** are shown. The red carboxylatido ligands are behind the page plane while the blue ones are in the front.

To synthesise **[1-4]**, the reaction mixture was heated to a constant internal temperature between 100 °C to 110 ºC. Temperature control during the reaction is important. If the temperature rises above 130 ºC the complex reductively decarboxylates which results in the formation of palladium black (Pd^0). The reaction mixture also needed to be kept under a stream of compressed air until all the acid was removed from the product. The stream of compressed air is also necessary to remove the NO_x gases formed during the reaction. The reaction can be followed by monitoring the disappearance of the carbonyl stretching frequency (C=O, at *ca.* 1700 cm^{-1}) of the reactant acid using ATR-FTIR. This carbonyl stretching frequency (C=O, at *ca.* 1700 cm^{-1}) is replaced by the coordinated carboxylatido stretching frequencies at *ca.* 1600 cm^{-1} and 1410 cm^{-1}.

The complexes can be stored indefinitely in air. Other carboxylatido complexes are also renowned to be stable.[1] Alcohols cannot be used as solvents during reactions because of their reducing ability towards palladium. Prolonged boiling in organic solvents also reduces the palladium component of the complexes to palladium black (Pd^0).[1]

The method of Stephenson[1] *et al.* was also tried where palladium black/sponge was oxidised using nitric acid in the presence of acetic acid.

[1] T. A. Stephenson, S. M. Morehouse, A. R. Powell, J. P. Heffer, and G. Wilkinson, *J. Chem. Soc.*, 1965, 3632

Hexaacetatidotripalladium(II), $Pd_3(C_2)_6$ **[42]**, the desired short-chain circular trimer, did form. It was decided not to follow this synthetic route, since the procedure described in **Scheme 3.3** to synthesise $Pd_3(C_6)_6$ **[1]**, $Pd_3(C_8)_6$ **[2]**, $Pd_3(C_{10})_6$ **[3]** or $Pd_3(C_{12})_6$ **[4]** gave purer compounds with higher yields. The synthesised long-chain circular aliphatic hexacarboxylatidotripalladium(II) complexes **[1-4]** were used as precursors in the preparation of the long-chain mixed-metal aliphatic paddlewheel carboxylatido complexes synthesised in this study.

3.2.2. Synthesis of ionic potassium carboxylates*

The synthesis of the long-chain aliphatic ionic potassium carboxylates will be discussed, see **Scheme 3.4**, $K[OOC(CH_2)_nCH_3]$, where n = 4 for **[5]**, 6 for **[6]**, 8 for **[7]** or 10 for **[8]**. For simplicity **[5-8]** will be abbreviated as KC_m where m = 6 for **[5]**, 8 for **[6]**, 10 for **[7]** or 12 for **[8]**. Here m represents the number of carbon atoms in the even numbered carboxylate backbone, while n represents the number of $-CH_2-$ groups in the even numbered carboxylate backbone therefore m is always n+2.

The long-chain aliphatic ionic potassium carboxylate precursors were synthesised by following a modified procedure from Ishioka *et al*.[2] The appropriate carboxylic acid (hexanoic-, octanoic-, decanoic-, or dodecanoic acid), was heated to 40 °C, to first melt the solid carboxylic acids. A slight excess of KOH(aq) was then added drop-wise to the melted or heated carboxylic acid until the acid was just neutralised. The volume doubled in sise because of the addition of the aqueous KOH.

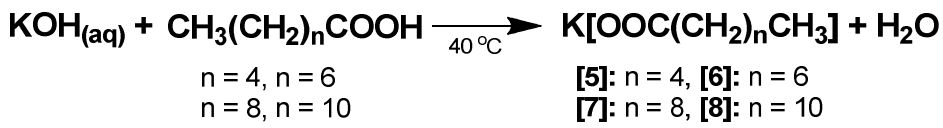

Scheme 3.4: Synthesis of long-chain aliphatic ionic potassium carboxylates **[5-8]** from the neutralisation reaction of KOH and the free long chain carboxylic acid.

A gelatinous mixture was observed when adding the aqueous KOH, which is an indication of the formation of the highly water-soluble long-chain ionic potassium carboxylates.

---

[2] T. Ishioka, H. Wakisaka, T. Saito and I. Kanesaka, *J. Phys. Chem. B*, 1998, **102**, 1239

*According to IUPAC, the term "carboxylate" implies that the anionic carboxylate ligand is ionically bound (i.e. electrostatically) to the K^+ cation, e.g. $K[OOC(CH_2)_4CH_3]$. The term "carboxylatido" implies that the anionic ligand is coordinatively (covalently) bound to a metal, e.g. $[Pd_3^{II}(\mu\text{-}OOC(CH_2)_4CH_3)_6]$.

The water was then removed under vacuum (care had to be taken to prevent excessive bumping during solvent removal) and the resultant white solid was then dissolved in the minimum amount of methanol (60 °C) to remove any excess KOH. Thereafter the solution was then decanted, leaving behind the excess KOH. Lastly the methanol was removed under reduced pressure and the white solid was then dried at 60°C, to give long-chain aliphatic ionic potassium carboxylates in almost quantitative yields.

3.2.3. Synthesis of non-paddlewheel dicarboxylatidocobalt(II) tetrahydrate complexes

The synthesis of long-chain aliphatic non-paddlewheel dicarboxylatidocobalt(II) tetrahydrate complexes, $[Co^{II}(OOC(CH_2)_nCH_3)_2]\cdot 4H_2O$, where n = 4 for **[9]**, 6 for **[10]**, 8 for **[11]** or 10 for **[12]** see **Scheme 3.5**. For simplicity $[Co^{II}(OOC(CH_2)_nCH_3)_2]\cdot 4H_2O$, complexes **[9-12]** will be abbreviated as $Co(C_m)_2$ where m is the number of carbon atoms in the carboxylatido backbone, 6 for **[9]**, 8 for **[10]**, 10 for **[11]** and 12 for **[12]**. The cobalt complexes, **[9-12]** were synthesised using a modified procedure from Pereira *et al.*[3]

The corresponding long-chain aliphatic ionic potassium carboxylates, KC_6 **[5]**, KC_8 **[6]**, KC_{10} **[7]** or KC_{12} **[8]** was dissolved in the minimum amount of water and to this solution was added an aqueous solution of cobalt(II) nitrate hexahydrate while stirring, resulting in the target long-chain aliphatic non-paddlewheel dicarboxylatidocobalt(II) tetrahydrate complexes **[9-12]**. Thereafter the resultant pink solid was filtered and washed with a water/ethanol (1:1) solution. Lastly drying the solid at 60 °C, the complexes **[9-12]** was obtained with yields ranging between 13 % and 48 %, depending on the number of carbons in the carboxylatido backbone see **Table 3.1**.

Table 3.1: Yields of long-chain non-paddlewheel dicarboxylatidocobalt(II) tetrahydrate complexes **[9-12]**.

$Co(C_m)_2$	**Yield %**
$Co(C_6)_2$, **[9]**	13
$Co(C_8)_2$, **[10]**	48
$Co(C_{10})_2$, **[11]**	34
$Co(C_{12})_2$, **[12]**	27

[3] R. F. P. Pereira, A. J. M. Valente, M. Fernandes and H. D. Burrows. *Phys. Chem. Chem. Phys.*, 2012, **14**, 7517

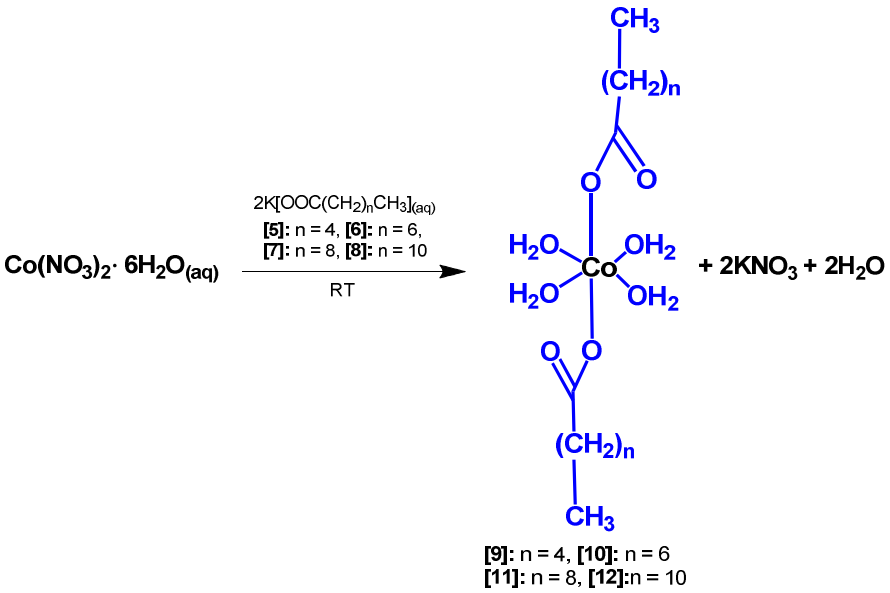

Scheme 3.5. Synthesis of long-chain aliphatic non-paddlewheel dicarboxylatidocobalt(II) tetrahydrate complexes **[9-12]** using the scheme shown. The complexes **[9-12]** were synthesised by reacting cobalt(II) nitrate with the appropriate long-chain aliphatic ionic potassium carboxylate complexes.

With the exception of $Co(C_6)_2$ **[9]**, there seems to be a linear decrease in the yield obtained for $Co(C_8)_2$ **[10]**, $Co(C_{10})_2$ **[11]** and $Co(C_{12})_2$ **[12]** as the number of carbons in the carboxylatido backbone increases, see **Figure 3.1**. This trend could possibly be attributed to steric influences. For example the long chains can coil around the complexing site, and would first need to unwrap before a reaction can take place. This makes the reaction rate slower. The low yields obtained for **[9-12]** could also possibly be attributed to its partial solubility in the water/ethanol (1:1) solution used to wash the carboxylatido complexes **[9-12]** with. This would cause some of the product to be washed away.

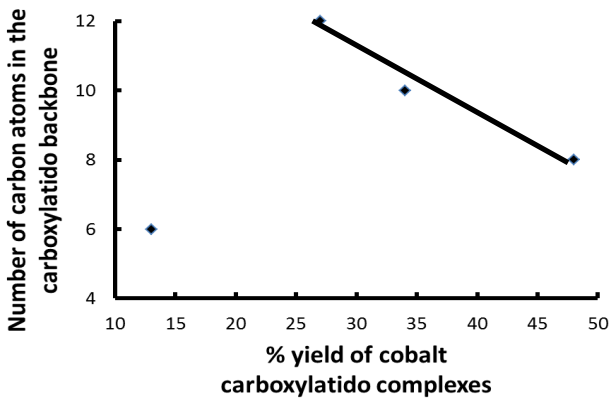

Figure 3.1: The correlation between the number of carbon atoms in the carboxylatido backbone and the yield of the dicarboxylatidocobalt(II) tetra hydrate complexes **[9-12]**.

3.2.4. Synthesis of non-paddlewheel dicarboxylatidometal(II) or tricarboxylatidocerium(III) complexes

The long-chain aliphatic non-paddlewheel mono-metal complexes, dicarboxylatidometal(II), $[M^{II}(OOC(CH_2)_8CH_3)_2]$ where M = Ni for **[13]**, Mn for **[14]**, Zn for **[15]**, Ca for **[16]**, Sr for **[17]** as well as tricarboxylatidocerium(III), $[Ce^{III}(OOC(CH_2)_8CH_3)_3]$ for **[18]** were all synthesised according to the same procedure, see **Scheme 3.6**.[3] The abbreviation $M(C_{10})_2$, applies to $[M^{II}(OOC(CH_2)_8CH_3)_2]$ where M = Ni for **[13]**, Mn for **[14]**, Zn for **[15]**, Ca for **[16]**, Sr for **[17]** while the abbreviation $Ce(C_{10})_3$ applies to $[Ce^{III}(OOC(CH_2)_8CH_3)_3]$ for **[18]**.

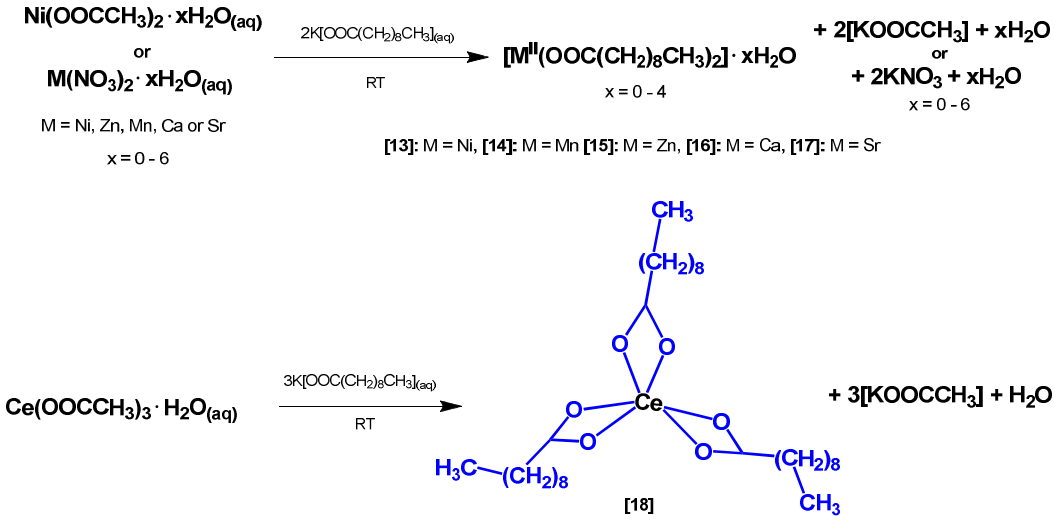

Scheme 3.6: Synthesis of aliphatic non-paddlewheel dicarboxylatidometal(II) or tricarboxylatidocerium(III) complexes **[13-18]**. The complexes were synthesised by reacting metal (Ni, Zn, Mn, Ca, Sr or Ce) nitrate/acetatido complexes with potassium decanoate **[7]**.

Potassium decanoate, KC_{10} **[7]**, was dissolved in the minimum amount of water and to this solution was added drop-wise an aqueous solution of the metal (Ni, Zn, Mn, Ca, Sr or Ce) nitrate/acetatido complexes while stirring which resulted in the target dicarboxylatidometal(II) or tricarboxylatidocerium(III) complexes **[13-18]**.

The resultant white solid was filtered and washed with a water/ethanol (1:1) solution and after drying at 60 °C, **[13-18]** was obtained with yields varying between 40 % and 87 %. These yields are significantly higher than that of the dicarboxylatidocobalt(II) tetrahydrate **[9-12]** complexes.

These mono-metal dicarboxylatidometal(II) or tricarboxylatidocerium(III) complexes are generally insoluble in polar and non-polar organic solvents like CH_2Cl_2, ether, ethanol and benzene (with the cobalt carboxylatido complexes being an exception) at room temperature. However the circular aliphatic tripalladium hexacarboxylatido complexes **[1-4]**, are soluble in chlorinated solvents at room temperature.

The metal di- or tricarboxylatido complexes **[13-18]** were recrystallised (twice) by dissolving the complexes in *n*-pentanol at 80 °C. The recrystallised di- or tricarboxylatido complexes were washed with a water/ethanol (1:1) mixture and dried at 60 °C.

Table 3.2: Yields of short- and long-chain mono-metal non-paddlewheel di- or tricarboxylatido complexes.

$Co(C_m)_2$ and $M(C_{10})_2$	**Yield %**	**$M(C_{10})_2$ or $Ce(C_{10})_3$**	**Yield %**
$Co(C_6)_2$, **[9]**	13	$Mn(C_{10})_2$, **[14]**	86
$Co(C_8)_2$, **[10]**	48	$Zn(C_{10})_2$, **[15]**	82
$Co(C_{10})_2$, **[11]**	34	$Ca(C_{10})_2$, **[16]**	80
$Co(C_{12})_2$, **[12]**	27	$Sr(C_{10})_2$, **[17]**	40
$Ni(C_{10})_2$, **[13]**	54	$Ce(C_{10})_3$, **[18]**	87

The mono-metal dicarboxylatido complexes $Mn(C_{10})_2$ **[14]**, $Zn(C_{10})_2$ **[15]**, $Ca(C_{10})_2$ **[16]** and the tricarboxylatido complex $Ce(C_{10})_3$ **[18]**, were obtained in excess of 80% while the dicarboxylatido complexes, $Ni(C_{10})_2$ **[13]** and $Sr(C_{10})_2$ **[17]** were isolated in yields of 54 % and 40 % respectively, see **Table 3.2**. The cobalt dicarboxylatido complexes all resulted in yields less than 50 %. Complexes $Co(C_6)_2$ **[9]** and $Co(C_{12})_2$ **[12]** yielded 13 % and 27 % respectively while $Co(C_{10})_2$ **[11]** and $Co(C_8)_2$ **[12]** yielded 34 % and 48 % respectively.

3.2.5. Synthesis of mixed-metal paddlewheel carboxylatido complexes[4,5,6]

As pointed out in the objectives in Chapter 1, the main purpose of this research is to prepare new mixed-metal paddlewheel carboxylatido complexes. Four carboxylatido ligands coordinate to the two different metals in a paddlewheel type structure. During the course of this study, these mixed-metal complexes were prepared by means of two different synthetic procedures.

[4] R.W. Brandon and D.V. Claridge, *Chem. Commun*. 1968, 677
[5] N. Y. Kozitsyna, S. E. Nefedov, F. M. Dolgushin, N. V. Cherkashina, M. N. Vergaftik and I. I. Moiseev, *Inorganica Chimica Acta*, 2006, **359**, 2072
[6] N. S. Akhmadullina, N. V. Cherkashina, N. Kozisyna, I. P. Stolarov, E. V. Perova, A. E. Gekhman, S. E. Nefedov, M. N. Vargaftik, I. I. Moiseev, *Inorg. Chim. Acta*, 2009, **362**, 1943

3.2.6. Synthesis of $[Pd^{II}M^{II}(\mu\text{-}OOC(CH_2)_nCH_3)_4]$ where n = 0, 4, 6, 8 or 10 as well as $[Pd^{II}Ce^{III}(\mu\text{-}OOC(CH_2)_nCH_3)_4]^+$ where n = 0 or 8

Method 1:

Method 1 involves the reaction between one equivalent of the circular aliphatic hexacarboxylatidotripalladium(II) complex and three equivalents of the aliphatic dicarboxylatidometal(II) or tricarboxylatidocerium(III) complexes in the appropriate long-chain aliphatic free acid which produces the desired mixed-metal aliphatic paddlewheel tetracarboxylatidopalladium(II)metal(II) or the tetracarboxylatidopalladium(II)cerium(III) complexes.

The synthesis of **[19-22]** will be discussed first, see **Scheme 3.7** below. Utilizing the first synthetic procedure, method 1, a series of long-chain aliphatic mixed-metal paddlewheel tertracarboxylatidopalladium(II)cobalt(II) complexes, $[Pd^{II}Co^{II}(\mu\text{-}OOC(CH_2)_nCH_3)_4]$, where n = 4 for **[19]**, 6 for **[20]**, 8 for **[21]** and 10 for **[22]** were synthesised according to **Scheme 3.7** with yields varying between 62 % to 89 % (**Table 3.3**). For simplicity $[Pd^{II}Co^{II}(\mu\text{-}OOC(CH_2)_nCH_3)_4]$ complexes will be abbreviated as $PdCo(C_m)_4$ where m is the number of carbons in the carboxylatido backbone; 6 for **[19]**, 8 for **[20]**, 10 for **[21]** or 12 for **[22]**.

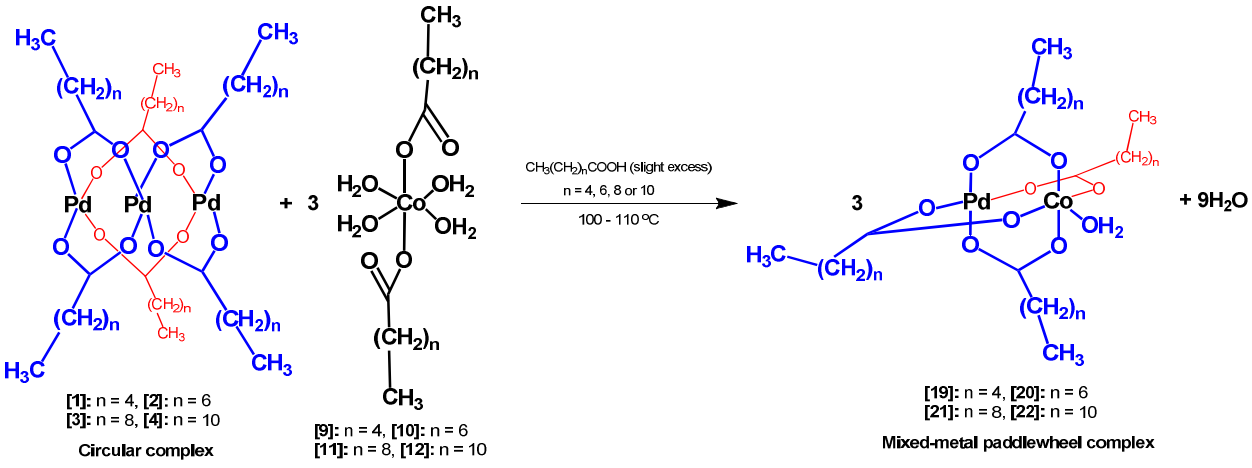

Scheme 3.7: The synthesis of long-chain aliphatic paddlewheel tetracarboxylatidopalladium(II)cobalt(II) mono hydrate mixed-metal paddlewheel complexes **[19-22]**. The complexes were synthesised by reacting one equivalent of the circular aliphatic hexacarboxylatidotripalladium(II) complex with three equivalents of the aliphatic dicarboxylatidocobalt(II) tetrahydrate complexes in the appropriate long chain free acid to produce the target mixed-metal paddlewheel tetracarboxylatidopalladium(II)cobalt(II) mono hydrate complexes. The red carboxylatido ligands are behind the page plane while the blue ones are in the front.

Mixed-metal, tetracarboxylatidopalladium(II)cobalt(II) monohydrate paddlewheel complexes **[19-22]** were synthesised to have different carboxylatido ligand chain lengths. For example one equivalent of the circular hexakis(hexacarboxylatido)tripalladium(II), $Pd_3(C_6)_6$, **[1]**, was reacted with three equivalent of dihexacarboxylatidocobalt(II) tetrahydrate, $Co(C_6)_2$ **[9]**, in hexanoic acid at temperatures of 100 °C to 110 ˚C to produce the target, paddlewheel aliphatic tetrahexanoatidopalladium(II)cobalt(II) monohydrate, $PdCo(C_6)_4$, **[19]**, complex. To synthesise $PdCo(C_8)_4$ **[20]**, $PdCo(C_{10})_4$ **[21]** or $PdCo(C_{12})_4$ **[22]** paddlewheel complexes, one equivalent of the circular tripalladium hexacarboxylatido complex, and three equivalent of the cobalt dicarboxylatido complex, octanoatido, decanoatido or dodecanoatido complexes were reacted in octanoic, decanoic and dodecanoic acid respectively to produce the target $PdCo(C_8)_4$, **[20]**, $PdCo(C_{10})_4$, **[21]**, or $PdCo(C_{12})_4$, **[22]**, mixed-metal aliphatic paddlewheel tetracarboxylatido complexes of appropriate chain length as shown in **Scheme 3.7**. The excess acid was removed from the reaction mixture by allowing a stream of compressed air to flow over the mixture at 100 °C to 110 ˚C. The reaction progress can be followed by monitoring the disappearance of the carbonyl stretching frequency (*ca.* 1700 cm^{-1}) of the free acid acid using ATR-FTIR. The carbonyl stretching frequency (*ca.* 1700 cm^{-1}) is replaced by the coordinated carboxylatido stretching frequency at *ca.* 1589 cm^{-1} and 1422 cm^{-1}.

Hereafter, the synthesis of mixed-metal paddlewheel tetracarboxylatidopalladium(II)metal(II) and tetracarboxylatidopalladium(II)cerium(III), $[Pd^{II}M^{II}(\mu\text{-}OOC(CH_2)_8CH_3)_4]$, where M = Ca for **[35]**, Zn for **[36]**, Sr for **[37]**, Ni for **[38]** and Mn for **[39]** as well as $[Pd^{II}Ce^{III}(\mu\text{-}OOC(CH_2)_8CH_3)_4]^+$ for **[41]** will be discussed. The mixed-metal paddlewheel complexes were synthesised according to **Scheme 3.8** with yields varying between 56 % and 95 %, see **Table 3.3**. For simplicity $[Pd^{II}M^{II}(\mu\text{-}OOC(CH_2)_8CH_3)_4]$ complexes will be abbreviated as $PdM(C_{10})_4$ where M = Ca for **[35]**, Zn for **[36]**, Sr for **[37]**, Ni for **[38]** or Mn for **[39]** as well as $PdCe(C_{10})_4^+$ for **[41]**. This synthetic procedure involves the reaction between one equivalent of the long-chain circular aliphatic complex $Pd_3(C_{10})_6$, **[3],** and three equivalents of the mono-metal aliphatic long-chain di- or tricarboxylatido complex, $Ni(C_{10})_2$ **[13]**, $Mn(C_{10})_2$ **[14]**, $Zn(C_{10})_2$ **[15]**, $Ca(C_{10})_2$ **[16]**, $Sr(C_{10})_2$ **[17]** or $Ce(C_{10})_3$ **[18]** in decanoic acid at temperatures of 100 °C to 110 ºC. This reaction results in the target long-chain mixed-metal aliphatic paddlewheel tetracarboxylatidopalladium(II)metal(II) or tetracarboxylatidopalladium(II)cerium(III) complexes, $PdCa(C_{10})_4$ **[35]**, $PdZn(C_{10})_4$ **[36]**, $PdSr(C_{10})_4$ **[37]**, $PdNi(C_{10})_4$ **[38]**, $PdMn(C_{10})_4$ **[39]** or $PdCe(C_{10})_4^+$ **[41]** as the final product.

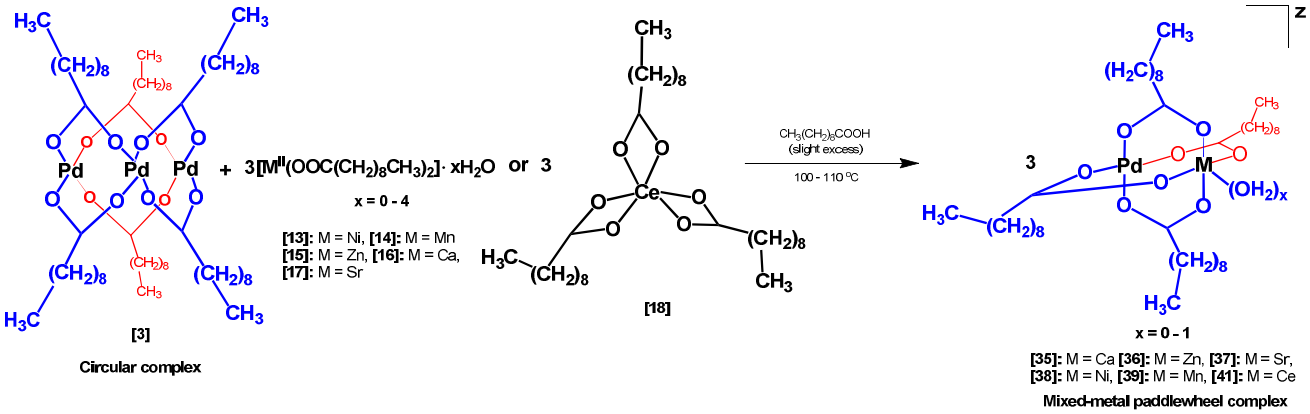

Scheme 3.8: The synthesis of long-chain paddlewheel aliphatic tetracarboxylatidopalladium(II)metal(II) and tetracarboxylatidopalladium(II)cerium(III) mixed-metal paddlewheel complexes **[35-39]** or **[41]**. The complexes were synthesised by reacting one equivalent of circular hexacarboxylatidotripalladium(II) complex with three equivalent of dicarboxylatidometal(II) or tricarboxylatidocerium(III) complexes to produce the target tetracarboxylatidopalladium(II)metal(II) or tetracarboxylatidopalladium(II)cerium(III)$^{+}$ mixed-metal paddlewheel complexes. The charge, z = 0 for all the complexes except for **[41]** where z = +1, counter ion: decanoate. The red carboxylatido ligands are behind the page plane while the blue ones are in the front.

The excess acid was removed from the reaction mixture by the same procedure described for the palladium cobalt tetracarboxylatido paddlewheel complexes. The reaction can be followed by monitoring the disappearance of the carbonyl stretching frequency (C=O, at *ca.* 1700 cm^{-1}) of the acid using ATR-FTIR. It is replaced by the coordinated carboxylatido stretching frequency at *ca.* 1540 cm^{-1} and 1407 cm^{-1} for the palladium metal tetracarboxylatido paddlewheel complexes. From **Table 3.3** it is clear that all the complexes have yields higher than 50 %.

Table 3.3: Yields of long-chain mixed-metal carboxylatido paddlewheel complex.

$PdCo(C_m)_4$ and $PdM(C_{10})_4$	**Yield %**	**$PM(C_{10})_4$**	**Yield %**
$PdCo(C_6)_4$, **[19]**	71	$PdZn(C_{10})_4$, **[36]**	56
$PdCo(C_8)_4$, **[20]**	89	$PdSr(C_{10})_4$, **[37]**	95
$PdCo(C_{10})_4$, **[21]**	62	$PdNi(C_{10})_4$, **[38]**	90
$PdCo(C_{12})_4$, **[22]**	62	$PdMn(C_{10})_4$, **[39]**	86
$PdCa(C_{10})_4$, **[35]**	58	$PdCe(C_{10})_4^{+}$, **[41]**	72

The synthesis of tetraacetatidopalladium(II)metal(II) and tetraacetatidopalladium(II)cerium(III), $[Pd^{II}M^{II}(\mu\text{-}OOCCH_3)_4]$, where M = Zn for **[23]**, Ba for **[24]**, Cd for **[25]**, Ca for **[26]**, Sr for **[27]**, Ni for **[28]**, Co for **[29]**, Mn for **[30]** and Cu for **[31]** as well as $[Pd^{II}Ce^{III}(\mu\text{-}OOCCH_3)_4]^{+}$ for **[32]** will be discussed next.

The acetatido complexes were synthesised according to **Scheme 3.9** with yields varying between 51 % - 90 %, see **Table 3.4**. For simplicity $[Pd^{II}M^{II}(\mu\text{-}OOCCH_3)_4]$ and $[Pd^{II}Ce^{III}(\mu\text{-}OOCCH_3)_4]^+$ complexes will be abbreviated as $PdM(C_2)_4$ with M as above.

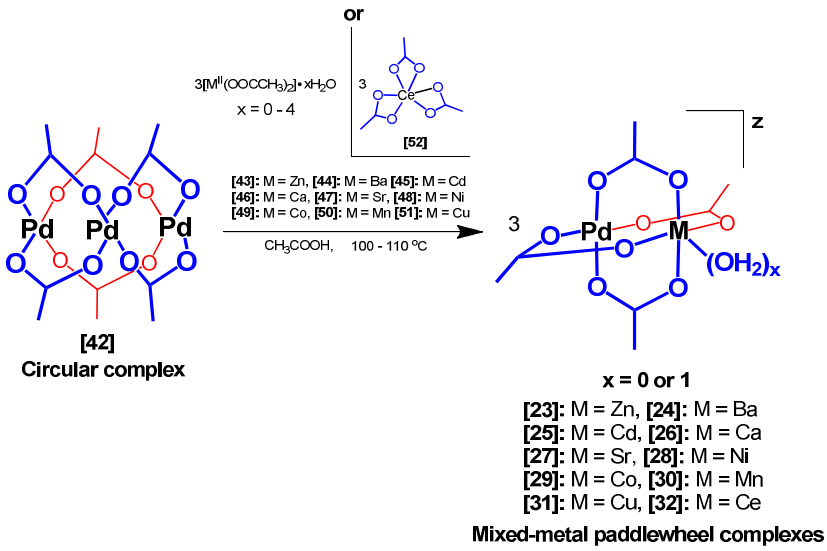

Scheme 3.9: Synthesis of short-chain tetraacetatidopalladium(II)metal(II) and tetraacetatidopalladium(II)cerium(III) mixed-metal paddlewheel complexes **[23-32]**. This is achieved by reacting one equivalent of hexaacetatidotripalladium(II) with three equivalents of diacetatidometal(II) and three moles of triacetatidocerium(III) complexes. The charge, z = 0 for all the complexes except **[32]** where z = 1. The red carboxylatido ligands are behind the page plane while the blue ones are in the front.

The reaction between one equivalent of hexaacetatidotripalladium(II) **[42]** and three equivalent of the appropriate diacetatidometal(II) complex **[43-51]** or triacetatidocerium(III) **[52]** (usually the hydrate) in acetic acid as the solvent at temperatures between 90 °C to 100 °C generates the desired short-chain tetraacetatidopalladium(II)metal(II) or tetraacetatidopalladium(II)cerium(III) mixed-metal paddlewheel complexes **[23-32]**. The reaction mixture was refluxed for two hours and was allowed to cool overnight and crystals were obtained the following day. After washing the crystals with cold benzene and n-hexane, the desired mixed-metal paddlewheel acetatido complexes, $PdM(C_2)_4$, **[23-32]** was isolated and characterised by ATR-FTIR.

These mixed metal acetatido complexes showed the characteristic symmetric and anti-symmetric ($C\overline{\cdots}O$) stretching frequencies of the product at *ca.* 1600 cm^{-1} and 1400 cm^{-1} respectively. The ATR-FTIR also showed that there is either water (OH stretching frequency at *ca.* 3400 cm^{-1}) and/or an acetic acid ligand (C=O stretching frequency at *ca.* 1700 cm^{-1}) in the axial position as well. This is in correlation to what was found for the short-chain carboxylatido complexes published in literature, determined from their single crystal structures.[5,6]

Table 3.4: Yields of short-chain mixed-metal tetracarboxylatido paddlewheel complexes.

$PdM(C_2)_4$	**Yield %**	**$PdM(C_2)_4$**	**Yield %**
$PdZn(C_2)_4$ **[23]**	86	$PdNi(C_2)_4$ **[28]**	79
$PdBa(C_2)_4$ **[24]**	76	$PdCo(C_2)_4$ **[29]**	90
$PdCd(C_2)_4$ **[25]**	51	$PdMn(C_2)_4$ **[30]**	77
$PdCa(C_2)_4$ **[26]**	54	$PdCu(C_2)_4$ **[31]**	62
$PdSr(C_2)_4$ **[27]**	67	$PdCe(C_2)_4^+$ **[32]**	71

Table 3.4 contains the yields of the palladium metal tetracarboxylatido mixed-metal paddlewheel complexes with yields varying between 51 % and 90 %. $PdCd(C_2)_4$ **[25]** and $PdCo(C_2)_4$ **[29]** have yields of 51 % and 90 % respectively.

3.2.7. Synthesis of $[Pd^{II}M^{II}(\mu\text{-}OOC(CH_2)_nCH_3)_4]$ as well as $[Pd^{II}Ce^{III}(\mu\text{-}OOC(CH_2)_8CH_3)_4]^+$

Method 2:

Method 2, involves the reaction between tetraacetatidopalladium(II)metal(II) or tetraacetatidopalladium(II)cerium(III) mixed-metal paddlewheel complexes and the appropriate, free long chain carboxylic acids which produces the desired mixed-metal paddlewheel aliphatic long-chain tetracarboxylatidopalladium(II)metal(II) or mixed-metal paddlewheel aliphatic long-chain tetracarboxylatidopalladium(II)cerium(III) complexes in a ligand exchange reaction.

Utilising method 2, the synthesis of $PdCo(C_m)_4$, where m is 6 for **[19]**, 8 for **[20]**, 10 for **[21]** or 12 for **[22]** will be discussed first. The complexes were synthesised according to **Scheme 3.10** with yields varying between 66 % and 99 %, see **Table 3.5**. To synthesise **[19-22]** mixed-metal paddlewheel complexes, the short-chain mixed-metal paddlewheel tetraacetatidopalladium(II)cobalt(II) monohydrate, $PdCo(C_2)_4$ **[29]**, was reacted with hexanoic, octanoic, decanoic or dodecanoic acid respectively at temperatures between 100 °C to 110 °C.
From this the target long-chain tetracarboxylatidopalladium(II)cobalt(II) monohydrate mixed-metal paddlewheel complexes were obtained **[19-22]** of desired chain length.

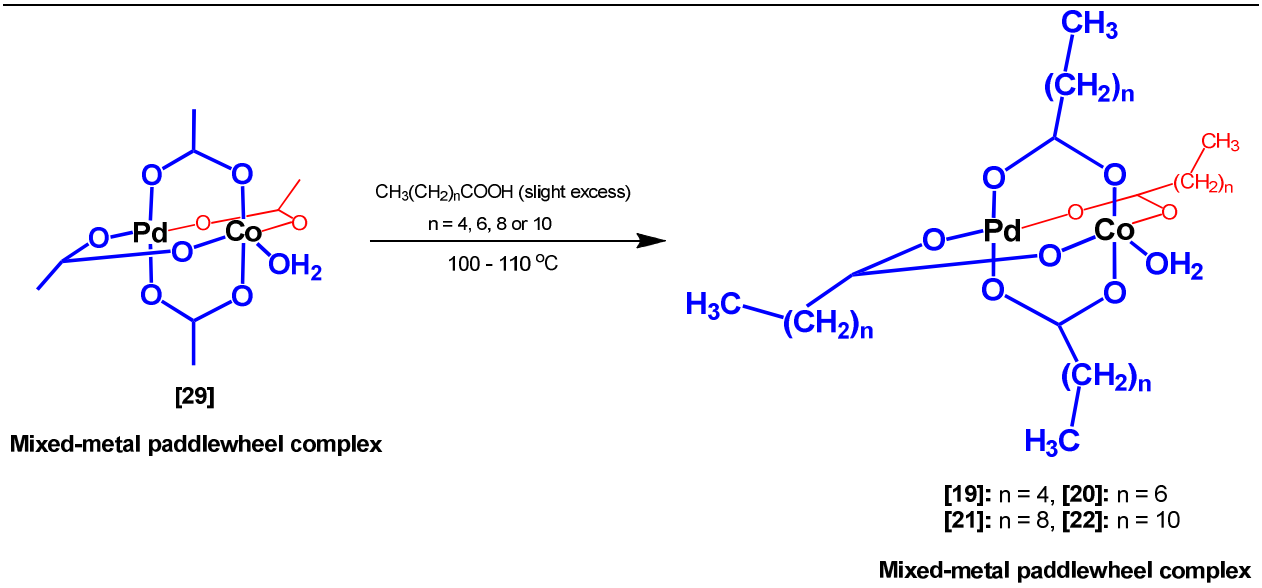

Scheme 3.10: The synthesis of long-chain tetracarboxylitidopalladium(II)cobalt(II) monohydrate mixed-metal paddlewheel complexes **[19-22]**. This is achieved by reacting short-chain tetraacetatidopalladium(II)cobalt(II) monohydrate mixed-metal **[29]** with the free carboxylic acids hexanoic, octanoic, decanoic or dodecanoic acid. The red carboxylatido ligands are behind the page plane while the blue ones are in the front.

The excess acid was removed from the reaction mixture by allowing a stream of compressed air to flow over the mixture, thereby evaporating the excess acid. The reaction was followed by monitoring the disappearance of the carbonyl stretching frequency (C=O, at *ca.* 1700 cm^{-1}) of the acid using ATR-FTIR. It is replaced by the coordinated carboxylatido stretching frequency at *ca.* 1589 cm^{-1} and 1422 cm^{-1}.

Lastly the synthesis of $PdM(C_{10})_4$, **[33-41]** were achieved. These complexes were synthesised according to **Scheme 3.11** with yields varying between 71 % and 95 % see **Table 3.5**. In a ligand exchange reaction, the short-chain tetraacetatidopalladium(II)metal(II) and short-chain tetraacetatidopalladium(II)cerium(III) mixed-metal paddlewheel complexes, $PdM(C_2)_4$, **[23-32]** were treated with decanoic acid at a temperature of 100 °C to 110 °C. This was done to replace the acetatido ligand with a decanoatido ligand which resulted in the formation of long-chain aliphatic tetracarboxylatidopalladium(II)metal(II) and long-chain aliphatic tetracarboxylatidopalladium(II)cerium(III) mixed-metal paddlewheel, $PdM(C_{10})_4$, **[33-41]** complexes. The excess acid was removed from the reaction mixture by allowing a stream of compressed air to flow over the mixture, thereby evaporating the excess acid.

The reaction was followed by monitoring the disappearance of the carbonyl stretching frequency (C=O, at *ca.* 1700 cm^{-1}) of the free acid using ATR-FTIR. It is replaced by the coordinated carboxylatido stretching frequency at *ca.* 1540 cm^{-1} and 1407 cm^{-1}.

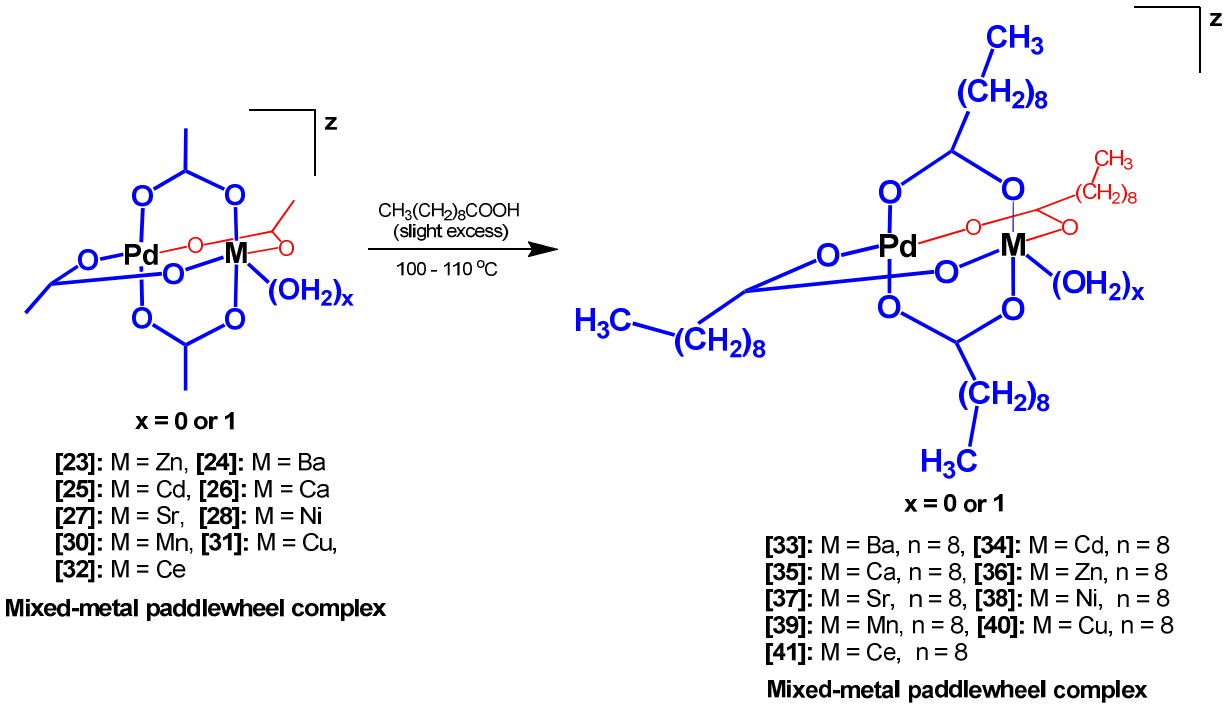

Scheme 3.11: Synthesis of long-chain aliphatic tetracarboxylitidopalladium(II)metal(II) and long-chain aliphatic tetracarboxylitidopalladium(II)cerium(III) mixed-metal paddlewheel complexes **[33-41]**. This is achieved by reacting short-chain tetraacetatidopalladium(II)metal(II) and short-chain tetraacetatidopalladium(II)cerium(III) mixed-metal paddlewheel complexes **[23-32]** with decanoic acid. The charge, z = 0 for all the complexes except **[32]** and **[41]** where z = +1, counter ion: decanoate. The red carboxylatido ligands are behind the page plane while the blue ones are in the front.

Table 3.5: Yields of long-chain tetracarboxylatido mixed-metal paddlewheel complexes.

$PdCo(C_m)_2$ and $PM(C_{10})_4$	**Yield %**	**$PM(C_{10})_4$**	**Yield %**
$PdCo(C_6)_4$ **[19]**	99	$PdZn(C_{10})_4$ **[36]**	95
$PdCo(C_8)_4$ **[20]**	81	$PdSr(C_{10})_4$ **[37]**	81
$PdCo(C_{10})_4$ **[21]**	66	$PdNi(C_{10})_4$ **[38]**	95
$PdCo(C_{12})_4$ **[22]**	88	$PdMn(C_{10})_4$ **[39]**	71
$PdBa(C_{10})_4$ **[33]**	75	$PdCu(C_{10})_4$ **[40]**	84
$PdCd(C_{10})_4$ **[34]**	88	$PdCe(C_{10})_4^+$ **[41]**	79
$PdCa(C_{10})_4$ **[35]**	71	-	-

The tetracarboxylatido mixed-metal paddlewheel complexes have yields varying between 66 % and 99 % see **Table 3.5**.

3.3. Characterisation (Spectroscopy)

3.3.1. Nuclear magnetic resonance spectroscopy

Figure 3.2 indicates the ^{1}H NMR spectra of the long-chain circular aliphatic tripalladium hexacarboxylatido complexes $Pd_3(C_6)_6$ **[1]** and $Pd_3(C_8)_6$ **[2]**, in chloroform-d_1 ($CDCl_3$). There are three distinct areas where peaks appear that can be observed for the tripalladium hexacarboxylatido complexes. The triplet belonging to the methyl group, CH_3, at the end of the alkyl chain is measured at *ca.* 0.75-0.95 ppm.

The methylene group adjacent to the carbonyl group, CH_2-COO, is shifted down field to *ca.* 2.0-2.4 ppm from *ca.* 0.4-1.9 ppm where the ligand's peaks normally appear, due to the deshielding by the carbonyl group. Lastly the carbon backbone methylene groups' chemical shifts, which are positioned between the methyl end group and the methylene adjacent to the carbonyl, are observed at *ca.* 0.95-1.55 ppm see **Figure 3.2**. Comparison of the ^{1}H NMR shifts of the methyl end group and the chain length of $Pd_3(C_6)_6$ **[1]**, $Pd_3(C_8)_6$ **[2]** $Pd_3(C_{10})_6$ **[3]** and $Pd_3(C_{12})_6$ **[4]** are shown in **Figure 3.3**.

It is not a linear relationship; however there is a clear down field shift of chemical shift of the methyl group as the carbon chain length increases. This trend can be explained by the increased electron-withdrawing influence of the carbonyl group through the carbon chain. Three distinct peaks can be observed for the chemical shifts of the hydrogen atoms of the three carbons in the circular tripalladium hexanoate carbon backbone of $Pd_3(C_6)_6$ **[1]**. Whereas when the chain length of the $Pd_3(C_8)_6$ **[2],** $Pd_3(C_{10})_6$ **[3]** and $Pd_3(C_{12})_6$ **[4]** carbon backbone increases, the peaks for the chemical shifts of the different -CH_2 groups start to overlap.

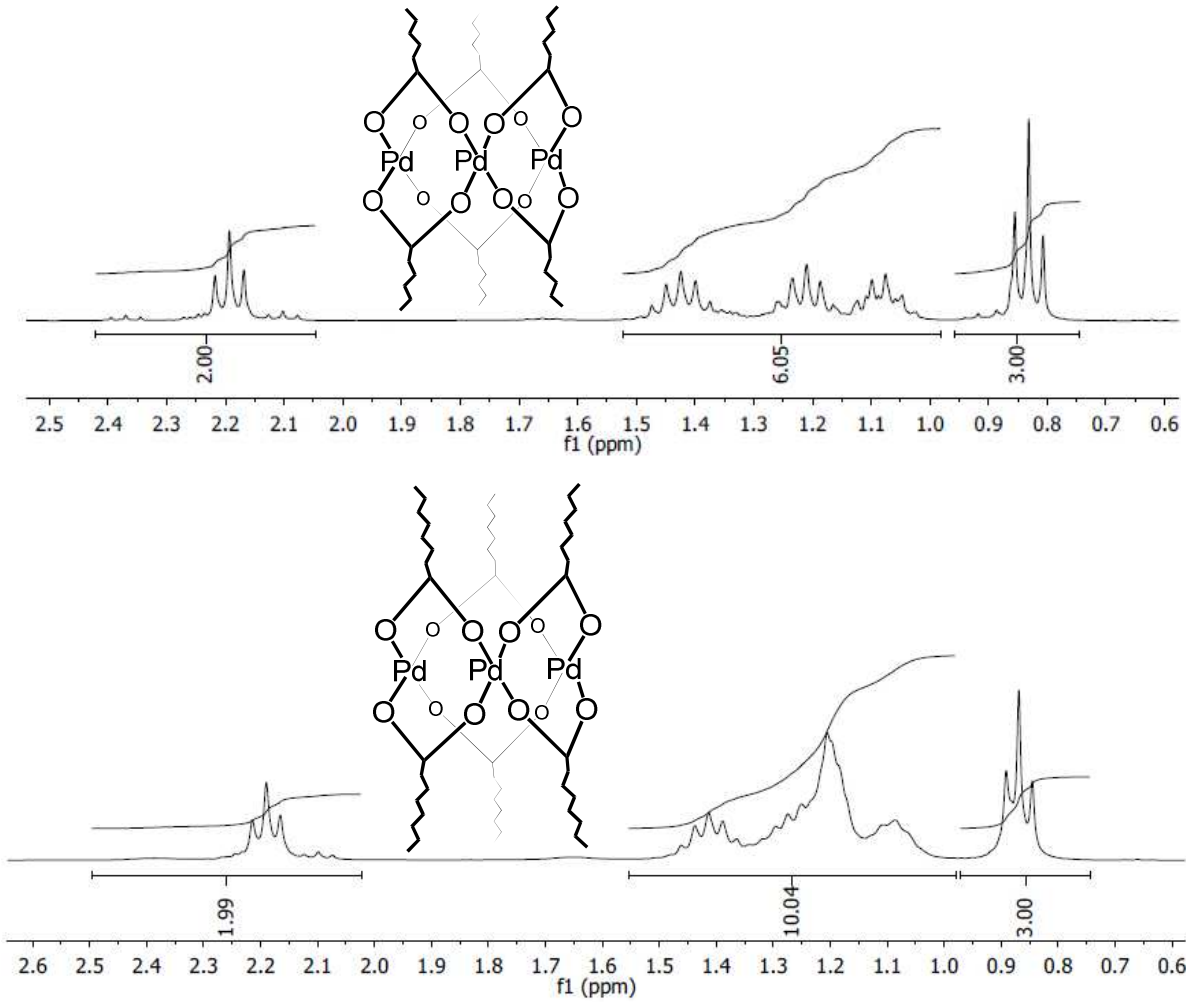

Figure 3.2: ^{1}H NMR spectra of the long-chain circular tripalladium hexacarboxylatido complexes $Pd_3(C_6)_6$ **[1]** (top) and $Pd_3(C_8)_6$ **[2]** (bottom) in chloroform-D_1 ($CDCl_3$).

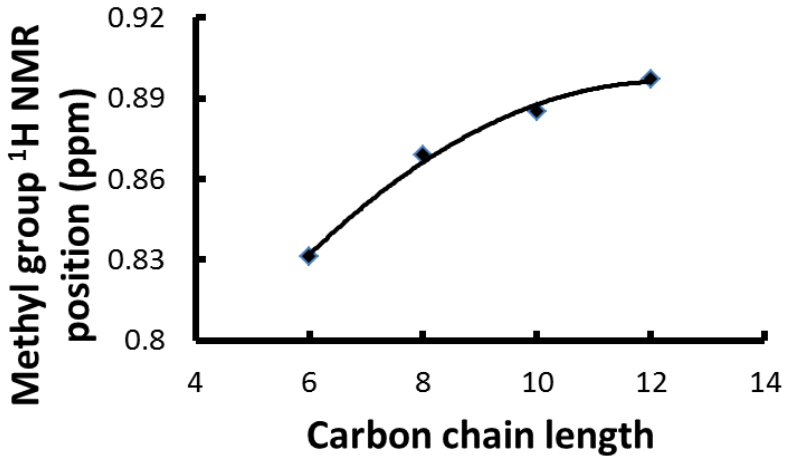

Figure 3.3: Relationship between the ^{1}H NMR shifts of the methyl end group (ppm values relative to TMS at 0.00 ppm) and the carbon chain length of $Pd_3(C_6)_6$ **[1]**, $Pd_3(C_8)_6$ **[2]** $Pd_3(C_{10})_6$ **[3]** and $Pd_3(C_{12})_6$ **[4]**.

3.3.2. Attenuated total reflectance Fourier transform infrared spectroscopy (ATR-FTIR)

3.3.2.1. Circular tripalladium hexacarboxylatido complexes

The ATR-FTIR spectra of the carboxylic acids and their corresponding long-chain circular aliphatic tripalladium hexacarboxylatido complexes $Pd_3(C_6)_6$ **[1]**, $Pd_3(C_8)_6$ **[2]** $Pd_3(C_{10})_6$ **[3]** and $Pd_3(C_{12})_6$ **[4]** are shown in **Figure 3.4** below.

Regarding the ATR-FTIR of the carboxylic acids, **Figure 3.4** (left), the broad band between *ca.* 3400-2400 cm^{-1} indicates the OH group in the carboxylic acid, while the stretching frequency at *ca.* 1700 cm^{-1} is associated with the carbonyl (C=O) of the carboxylic acid. Overlapping with the broad band of the OH stretching frequency at 3400-2400 cm^{-1} is the CH_2 stretching frequencies at *ca.* 3000-2800 cm^{-1}. The intensity of the CH_2 stretching frequencies at *ca.* 3000-2800 cm^{-1} increases as the chain length of the carbon backbone gets longer.

In the ATR-FTIR spectra of the long-chain circular tripalladium hexacarboxylatido complexes, **Figure 3.4** (right), $Pd_3(C_6)_6$ **[1]**, $Pd_3(C_8)_6$ **[2]** $Pd_3(C_{10})_6$ **[3]** and $Pd_3(C_{12})_6$ **[4]**, the free acid stretching frequency at *ca.* 1700 cm^{-1} is replaced by two very distinct carboxylatido stretching frequencies at *ca.* 1600 cm^{-1} and 1410 cm^{-1}. The stretching frequency at *ca.* 1600 cm^{-1} is associated with the anti-symmetric carboxylatido stretching frequency, while the stretching frequency at *ca.* 1410 cm^{-1} is associated with the symmetric carboxylatido stretching frequency of the circular tripalladium hexacarboxylatido complexes.

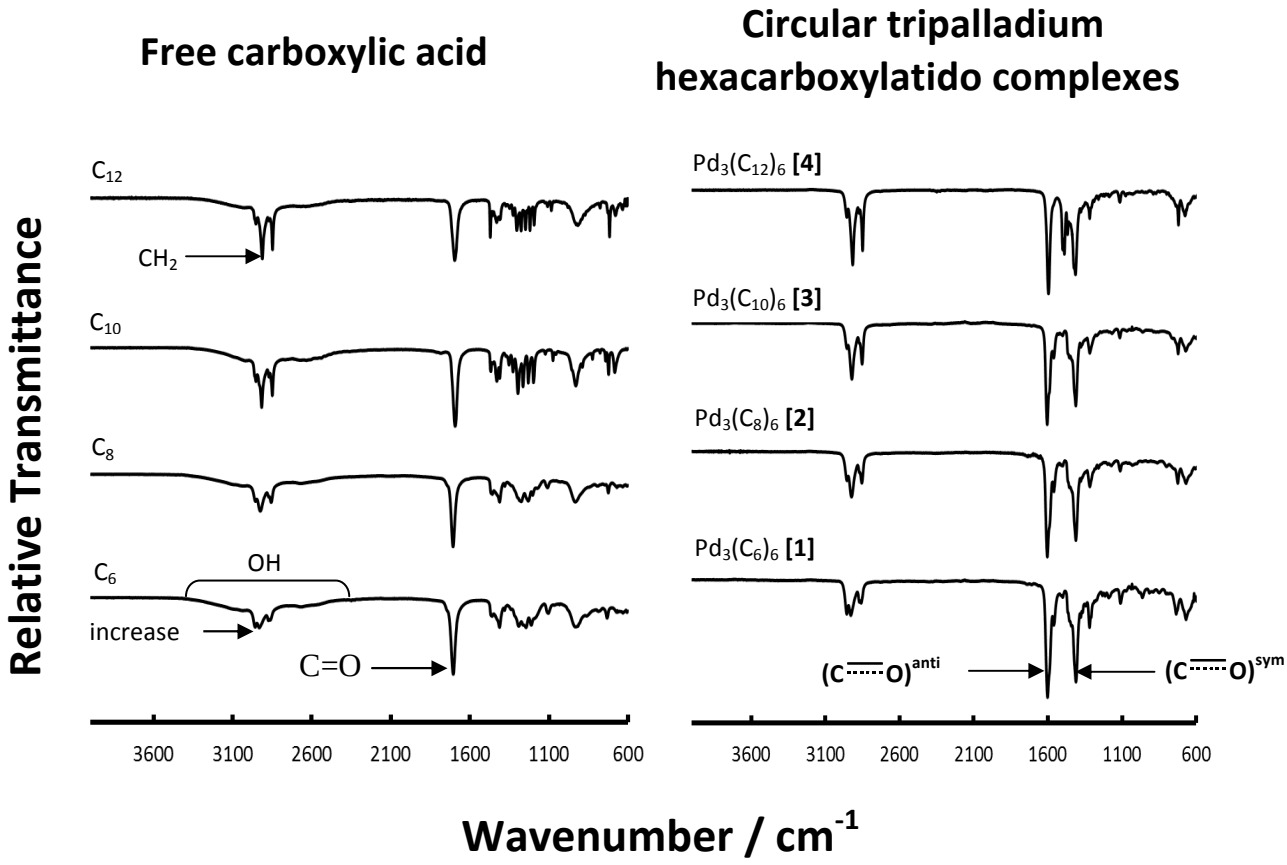

Figure 3.4: Left: ATR-FTIR of the indicated free carboxylic acids. **Right:** ATR-FTIR of the indicated circular aliphatic tripalladium hexacarboxylatido complexes.

The appearance of the new anti-symmetric carboxylatido stretching frequency at *ca.* 1600 cm^{-1} and the symmetric carboxylatido stretching bond at *ca.* 1410 cm^{-1} coincides with the disappearance of the carboxylatido stretching frequency of the free carboxylic acid at *ca.* 1700 cm^{-1} and the OH stretching frequency at *ca.* 3400-2400 cm^{-1}.

The difference between the carboxylatido stretching anti-symmetric and symmetric frequencies is calculated as follows:

$$\Delta_{Difference} = (C\overline{\cdots}O)^{anti} - (C\overline{\cdots}O)^{sym}$$

In the above equation $(C\overline{\cdots}O)^{anti}$ is the wavenumber of the anti-symmetric frequencies and $(C\overline{\cdots}O)^{sym}$ is the wavenumber of the symmetric frequencies. For a $\Delta_{Difference} > 200$ cm^{-1}, the carboxylatido binding mode to the metal is considered to be unidentate.[7]

[7] G.B. Deacon and R. J. Phillips, *J. Coord. Chem. Rev.*, 1980, **33**, 227

For a $\Delta_{Difference}$ < 120 cm^{-1}, the binding mode is considered to be bidentate. When a series of symmetric and anti-symmetric stretching frequencies are observed that results in a $\Delta_{Difference}$ = 120 - 200 cm^{-1}, the binding mode is considered to be bridging. For a $\Delta_{Difference}$ = 150 - 200 cm^{-1}, (mostly close to 150 cm^{-1} only) the binding mode is considered to be ionic. This well-established characterisation method, originally developed by Nakamoto[8] and Deacon and Phillips,[7] was used to deduce the structure for the published and the novel (new) compounds synthesised in this study. See crystallographic section 3.4, where the binding modes are identified.

This latter range overlaps with the $\Delta_{Difference}$ region of the bridging mode.[7] The difference between the anti-symmetric and symmetric stretching frequency of, $Pd_3(C_6)_6$ **[1]**, $Pd_3(C_8)_6$ **[2]** $Pd_3(C_{10})_6$ **[3]** and $Pd_3(C_{12})_6$ **[4]** is *ca.* 182-193 cm^{-1} which is consistent with the binding mode as being bridging, shown in **Table 3.6**.

The difference between the carbonyl stretching frequency of the free acid and anti-symmetric stretching frequency of the coordinated carboxylatido ligand were calculated as follows:

$$\Delta_{Shift} = (C\overset{\cdots}{=}O)^{anti} - (C{=}O)^{free\ acid}$$

In the above equation $(C\overset{\cdots}{=}O)^{anti}$ is the wavenumber of the anti-symmetric carboxylatido complex stretching frequency and $(C\overset{\cdots}{=}O)^{free\ acid}$ is the wavenumber of the free acid carbonyl stretching frequency. The shift in stretching frequency for the carbonyl from the free acid (*ca.* 1700 cm^{-1}) to the metal coordinated carboxylatido complex relative to the anti-symmetric stretching frequency (*ca.* 1600 cm^{-1}) is *ca.* 90-101 cm^{-1}.

The anti-symmetric stretching frequencies of $Pd_3(C_6)_6$ **[1]**, $Pd_3(C_8)_6$ **[2]** $Pd_3(C_{10})_6$ **[3]** and $Pd_3(C_{12})_6$ **[4]** are observed between 1596-1604 cm^{-1} and the symmetric stretching frequencies are observed between 1411-1414 cm^{-1}. Bakhmutov *et al.*[9] observed the anti-symmetric and symmetric stretching frequencies of the circular hexaacetatidotripalladium(II) at 1600 cm^{-1} and 1430 cm^{-1} respectively while Stephenson *et al.*[10] observed the anti-symmetric and symmetric stretching frequencies of circular hexaacetatidotripalladium(II) at 1600 cm^{-1} and 1427 cm^{-1} respectively. These values are within experimental error all mutually consistent.

---

[8] K. Nakamoto, *Infrared and Raman Spectra of Inorganic and Coordination Compounds*, John Wiley & Sons, Inc., 231 - 233 (1997).

[9] V. I. Bakhmutov, J. F. Berry, F. A. Cotton, S. Ibragimov and C. A. Murillo, *Dalton Trans.*, 2005, 1989

[10] T. A. Stephenson, S. M. Morehouse, A**.** R. Powell, J. P. Heffer, and G. Wilkinson, *J. Chem. Soc.*, 1965, 3632

The fact that the $\Delta_{Differences}$ are all between 181 cm^{-1} and 193 cm^{-1}, is indicative of the fact that the carboxylatido coordination mode is exclusively the bridging mode.

Table 3.6: ATR-FTIR data obtained for the indicated free carboxylic acids and the indicated circular tripalladium hexacarboxylatido complexes.

$Pd_3(C_m)_6$ where m = 6, 8, 10 or 12 (Free carboxylic acid)	**$(C\overline{\cdots}O)^{anti}$ and $(C\overline{\cdots}O)^{free\ acid}$**	**$(C\overline{\cdots}O)^{sym}$**	**Δ_{Shift} [a]**	**$\Delta_{Difference}$ [b]**
$Pd_3(C_6)_6$, **[1]** (hexanoic acid)	1602 (1702)	1411	100	191 Bridging
$Pd_3(C_8)_6$, **[2]** (octanoic acid)	1604 (1704)	1411	100	193 Bridging
$Pd_3(C_{10})_6$, **[3]** (decanoic acid)	1604 (1694)	1412	90	192 Bridging
$Pd_3(C_{12})_6$, **[4]** (dodecanoic acid)	1596 (1697)	1414	101	182 Bridging

[a] $\Delta_{Shift} = (C\overline{\cdots}O)^{anti} - (C{=}O)^{free\ acid}$

[b] $\Delta_{Difference} = (C\overline{\cdots}O)^{anti} - (C\overline{\cdots}O)^{sym}$

The binding mode type associated with each $\Delta_{Difference}$ is provided below each value, assignments was made according to the criteria presented on page 52 and 53, utilising reference 7.

3.3.2.2. Ionic potassium carboxylates

In **Figure 3.5** below the ATR-FTIR of the potassium carboxylates KC_6 **[5]**, KC_8 **[6]**, KC_{10} **[7]** and KC_{12} **[8]** are shown. When aqueous potassium hydroxide was reacted with a carboxylic acid the carbonyl (*ca.* 1700 cm^{-1}) stretching frequency disappeared and two new stretching frequencies appeared at *ca.* 1560 cm^{-1} and *ca.* 1408 cm^{-1}. This is the result of the metal cation being electrostatically attracted to the carboxylate anion in the compound at room temperature. From these two stretching frequencies (anti-symmetric and symmetric) conclusions regarding the binding modes can be drawn. From **Table 3.7**, the differences between the anti-symmetric and symmetric stretching frequencies are between *ca.* 150 – 154 cm^{-1}, this is an indication that the binding mode is exclusively ionic.

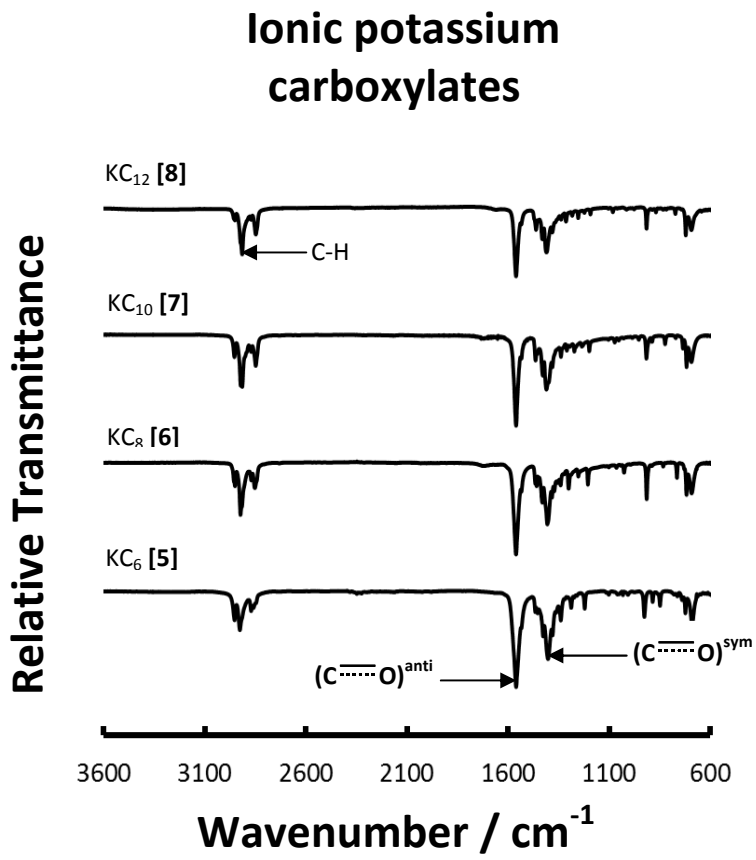

Figure 3.5: ATR-FTIR of the indicated ionic potassium carboxylates.

Table 3.7: ATR-FTIR data obtained for the indicated carboxylic acids and the indicated ionic potassium carboxylates.

KC_m m = 6, 8, 10 or 12 (Carboxylic acid)	**$(C\overline{\cdots}O)^{anti}$ $(C=O)^{free\ acid}$**	**$(C\overline{\cdots}O)^{sym}$**	**Δ_{Shift} [a]**	**$\Delta_{Difference}$ [b]**
KC_6, **[5]** (hexanoic acid)	1560 (1702)	1410	142	150 Ionic
KC_8, **[6]** (octanoic acid)	1560 (1704)	1410	144	150 Ionic
KC_{10}, **[7]** (decanoic acid)	1560 (1694)	1406	134	154 Ionic
KC_{12}, **[8]** (dodecanoic acid)	1560 (1697)	1406	137	154 Ionic

[a] $\Delta_{Shift} = (C\overline{\cdots}O)^{anti} - (C=O)^{free\ acid}$

[b] $\Delta_{Difference} = (C\overline{\cdots}O)^{anti} - (C\overline{\cdots}O)^{sym}$

The binding mode type associated with each $\Delta_{Difference}$ is provided below each value, assignments was made according to the criteria presented on page 52 and 53, utilising reference 7.

3.3.2.3. Non-paddlewheel cobalt carboxylatido complexes

The ATR-FTIR spectra of all the non-paddlewheel cobalt carboxylatido complexes have intense stretching frequencies between 3000–2800 cm^{-1} which is assigned to the methylene stretching frequencies. The intensity of the CH_2 stretching frequencies at *ca.* 3000-2800 cm^{-1} increases as the chain length of the carbon backbone gets longer. The anti-symmetric stretching frequencies are observed between 1543-1626 cm^{-1} while the symmetric stretching frequencies are observed between 1350-1409 cm^{-1}. From **Table 3.8**, all four cobalt complexes have two binding modes. These include unidentate and pseudo-bridging binding mode, because of these binding modes that exist in the complex, the anti-symmetric and symmetric stretching frequencies are split into more than one stretching frequency.

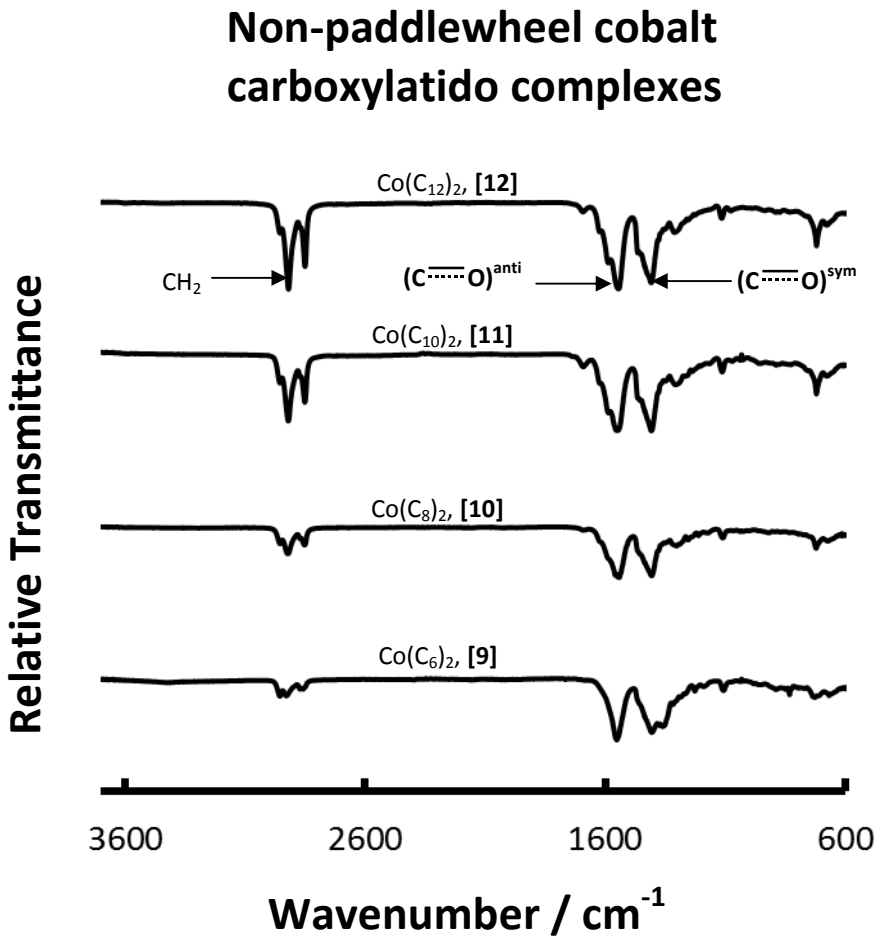

Figure 3.6: ATR-FTIR of the indicated non-paddlewheel cobalt carboxylatido complexes.

Table 3.8: ATR-FTIR data obtained for the indicated cobalt carboxylatido complexes.

$Co(C_m)_2$	**A (cm^{-1})**	**B (cm^{-1})**	**Δ_{Shift}[a] A1-C**	**$\Delta_{Difference}$[b] A1-B1**	**$\Delta_{Difference}$[b] A2-B1**	**$\Delta_{Difference}$[b] A3-B1**	**$\Delta_{Difference}$[b] A1-B2**
$Co(C_6)_2$ **[9]**	A1=1556	B1=1402 B2=1350	138	154 Pseudo-Bridging	-	-	206 Unidentate
$Co(C_8)_2$ **[10]**	A1=1623 A2=1589 A3=1543	B1=1406	71	217 Unidentate	183 Pseudo-Bridging	137 Pseudo-Bridging	-
$Co(C_{10})_2$ **[11]**	A1=1610 A2=1588 A3=1547	B1=1406	84	204 Unidentate	182 Pseudo-Bridging	141 Pseudo-Bridging	-
$Co(C_{12})_2$ **[12]**	A1=1626 A2=1593 A3=1541	B1=1409	68	217 Unidentate	184 Pseudo-Bridging	132 Pseudo-Bridging	-

anti-symmetric peak $(C\overline{\cdots}O)^{anti}$ = A

symmetric peak $(C\overline{\cdots}O)^{sym}$ = B

For the free acid, the stretching frequency is *ca.* 1694 cm^{-1} = C

[a] $\Delta_{Shift} = (C\overline{\cdots}O)^{anti} - (C{=}O)^{free\ acid}$ = A-C

[b] $\Delta_{Difference} = (C\overline{\cdots}O)^{anti} - (C\overline{\cdots}O)^{sym}$ = A-B

Because different binding modes lead to small but noticeable changes in frequencies of symmetric and anti-symmetric vibrations of the carbonyl group, FTIR is often by necessity (due to poor solubility etc.) the preferred instrumental technique to obtain structural information.

The binding mode type associated with each $\Delta_{Difference}$ is provided below each value, assignments was made according to the criteria presented on page 52 and 53, utilising reference 7.

3.3.2.4. Non-paddlewheel metal carboxylatido complexes of the type $M(C_{10})_2$ and $Ce(C_{10})_3$

Some metal carboxylatido complexes synthesised in this study have broad peaks around 3600-3100 cm^{-1} which indicates the presence of crystal or adsorbed water in the complex, see **Figure 3.7**. At *ca.* 3000–2800 cm^{-1} sharp intense bands are observed which are assigned to the methylene (CH_2) stretching frequency of the long chain carboxylatido complexes. Marques *et al.*[11] observed the anti-symmetric and symmetric stretching frequencies of $Ce(C_{10})_3$ **[18]** and $Zn(C_{10})_2$ **[15]** at 1530-1410 cm^{-1} and 1543-1400 cm^{-1} respectively. Pereira *et al.*[12] observed the anti-symmetric and symmetric stretching frequency of $Ca(C_{10})_2$ **[16]** to be at 1539 cm^{-1} and 1435 cm^{-1} respectively.

[11] E. F. Marques, H. D. Burrows and M. da Graca Miguel, *J. Chem. Soc., Faraday Trans.*, 1998, (94), 1729

[12] R. F. P. Pereira, A. J. M. Valente, M. Fernandes and H. D. Burrows, *Phys. Chem. Chem. Phys.*, 2012, **14**, 7517

In this study the non-paddlewheel metal carboxylatido complexes $Ni(C_{10})_2$ **[13]**, $Mn(C_{10})_2$ **[14]**, $Zn(C_{10})_2$ **[15]**, $Ca(C_{10})_2$ **[16]**, $Sr(C_{10})_2$ **[17]** and $Ce(C_{10})_3$ **[18]**, the anti-symmetric and symmetric stretching frequencies were observed between 1627-1510 cm^{-1} and 1466-1396 cm^{-1} respectively. These stretching frequencies are intense and give an indication to the symmetry i.e. the binding mode of the carboxylatido ligand to the metal. Because of the binding modes that exist in the complex, the anti-symmetric and symmetric stretching frequencies are split into more than one stretching frequency.

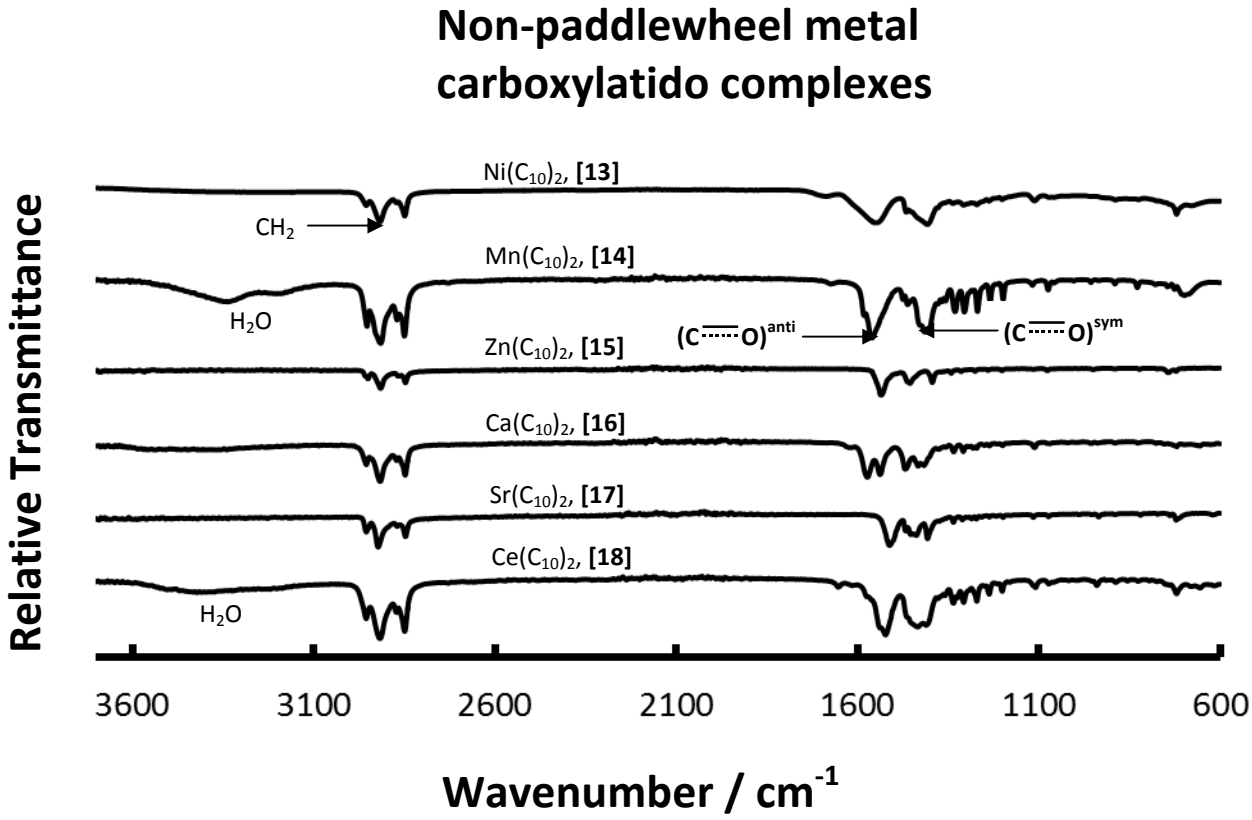

Figure 3.7: ATR-FTIR of the indicated non-paddlewheel metal carboxylatido complexes.

From the results summarised in **Table 3.9**, the non-paddlewheel metal carboxylatido complexes $Ni(C_{10})_2$ **[13]**, $Mn(C_{10})_2$ **[14]**, $Zn(C_{10})_2$ **[15]**, $Ca(C_{10})_2$ **[16]** and $Ce(C_{10})_3$ **[18]** clearly have more than one type of binding mode. These are unidentate, bridging and bidentate binding modes as seen from the difference between the anti-symmetric and symmetric stretching frequencies. The complex **[16]** has a mixture of bridging, unidentate and bidentate coordination while **[13-15]** and **[18]** have bidentate and bridging binding modes while **[17]** is exclusively bidentate.

Table 3.9: ATR-FTIR stretching frequencies of the indicated non-paddlewheel metal carboxylatido complexes.

$M(C_{10})_2$ or $Ce(C_{10})_3$	**A (cm^{-1})**	**B (cm^{-1})**	**Δ_{Shift}[a] A1-C**	**$\Delta_{Difference}$[b] A1-B1**	**$\Delta_{Difference}$[b] A1-B2**	**$\Delta_{Difference}$[b] A1-B3**	**$\Delta_{Difference}$[b] A2-B1**	**$\Delta_{Difference}$[b] A2-B2**	**$\Delta_{Difference}$[b] A2-B3**
$Ni(C_{10})_2$, **[13]**	A1=1544	B1=1464 B2=1405	150	80 Bidentate	139 Bridging	-	-	-	-
$Mn(C_{10})_2$, **[14]**	A1=1583 A2=1562	B1=1413 B2=1460	111	170 Bridging	123 Bridging	-	149 Bridging	102 Bidentate	-
$Zn(C_{10})_2$, **[15]**	A1=1534	B1=1455, B2=1396	160	79 Bidentate	138 Bridging	-	-	-	-
$Ca(C_{10})_2$, **[16]**	A1=1627 A2=1576	B1=1466 B2=1431 B3=1415	67	161 Bridging	196 Bridging	212 Unidentate	110 Bidentate	145 Bridging	161 Bridging
$Sr(C_{10})_2$, **[17]**	A1=1510	B1=1458 B2=1448 B3=1407	184	52 Bidentate	62 Bidentate	103 Bidentate	-	-	-
$Ce(C_{10})_3$, **[18]**	A1=1534 A2=1523	B1=1432, B2=1411	160	102 Bidentate	123 Bridging	-	91 Bidentate	112 Bidentate	-

anti-symmetric peak $(C\overline{\cdots}O)^{anti}$ = A

symmetric peak $(C\overline{\cdots}O)^{sym}$ = B

For the free acid $(CH_3(CH_2)_8COOH)^{free\ acid}$ = *ca.* 1694 cm^{-1} = C

[a] $\Delta_{Shift} = (C\overline{\cdots}O)^{anti} - (C{=}O)^{free\ acid}$ = A-C

[b] $\Delta_{Difference} = (C\overline{\cdots}O)^{anti} - (C\overline{\cdots}O)^{sym}$ = A-B

Because different binding modes lead to small but noticeable changes in frequencies of symmetric and anti-symmetric vibrations of the carbonyl group, FTIR is often by necessity (due to poor solubility etc.) the preferred instrumental technique to obtain structural information.

The binding mode type associated with each $\Delta_{Difference}$ is provided below each value, assignments was made according to the criteria presented on page 52 and 53, utilising reference 7.

3.3.2.5. Mixed-metal paddlewheel carboxylatido complexes

The mixed metal paddlewheel carboxylatido complexes $PdCo(C_{10})_4$ **[21]**, $PdBa(C_{10})_4$ **[33]**, $PdCd(C_{10})_4$ **[34]**, $PdCa(C_{10})_4$ **[35]**, $PdZn(C_{10})_4$ **[36]**, $PdSr(C_{10})_4$ **[37]**, $PdNi(C_{10})_4$ **[38]**, $PdMn(C_{10})_4$ **[39]**, $PdCu(C_{10})_4$ **[40]** and $PdCe(C_{10})_4$ **[41]** were characterised using ATR-FTIR. This is a quick and easy way to follow the reaction and also to determine when all the free carboxylic acid has been removed from the reaction mixture. The ATR-FTIR spectra of all the mixed-metal paddlewheel carboxylatido complexes have intense stretching frequencies between 3000–2800 cm^{-1} which is assigned to the methylene stretching frequencies. The anti-symmetric stretching frequencies are observed between 1573-1629 cm^{-1} while the symmetric stretching frequencies are observed between 1387-1408 cm^{-1}.

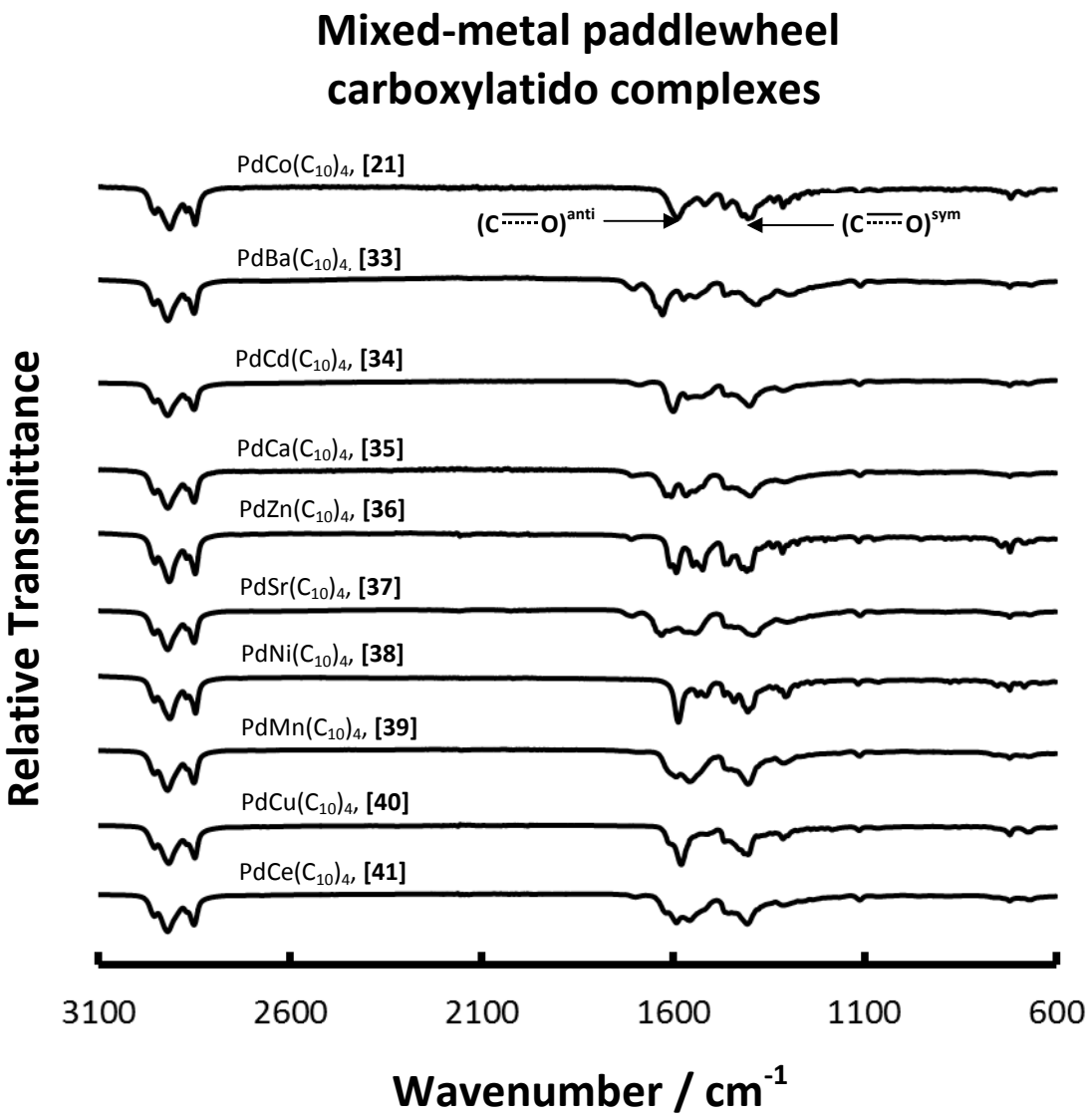

Figure 3.8: ATR-FTIR spectra of mixed-metal paddlewheel carboxylatido complexes.

Table 3.10 contains the anti-symmetric and symmetric data obtained from the ATR-FTIR study of the mixed-metal paddlewheel carboxylatido complexes. $\Delta_{Difference}$ between the carboxylatido complex stretching frequency of the anti-symmetric and the symmetric stretching frequency was found between 49-242 cm^{-1} (**Table 3.10**) which indicates that three binding modes are present, unidentate binding mode, bridging binding mode and bidentate binding mode. Because of these binding modes that exist in the complex, the anti-symmetric and symmetric stretching frequencies are split into more than one stretching frequency. Some of the complexes have a mixture of unidentate and bridging binding modes for example **[21]**, **[34]**, **[36]**, **[37]** and **[40]**, while **[33]**, **[35]** and **[41]** has a mixture of unidentate, bridging and bidentate binding mode. The complexes **[38]** and **[39]** have bridging and bidentate binding mode as well as exclusively bridging binding mode respectively.

Table 3.10: Selected data obtained from the FTIR spectra of the indicated mixed-metal paddlewheel carboxylatido complexes.

$PdM(C_{10})_4$	**A (cm^{-1})**	**B (cm^{-1})**	**Δ_{Shift}[a] A1-C**	**$\Delta_{Difference}$[b] A1-B1**	**$\Delta_{Difference}$[b] A1-B2**	**$\Delta_{Difference}$[b] A1-B3**	**$\Delta_{Difference}$[b] A2-B1**	**$\Delta_{Difference}$[b] A2-B2**
$PdCo(C_{10})_4$, **[21]**	A1=1589 A2=1518	B1=1418 B2=1465 B3=1376	105	171 Bridging	-	213 Unidentate	100 Bidentate	53 Bidentate
$PdBa(C_{10})_4$, **[33]**	A1=1629 A2=1573	B1=1387 B2=1465	65	242 Unidentate	-	-	186 Bridging	108 Bidentate
$PdCd(C_{10})_4$, **[34]**	A1=1600 A2=1564	B1=1400	94	200 Unidentate	-	-	164 Bridging	-
$PdCa(C_{10})_4$, **[35]**	A1=1606 A2=1568	B1=1400 B2=1455	88	206 Unidentate	-	-	168 Bridging	113 Bidentate
$PdCe(C_{10})_4$, **[36]**	A1=1591 A2=1617	B1=1408	103	183 Bridging	-	-	209 Unidentate	-
$PdSr(C_{10})_4$, **[37]**	A1=1628 A2=1540	B1=1395	66	233 Unidentate	-	-	145 Bridging	-
$PdNi(C_{10})_4$, **[38]**	A1=1588 A2=1515	B1=1405 B2=1466	106	183 Bridging	-	-	-	49 Bidentate
$PdMn(C_{10})_4$, **[39]**	A1=1559 A2=1591	B1=1406	135	153 Bridging	-	-	185 Bridging	-
$PdCu(C_{10})_4$, **[40]**	A1=1580	B1=1403 B2=1466	114	177 Bridging	114 Unidentate	-	-	-
$PdZn(C_{10})_4$, **[41]**	A1=1593 A2=1523	B1=1407 B2=1465 B3=1375	101	186 Bridging	128 Bridging	218 Unidentate	116 Bidentate	58 Bidentate

anti-symmetric peak $(C\overline{\cdots}O)^{anti}$ = A, symmetric peak $(C\overline{\cdots}O)^{sym}$ = B

For the free acid $(C=O)^{free\ acid}$ = *ca.* 1694 cm^{-1} = C

[a] $\Delta_{Shift} = (C\overline{\cdots}O)^{anti} - (C=O)^{free\ acid}$ = A-C

[b] $\Delta_{Difference} = (C\overline{\cdots}O)^{anti} - (C\overline{\cdots}O)^{sym}$ = A-B

Because different binding modes lead to small but noticeable changes in frequencies of symmetric and anti-symmetric vibrations of the carbonyl group, FTIR is often by necessity (due to poor solubility etc.) the preferred instrumental technique to obtain structural information.

The binding mode type associated with each $\Delta_{Difference}$ is provided below each value, assignments was made according to the criteria presented on page 52 and 53, utilising reference 7.

3.3.2.6. Palladium cobalt mixed-metal paddlewheel carboxylatido complexes

For the title complexes, the region between 3000-2800 cm^{-1}, the methylene stretching frequencies are observed. $PdCo(C_{12})_4$ **[22]** and $PdCo(C_8)_4$ **[20]** still has some free acid in the complex as indicated by the stretching frequency at *ca.* 1700 cm^{-1} see **Figure 3.9**. Prolonged stirring at 100-110 ˚C results in decarboxylation; therefore the reaction had to be stopped before this happens. The characteristic anti-symmetric and symmetric carbonyl stretching frequencies are observed between 1589-1422 cm^{-1}. Because of the binding modes that exist in the complex, the anti-symmetric and symmetric stretching frequencies are split into more than one stretching frequency.

The anti-symmetric stretching frequency of the carboxylatido group for $PdCo(C_8)_4$ **[20]**, $PdCo(C_{10})_4$ **[21]** and $PdCo(C_{12})_4$ **[22]** is observed at 1591 cm^{-1} while for $PdCo(C_6)_4$ **[19]**, the carboxylatido stretching frequency is observed at 1589 cm^{-1}. The symmetric stretching frequency is observed between 1393 cm^{-1} and 1422 cm^{-1}.

The most intense carboxylatido stretching frequency of the symmetric stretching frequency seems to be dependent on the amount of carbons within the carboxylatido backbone, see **Figure 3.10**. According to this graph, an increase in the amount of carbon in the carboxylatido backbone leads to an increase in the carboxylatido symmetric stretching frequency of the mixed metal paddlewheel carboxylatido complexes **[19-22]** and accordingly to a smaller $\Delta_{Difference}$. The difference between the carbonyl stretching frequency of the anti-symmetric and the symmetric stretching frequencies, are shown in **Table 3.11**. Lastly $\Delta_{Difference}$ between the carboxylatido stretching frequency of the anti-symmetric and the symmetric stretching frequency indicates that the carboxylatido groups have a mixture of unidentate, bidentate and bridging binding modes with the palladium and cobalt metal centres. Also $PdCo(C_6)_4$ **[19]**, only have bidentate and bridging binding modes.

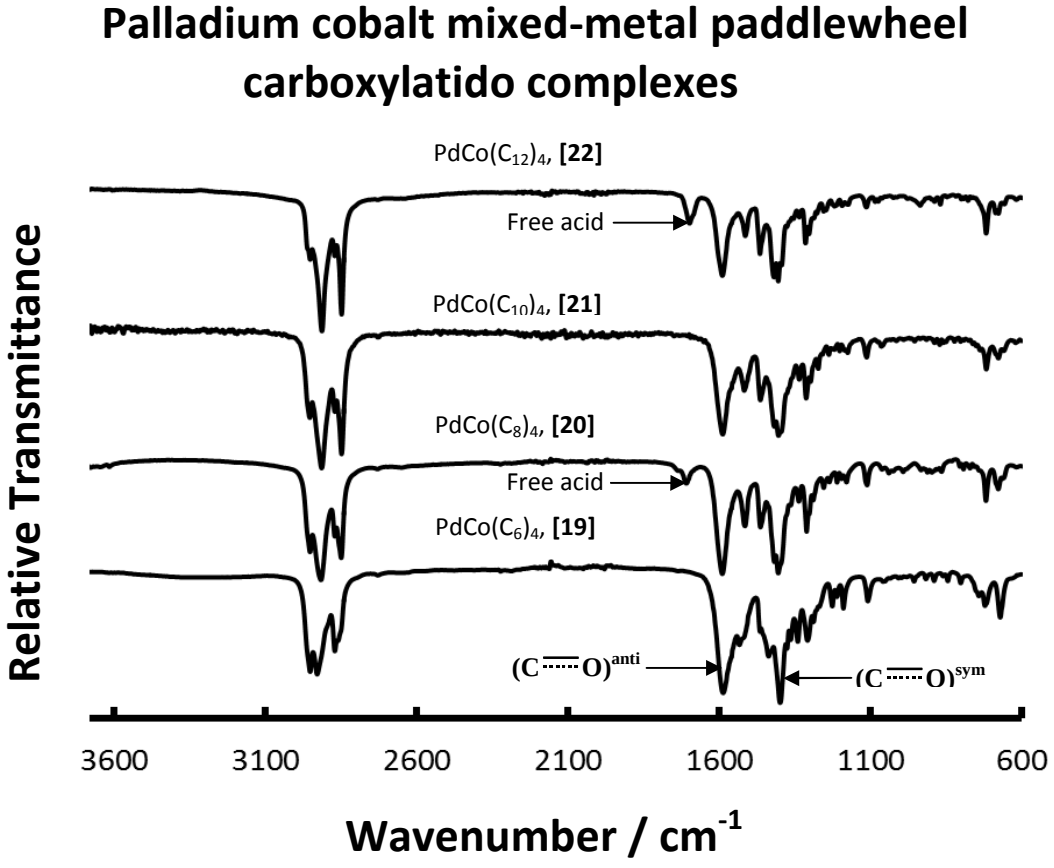

Figure 3.9: ATR-FTIR of the indicated palladium cobalt mixed-metal paddlewheel carboxylatido complexes

Table 3.11: ATR-FTIR spectra of the indicated palladium cobalt mixed-metal paddlewheel carboxylatido complexes.

$PdCo(C_m)_4$	**A (cm^{-1})**	**B (cm^{-1})**	**Δ_{Shift}[a] A-C**	**$\Delta_{Difference}$[b] A1-B1**	**$\Delta_{Difference}$[b] A1-B2**	**$\Delta_{Difference}$[b] A1-B3**	**$\Delta_{Difference}$[b] A2-B1**	**$\Delta_{Difference}$[b] A2-B2**	**$\Delta_{Difference}$[b] A2-B3**
$PdCo(C_{12})_4$ **[22]**	A1=1591 A2=1517	B1=1422 B2=1405 B3=1377	103	169 Bridging	186 Bridging	214 Unidentate	95 Bidentate	112 Bidentate	124 Bridging
$PdCo(C_{10})_4$ **[21]**	A1=1589 A2=1518	B1=1465 B2=1418 B3=1376	103	124 Bridging	171 Bridging	213 Unidentate	53 Bidentate	100 Bidentate	142 Bridging
$PdCo(C_8)_4$ **[20]**	A1=1591 A2=1514	B1=1418 B2=1404 B3=1375	103	173 Bridging	187 Bridging	216 Unidentate	96 Bidentate	110 Bidentate	50 Bidentate
$Pd(Co(C_6)_4$ **[19]**	A1=1589 A2=1533	B1=1398 B2=1437	105	191 Bridging	152 Bridging	-	135 Bridging	96 Bidentate	-

anti-symmetric peak $(C\overline{\cdots}O)^{anti}$ = A

symmetric peak $(C\overline{\cdots}O)^{sym}$ = B

For the free acid $(C=O)^{free\ acid}$ = ca. 1694 cm^{-1} = C

[a] $\Delta_{Shift} = (C\overline{\cdots}O)^{anti} - (C=O)^{free\ acid}$ = A-C

[b] $\Delta_{Difference} = (C\overline{\cdots}O)^{anti} - (C\overline{\cdots}O)^{sym}$ = A-B

Because different binding modes lead to small but noticeable changes in frequencies of symmetric and anti-symmetric vibrations of the carbonyl group, FTIR is often by necessity (due to poor solubility etc.) the preferred instrumental technique to obtain structural information.

The binding mode type associated with each $\Delta_{Difference}$ is provided below each value, assignments was made according to the criteria presented on page 52 and 53, utilising reference 7.

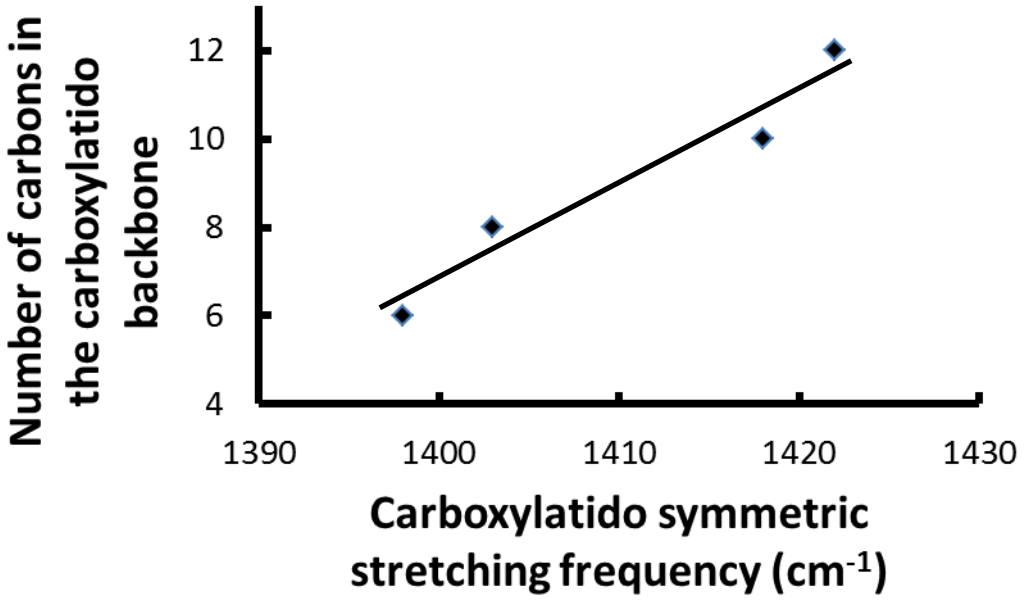

Figure 3.10: The relationship between the number of carbons in the carboxylatido complex backbone and the carboxylatido symmetric stretching frequency of the palladium cobalt mixed-metal paddlewheel carboxylatido complexes $PdCo(C_6)_4$ **[19]**, $PdCo(C_8)_4$ **[20]**, $PdCo(C_{10})_4$ **[21]** and $PdCo(C_{12})_4$ **[22]**.

3.4. Crystallography

Crystallographic quality crystals were obtained for $Pd^{II}Co^{II}(\mu\text{-}OOC(CH_2)_8CH_3)_4$ **[21]** $Pd^{II}Zn^{II}(\mu\text{-}OOC(CH_2)_8CH_3)_4$ **[36]** and $Pd^{II}Ni^{II}(\mu\text{-}OOC(CH_2)_8CH_3)_4$ **[38]** by dissolving the complex in DCM and overlaying with *n*-hexane and allowing the crystals to grow.

3.4.1. Crystal and structure refinement data for $Pd^{II}Co^{II}(\mu\text{-}OOC(CH_2)_8CH_3)_4$ [21]

The author would like to acknowledge Dr. Alice Brink for the data collection and solving the crystal structure at the University of the Free State. A perspective view of $PdCo(C_{10})_4$ **[21]**, showing atom labelling in **Figure 3.11**. The crystal data is summerised in **Table 3.12** while some of the most important bond lengths and angles are given in **Table 3.13**. $PdCo(C_{10})_4$ **[21]** crystallises in a monoclinic crystal system and a $P2_1/c$ space group with two formula units per unit cell (Z = 2).

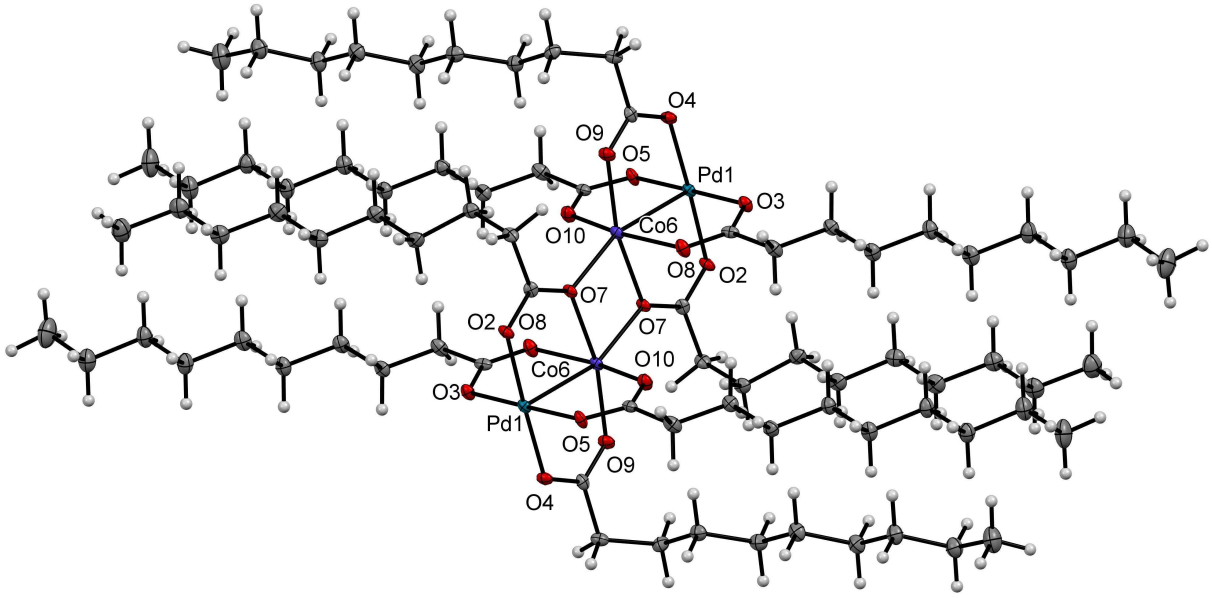

Figure 3.11: Molecular structure of the paddlewheel complex, $PdCo(C_{10})_4$ **[21]**. Hydrogen and carbon atom labelling numbers are omitted for clarity.

The $PdCo(C_{10})_4$ **[21]** molecule has a cobalt and palladium metal atom with four oxygen atoms around the two metal atoms forming a paddlewheel structure. The long carboxylatido carbon atom tails are orientated parallel to each other. The carboxylatido –COO portion of the ligands are situated in a bridged conformation around the two metal atoms.

Each paddlewheel structure acts as the axial ligand for the neighbouring paddlewheel structure via the Co(6a)-O(7b) bond and vice versa.

The cobalt atom has a distorted square-pyramidal conformation in a direction away from the palladium atom, while the palladium atom has a square-planar conformation. The intermolecular bonds Co(6a)-O(7b) and Co(6b)-O(7a) are short enough (2.029 Å) to involve intermolecular atomic interaction, binding the two molecules together. The intramolecular bonds Co(6a)-O(7a) and Co(6b)-O(7b) with a bond length of 2.170 Å are involved in intramolecular bonding.

Table 3.12: Crystal and structure refinement data for $PdCo(C_{10})_4$, **[21]**.

Empirical formula	$C_{80}H_{152}O_{16}Co_2Pd_2$	**Crystal sise (mm)**	0.02x0.24x0.27
Formula weight	1700.68	**Theta range for data collection**	2.2-28.0
Temperature (K)	100(2)	**Reflections collected**	10100
Wavelength	0.71069	**R_{int}**	0.0396
Crystal system	Monoclinic	**Independent reflections**	7547
Space group	$P2_1/c$	**Completeness to theta = 28 °C**	100 %
Unit cell dimensions	a = 28.300(5) Å b = 9.862(2) Å c = 15.562 Å α = 90.00 ° β = 105.48 ° γ = 90.00 °	**Index ranges**	-34<=h<=37 -12<=k<=13 -20<=l<=28
Volume	4185.69 $Å^3$	**Refinement method**	Full matrix least squares on F^2
Z	2	**Data / restraints / parameters**	10100/0/455
Density (calculated)	1.349 Mg m^3	**Goodness-of-fit on F^2**	1.011
Absorption coefficient	0.873 mm^{-1}	**Final R indices [I>2sigma(I)]**	R = 0.0396, wR2 = 0.0975
F(000)	1812	**R indices (all data)**	R1 = 0.0651, wR2 = 0.0858
-	-	**Largest diff. peak and hole e.$Å^{-3}$**	0.803 and -1.052

Regarding the structure of $PdCo(C_{10})_4$, **[21]**, correlations can be made with ATR-FTIR to explain the $\Delta_{Difference}$ ($\Delta_{Difference}$ = $(C\overline{\cdots}O)^{anti}$ - $(C\overline{\cdots}O)^{sym}$) obtained. The bond, O(7a)-Co(6b) can be considered as a unidentate binding mode, see **Figure 3.12**. The bond, O(7a)-Co(6a)-O(7b) can be considered to be a bidentate binding mode and the bond, Pd(1)-O(5)-C-O(10)-Co(6a) can be considered as a bridging *syn-syn* binding mode. Lastly Pd(1)-O(2)-C-O(7a)-Co(6a) can be considered as a bridging tridentate binding mode. Therefore the crystal structure of $PdCo(C_{10})_4$, **[21]**, demonstrates a total of four different binding modes, see **Figure 3.12**. Each of these were also clearly identified by the ATR-FTIR spectra obtained, see ATR-FTIR section.

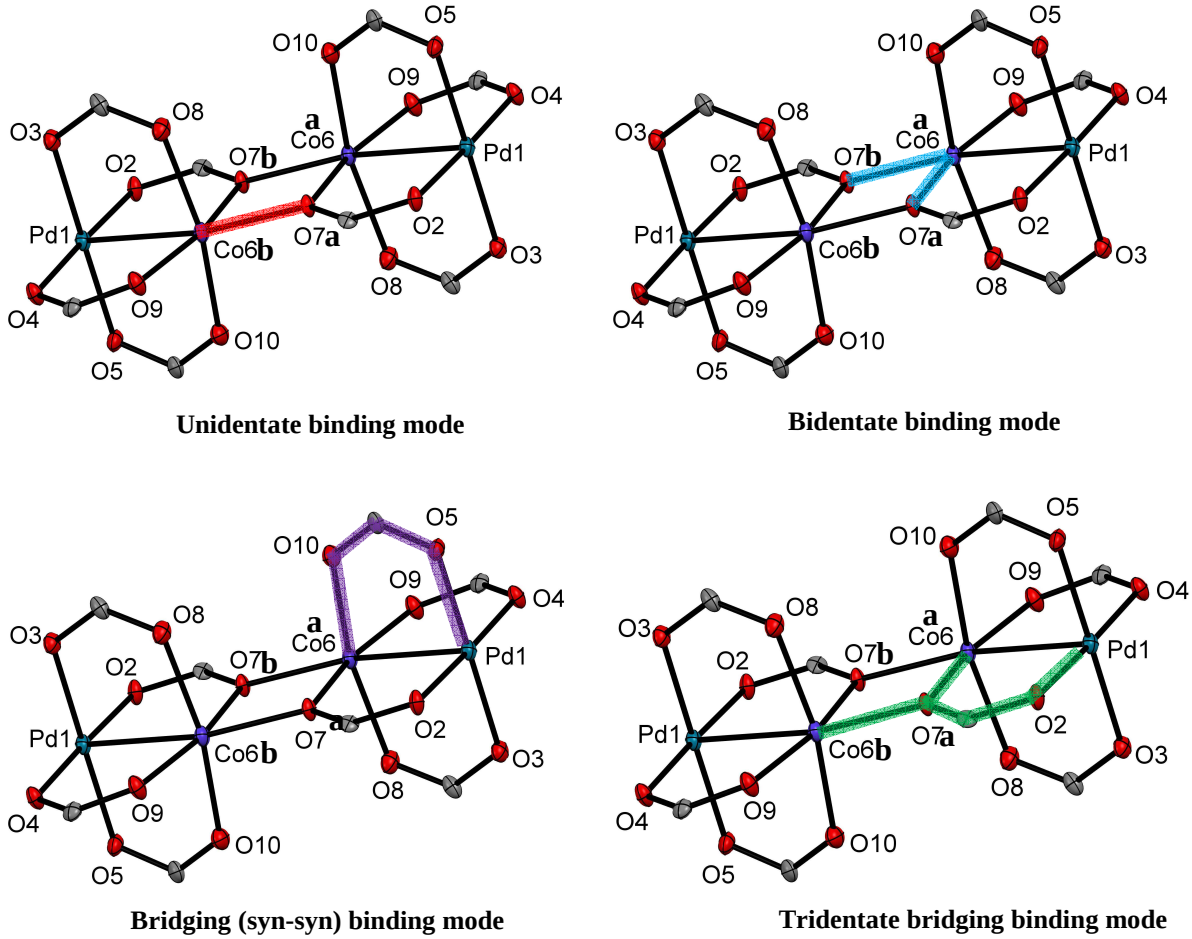

Figure 3.12: Different binding modes for $PdCo(C_{10})_4$, **[21]**, unidentate binding mode (top left), bidentate binding mode (top right), bridging (syn-syn) binding mode (bottom left) and tridentate bridging binding mode (bottom right) all of the mentioned binding modes are observed in the ATR-FTIR spectra.

Kozitsyna, *et al.*[13] reported Pd-Co bond lengths of 2.515(3), 2.551(3), 2.5304(8) and 2.4591(1) Å for tetraacetatidopalladium(II)cobalt(II) with acetonitrile as axial ligand. In this study a dimer was obtained. The Pd-Co bond length determined for $PdCo(C_{10})_4$, **[21],** was found to be 2.5514(6) Å, which is within experimental error the same as observed for the tetraacetatidopalladium(II)cobalt(II).

[13] N. Y. Kozitsyna, S. E. Nefedov, F. M. Dolgushin, N. V. Cherkashina, M. N. Vergaftik and I. I. Moiseev, *Inorganica Chimica Acta*, 2006, **359**, 2072

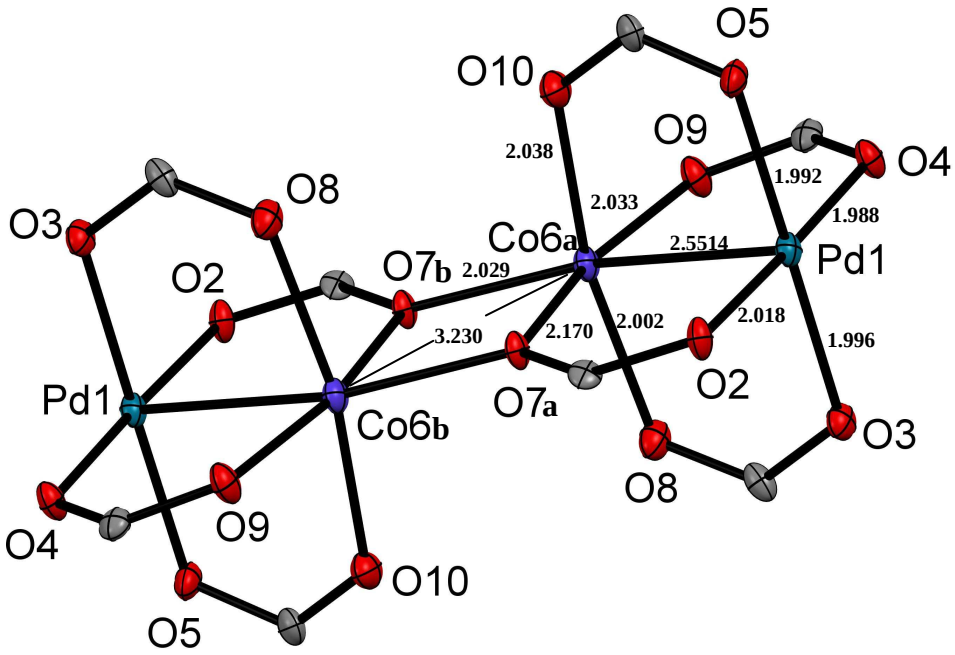

Figure 3.13: Dimeric structure of $PdCo(C_{10})_4$, **[21]**. With selected bond lengths (Å) shown. The long chain carbons and hydrogens are omitted for clarity.

The cobalt atoms in adjacent molecules are separated by a distance of 3.230 Å. The Co-O bonds within the same paddlewheel structure are not equivalent. The bond length Co(6a)-O(7a), 2.170 Å, is significantly longer than the other three Co-O bonds. These were Co(6a)-O(10), 2.038 Å, Co(6a)-O(8), 2.002 Å, and Co(6a)-O(9) with a bond length of 2.033 Å. The reason for the extra-long Co(6a)-O(7a) bond length is most probably that the oxygen atoms O(7a) and O(7b) are responsible for the intermolecular bonding, of the two paddlewheel structures as well as the intramolecular bonding. The longest Pd-O bond, Pd(1)-O(2) = 2.018 Å, is in the same carboxylatido ligand as the longest Co-O bond. This means this particular carboxylatido ligand is bound less tightly than the other three carboxylatido ligands, probably because of the dual intermolecular and intramolecular bonding motifs.

Comparison of the bond lengths and angles of $PdCo(C_{10})_4$, **[21]** and the previously published complex $PdCo(C_2)_4$, **[29]**[13] see **Table 3.13,** shows that there is not much difference in the measured equivalent bond lengths. The biggest difference is between Co(6a)-O(7a) and Co-O(2) with 0.085 Å. For the angles, however, the two complexes do have differences. For example O(3)-Pd(1)-O(4) with an angle of 92.62 (7)˚ and O(7)-Pd-O(5) with an angle of 88.97 (16)˚ has a difference of 3.65˚, O(2)-Pd(1)-O(3) with an angle of 88.56(7)˚ and O(8)-Pd-O(5) with an angle of 90.33(16)˚ has a difference of 1.77˚ and Co(6)-Pd(1)-O(4) with an angle of 87.16(6)˚ and Co-Pd-O(7) with an angle of 90.96(10)˚ has a difference of 3.8˚.

These differences is mainly are because the $PdCo(C_2)_4$, **[29]**,[13] crystallise with axial ligands for example acetonitrile, while the $PdCo(C_{10})_4$, **[21]**, crystallises as a dimer.

Table 3.13: Selected bond lengths (Å) and angles (°) for $PdCo(C_{10})_4$ **[21]** and $PdCo(C_2)_4$ **[29]**[13].

$PdCo(C_{10})_4$ [21]		$PdCo(C_2)_4$ [29][13]		$PdCo(C_{10})_4$ [21]		$PdCo(C_2)_4$ [29][13]	
Atoms	**Length (Å)**	**Atoms[a]**	**Length (°)[a]**	**Atoms**	**Angles (°)**	**Atoms[a]**	**Angles (°)[a]**
Pd(1)-Co(6)	2.55(6)	Pd-Co	2.5304(8)	Pd(1)-Co(6)-O(7)	79.83(5)	-	-
Co(6a)-O(8)	2.002(2)	Co-O(1)	2.061(4)	Pd(1)-Co(6)-O(8)	81.86(6)	-	-
Co(6a)-O(7a)	2.170(2)	Co-O(2)	2.085(4)	Pd(1)-Co(6)-O(9)	84.16(6)	-	-
Co(6a)-O(10)	2.038(2)	Co-O(3)	2.037(4)	O(3)-Pd(1)-O(4)	92.62(7)	O(7)-Pd-O(5)	88.97(16)
Co(6a)-O(9)	2.033(2)	Co-O(4)	2.061(4)	O(2)-Pd(1)-O(3)	88.56(7)	O(8)-Pd-O(5)	90.33(16)
Pd(1)-O(3)	1.996(2)	Pd-O(5)	2.006(4)	O(2)-Pd(1)-O(5)	91.11(8)	O(8)-Pd-O(6)	89.43(17)
Pd(1)-O(5)	1.992(2)	Pd-O(6)	1.996(4)	O(4)-Pd(1)-O(5)	87.71(8)	O(6)-Pd-O(7)	91.29(17)
Pd(1)-O(4)	1.988(2)	Pd-O(7)	2.000(4)	Co(6)-Pd(1)-O(4)	87.16(6)	Co-Pd-O(7)	90.96(10)
Pd(1)-O(2)	2.018(2)	Pd-O(8)	1.994(4)	Co(6)-Pd(1)-O(3)	89.08(5)	Co-Pd-O(5)	89.77(11)
-	-	-	-	Co(6)-Pd(1)-O(2)	91.31(5)	Co-Pd-O(8)	90.24(11)
-	-	-	-	Co(6)-Pd(1)-O(4)	87.16(6)	Co-Pd-O(7)	89.26(11)

[a] Although the numbering system of the published structure, **[29]**, is different than those of **[21]**, the bond lengths and angles that are compared are equivalent bond lengths and angles.

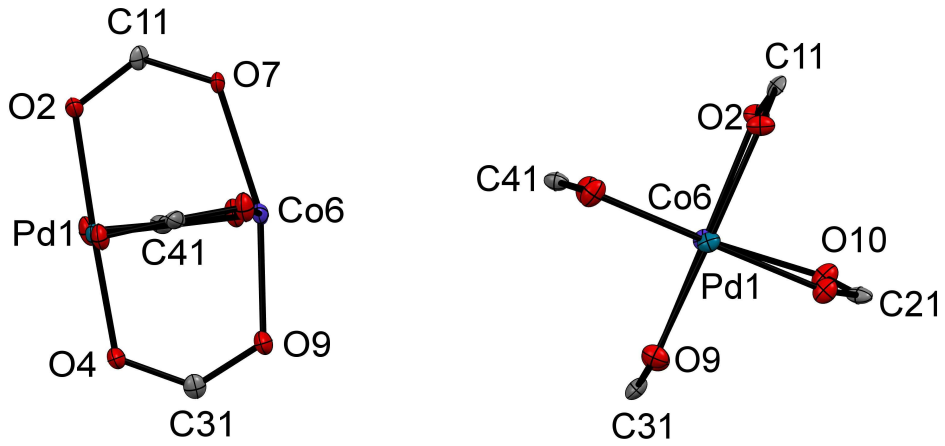

Figure 3.14: Two views of $PdCo(C_{10})_4$, **[21]**, indicating the distortions, from the side view (the cobalt atom has an oxygen atom in front and behind it, and the palladium atom also has an oxygen atom in front and behind it, as well as the carbon atom, in the same plane as the palladium and cobalt atom, has a carbon atom behind it) and also from the front view (the cobalt atom is behind the palladium atom, and each oxygen atom has another oxygen atom behind it).

Figure 3.14 depicts the distortions observed for $PdCo(C_{10})_4$ **[21]**. The cobalt atom (purple) distortion can clearly be seen as it bulges outward away from the palladium atom (see side view). The oxygen atoms (red) also are distorted as can be seen from the front view, where the one oxygen is distorted out of the plane of the rest of the oxygen atoms.

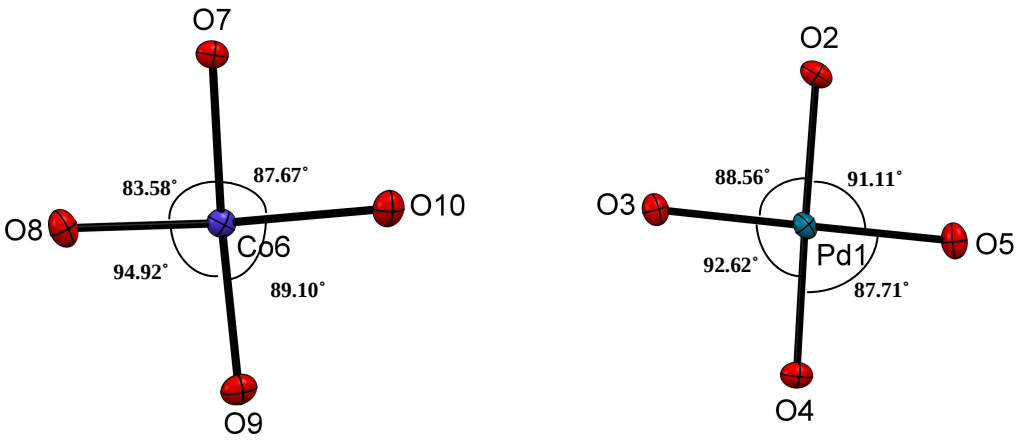

Angles for cobalt coordination centre **Angles for palladium coordination centre**

Figure 3.15: Angles (°) associated with $PdCo(C_{10})_4$,**[21]**, around the cobalt and palladium coordination centres.

Figure 3.15 depicts the angles associated with the cobalt and palladium coordination centres for $PdCo(C_{10})_4$ **[21]**, each metal is bonded to four oxygen atoms. The O-Pd-O and O-Co-O angles are close to, but deviate from the expected 90° for a square-planar orientation. O(7)-Co(6)-O(8) and O(9)-Co(6)-O(8) deviates the most with angles of 83.58° and 94.92° respectively, while O(5)-Pd(1)-O(4) and O(3)-Pd(1)-O(4) with values of 87.71˚ and 92.62˚ respectively, deviates the most from 90°.

3.4.2. Crystal and structure refinement data for $Pd^{II}Zn^{II}(\mu\text{-}OOC(CH_2)_8CH_3)_4$ [36]

The author would like to acknowledge Dr. Marilé Landman for data collection and solving the crystal structure at the University of Pretoria. A perspective view of $PdZn(C_{10})_4$, **[36]**, showing the molecular structure and atom labelling presented in **Figure 3.16**. The crystal data are summarised in **Table 3.14** while some of the most important bond lengths and angles are given in **Table 3.15**. Like, $PdCo(C_{10})_4$, **[21]**, the $PdZn(C_{10})_4$, **[36]**, complex crystallises in a monoclinic crystal system and $P2_1/c$ space group with two formula units per unit cell (Z = 2).

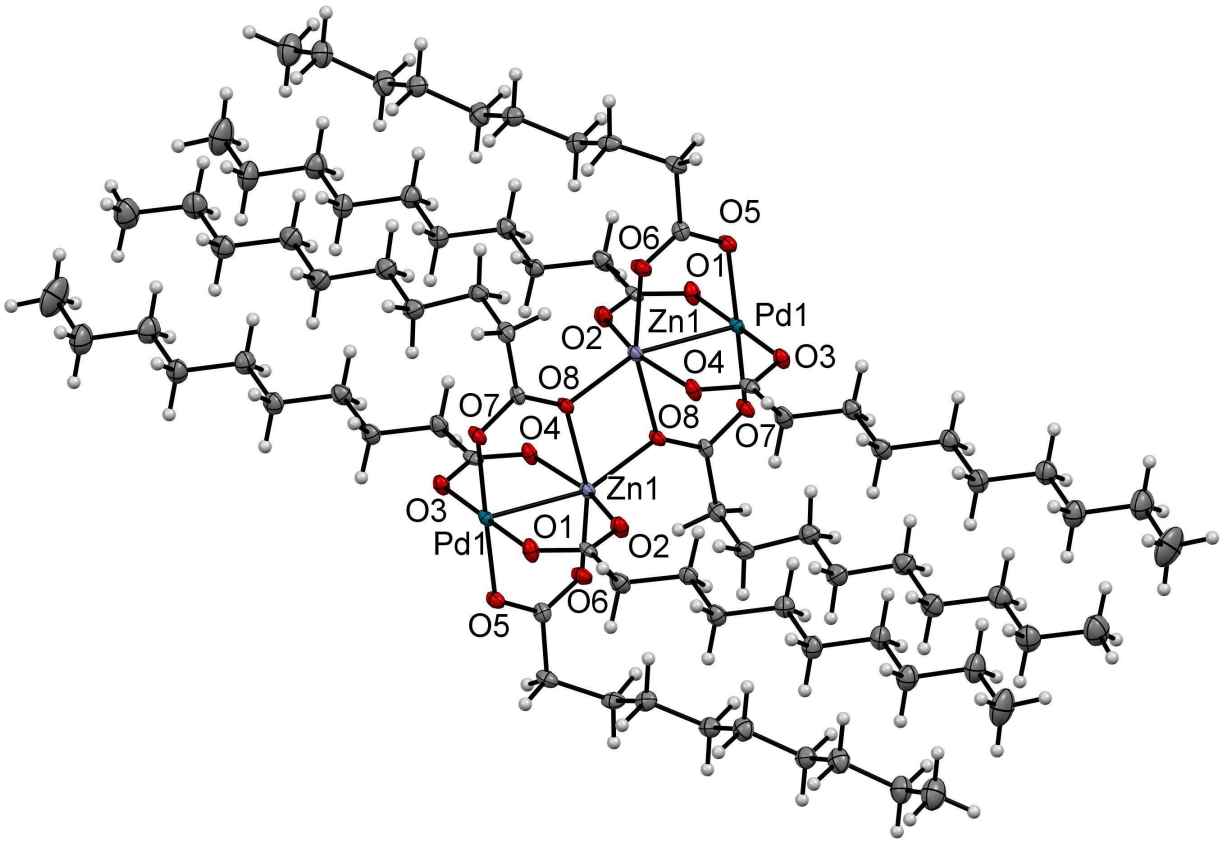

Figure 3.16: Molecular structure of the paddlewheel complex, $PdZn(C_{10})_4$, **[36]**. Hydrogen and carbon atom labelling numbers are omitted for clarity.

The $PdZn(C_{10})_4$, **[36]**, crystal has a zinc and a palladium atom in its core and each metal has four oxygen atoms coordinated to them to form a paddlewheel structure. The long chain carboxylatido ligands hold the metals adjacent to each other. The ligands are situated in a bridged conformation around the two metal atoms.

The zinc atom has a distorted square-pyramidal conformation in a direction away from the palladium atom. The palladium atom has a square-planar conformation with respect to the oxygen atoms.

Similar to $PdCo(C_{10})_4$, **[21]**, the zinc atom is connected to five oxygen atoms, four of these belong the carboxylatido ligand of its particular paddlewheel structure, while the fifth oxygen atom is from the adjacent paddlewheel structure which is connected to the zinc, acting as an axial ligand.

Each paddlewheel structure acts as the axial ligand to the neighbouring paddlewheel structure via the Zn(1)-O(8) bond and vice versa. As observed for, $PdCo(C_{10})_4$, **[21]**, four binding modes were identified in the $PdZn(C_{10})_4$, **[36]**, crystal i.e. unidentate binding mode, bidentate binding mode, tridentate bridging binding mode and lastly bridging binding mode.

Table 3.14: Crystal data and structure refinement for $PdZn(C_{10})_4$ **[36].**

Empirical formula	$C_{40}H_{76}O_8PdZn$	**Crystal sise**	0.257 x 0.226 x 0.054 mm^3
Formula weight	856.77	**Theta range for data collection**	2.182 to 26.371°
Temperature	150(2) K	**Refinement method**	Full-matrix least-squares on F^2
Wavelength	0.71073 Å	**Reflections collected**	86226
Crystal system	Monoclinic	**Independent reflections**	8764 [R(int) = 0.0591]
Space group	*P*21/*c*	**Completeness to theta = 25.242°**	99.9 %
Unit cell dimensions	a = 28.5413(15) Å b = 9.9274(5) Å c = 15.7047(8) Å α = 90° β = 105.9190(18)° γ = 90°	**Index ranges**	-35<=h<=35 -11<=k<=12 -19<=l<=19
Volume	4279.1(4) $Å^3$	**Data / restraints / parameters**	8764 / 0 / 455
Z	4	**Goodness-of-fit on F^2**	1.023
Density (calculated)	1.330 Mg m^3	**Final R indices [I>2sigma(I)]**	R1 = 0.0389, wR2 = 0.0980
Absorption coefficient	1.027 mm^{-1}	**R indices (all data)**	R1 = 0.0503, wR2 = 0.1055
F(000)	1824	**Largest diff. peak and hole**	2.841 and -0.948 e.$Å^{-3}$

Kozitsyna, *et al.*[13] reported a Pd-Zn bond length of 2.5811(6) Å for tetraacetatidopalladium(II)zinc(II) **[23]**[13], with water as axial ligand. In this study a dimer was obtained for **[36]**. The Pd-Zn bond length determined for $PdZn(C_{10})_4$, **[36]**, was found to be 2.5972(4) Å. This metal-metal bond length is close to that observed for the tetraacetatidopalladium(II)zinc(II), **[23]**.

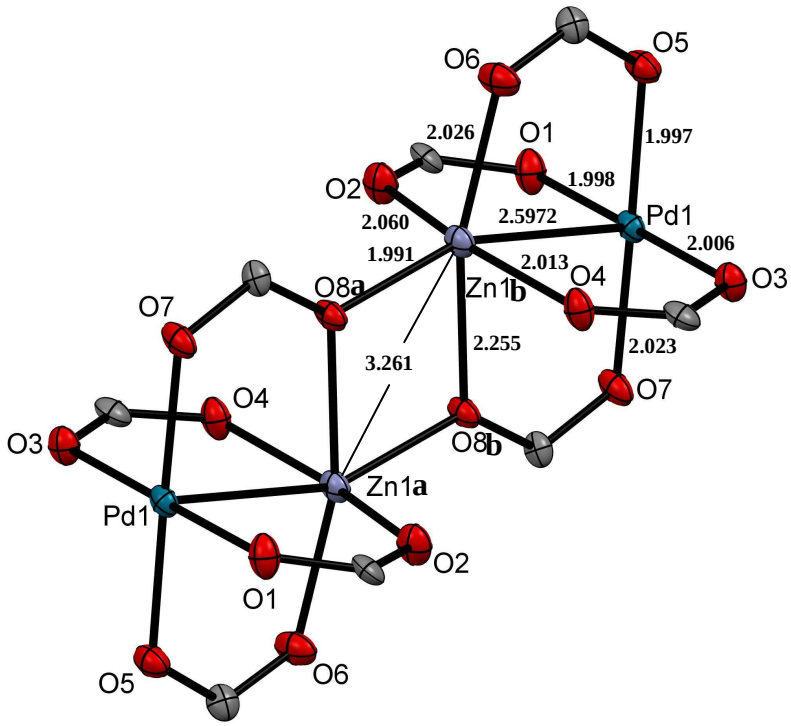

Figure 3.17: Dimeric structure of $PdZn(C_{10})_4$ **[36]** is shown. With selected bond lengths (Å) shown. The long chain carbons and hydrogens are omitted for clarity.

The zinc atoms in adjacent molecules are separated by a distance of 3.261 Å. The Zn-O bonds within the same paddlewheel structure are not equivalent, with Zn(1b)-O(8b) with a bond length of 2.255 Å. This molecular Zn-O bond is longer than the other three Zn-O bonds. Zn(1)-O(4) with a length of 2.013 Å, Zn(1)-O(2), 2.060 Å and Zn(1)-O(6) with a length of 2.026 Å. The Zn(1b)-O(8a) and Zn(1b)-O(8b) atoms are involved in intermolecular and intramolecular bonding with bond lengths of 1.991 Å and 2.255 Å respectively. This atom is responsible for binding the two paddlewheels together. The intermolecular bonding motif to the adjacent molecules' zinc atom is the most likely cause of the intramolecular bond elongation. The elongated bond observed in Zn(1a)-O(8a) or Zn(1b)-O(8b) bond is within the same ligand as the elongated Pd(1)-O(7) having length of 2.023Å. Thus this molecular carboxylatido ligand is bound less tightly than the other three carboxylatido ligands because of the intermolecular bonding within the adjacent paddlewheel molecule. Comparing the bond lengths and angles of $PdZn(C_{10})_4$, **[36]**, and $PdZn(C_2)_4$, **[23]**[13], see **Table 3.15**, it is observed that there is not much difference for most of the bond lengths.

The large difference observed was 0.206 Å for the Zn(1a)-O(8b) and Zn-O(1) bond lengths. For the angles, some differences are observed between the short and long chain crystals. For example Zn(1)-Pd(1)-O(7) with an angle of 93.83(6)˚ and Zn-Pd-O(5) with an angle of 88.93(8)˚ has a difference of 4.9˚, similarly Zn(1)-Pd(1)-O(5) with an angel of 85.89(6)˚ and Zn-Pd-O(6)˚ with an angel of 90.56(7)˚ has a difference of 4.37˚. As mentioned for $PdCo(C_{10})_4$ **[21]** the reason for the differences is most probably because the crystals of **[36]** are dimeric in nature, while crystals of $PdZn(C_2)_4$ **[23]**[13], are monomeric with water as axial ligand.

Table 3.15: Selected bond lengths (Å) and angles (°) for $PdZn(C_{10})_4$, **[36],** and $PdZn(C_2)_4$, **[23]**[13].

$PdZn(C_{10})_4$ [36]		**$PdZn(C_2)_4$ [23]**[13]		**$PdZn(C_{10})_4$ [36]**		**$PdZn(C_2)_4$ [23]**[13]	
Atoms	**Length (Å)**	**Atoms**[a]	**Length (Å)**[a]	**Atoms**	**Angles (°)**	**Atoms**[a]	**Angles (°)**[a]
Pd(1)-Zn(1)	2.5972(4)	Pd-Zn	2.5811(6)	Zn(1)-Pd(1)-O(7)	93.83(6)	Zn-Pd-O(5)	88.93(8)
Pd(1)-O(7)	2.023(2)	Pd-O(5)	2.003(3)	Zn(1)-Pd(1)-O(3)	89.01(5)	Zn-Pd-O(8)	89.52(7)
Pd(1)-O(5)	1.997(2)	Pd-O(6)	1.999(3)	Zn(1)-Pd(1)-O(1)	90.48(6)	Zn-Pd-O(7)	91.25(7)
Pd(1)-O(1)	1.998(2)	Pd-O(7)	1.998(3)	Zn(1)-Pd(1)-O(5)	85.89(6)	Zn-Pd-O(6)	90.56(7)
Pd(1)-O(3)	2.006(2)	Pd-O(8)	1.998(3)	O(3)-Pd(1)-O(5)	92.36(8)	O(8)-Pd-O(6)	89.83(11)
Zn(1a)-O(8b)	2.255(2)	Zn-O(1)	2.049(3)	O(1)-Pd(1)-O(7)	91.01(8)	O(7)-Pd-O(5)	89.94(11)
Zn(1)-O(4)	2.013(2)	Zn-O(2)	2.068(3)	O(1)-Pd(1)-O(5)	87.68(8)	O(6)-Pd-O(7)	90.02(11)
Zn(1)-O(6)	2.026(2)	Zn-O(3)	2.064(2)	O(3)-Pd(1)-O(7)	88.94(8)	O(8)-Pd-O(5)	90.21(11)
Zn(1)-O(2)	2.060(2)	Zn-O(4)	2.135(3)	-	-	-	-

[a] Although the numbering system of the published structure, **[23]**, is different than those of **[36]**, the bond lengths and angles that are compared are equivalent bond lengths and angles.

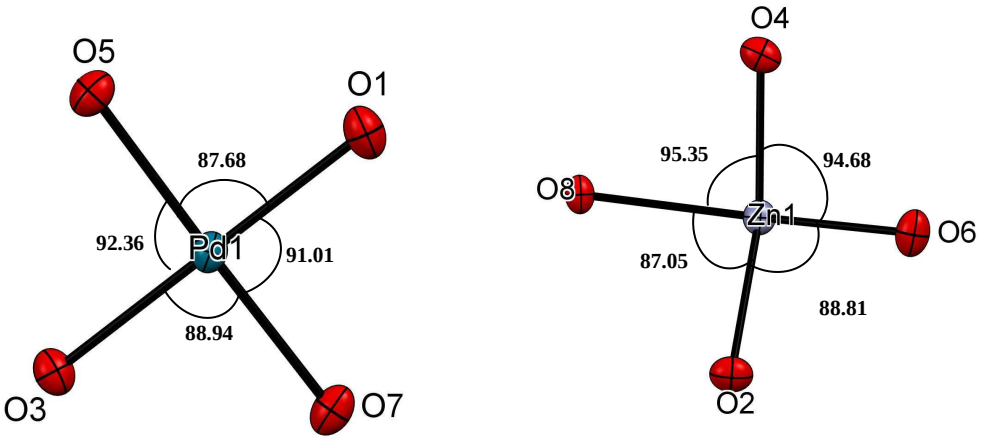

Angles for palladium coordination centre **Angles for zinc coordination centre**

Figure 3.18: Angels (°) associated with $PdZn(C_{10})_4$ **[36]**, around the zinc and palladium coordination centres.

Figure 3.18 depicts the angles associated with the O-Pd-O and O-Zn-O in the paddlewheel, plane of $PdZn(C_{10})_4$, **[36]**. Each metal is bonded to four oxygen atoms. The O-Pd-O and O-Zn-O angles are close to but distorted from the expected 90° for a square planar orientation. O(5)-Pd(1)-O(1) and O(3)-Pd(1)-O(5) deviates the most with angels of 87.68° and 92.36°

respectively, while O(8)-Zn(1)-O(2) and O(8)-Zn(1)-O(4) have angles of 87.05˚ and 95.35˚ respectively around the zinc coordination centre.

3.4.3. Crystal and structure refinement data for $Pd^{II}Ni^{II}(\mu\text{-}OOC(CH_2)_8CH_3)_4$ [38]

The author would like to acknowledge Dr. Marilé Landman for data collection and solving the crystal structure at the University of Pretoria. A perspective view of $PdNi(C_{10})_4$, **[38]**, highlighting the molecular structure and the labelling is presented in **Figure 3.19**. The crystal data are summerised in **Table 3.16** while some of the most important bond lengths and angels are given in **Table 3.17**. $PdNi(C_{10})_4$ **[38]** crystallises as a monoclinic crystal system in the *P* -1 space group with two formula units per unit cell (Z = 2).

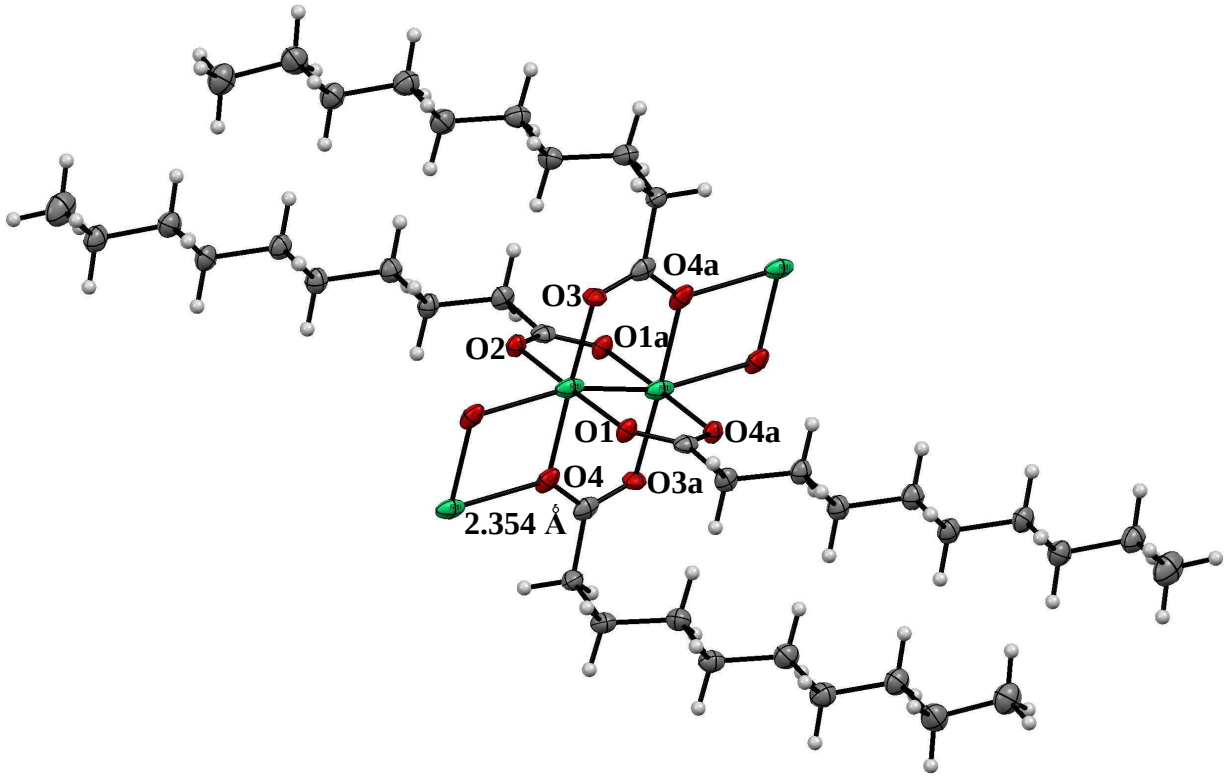

Figure 3.19: Crystal structure of the paddlewheel complex of $PdNi(C_{10})_4$, **[38]**. Hydrogen and carbon label numbers are omitted for clarity.

Unlike the crystal structures of $PdCo(C_{10})_4$, **[21]** and $PdZn(C_{10})_4$, **[36]**, the Pd-Ni crystal has 44 % Pd and 56 % Ni probability mixture at each metal coordinate site in the crystal structure. The paddlewheel molecules are linked together through axial metal-oxygen bonds. The metal-metal bond length for the Pd-Ni **[38]** crystal, 2.3450(8) Å is significantly shorter than the metal-metal

bond of $PdCo(C_{10})_4$, **[21]**, with a length of 2.55(6) Å and $PdZn(C_{10})_4$ **[36]** with a length of 2.5972(4) Å. This most probably is because the Pd and Ni atoms occupy the same positions in the crystal with a 56% (Ni) : 44% (Pd) probability. The characteristic distortion observed in the other mixed-metal paddlewheel carboxylatido complexes, $PdCo(C_{10})_4$, **[21]**, and $PdZn(C_{10})_4$, **[36]**, is absent in the $PdNi(C_{10})_4$, **[38]**, crystal. The crystal structure also shows that, as for the $PdCo(C_{10})_4$, **[21]**, and $PdZn(C_{10})_4$, **[36]**, complexes where four binding modes were observed, only three binding modes can be identified for $PdNi(C_{10})_4$. These are namely bidentate, tridentate bridging and also the bridging binding mode. The author would like to point out that no unidentate binding mode was observed for $PdNi(C_{10})_4$, **[38]**, in the FTIR studies see discussion on ATR-FTIR.

Table 3.16: Crystal and structure refinement data for $PdNi(C_{10})_4$, **[38]**.

Empirical formula	$C_{40}H_{76}O_8Pd_{0.44}Ni_{0.56}$	**Crystal sise**	0.347 x 0.068 x 0.042 mm^3
Formula weight	422.20	**Theta range for data collection**	2.367 to 26.371°
Temperature	150(2) K	**Refinement method**	Full-matrix least-squares on F^2
Wavelength	0.71073 Å	**Reflections collected**	29082
Crystal system	Triclinic	**Independent reflections**	4307 [R(int) = 0.0670]
Space group	*P* -1	**Completeness to theta = 25.242°**	99.9 %
Unit cell dimensions	a = 5.2270(6) Å b = 12.7086(17) Å c = 16.494(2) Å α = 74.079(3)° β = 86.346(3)° γ = 85.680(3)°	**Index ranges**	-6<=h<=6 -15<=k<=15 -20<=l<=20
Volume	1049.6(2) $Å^3$	**Data / restraints / parameters**	4307 / 0 / 228
Z	2	**Goodness-of-fit on F^2**	1.060
Density (calculated)	1.336 Mg m^3	**Final R indices [I>2sigma(I)]**	R1 = 0.0644, wR2 = 0.1180
Absorption coefficient	0.926 mm^{-1}	**R indices (all data)**	R1 = 0.0940, wR2 = 0.1346
F(000)	452	**Largest diff. peak and hole**	1.327 and -1.782 e.$Å^{-3}$

Table 3.17 contains selected crystal data for $PdNi(C_{10})_4$ **[38]** and $PdNi(C_2)_4$ **[23]**[13]. Regarding the Pd-O and Ni-O bonds no significant differences are observed, the largest deviation was 0.0673 Å. The bond angles do have significant differences. For example the angle O(4)-Ni-Pd was 81.03° for **[28]**, while the angle Ni(1)-Pd(1)-O(2a) has a value of 88.16° for **[38]**, with a difference of 7.13°.

Comparison of $PdCo(C_{10})_4$, **[21]** and $PdZn(C_{10})_4$, **[36]** with $PdNi(C_{10})_4$, **[38]**, shows that the metal-metal distance between two separate paddlewheels for the $PdNi(C_{10})_4$, **[38]**, is 3.464 Å, for $PdCo(C_{10})_4$, **[21]**, the distance between separate paddlewheels is 3.230 Å and for $PdZn(C_{10})_4$, **[36]**, the distance between separate paddlewheels is 3.261 Å respectively. The intermolecular distance in $PdNi(C_{10})_4$, **[38]**, is therefore 0.234 Å longer than the equivalent bond between two

$PdCo(C_{10})_4$, **[21]**, molecules and 0.203 Å longer than the equivalent bond length between two $PdZn(C_{10})_4$, **[36]**, molecules.

Table 3.17: Selected bond lengths (Å) and angles (°) for $PdNi(C_{10})_4$ **[38]** and $PdNi(C_2)_4$ **[28]**[13].

$PdNi(C_{10})_4$ [38]		$PdNi(C_2)_4$ [28][13]		$PdNi(C_{10})_4$ [38]		$PdNi(C_2)_4$ [28][13]	
Atoms	**Length (Å)**	**Atoms[a]**	**Length (Å)[a]**	**Atoms**	**Angles (°)**	**Atoms[a]**	**Angles (°)[a]**
Pd(1)-Ni(1)	2.3450(8)	Pd-Ni	2.483(2)	O(3)-Pd(1)-O(1)	91.27	O(5)-Pd-O(7)	90.82(18)
Ni(1)-O(3a)	2.013(3)	Ni-O(1)	2.028(6)	O(3)-Pd(1)-O(2)	88.98	O(8)-Pd-O(5)	89.53(19)
Ni(1)-O(2a)	1.999(4)	Ni-O(2)	2.055(6)	O(1)-Pd(1)-O(4)	92.24	O(7)-Pd-O(6)	88.85(18)
Ni(1)-O(3a)	2.013(3)	Ni-O(3)	2.076(6)	O(2)-Pd(1)-O(4)	90.20	O(8)-Pd-O(6)	90.56(18)
Ni(1)-O(1a)	1.997(4)	Ni-O(4)	2.040(6)	Ni(1)-Pd(1)-O(3a)	91.55(9)	O(3)-Ni-Pd	80.83(12)
Pd(1)-O(4)	2.053(3)	Pd-O(5)	2.027(4)	Ni(1)-Pd(1)-O(4a)	85.86(1)	O(1)-Ni-Pd	82.34(13)
Pd(1)-O(3)	2.013(3)	Pd-O(6)	2.036(4)	Ni(1)-Pd(1)-O(1a)	89.22(1)	O(2)-Ni-Pd	82.31(12)
Pd(1)-O(2)	1.999(4)	Pd-O(7)	2.034(5)	Ni(1)-Pd(1)-O(2a)	88.16(1)	O(4)-Ni-Pd	81.03(12)
Pd(1)-O(1)	1.997(4)	Pd-O(8)	2.020(5)	-		-	-

[a] Although the numbering system of the published structure, **[28]**, is different than those of **[38]**, the bond lengths and angles that are compared are equivalent bond lengths and angles.

3.5. Thermal Studies

Three thermal analyses techniques were employed during the course of this study.

3.5.1. Differential Scanning Calorimetry (DSC)

To investigate the thermal properties of selected complexes, the thermal analysis technique Differential Scanning Calorimetry, (DSC), was used. A simple heating and cooling cycle was not sufficient to understand the results obtained for the complexes synthesised. Therefore, the following cycle method was employed:

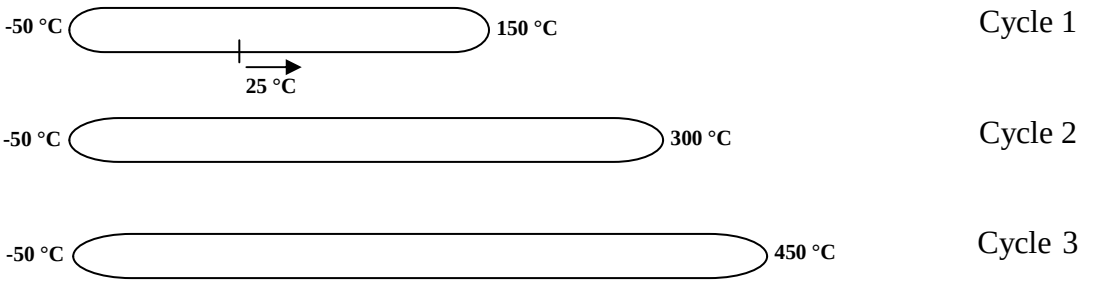

Figure 3.20: Details of three successive heating and cooling cycles used in the DSC investigation of the complexes synthesised.

The above successive scans are necessary to interpret the obtained thermograms. In the first and second cycles between -50 to 150 °C, for the mixed-metal complexes, and then between -50 to 300 °C, for the mono-metal complexes, low temperature events could be identified without destroying the compound.

The third or last cycle usually involved the decomposition of the complex. The temperature boundaries sited above are just guide lines; they were tailored to be optimum for each complex.

3.5.2. Variable temperature polarised light microscopic studies

Since DSC does not allow for visual inspection of the sample during thermal changes, variable temperature polarised light microscopy was employed to study the optical changes associated with thermal events observed in a DSC experiment. Apart from obtaining visual evidence of a melting point thermal event, solid state transitions and mesophase behaviour can also be identified using this technique. The same thermal cycle sequences that were followed for the DSC experiments were followed. These included the rate of temperature increase and decrease, and the same heating and cooling temperature range. However, variable temperature polarised light microscope studies were performed under atmospheric conditions and not under nitrogen.

3.5.3. Thermal gravimetric analysis coupled with mass spectroscopy (TGA-MS)

All synthesised complexes were analysed for their percentage (%) weight loss upon heating utilising TGA in the temperature range 30 - 700 °C under an argon atmosphere. In addition, TGA-MS was used to study the circular aliphatic palladium complexes **[1-4]** as well as the palladium cobalt aliphatic paddlewheel complexes **[19-22]** under an argon atmosphere.

3.5.4. Thermal analysis of the circular long-chain aliphatic hexacarboxylatidotripalladium(II) complexes

The circular palladium complexes **[1-3]** are viscous liquids, while **[4]** is a waxy solid. Complexes **[1]** and **[2]** both only showed decomposition at 212.74 °C and 229.68 °C respectively. The circular palladium complex **[3]** showed solid state transition and cold crystallisation while **[4]** showed cold crystallisation. Complexes, **[1-4]**, go through a one-step decomposition process with numerous gaseous products.

3.5.4.1. DSC of $[Pd_3^{II}(\mu\text{-}OOC(CH_2)_nCH_3)_6]$, n = 4 for [1] and 6 for [2]

Complexes, $Pd_3(C_6)_6$, **[1]**, (left) and $Pd_3(C_8)_6$, **[2]**, (right) both only showed decomposition at 212.74 °C and 229.68 °C respectively, see **Figure 3.21**.

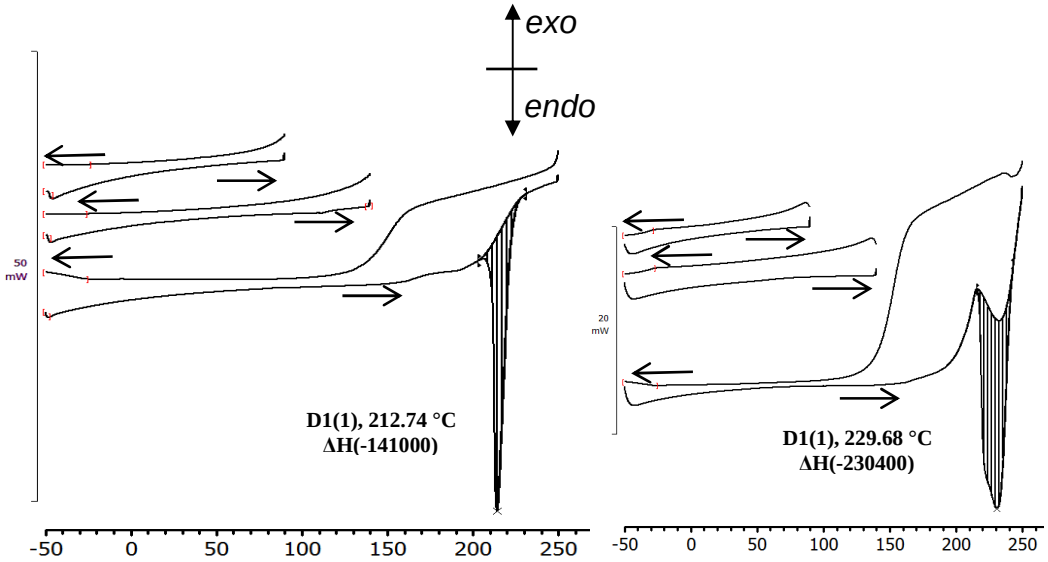

Figure 3.21: DSC of $Pd_3(C_6)_6$, **[1]**, (left) and $Pd_3(C_8)_6$, **[2]**, (right) with a scan rate of 10 °C min^{-1} under nitrogen. The arrows pointing left indicate cooling segments while the arrows pointing to the right indicates heating segments. The temperatures (°C) are peak temperatures and the energies are enthalpies (ΔH) in J mol^{-1}.

3.5.4.2. DSC of $[Pd_3^{II}(\mu\text{-}OOC(CH_2)_8CH_3)_6]$, [3]

The successive heating and cooling segments, at a heating rate of 10 °C min^{-1} under nitrogen for $Pd_3(C_{10})_6$, **[3]**, is shown in **Figure 3.22**. **Table 3.18** contains the DSC data of $Pd_3(C_{10})_6$, **[3]**.

The complex was first cooled to -50 °C in the cooling segment of cycle 1, with only one peak **C1(1)** (-22.40 °C, 20300 J mol^{-1}) appearing in this cooling segment. Peak **C1(1)** is assigned to the crystallisation of the isotropic liquid. The crystallisation peak temperature is *ca.* 43 °C lower than the peak temperature associated with melting **M4(1)** (20.80°C, -34300 J mol^{-1}). It indicates that super-cooling is prevalent under the cooling conditions employed. The heating segment in cycle 1 shows three thermal events before melting is observed at peak **M4(1)**. Heating the sample from -50 °C to 150 °C, the endothermic peak **H1(1)** (-33.98 °C, -17900 J mol^{-1}) is assigned to be a low temperature solid state transition and is followed by cold crystallisation at the exothermic peak **H2(1)** (-12.43 °C, 44800 J mol^{-1}). The small peak **H3(1)** (8.21 °C, -3500 J mol^{-1}) indicates the formation of a high temperature solid state transition.

Cycle 2 shows the same thermal events as cycle 1. The peak **H2(1)** is no longer observed because of the thermal event between 94.5 °C to 94.9 °C, see insert on cycle 1, and is assigned as partial decomposition. The crystallisation peak **C1(2)** (-6.28 °C, 50300 J mol^{-1}) in the cooling segment of cycle 2 is a sharper peak compared to that of **C1(1)**. The peak **C1(2)** (-6.28 °C, 50300 J mol^{-1}) has shifted by 16.12 °C compared to **C1(1)** (-22.40 °C, 20316 J mol^{-1}). All these changes are due to the onset of partial decomposition in the heating segment of cycle 1. The solid state transition peak **H2(2)** (15.61 °C, -8300 J mol^{-1}), is sharper than **H3(1)** (8.21 °C, -3500 J mol^{-1}), and is also at a higher temperature. The peak **H2(2)** is assigned to be the melting of the products formed during partial decomposition. The melting peak **M3(2)** (22.11 °C, -31400 J mol^{-1}) has shifted by 1.31 °C compared to **M4(1)** (20.80 °C, -34300 J mol^{-1}). These changes are attributed to thermal annealing of the sample during the fourth time thermal changes took place in cycle 1 and cycle 2.

Cycle 3 has three thermal events but does not include the solid state transition observed in cycle 1 and 2 at peaks **H1(1)** and **H1(2)** respectively. No crystallisation peak is observed for the cooling segment of cycle 3 because of the destructive decomposition of the complex at peak **D3(3)** (220.12 °C, 164700 J mol^{-1}). For the heating segment of cycle 3 the following peaks are observed, **H1(3)** (15.07 °C, -1900 J mol^{-1}) and **M2(3)** (22.26 °C, -47900 J mol^{-1}) as well as the decomposition of **[3]**, which starts at *ca.* 150 °C.

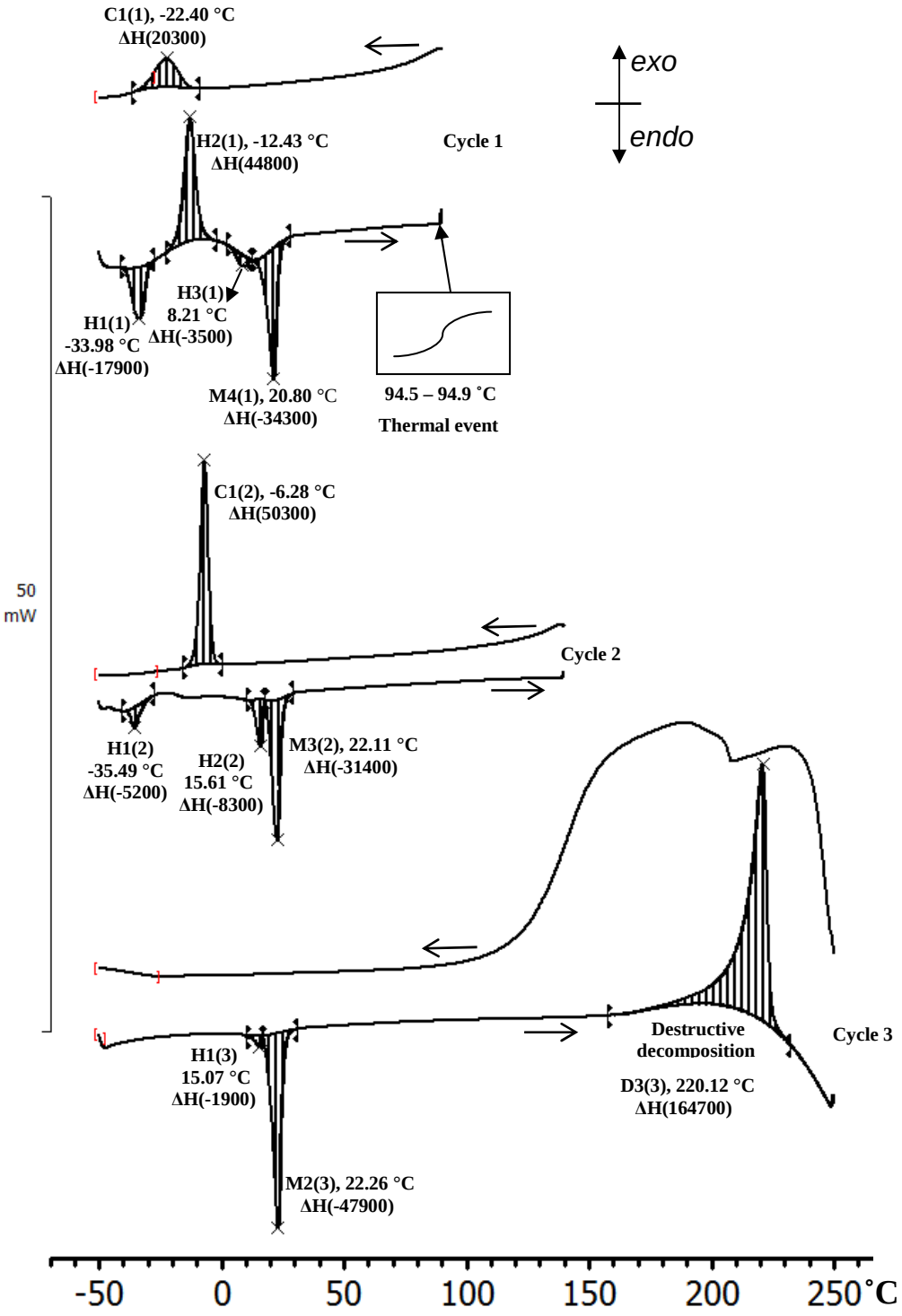

Figure 3.22: The DSC of $Pd_3(C_{10})_6$, **[3]**, utilising a scan rate of 10 °C min^{-1} under nitrogen. The arrows pointing left indicate cooling segments while the arrows pointing to the right indicates heating segments. **H** and **C** denote heating and cooling respectively, while **M** is associated with melting. The number in brackets is the cycle number while the middle number is peak number. For example **H3(1)** would indicate the third peak in the heating segment of cycle 1. The temperatures (°C) are peak temperatures and the energies are enthalpies (ΔH) in J mol^{-1}.

Table 3.18: DSC data of $Pd_3(C_{10})_6$, **[3]**, relating each thermal event with, temperature (˚C) and enthalpy change (J mol^{-1}).

Peak	Temperature °C	ΔH J mol^{-1}	Peak	Temperature °C	ΔH J mol^{-1}	Peak	Temperature °C	ΔH J mol^{-1}
Cycle 1			**Cycle 2**			**Cycle 3**		
C1(1)	-22.40	20300	**C1(2)**	-6.28	50300	**H1(3)**	15.07	-1900
H1(1)	-33.98	-17900	**H1(2)**	-35.49	-5200	**M2(3)**	22.26	-47900
H2(1)	-12.43	44800	**H2(2)**	15.61	-8300	**Destructive decomposition**	220.12	164700
H3(1)	8.21	-3500	**M3(2)**	22.11	-31400	-	-	-
M4(1)	20.80	-34300	-	-	-	-	-	-

3.5.4.3. Variable temperature polarised light microscopic studies of $[Pd_3^{II}(\mu\text{-}OOC(CH_2)_8CH_3)_6]$, [3]

Following the DSC study, the samples were further investigated by polarised light microscopy. Since **[3]**, is an isotropic liquid at room temperature, the sample had to be cooled to -50 °C in order to obtain the proper images of phase changes when heating. **Figure 3.23** shows the photos obtained of the heating of $Pd_3(C_{10})_6$, **[3]**, after it was cooled to -50 °C. Even after cooling to -50 °C, no optical difference could be observed. It implies the DSC peak C1(1) is not optically observable. During the heating of the sample small crystals began to appear at -22 °C, due to cold crystallisation. As the liquid is heated, crystals start to appear and at 5 °C, the sample is solidified. After further heating, the solid starts to melt at 14 °C and at 20 °C all the crystals have melted into an isotropic liquid. It is concluded that only the DSC peaks H2(1) and M4(1) are identifiable with variable temperature optical microscopy. The images illustrate the onset of cold crystallisation to melting of the crystalline solid to an isotropic liquid.

Heating

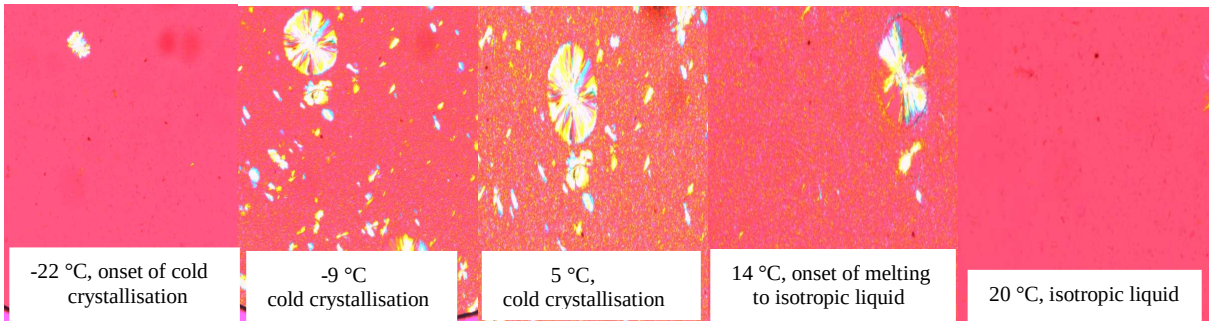

Figure 3.23: Polarised light microscope photos of $Pd_3(C_{10})_6$, **[3]**, indicating cold crystallisation and melting of the crystalline solid.

3.5.4.4. DSC of $[Pd_3^{II}(\mu\text{-}OOC(CH_2)_{10}CH_3)_6]$, [4]

Figure 3.24 depicts the DSC thermogram of $Pd_3(C_{12})_6$, **[4]**, utilising a scan rate of 10 ˚C min^{-1} under nitrogen atmosphere. **Table 3.19** contains the DSC data values of **[4]**.

Cycle 1 has two thermal events, **C1(1)** (23.26 ˚C, 69300 J mol^{-1}) and **M1(1)** (40.89 ˚C, -66400 J mol^{-1}), these are assigned as crystallisation and melting peaks of $Pd_3(C_{12})_6$, **[4]**, respectively.

Cycle 2 shows the same peaks as that of cycle 1, except for peak **D2(2)** (155.44 ˚C, -7100 J mol^{-1}). In the heating segment of cycle 2, peak **M1(2)** (40.88 ˚C, -68000 J mol^{-1}) is assigned to the partial melting of the crystalline solid. Peak **D2(2)** represents initial but partial decomposition of $Pd_3(C_{12})_6$, **[4]**. In the cooling segment of cycle 2, peak **C1(2)** (10.30 ˚C, 80900 J mol^{-1}) is assigned as the crystallisation of $Pd_3(C_{12})_6$, **[4]**, together with the partial decomposition product/s formed at **D2(2)**. Peak **C1(2)** is 12.96 ˚C lower in the temperature than the crystallisation peak **C1(1)**. The crystallisation peak of the isotropic liquid and the partial decomposition product/s are superimposed in peak **C1(2)**. Evidence of this is seen at the base of peak **C1(2)** which is wider than peak **C1(1)**. Peak **C1(2)** has a small shoulder just before crystallisation.

Cycle 3 has three thermal events two in the heating segment and one in the cooling segment. In the heating segment of cycle 3, **H1(3)** (15.14 ˚C, 13000 J mol^{-1}) is assigned to be the cold crystallisation of the product/s formed at peak **D2(2)**. Peak **M2(3)** (37.66 ˚C, -96800 J mol^{-1}) consists of two peaks, the one peak is the melting of the decomposition product/s and the other peak is the melting of $Pd_3(C_{12})_6$, **[4]**, into an isotropic liquid. Peak **M2(3)** is 3.22 ˚C lower in temperature than that of **M1(2)** most probably because of the decomposition product/s lowering the melting point of $Pd_3(C_{12})_6$, **[4]**. On the cooling segment, peak **C1(3)** (8.14 ˚C, 81600 J mol^{-1}) is assigned to the crystallisation of $Pd_3(C_{12})_6$, **[4]** and the decomposition product/s. Peak **C1(3)** is 15.12 ˚C lower in temperature than the original crystallisation peak **C1(1)** of $Pd_3(C_{12})_6$, **[4]**.

Cycle 4 has three thermal events all three in the heating segment, which includes the principle decomposition peak **D3(4)** (211.28 ˚C, 114200 J mol^{-1}). Peak **H1(4)** (16.99 ˚C, 14200 J mol^{-1}) is assigned to the cold crystallisation of the product/s formed at peak **D2(2)**. Peak **M2(4)** (33.70 ˚C, -98100 J mol^{-1}) is assigned to the melting of the product/s formed at peak **D2(2)**. Peak **M2(4)** have a small shoulder just after the melting peak, this most probably is the melting peak of the remaining original sample $Pd_3(C_{12})_6$, **[4]**. Peak **M2(4)** is 7.19 ˚C lower in temperature than the original melting peak **M1(1)**. Although the original sample **[4]**, was gradually destroyed since the thermal event at peak **D2(2)**, it was finally completely destroyed at peak **D3(4)**. No

thermal events are observed in the cooling segment, which is further proof of complete sample destruction at peak **D3(4)**.

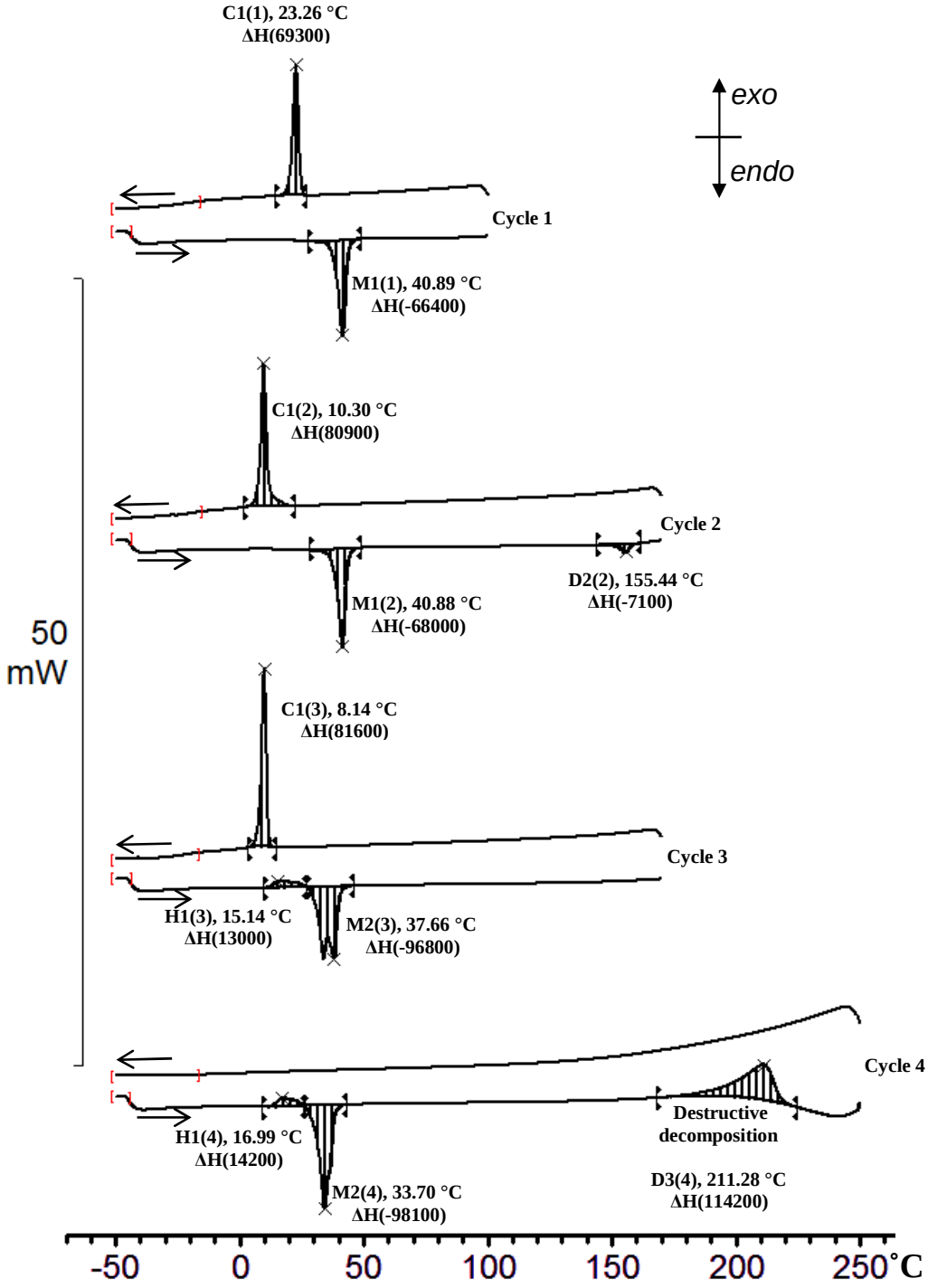

Figure 3.24: DSC of $Pd_3(C_{12})_6$, **[4]**, scan rate 10 °C min^{-1} under nitrogen. The arrow pointing left indicates the cooling segment while the arrow pointing to the right indicates the heating segment. **H** and **C** denote heating and cooling respectively, while **M** is associated with melting. The number in brackets is the cycle number while the middle number is peak number. For example **H1(3)** would indicate the first peak in the heating segment of cycle 3. The temperatures (°C) are peak temperatures and the energies are enthalpies (ΔH) in J mol^{-1}.

Table 3.19: DSC data of $Pd_3(C_{12})_6$, **[4]**, relating each thermal event with, temperature (˚C) and enthalpy change (J mol^{-1}).

Peak	Temperature °C	ΔH J mol^{-1}	Peak	Temperature °C	ΔH J mol^{-1}
Cycle 1			**Cycle 2**		
C1(1)	23.26	69300	**C1(2)**	10.30	80900
M1(1)	40.89	-66400	**M1(2)**	40.88	-68000
-	-	-	**D2(2)**	155.44	-7100
Cycle 3			**Cycle 4**		
C1(3)	8.14	81600	**H1(4)**	16.99	14200
H1(3)	15.14	13000	**M2(4)**	33.70	-98100
M2(3)	37.66	-96800	**Destructive decomposition**	211.28	114200

3.5.4.5. Variable temperature polarised light microscopic studies of $[Pd_3^{II}(\mu\text{-}OOC(CH_2)_{10}CH_3)_6]$, [4]

Variable temperature polarised light microscopy studies were employed to further investigate the peaks observed in the DSC study of **[4]**. The first image in **Figure 3.25**, Top, of $Pd_3(C_{12})_6$, **[4]**, at a temperature of 25 °C shows a crystalline solid. The next image labelled 41 °C is the partially melted solid of **[4]**. In the cooling segment the partially melted solid is cooled to 30 °C resulting in a crystalline solid.

Using a fresh sample of $Pd_3(C_{12})_6$, **[4]**, see **Figure 3.25**, bottom, the sample was heated to 41 °C and then to 131 °C. The image labelled 131 °C is a liquid with partially melted sample contained in it. The sample was than further heated to a temperature of 160 °C, where the sample melted into an isotropic liquid, simultaneously partial decomposition was observed. The melting points and existence of an isotropic liquid obtained by the DSC study of **[4]** (see section 3.5.4.4.) was confirmed by the images obtained by the variable temperature polarised light microscopy, see **Figure 3.24**, peak **D2(2)** in the heating segment of cycle 2. Therefore this decomposition product/s is responsible for the shift to lower temperatures of the crystallisation and melting peaks of the original sample see **Figure 3.24**, cycle 3 and cycle 4.

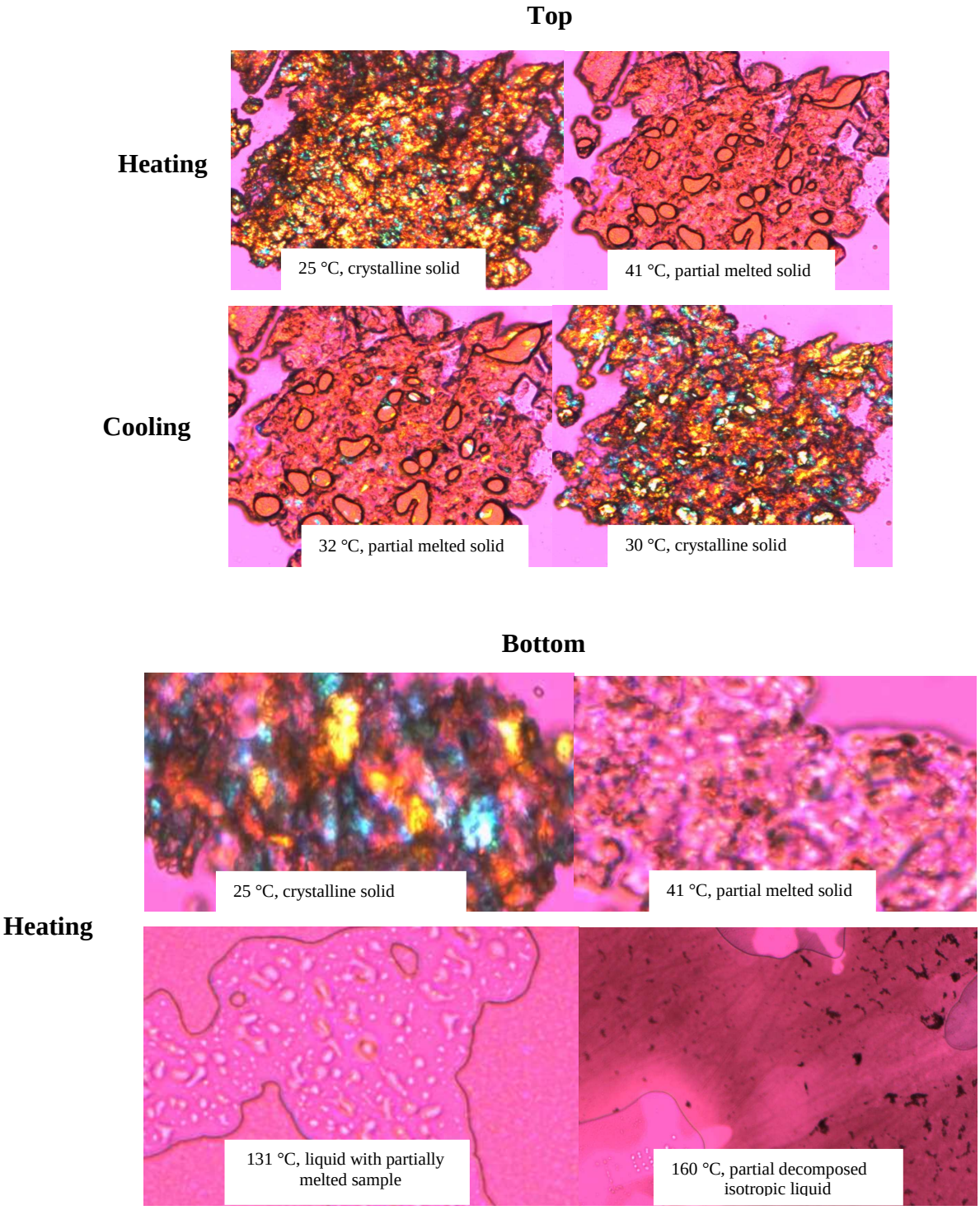

Figure 3.25: Top: heating and cooling of $Pd_3(C_{12})_6$, **[4]**, using a polarised light microscope. **Bottom:** Heating of $Pd_3(C_{12})_6$, **[4]**, until partial decomposition was observed, using a fresh sample.

3.5.4.6. Thermal gravimetric analysis with coupled mass spectroscopy of [1-4]

$Pd_3(C_m)_6$, **[1-4]**, was subjected to thermal gravimetric analysis coupled with mass spectroscopy (TGA-MS). This technique allows for the measurement of continuous mass loss while gaseous decomposition products can be analysed. The heating rate was 10 °C min^{-1} in argon. **Figure 3.26** depicts the TGA of $Pd_3(C_{10})_6$, **[3]**, while decomposition data and the analysis of the gaseous products from the decomposition of **[1-4]** are tabulated in **Table 3.20** and **Table 3.21** respectively. The decomposition of $Pd_3(C_m)_6$, **[1-4]**, proceeds in one global pyrolytic process comprising of many overlapping steps with a total mass loss of 63.70 % to 74.23 %. The experimental mass loss for **[1]** is 63.70 %. Theoretically it was calculated that if Pd, PdO and PdO_2 formed during pyrolysis, the mass loss should be 63.41%. This pyrolysis product distribution was also found to hold for **[2]** (experimental mass loss = 67.71%, theoretical mass loss = 68.83%), **[3]** (experimental mass loss = 71.43%, theoretical mass loss = 72.73%) and **[4]** (experimental mass loss = 74.23%, theoretical mass loss = 75.76%).

Analysis of the thermal decomposition gases showed that numerous gaseous products were released. These include oxygenated species such as water, carbon dioxide, carbon monoxide and alcohols as well as hydrocarbon fragments.

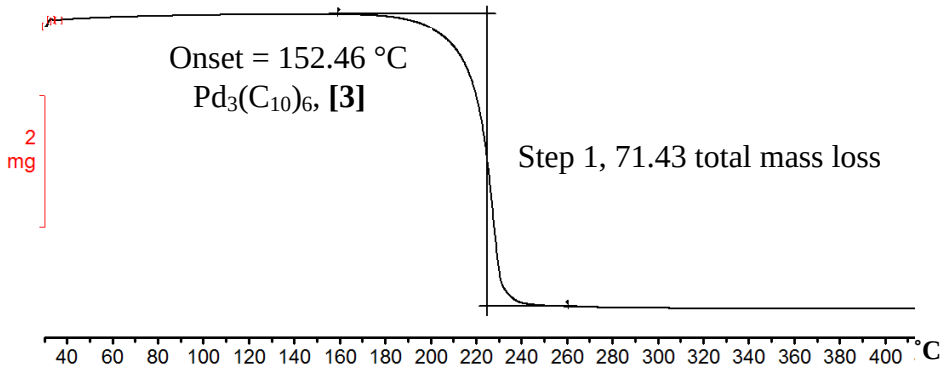

Figure 3.26: TGA of $Pd_3(C_{10})_6$, **[3]**, with a scan rate of 10 °C min^{-1} under argon atmosphere. The TGA of $Pd_3(C_{10})_6$, **[3]**, is given as an example for **[1]**, **[2]** and **[4]**.

Table 3.20: TGA data of **[1-4]**, which includes the decomposition temperature range (°C) and mass loss (%)

$Pd_3(C_m)_6$	Step	Decomposition Temperature range / °C	Mass loss / %
$Pd_3(C_6)_6$, [1]	1	134.23 – 236.98 °C	63.70
$Pd_3(C_8)_6$, [2]	1	126.28 – 237.34 °C	67.71
$Pd_3(C_{10})_6$, [3]	1	152.46 – 254.26 °C	71.43
$Pd_3(C_{12})_6$, [4]	1	145.81 – 284.60 °C	74.23

From **Table 3.20**, an increase in the percentage mass loss of the complexes **[1-4]** is observed as the aliphatic chain length gets longer, with the lowest percentage being 63.70 % for **[1]** and 74.23 % for **[4]** being the highest percentage. A linear relationship is illustrated in **Figure 3.27** between the number of carbons in the aliphatic carboxylatido backbone compared to the percentage mass loss of **[1-4]**.

This clearly corresponds to the fractions of decomposition products from the aliphatic chain during the pyrolysis of **[1-4]**. **Table 3.21** summarises the observed decomposition (pyrolysis) products and mass charge ratios for molecular fragments that was detected by the mass spectrometer during pyrolysis of **[1-4]**. These included OH, H_2O, C_2H_2, CO, O_2, CH_3OH, C_3H_4 and CO_2 for **[1],** with methylene and methane for **[2-4]**. During the pyrolysis of **[4]** C_2H_6, C_2H_5, CH_2O and C_3H_2 could additionally be identified as decomposition products.

Table 3.21: Mass charge ratio (m/z) and compounds detected while using mass spectroscopy coupled with TGA for **[1-4]**.

m/z	**$Pd_3(C_6)_6$, [1]**	**$Pd_3(C_8)_6$, [2]**	**$Pd_3(C_{10})_6$, [3]**	**$Pd_3(C_{12})_6$, [4]**
14	-	CH_2	CH_2	CH_2
16	-	CH_4	CH_4	CH_4
17	OH	OH	OH	OH
18	H_2O	H_2O	H_2O	H_2O
26	C_2H_2	C_2H_2	C_2H_2	C_2H_2
28	CO	CO	CO	CO
29	-	-	-	C_2H_5
30	-	-	-	C_2H_6, CH_2O
32	O_2, CH_3OH	O_2, CH_3OH	O_2, CH_3OH	O_2, CH_3OH
38	-	-	-	C_3H_2
40	C_3H_4	C_3H_4	C_3H_4	C_3H_4
44	CO_2	CO_2	CO_2	CO_2

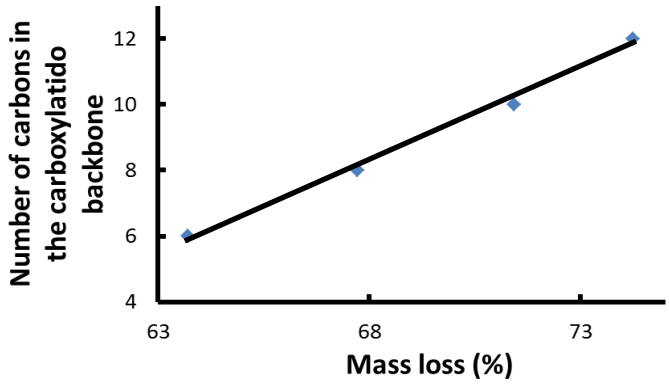

Figure 3.27: Linear relationship between the number of carbons in the aliphatic carboxylatido backbone compared to the percentage mass loss of **[1-4]**.

3.5.5. Thermal analysis of $[Zn^{II}(OOC(CH_2)_8CH_3)_2]$, [15]

The thermal analysis of **[15]**, will be discussed, focussing on solid state transitions and decomposition of the complex.

3.5.5.1. Differential scanning calorimetry, (DSC)

Figure 3.28 represents the thermogram for $Zn(C_{10})_2$, **[15]**, showing the successive heating and cooling cycles with a scan rate of 10 °C min^{-1} under nitrogen atmosphere. **Table 3.22** contains the DSC data for **[15]**. Cycle 1 shows $Zn(C_{10})_2$, **[15]**, does not have any thermal activity below 100 °C.

Cycle 2 has two main thermal events one for the heating segment and one for the cooling segment. On the heating segment, peak **M1(2)** (136.26 °C, -57100 J mol^{-1}) has a well-defined shoulder, which is a thermal event that happens just before the powder melts. This thermal event can be a solid state transition e.g. repositioning of the long-chains, which almost overlaps with the main melting event of the powder. The cooling peak, **C1(2)** (99.29 °C, 46400 J mol^{-1}) of cycle 2 has two shoulders, one shoulder just before the main crystallisation event and one just after the main crystallisation event. These two shoulders may be interpreted as various stages in the ordering process of the long aliphatic chains of the complex. The crystallisation peak is 36.97 °C lower than the melting peak because of super-cooling.

Cycle 3 depicts an apparent different thermogram from that of cycle 2. The heating segment of cycle 3 boasts three separate heating peaks while the cooling segment only shows one cooling peak with various shoulders. Even though both these peaks **H1(3)** (98.18 °C, -3300 J mol^{-1}) and **H2(3)** (110.39 °C, -1500 J mol^{-1}) are close to the boiling point of water, the release of moisture and/or water is excluded since this is already the third heating cycle. Peaks **H1(3)** (98.18 °C, -3300 J mol^{-1}) and **H2(3)** (110.39 °C, -1500 J mol^{-1}) are solid state transitions which is associated with slow kinetic reordering of the long aliphatic chains in the molecular structure of **[15]**, while **M3(3)** (135.05 °C, -42200 J mol^{-1}) represents the melting process of the sample. Super-cooling occurred during the cooling segment because **C1(3)** is observed at a temperature of 79.33 °C lower than **M3(3)**. In the cooling segment, the crystallisation thermal event with peak **C1(3)** (55.72 °C, 19200 J mol^{-1}) involves crystallisation of the isotropic liquid into a crystalline solid. It is observed as a broad peak of much lower energy than **C1(2)** probably because partial decomposition has already set in at 300 °C.

Cycle 4 has five thermal events all in the heating segment. No thermal events were observed in the cooling segment. Peaks **H1(4)** (63.15 °C, -2400 J mol^{-1}), **H2(4)** (97.68 °C, -4400 J mol^{-1}) and **H3(4)** (110.40 °C, -300 J mol^{-1}) correspond to solid state transitions. Peak **M4(4)** (129.89 °C, -13700 J mol^{-1}) represents the melting of the complex, from 320 °C decomposition set in. Comparison of the melting event **M** for cycles 2, 3 and 4, shows a marked decrease in intensity of the melting peak, this implies that the sample gradually decomposes during these heating and cooling cycles. This is further confirmed by looking at the cooling segment of cycle 3, which no longer depicts a proper crystallisation peak.

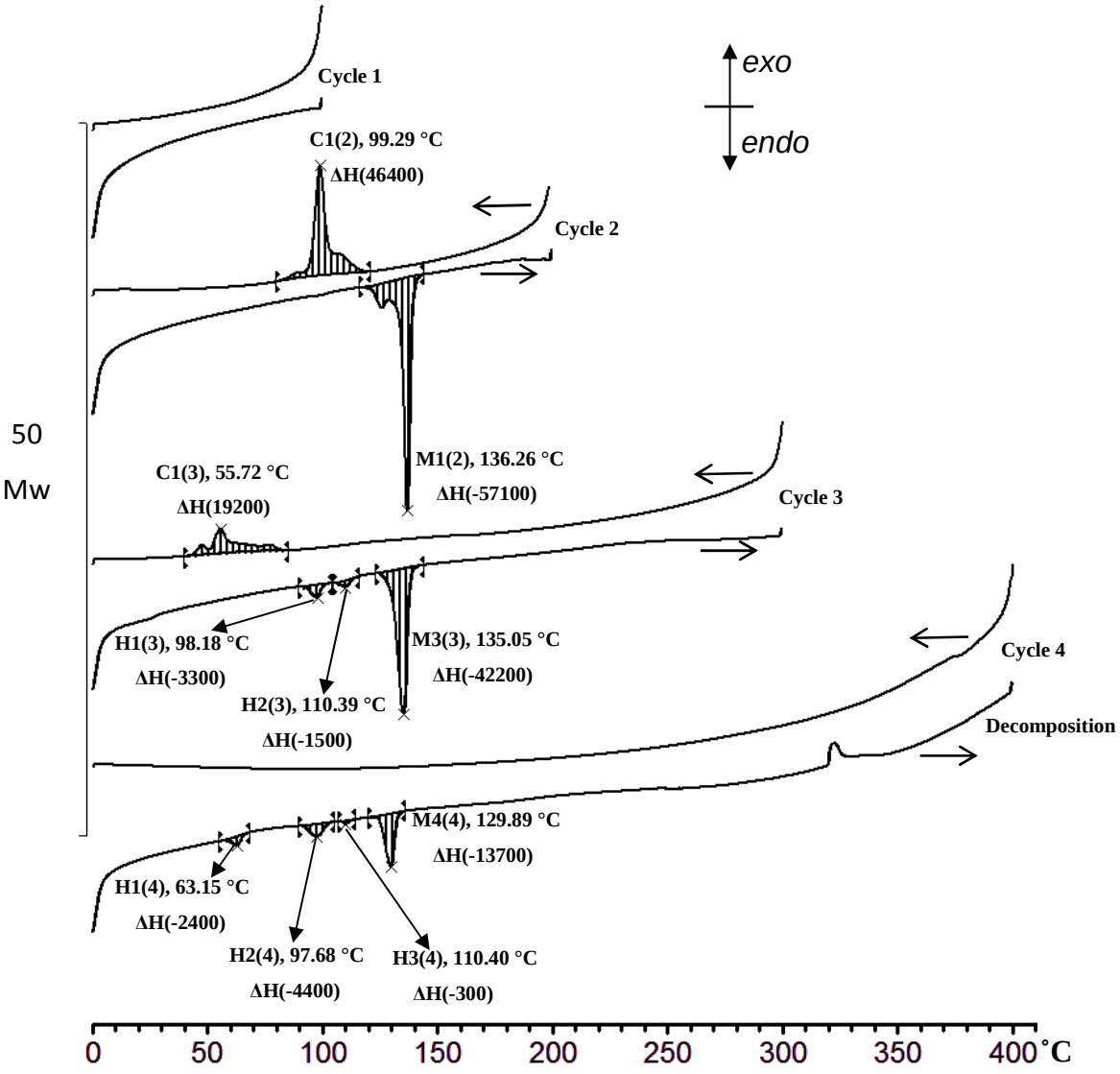

Figure 3.28: DSC of $Zn(C_{10})_2$, **[15]**, with a scan speed of 10 °C min^{-1} under an inert atmosphere of nitrogen. The arrow pointing left indicates the cooling segment while the arrow pointing to the right indicates the heating segment. **H** and **C** denote heating and cooling respectively, while **M** is associated with melting. The number in brackets is the cycle number while the middle number is the peak number. For example **H2(4)** would indicate the second peak in the heating segment of cycle 4. The temperatures (°C) are peak temperatures and the energies are enthalpies (ΔH) in J mol^{-1}.

Table 3.22: DSC data of $Zn(C_{10})_2$, **[15]**, relating each thermal event with, temperature (°C) and enthalpy change (J mol^{-1}).

Peak	Temperature °C	ΔH J mol^{-1}	Peak	Temperature °C	ΔH J mol^{-1}
Cycle 1			**Cycle 2**		
-	-	-	**C1(2)**	99.29	46400
-	-	-	**M1(2)**	136.26	-57100
Cycle 3			**Cycle 4**		
C1(3)	55.72	19200	**H1(4)**	63.15	-2400
H1(3)	98.18	-3300	**H2(4)**	97.68	-4400
H2(3)	110.39	-1500	**H3(4)**	110.40	-300
M3(3)	135.05	-42200	**M4(4)**	129.89	-13700

3.5.5.2. Variable temperature polarised light microscopy

Figure 3.28 shows the images obtained when heating and cooling a sample of $Zn(C_{10})_2$, **[15]**, utilising a variable temperature polarised light microscope.

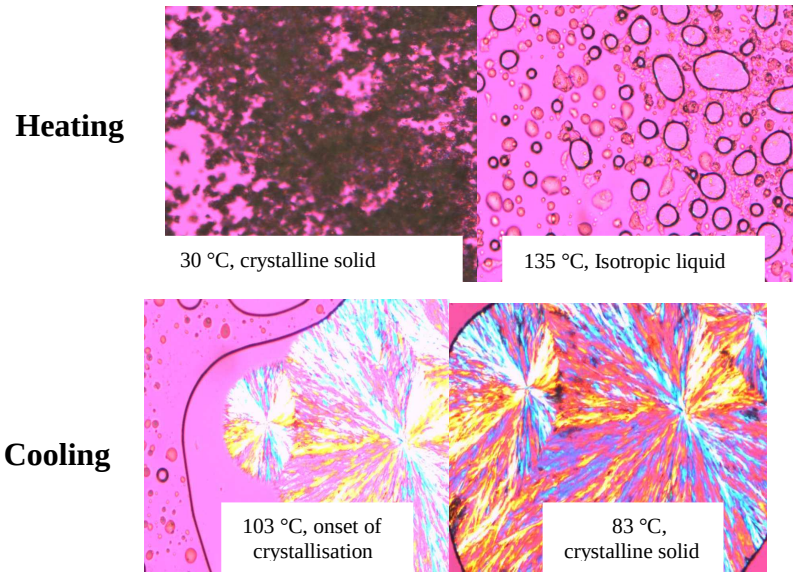

Figure 3.29: Thermal behaviour of $Zn(C_{10})_2$ **[15]** between 30 °C to 135 °C, observed through a variable temperature polarised light microscope. Heating rate was 10 °C min^{-1} in an open atmosphere.

The first image (30 ºC) shows $Zn(C_{10})_2$, **[15]**, as a crystalline solid. The image labelled 135 ºC shows **[15]** as an isotropic liquid. The next two images shows the cooling segment for **[15]**. The successive images labelled 103 ºC to 83 ºC show conversion of an isotropic liquid to a crystalline solid.

3.5.5.3. Thermal Gravimetric Analysis

The TGA thermogram of $Zn(C_{10})_2$, **[15]**, in **Figure 3.30**, under argon, shows that the complex decomposition takes place in two steps. The first step starts at an onset temperature of 206.39 ºC and shows a 20.30 % mass loss until 346.77 ºC. While the second step starts at an onset temperature of 346.77 ºC and shows a 58.78 % mass loss. The total mass loss of 79.08 % corresponds well with the formation of ZnO as the final decomposition product, which would yield a theoretical mass loss of *ca.* 80%.

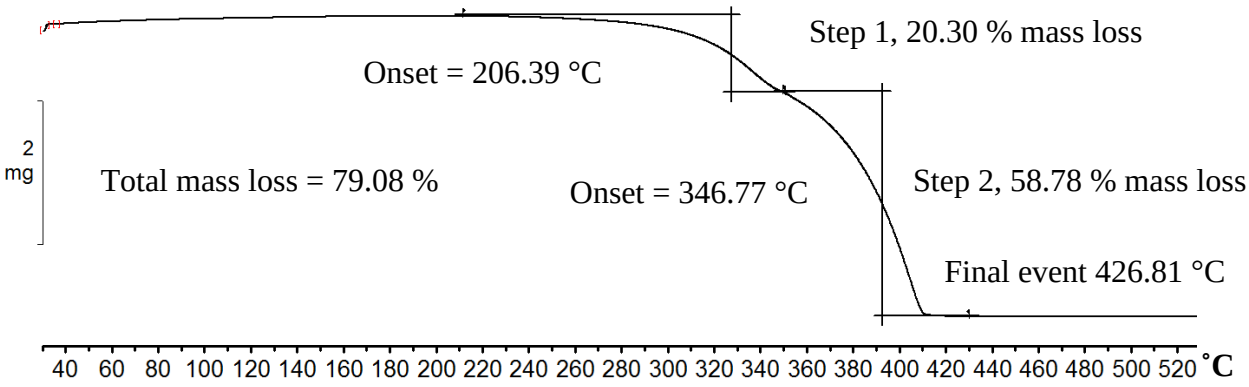

Figure 3.30: TGA of $Zn(C_{10})_2$, **[15]**, with a heating rate of 10 °C min^{-1} in an argon atmosphere.

3.5.6. Thermal analysis of $[Ca^{II}(OOC(CH_2)_8CH_3)_2]$, [16]

The thermal analysis of **[16]**, will be discussed, focussing on solid state transitions and decomposition of the complex.

3.5.6.1. Differential scanning calorimetry, (DSC)

Figure 3.31 depicts the DSC thermogram of $Ca(C_{10})_2$, **[16]**, in an inert atmosphere of nitrogen with a heating rate of 10 °C min^{-1}. **Table 3.23** gives a summary of the DSC data for **[16]**.

Cycle 1, exhibits six weak thermal events, three in the heating segment and three in the cooling segment, but this is attributed to the storage history of the sample and was ignored.

Cycle 2, which is measured within the same temperature limits as cycle 1, shows only one thermal event **H1(2)** (75.63 °C, -500 J mol^{-1}). This is most likely a solid state transition with no corresponding cooling segment thermal events.

Cycle 3, shows three heating segment thermal events and two cooling segment thermal events. Peaks **H1(3)** (98.30 °C, -1100 J mol^{-1}), **H2(3)** (127.81 °C, -3400 J mol^{-1}) and **H3(3)** (164.90 °C, -1700 J mol^{-1}) are consistent with solid state transitions of the long aliphatic chains, of the carboxylatido ligands, settling into different conformations. On the cooling segment of cycle 3, **C1(3)** (103.24 °C, 800 J mol^{-1}) and **C2(3)** (173.32 °C, 700 J mol^{-1}) are consistent with reordering of the long aliphatic chains into lower temperature conformations for the crystal.

Cycle 4, has six thermal events; three are found in the heating segment and three in the cooling segment. Peaks **H1(4)** (104.12 °C, -1900 J mol^{-1}) and **H2(4)** (195.36 °C, -900 J mol^{-1}) are solid state transitions, while **M3(4)** (220.35 °C, -2700 J mol^{-1}) represents the melting of the sample to the isotropic liquid. The **C3(4)** (197.62 °C, 1800 J mol^{-1}) cooling peak is found at lower temperature than that of the melting peak **M1(4)** and this indicates super-cooling. Peaks **C2(4)** (174.09 °C, 600 J mol^{-1}) and **C1(4)** (108.72 °C, 4200 J mol^{-1}) in the cooling segment of cycle 4 is attributed to different degrees of super cooling or reordering of the crystal structure into a more stable conformation.

Cycle 5 shows three thermal events for the heating segment and no thermal events for the cooling segment. The final high temperature thermal event is assigned to the decomposition of $Ca(C_{10})_2$, **[16]**. Again, **H1(5)** (109.47 °C, -2400 J mol^{-1}) and **H2(5)** (196.35 °C, -500 J mol^{-1}) are assigned to solid state transitions, during the heating segment of cycle 5. The melting peak **M3(5)** (221.36 °C, -1700 J mol^{-1}) is much smaller in intensity confirming that decomposition was already initiated in cycle 4. The absence of significant thermal events in the cooling

segment of cycle 5, is consistent with total decomposition of $Ca(C_{10})_2$, **[16]**, at *ca.* 250 °C during the heating segment of cycle 5.

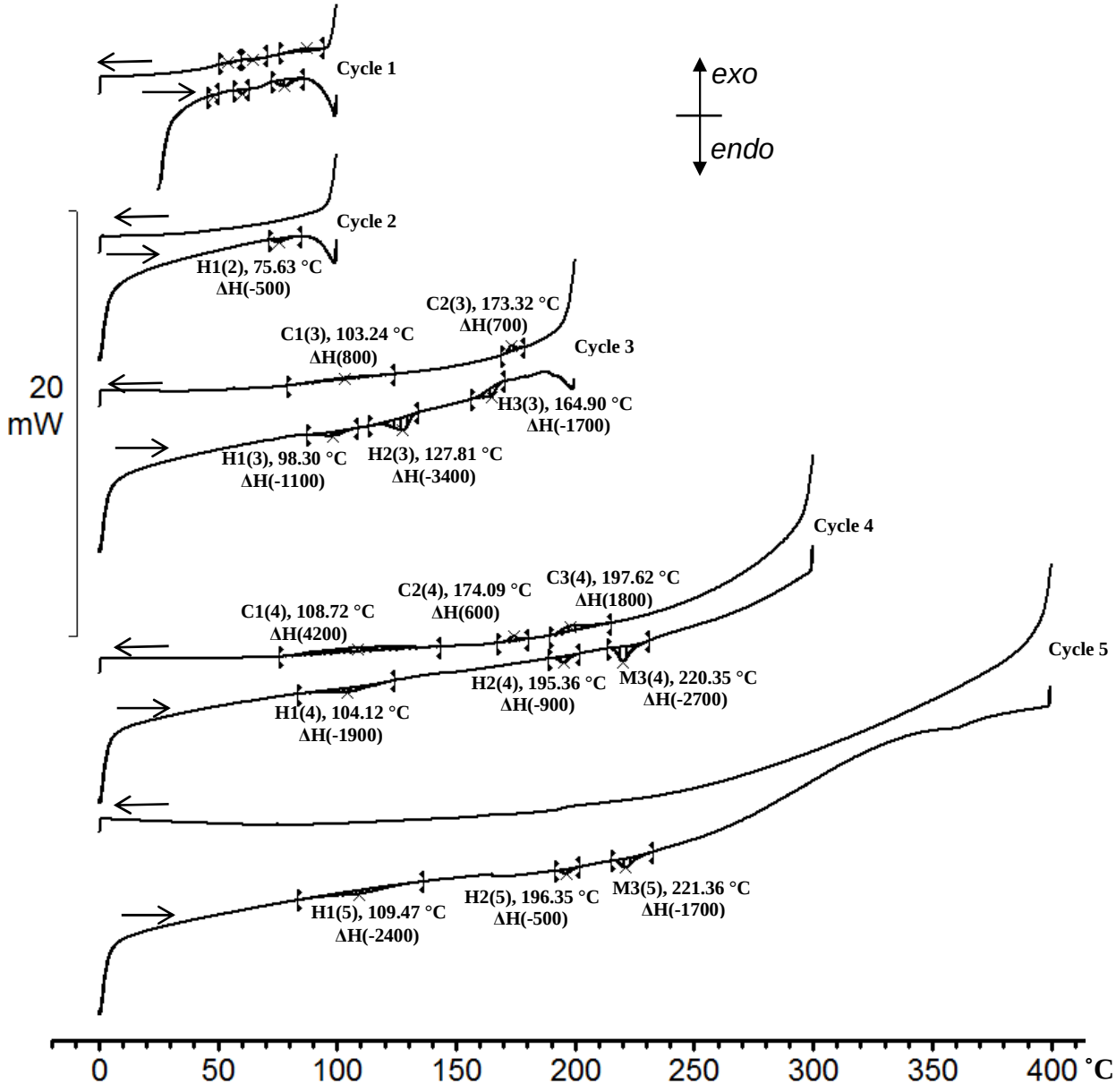

Figure 3.31: DSC of $Ca(C_{10})_2$, **[16]**, with a scan speed of 10 °C min^{-1} under an inert atmosphere of nitrogen. The arrow pointing left indicates the cooling segment while the arrow pointing to the right indicates the heating segment. **H** and **C** denote heating and cooling respectively, while **M** is associated with melting. The number in brackets is the cycle number while the middle number is the peak number. For example **C2(4)** would indicate the second peak in the cooling segment of cycle 4. The temperatures (°C) are peak temperatures and the energies are enthalpies (ΔH) in J mol^{-1}.

Table 3.23: DSC data of $Ca(C_{10})_2$, **[16]**, which includes the peak temperature (°C) and enthalpy change (J mol^{-1}) of each thermal event. Cycle 1 is omitted due to the storage history of the sample.

Peak	Temperature °C	ΔH J mol^{-1}	Peak	Temperature °C	ΔH J mol^{-1}
Cycle 2			**Cycle 3**		
H1(2)	75.63	-500	**C1(3)**	103.24	800
-	-	-	**C2(3)**	173.32	700
-	-	-	**H1(3)**	98.30	-1100
-	-	-	**H2(3)**	127.81	-3400
-	-	-	**H3(3)**	164.90	-1700
Cycle 4			**Cycle 5**		
C1(4)	108.72	4200	**H1(5)**	109.47	-2400
C2(4)	174.09	600	**H2(5)**	196.35	-500
C3(4)	197.62	1800	**M3(5)**	221.36	-1700
H1(4)	104.12	-1900	-	-	-
H2(4)	195.36	-900	-	-	-
M3(4)	220.35	-2700	-	-	-

3.5.6.2. Variable Temperature Polarised Light Microscopy

Figure 3.32 depicts the thermal study performed on a variable temperature polarised light microscope of $Ca(C_{10})_2$, **[16]**, with a heating rate of 10 °C min^{-1} under atmospheric conditions.

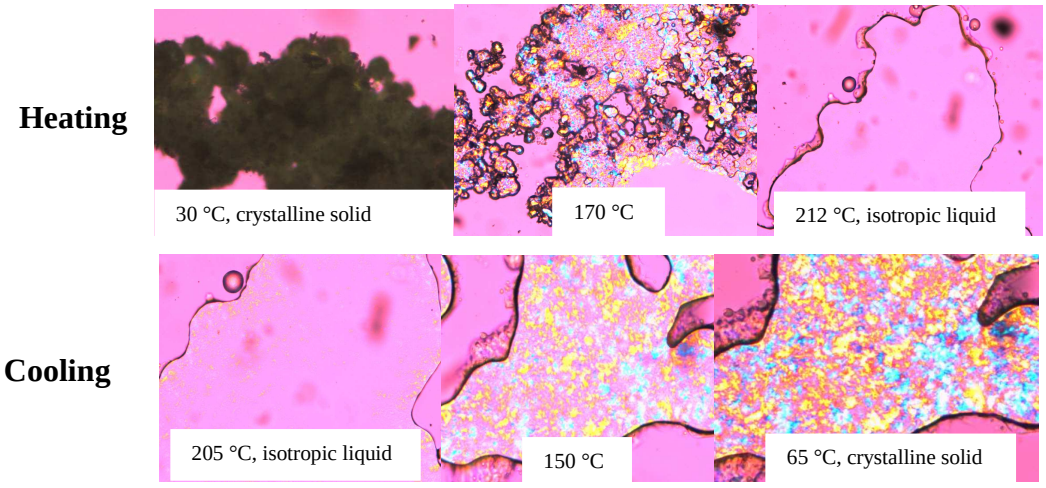

Figure 3.32: Thermal behavior of $Ca(C_{10})_2$, **[16]**, between 30 °C to 212 °C. Viewed through a variable temperature polarised light microscope at a heating rate of 10 °C min^{-1}. Top: heating from 30 °C to 212 °C and Bottom: cooling from 205 °C to 65 °C.

Despite evidence for three possible different solid state phase transition from the DSC study. No clear optical changes were observed upon heating or cooling the sample other than melting to an isotropic liquid, see photos labelled 170 °C and 212 °C or crystallisation during the cooling segment, see photos labelled 205 °C to 65 °C.

3.5.6.3. Thermal Gravimetric Analysis

Two steps or phases are observed during the heating and mass loss measurement of $Ca(C_{10})_2$, **[16]**, see **Figure 3.33**. The first decomposition phase has a small mass loss of *ca.* 3.2 % at 83.87 - 119.39 °C and is associated with the loss of water. The measured mas loss correlates well with the theoretical mass loss of 4.5 % if only one water molecule is associated with one molecule of $Ca(C_{10})_2$, **[16]**. Decomposition of $Ca(C_{10})_2$ **[16]** starts at 335.96 °C (phase 2) and proceed *via* many overlapping steps. A mass loss of 69.33 %, is lower than would be expected for the formation of calcium oxide (CaO), which shows a theoretical mass loss of 86%. It is concluded that up to 540 °C pyrolysis was still incomplete to liberate CaO.

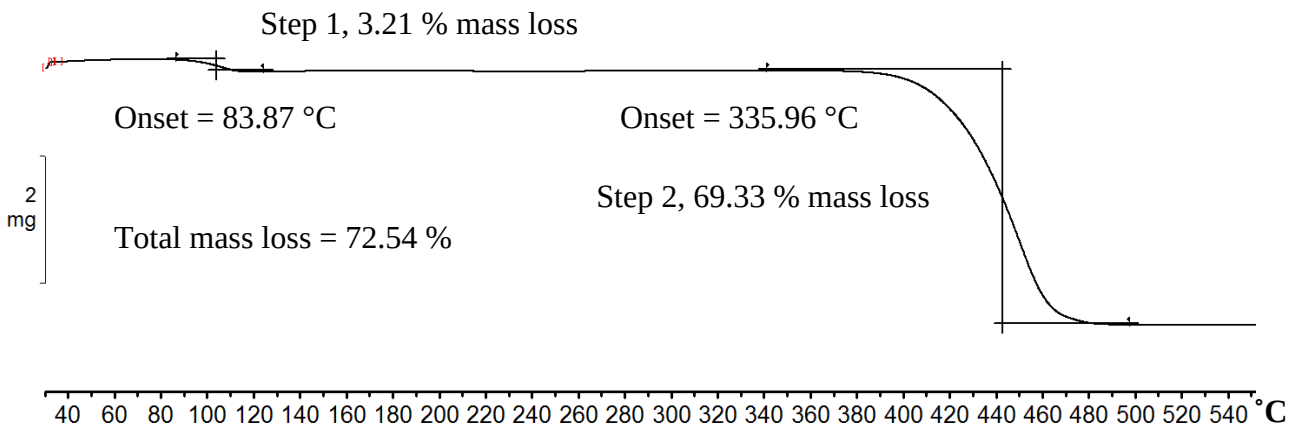

Figure 3.33: TGA of $Ca(C_{10})_2$, **[16]**, with a heating rate of 10 °C min^{-1} under an inert atmosphere of argon.

3.5.7. Thermal analysis of $[Ni^{II}(OOC(CH_2)_8CH_3)_2]\cdot 4H_2O$, [13]

Four steps are observed during the heating and mass loss measurement of $Ni(C_{10})_2$, **[13]**, see **Figure 3.34**. The first decomposition phase has a mass loss of *ca.* 7.89 % at 95.07 – 257.30 °C and is associated with the loss of water. The measured mass loss correlates well with the theoretical mass loss of 7.62 % if two water molecules are released. The second step is also associated with a loss of two molecules of water, *ca*. 7.36 % at 257.30 – 300.83 °C which corresponds well with the theoretical mass loss of 7.62 %. Decomposition of $Ni(C_{10})_2$ **[13]** starts at 300.83 °C after the last two water molecules has been released. The decomposition proceeds *via* many overlapping steps with a mass loss of 61.01 %, followed by a tiny mass loss of 1.54 %. A total mass loss of 78.06 % is observed and corresponds fairly well with a theoretical mass loss of 71.82 % if the final decomposition products are Ni(0) and NiO.

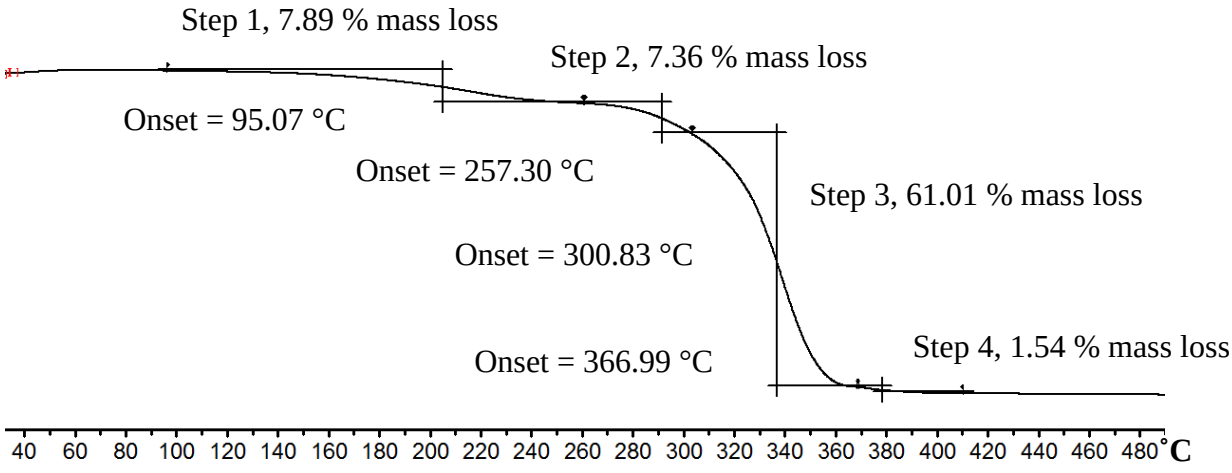

Figure 3.34: TGA of $Ni(C_{10})_2$, **[13]**, with a heating rate of 10 °C min^{-1} under an inert atmosphere of argon.

3.5.8. Thermal analysis of $[Pd^{II}Co^{II}(OOC(CH_2)_nCH_3)_4]$, where n = 4, 6, 8 or 10

The thermal analysis of $PdCo(C_m)_4$, m = 6 for **[19]**, 8 for **[20]**, 10 for **[21]** or 12 for **[22]** will be discussed. This section will focus on the mesophase behaviour of $PdCo(C_8)_4$, **[19]**, and also the decomposition and gaseous products released during pyrolysis of the complexes **[19-22]**.

3.5.8.1. DSC of $[Pd^{II}Co^{II}(\mu\text{-}OOC(CH_2)_4CH_3)_4]$, [19]

Figure 3.35 depicts the DSC thermogram of $PdCo(C_6)_4$, **[19]**, in a nitrogen atmosphere with a heating rate of 10 °C min^{-1}. **Table 3.24** contains a summary of the DSC data for **[19]**.

Cycle 1, depicts four thermal events, three thermal events in the heating segment and one thermal event in the cooling segment. The exothermic peaks **H1(1)** (-8.38 °C, 300 J mol^{-1}) and **H2(1)** (6.97 °C, 1700 J mol^{-1}) are assigned as cold crystallisation. Peak **M3(1)** (52.73 °C, -9000 J mol^{-1}) is the melting of $PdCo(C_6)_4$, **[19]**. In the cooling segment, **C1(1)** (-20.12 °C, 2600 J mol^{-1}) is assigned as the crystallisation peak of $PdCo(C_6)_4$, **[19]**. The crystallisation peak **C1(1)** is 72.85 °C lower in temperature than the melting peak **M3(1)**, illustrating super-cooling.

Cycle 2, have the same peaks as that of cycle 1, and possibly partial decomposition between 110 °C to 150 °C. Peaks **H1(2)** (-9.38 °C, 400 J mol^{-1}) and **H2(2)** (7.30 °C, 1300 J mol^{-1}) are assigned as cold crystallisations. Peak **M3(2)** (52.73 °C, -9700 J mol^{-1}) is the melting of $PdCo(C_6)_4$, **[19]**. In the cooling segment, peak **C1(2)** (-20.12 °C, 1300 J mol^{-1}) is assigned as the crystallisation peak of $PdCo(C_6)_4$, **[19]**.

Cycle 3, has three thermal events, two thermal events in the heating segment and one thermal event in the cooling segment. The exothermic peak **H1(3)** (25.13 °C, 4800 J mol^{-1}) has replaced the two cold crystallisation peaks in cycle 1 and cycle 2. This exothermic peak **H1(3)** can be the cold crystallisation of the decomposition product/s that formed during the partial decomposition between 110 °C to 150 °C observed in cycle 2, together with still intact **[19]**. The endothermic melting peak **M2(3)** (47.08 °C, -6000 J mol^{-1}) has a large shoulder, which can be assigned to the melting of the decomposition products formed during the partial decomposition between 110 °C to 150 °C observed in cycle 2. Therefore **M2(3)** is the melting of a mixture of the decomposition products and also the melting of the remaining original sample, $PdCo(C_6)_4$, **[19]**.

Cycle 4, contains the destructive decomposition peak, **D1(4)** (152.49 °C, 24000 J mol^{-1}) of the partial decomposition products and of the remaining $PdCo(C_6)_4$, **[19]** complex.

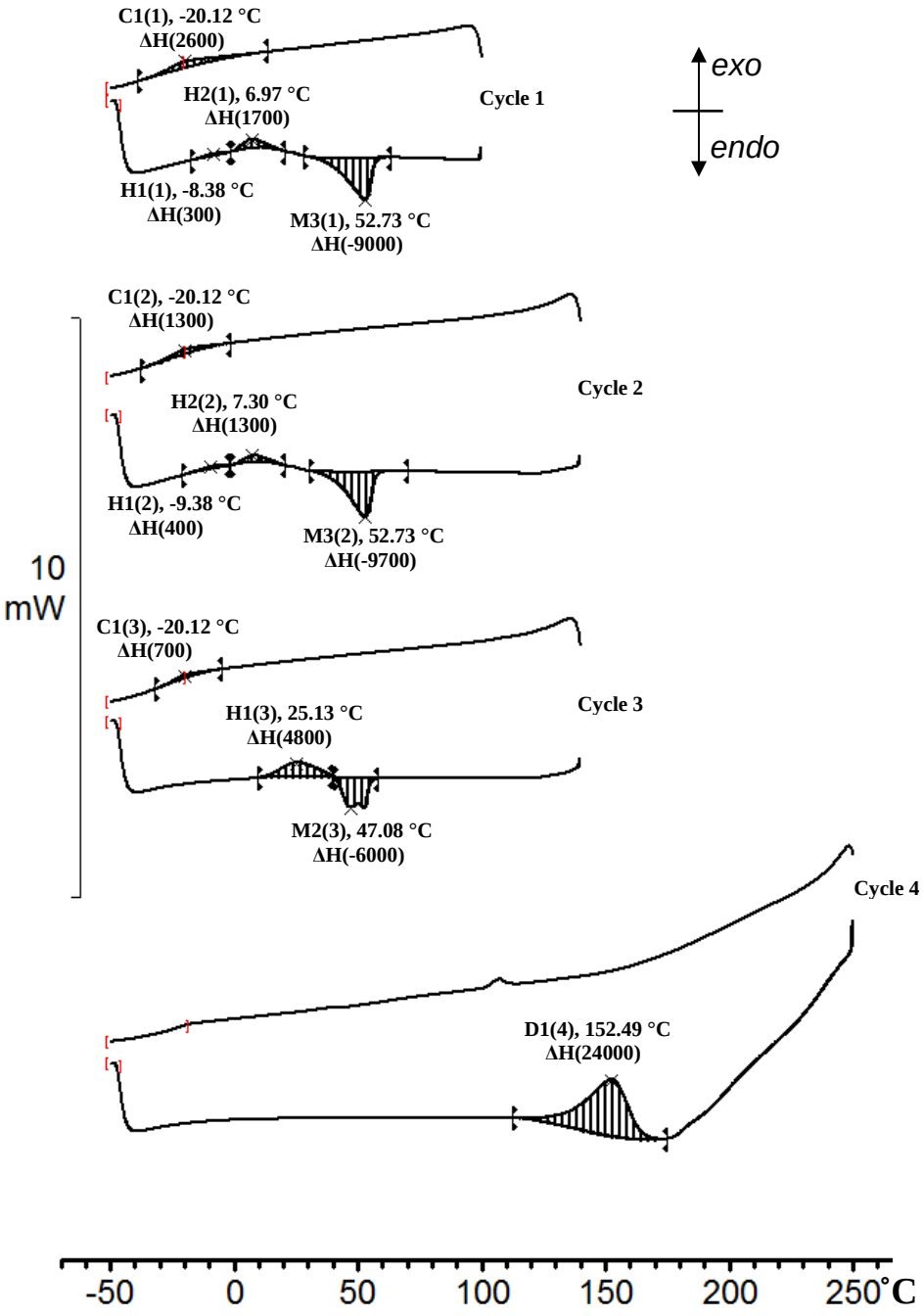

Figure 3.35: DSC of $PdCo(C_6)_4$, **[19]**, utilising a scan speed of 10 °C min^{-1} under nitrogen. The arrow pointing left indicates the cooling segment while the arrow pointing to the right indicates the heating segment. **H** and **C** denote heating and cooling respectively, while **M** is associated with melting. The number in brackets is the cycle number while the middle number is the peak number. For example **H1(3)** would indicate the first peak in the heating segment of cycle 3. The temperatures (°C) are peak temperatures and the energies are enthalpies (ΔH) in J mol^{-1}.

Table 3.24: DSC data of $PdCo(C_6)_4$, **[19]**, relating the peak temperature (°C) and enthalpy change (J mol^{-1}).

Peak	Temperature °C	ΔH J mol^{-1}	Peak	Temperature °C	ΔH J mol^{-1}
Cycle 1			**Cycle 2**		
C1(1)	-20.12	2600	**C1(2)**	-20.12	1300
H1(1)	-8.38	300	**H1(2)**	-9.38	400
H2(1)	6.97	1700	**H2(2)**	7.30	1300
M3(1)	52.73	-9000	**M3(2)**	52.73	-9700
Cycle 3			**Cycle 4**		
C1(3)	-20.12	700	**D1(4)**	152.49	24000
H1(3)	25.13	4800	**-**	-	-
M2(3)	47.08	-6000	**-**	-	-

3.5.8.2. Variable temperature polarised light microscopic study of $[Pd^{II}Co^{II}(\mu\text{-}OOC(CH_2)_4CH_3)_4]$, [19]

Following the DSC study of $PdCo(C_6)_4$, [19], variable temperature polarised light microscopy was used to further investigate the peaks observed.

Figure 3.36 depicts the images obtained from a thermal study performed on a variable temperature polarised light microscope of $PdCo(C_6)_4$, **[19]**, with a heating rate of 10 °C min^{-1} under atmospheric conditions. Heating the crystalline solid from 51 °C to 140 °C, reveals that partial decomposition has occurred, the sample became darker with an increase in temperature. Heating the sample to *ca*. 165 °C, results in destructive decomposition, destroying the original sample and also the decomposition product/s.

The same thermal behaviour was observed for the $Pd_3(C_{12})_4$, **[4]**, complex, see **Figure 3.24** and discussion. It can be concluded that the palladium coordinated moiety of the $PdCo(C_6)_4$, **[19]**, complex melted, leaving the cobalt coordinated moiety as a crystalline solid, see section 3.5.7.9. The cold crystallisation peak **H1(3)** observed in the DSC study of $PdCo(C_6)_2$, **[19]**, can be assigned to the crystallisation of the decomposition product/s produced by the palladium coordinated moiety of the complex.

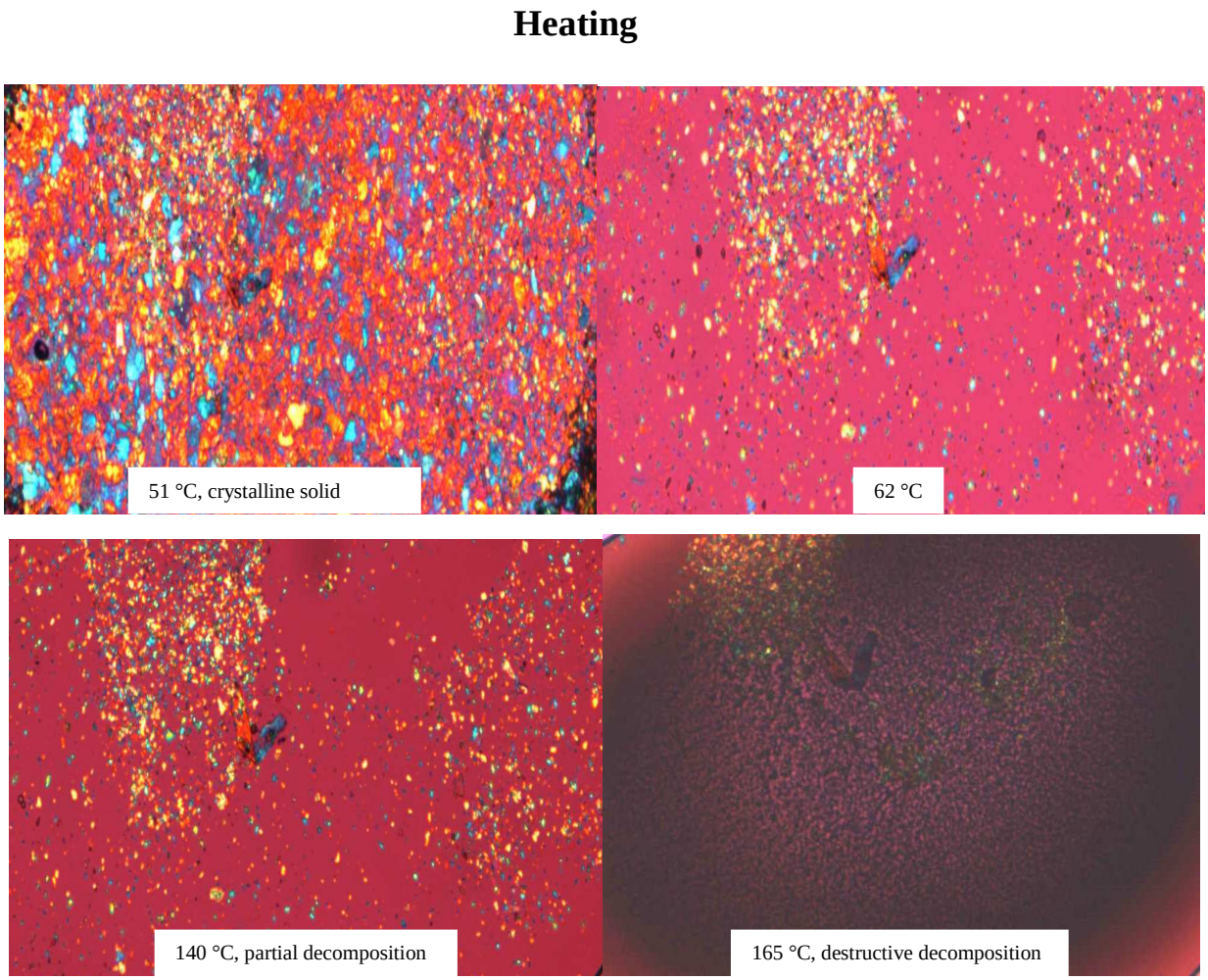

Figure 3.36: Thermal behaviour of $PdCo(C_6)_4$, **[19]**, between 51 °C to 165 °C. Partial decomposition (140 °C) and destructive decomposition (165 °C) is illustrated. The images are viewed through a variable temperature polarised light microscope at a heating rate of 10 °C min^{-1}.

3.5.8.3. DSC of $[Pd^{II}Co^{II}(\mu\text{-}OOC(CH_2)_6CH_3)_4]$, [20]

Figure 3.37 shows the DSC thermogram of $PdCo(C_8)_4$, **[20]**, under nitrogen utilising a heating rate of 10 °C min^{-1}. **Table 3.25** summarises the DSC data of **[20]**. The DSC study of **[20]**, is consistent with smectic liquid crystalline mesophase behaviour.[14]

Cycle 1, has a heating and cooling event. Peaks, **M1(1)** (68.97 °C, -32000 J mol^{-1}) and **C1(1)** (33.83 °C, 29900 J mol^{-1}) are assigned to the melting and crystallisation of **[20]**. The crystallisation peak **C1(1)** is 35.14 °C, lower than **M1(1)** which illustrates supercooling.

Cycle 2, have the same main thermal events as that of cycle 1, **H1(2)** (67.63 °C, -30300 J mol^{-1}) and **C1(2)** (33.67 °C, 29700 J mol^{-1}), at almost the same temperatures. The energy absorbed and liberated is also inherently the same for both cycles. The crystallisation peak **C1(2)** is 33.96 °C, lower than **H1(2)** and is attributed to super-cooling. The heating segment, illustrates the conversion of the crystalline solid phase at peak **H1(2)** (67.63 °C, -30300 J mol^{-1}), to the smectic liquid crystalline mesophase, **M2(2)** (76.26 °C, -100 J mol^{-1}) to the isotropic liquid phase. The cooling segment, illustrates the conversion of the isotropic liquid phase, **C3(2)** (72.66 °C, 100 J mol^{-1}), to the smectic liquid crystalline mesophase at peak **C1(2)** (33.67 °C, 29700 J mol^{-1}) represents conversion of the smectic mesophase to the crystalline solid phase. The peak **C2(2)** (55.45 °C, -200 J mol^{-1}), is the ordering of the liquid crystal into a lower temperature mesophase.

Cycle 3, shows the same thermal events as that of cycle 2, with partial decomposition at **D3(3)**, as illustrated by the change in the slope of the heating segment base line. The heating segment, illustrates the conversion of the crystalline solid phase, **H1(3)** (67.63 °C, -30400 J mol^{-1}), to the smectic liquid crystalline mesophase, **M2(3)** (77.74 °C, -100 J mol^{-1}), to the isotropic liquid phase. Partial decomposition sets in at *ca.* 120 °C. The cooling segment, illustrates the conversion of the isotropic liquid phase, **C3(3)** (79.28 °C, 300 J mol^{-1}), to the smectic liquid crystalline mesophase, **C1(3)** (15.00 °C, 31900 J mol^{-1}), to the crystalline phase. The peak **C2(3)** (32.24 °C, -200 J mol^{-1}), is the ordering of the liquid crystal into a lower temperature mesophase. The peaks **C1(3)** and **C2(3)** are much lower in temperature than **C1(2)** and **C2(2)**. This is probably due to the partial decomposition initiated at *ca.* 120 °C. These products lower the crystallisation temperatures. The relatively small enthalpy values of **M2(2)** (-100 J mol^{-1}) and **C3(2)** (100 J mol^{-1}) with small temperature differences (3.58 °C) are consistent with isotropic liquid phase to the smectic liquid crystalline mesophase conversion and vice versa.

---

[14] P.G. de Gennes and J. Prost, *The Physics of Liquid Crystals*. Oxford: Clarendon Press. (1993).

From this study $PdCo(C_8)_4$, **[20]**, has a liquid crystal range of 8.61 °C, as measured from the peak temperatures of **H1(2)** and **M2(2)**.

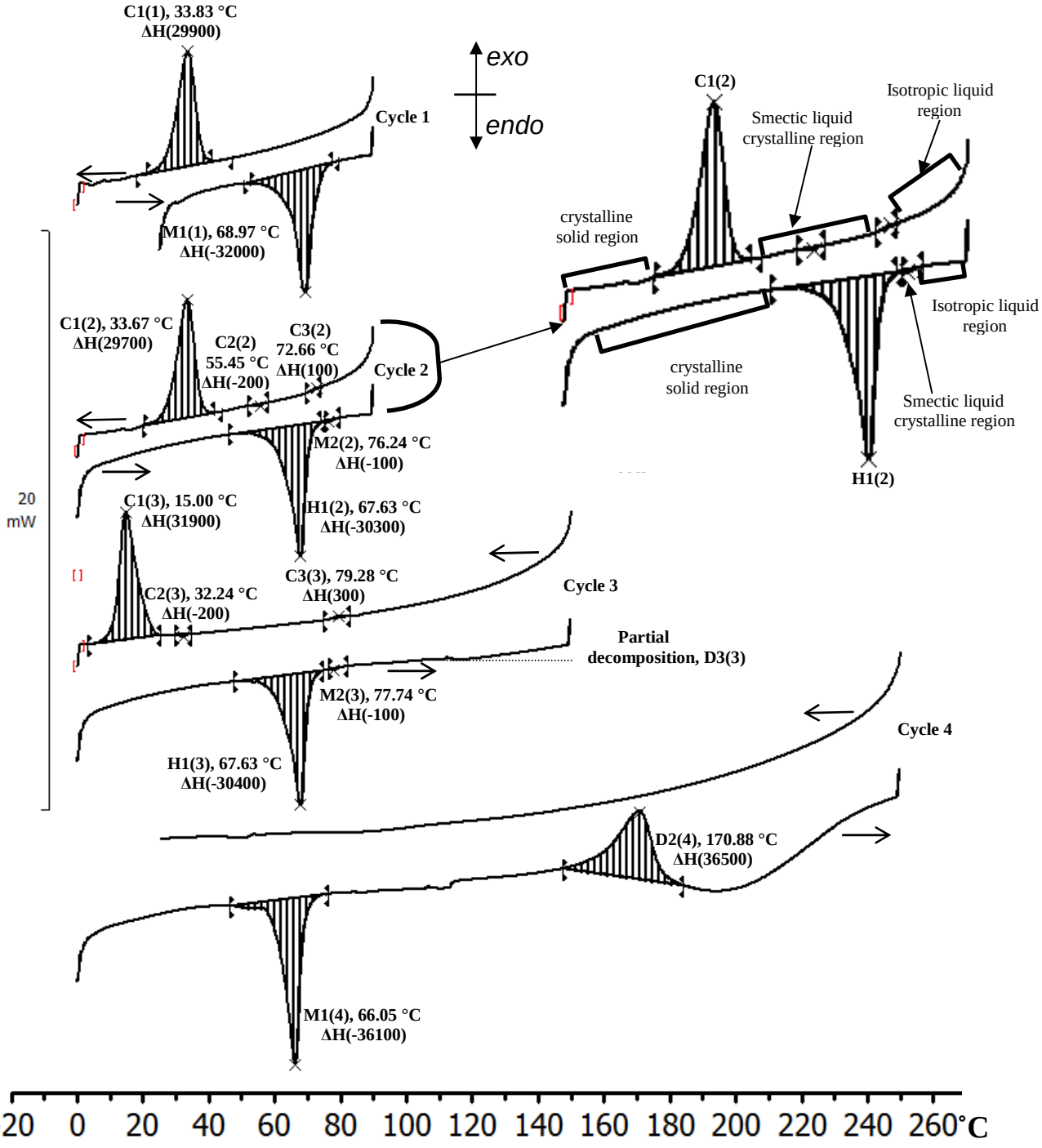

Figure 3.37: DSC of $PdCo(C_8)_4$, **[20]**, utilising a scan speed of 10 °C min^{-1} under a nitrogen atmosphere. The arrow pointing left indicates the cooling segment while the arrow pointing to the right indicates the heating segment. **H** and **C** denote heating and cooling respectively, while **M** is associated with melting. The number in brackets is the cycle number while the middle number is the peak number. For example **C1(2)** would indicate the first peak in the cooling segment of cycle 2. The temperatures (°C) are peak temperatures and the energies are enthalpies (ΔH) in J mol^{-1}.

Table 3.25: DSC data of $PdCo(C_8)_4$, **[20]**, which includes the peak temperature (°C) and enthalpy change (J mol^{-1}) of each thermal event.

Peak	Temperature °C	ΔH J mol^{-1}	Peak	Temperature °C	ΔH J mol^{-1}
Cycle 1			**Cycle 2**		
C1(1)	33.83	29900	**C1(2)**	33.67	29700
M1(1)	68.97	-32000	**C2(2)**	55.45	-200
-	-	-	**C3(2)**	72.66	100
-	-	-	**H1(2)**	67.63	-30300
-	-	-	**M2(2)**	76.24	-100
Cycle 3			**Cycle 4**		
C1(3)	15.00	31900	**M1(4)**	66.05	-36100
C2(3)	32.24	-200	**D2(4)**	170.88	36500
C3(3)	79.28	300	-	-	-
H1(3)	67.63	-30400	-	-	-
M2(3)	77.74	-100	-	-	-

3.5.8.4. Variable temperature polarised light microscopic study of $[Pd^{II}Co^{II}(\mu\text{-}OOC(CH_2)_6CH_3)_4]$, [20]

Figure 3.38 exhibits the polarised light microscope photographs of $PdCo(C_8)_4$, **[20]**, obtained at a heating rate of 10 °C min^{-1}, under atmospheric conditions at the indicated temperatures. The first image labelled 30 ºC, shows $PdCo(C_8)_4$, **[20]**, in its crystalline solid form. The image labelled 62 ºC shows the initial stages of the transition of a crystalline solid to smectic liquid-crystalline mesophase. The liquid crystal in the smectic phase of $PdCo(C_8)_4$, **[20]**, is clearly observable as blue and yellow fibres in the image labelled 68 ºC. The image labelled 73 ºC shows $PdCo(C_8)_4$, **[20]**, after melting into an isotropic liquid. The cooling images in **Figure 3.38** shows pictures from a cooling segment and also shows smectic mesophases of $PdCo(C_8)_4$, **[20]**.

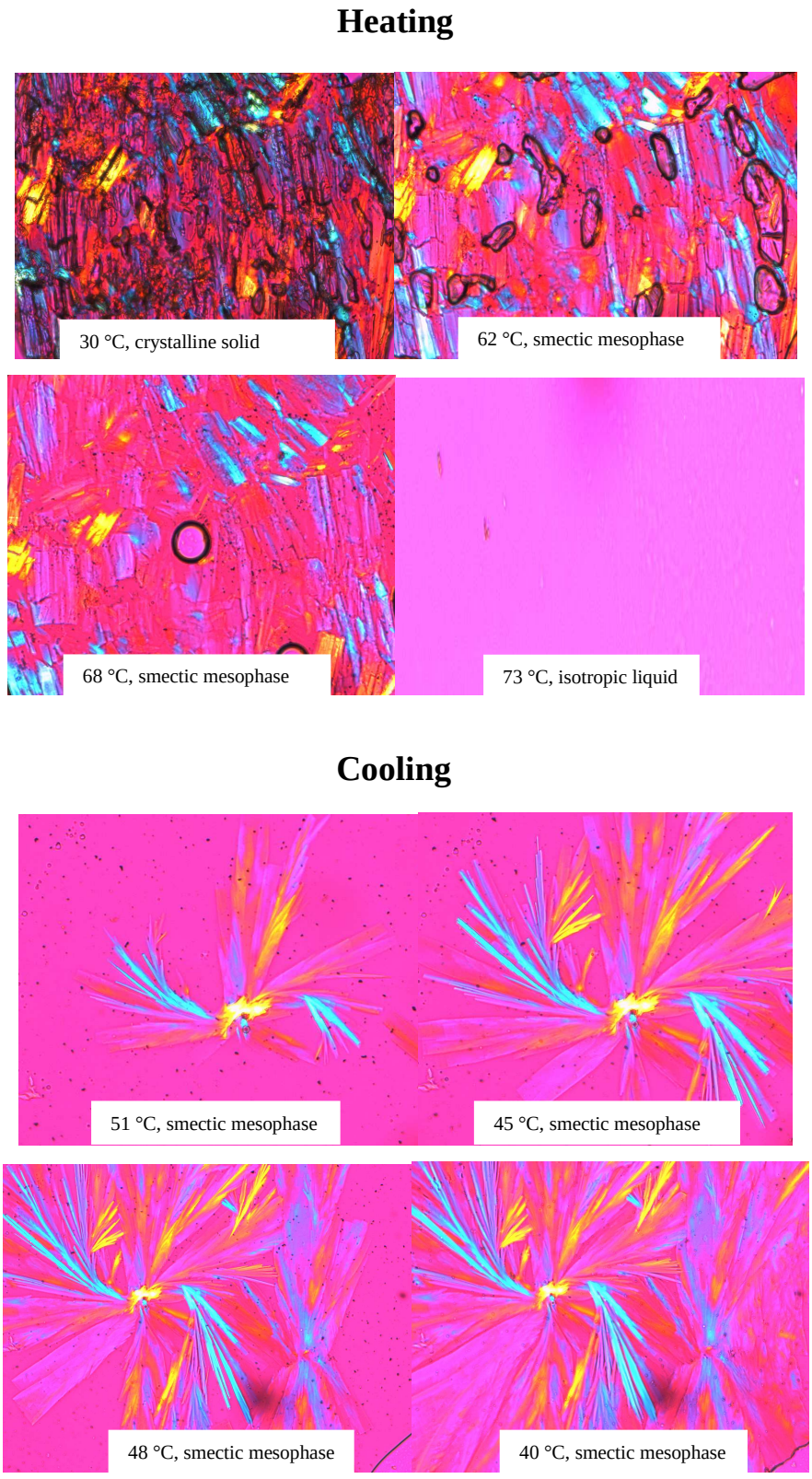

Figure 3.38: Polarised light microscope pictures of $PdCo(C_8)_4$, **[20]**, at the indicated temperatures, illustrating smectic mesophase behaviour. **Top:** Heating segment illustrating the crystalline solid phase change to smectic mesophase and finally to the isotropic liquid. **Bottom:** Cooling segment illustrating the phase change of the initial smectic mesophase to the crystalline solid phase.

3.5.8.5. DSC of $[Pd^{II}Co^{II}(\mu\text{-}OOC(CH_2)_8CH_3)_4]$, [21]

Figure 3.39 depicts the DSC thermogram of $PdCo(C_{10})_4$, **[21]**, showing the heating and cooling segments, under an atmosphere of nitrogen utilising a heating rate of 10 °C min^{-1}. **Table 3.26** summarises the DSC data of **[21]**.

Cycle 1, have one heating event and one cooling event. Peaks, **M1(1)** (83.04 °C, -84000 J mol^{-1}) and **C1(1)** (68.83 °C, 51700 J mol^{-1}) are assigned to the melting and crystallisation of **[21]**.

Cycle 2, have the same thermal events as cycle 1, with an extra cold crystallisation peak in the heating segment. The exothermic peak, **H1(2)** (62.55 °C, 13400 J mol^{-1}) is assigned to cold crystallisation of a small portion of amorphous **[21]**. The endothermic peak **M2(2)** (82.08 °C, -76400 J mol^{-1}) is assigned to the melting of the bulk **[21]**. The peak, **C1(2)** (67.49 °C, 51600 J mol^{-1}) is assigned to the crystallisation of **[21]**.

Cycle 3, have the same thermal events as that of cycle 2. The exothermic peak, **H1(3)** (64.41 °C, 14900 J mol^{-1}) is again assigned to the cold crystallisation of a small portion of amorphous **[21]**. The endothermic peak **M2(3)** (81.90 °C, -71400 J mol^{-1}) is assigned to the melting of the bulk sample of **[21]**. The peak, **C1(3)** (68.14 °C, 50000 J mol^{-1}) is assigned to the crystallisation of **[21]**.

Cycle 4, has three thermal events, cold crystallisation, melting and destructive decomposition. The exothermic peak, **H1(4)** (64.25 °C, 12800 J mol^{-1}) is again assigned to the cold crystallisation of a small amorphous portion of **[21]**. The endothermic peak **M2(4)** (81.89 °C, -73900 J mol^{-1}) is assigned to the melting of the bulk sample of **[21]**. The peak **D3(4)** (188.13 °C, 37200 J mol^{-1}) and the change in base line slope at 230 °C signals destructive decomposition of $PdCo(C_{10})_4$, **[21]**. The cooling segment has no thermal events proving all remaining material are thermally inactive in the utilised temperature. The volatiles that come of will be discussed in the TGA-MS section see paragraph 3.5.7.9.

An additional remark is important to make at this stage. From the DSC thermogram in **Figure 3.39**, no evidence of mesophase behaviour could be found. However, in section 3.5.7.9, the polarised light microscope investigation is discussed. From the images in **Figure 3.40** it is clear that **[21]** do have a smectic liquid crystalline mesophase temperature region between *ca*. 75 to 66 °C. This means that the energy required to switch from isotropic liquid to liquid crystalline smectic mesophase at 75 °C is just too little to be measured by DSC techniques.

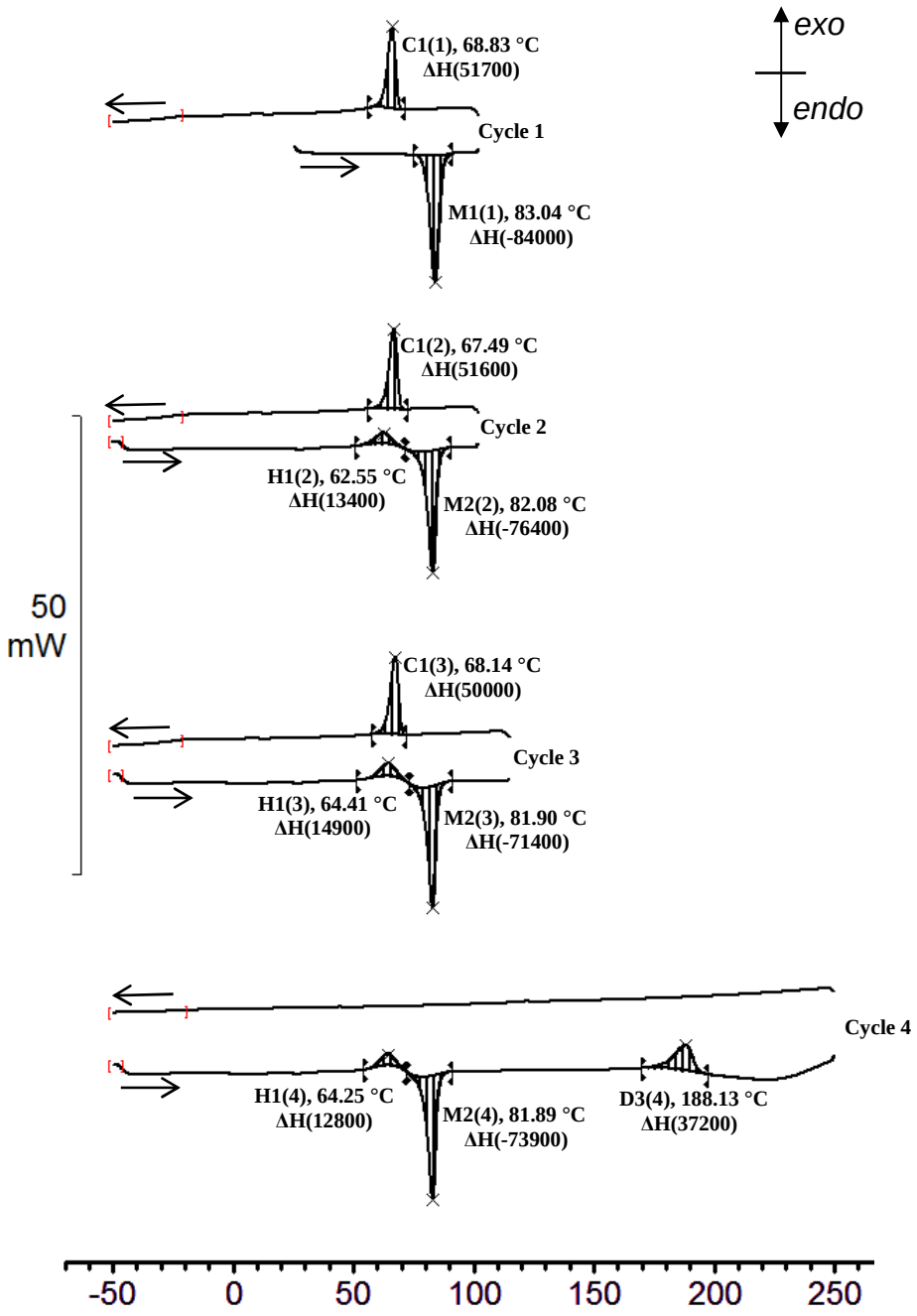

Figure 3.39: DSC of $PdCo(C_{10})_4$ **[21]** with a scan speed of 10 °C min^{-1} under nitrogen. The arrow pointing left indicates the cooling segment while the arrow pointing to the right indicates the heating segment. **H** and **C** denote heating and cooling respectively, while **M** is associated with melting. The number in brackets is the cycle number while the middle number is the peak number. For example **C1(2)** would indicate the first peak in the cooling segment of cycle 2. The temperatures (°C) are peak temperatures and the energies are enthalpies (ΔH) in J mol^{-1}.

Table 3.26: DSC data of $PdCo(C_{10})_4$ **[21]**, relating each thermal event with peak temperature (°C) and enthalpy change (J mol^{-1}).

Peak	**Temperature °C**	**ΔH J mol^{-1}**	**Peak**	**Temperature °C**	**ΔH J mol^{-1}**
Cycle 1			**Cycle 2**		
C1(1)	68.83	51700	**C1(2)**	67.49	51600
M1(1)	83.04	-84000	**H1(2)**	62.55	13400
-	-	-	**M2(2)**	82.08	-76400
Cycle 3			**Cycle 4**		
C1(3)	68.14	50000	**H1(4)**	64.25	12800
H1(3)	64.41	14900	**M2(4)**	81.89	-73900
M2(3)	81.90	-71400	**D3(4)**	188.13	37200

3.5.8.6. Variable Temperature Polarised Light Microscopic study of $[Pd^{II}Co^{II}(\mu\text{-}OOC(CH_2)_8CH_3)_4]$, [21]

Figure 3.40, exhibits the polarised light microscope photographs of $PdCo(C_{10})_4$, **[21]**, obtained utilising a heating rate of 10 °C min^{-1}, under atmospheric conditions at the indicated temperatures. The first image in the cooling segment at 25 ˚C, of **Figure 3.40**, depicts **[21]**, as a crystalline solid. The images labelled 77 ˚C and 79 ˚C is the phase change of **[21]**, into a smectic mesophase liquid crystal. The isotropic liquid phase is observed in the image labelled 81 ˚C. The cooling of **[21]**, is depicted in **Figure 3.40**. It is clear from the photographs that are shown that the material assumed a smectic mesophase liquid crystal state and that the crystalline solid only forms at 66 °C. This result appends the DSC section discussed in the previous paragraph that failed to uniquely identify a mesophase. The smectic mesophase liquid crystal crystallises at peaks **C1(1)**, **C1(2)** and **C1(3)** into mostly a crystalline solid but partially also in to an amorphous solid. This amorphous portion is shown in **Figure 3.39** to cold crystallise into a crystalline solid at peaks **H1(2)**, **H1(3)** and **H1(4)**.

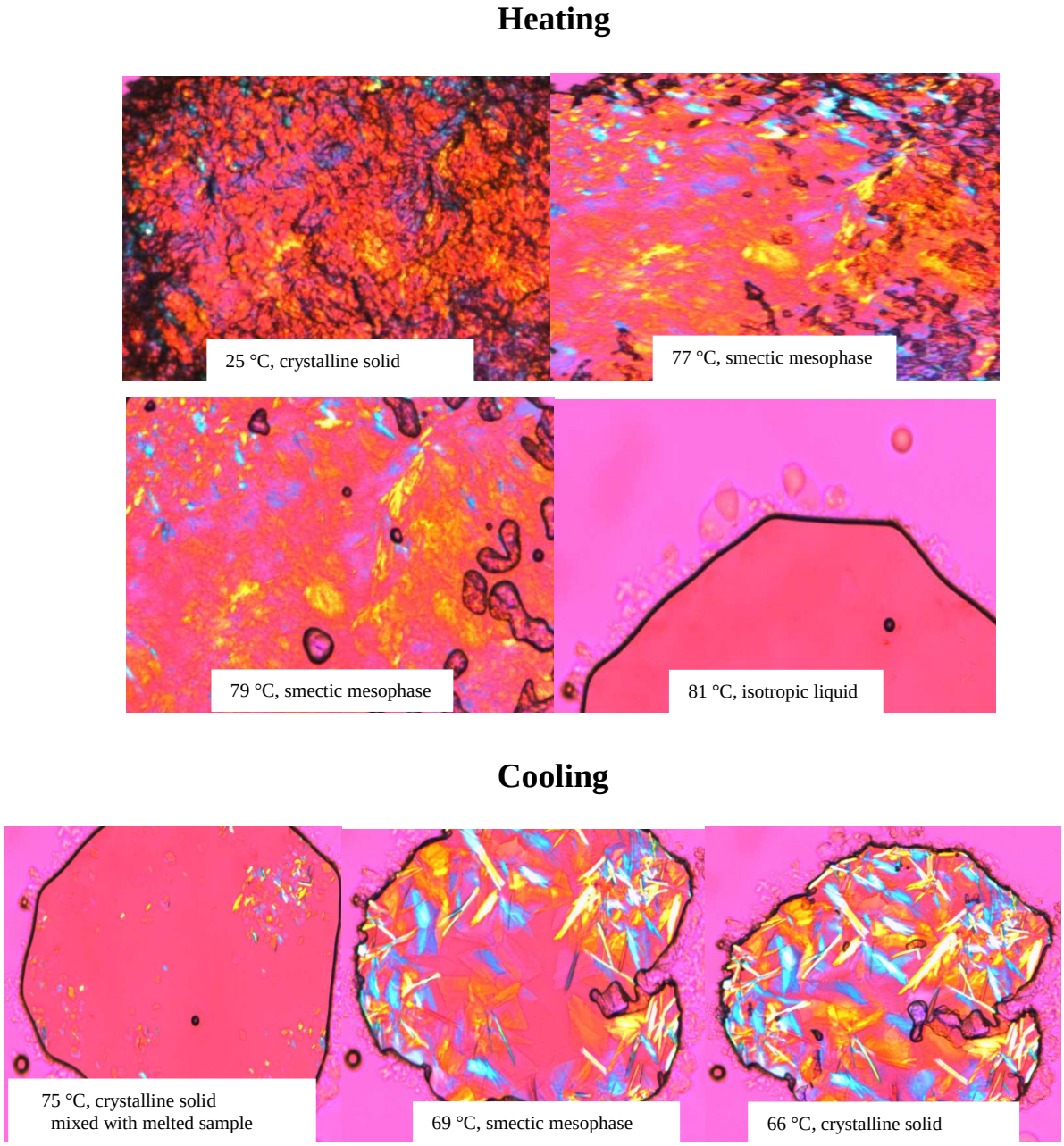

Figure 3.40: Polarised light microscope pictures of $PdCo(C_{10})_4$, **[21]** at the indicated temperatures. **Top:** Heating segment illustrating the phase change of the crystalline solid to the isotropic liquid and **Bottom:** Cooling segment illustrating the phase change of the isotropic liquid to the smectic mesophase.

3.5.8.7. DSC of $[Pd^{II}Co^{II}(\mu\text{-}OOC(CH_2)_{10}CH_3)_4]$, [22]

Figure 3.41, depicts the DSC thermogram of $PdCo(C_{12})_4$, **[22]**, showing the heating and cooling segments, under an atmosphere of nitrogen utilising a heating rate of 10 °C min^{-1}. **Table 3.27** summarises the DSC data of **[22]**.

Cycle 1, have four thermal events, two heating events and two cooling events. The exothermic peak, **H1(1)** (41.86 °C, -14600 J mol^{-1}) is assigned to a solid state transition, resulting in the reordering of the long aliphatic chains in the molecular structure of **[22]**. This solid state transition is followed by the melting of **[22]**, at peak **M2(1)** (84.35 °C, -79600 J mol^{-1}). In the cooling segment, the exothermic peak **C2(1)** (47.30 °C, 78000 J mol^{-1}) is assigned as the crystallisation of **[22]**, and is followed by a solid state repositioning of the aliphatic long chains of the molecule into a low temperature conformation at **C1(1)** (30.87 °C, 14800 J mol^{-1}). The two peaks **H1(1)** and **C1(1)** are not assigned to two separate substances. An elemental analysis of $PdCo(C_{12})_4$, **[22]**, proved that the required CHN analysis were within 0.4 % error. The crystallisation peak **C2(1)** is 37.05 °C lower than **M2(1)**, illustrating, super-cooling.

Cycle 2, have five thermal events, three thermal events in the heating segment and two thermal events in the cooling segment between temperatures -50 °C to 150 °C. The peaks **H1(2)** (41.87 °C, -14600 J mol^{-1}) and **H2(2)** (55.12 °C, -500 J mol^{-1}) are solid state transitions, resulting in repositioning of the long aliphatic chains in the molecular structure of **[22]**. Peak **H2(2)** is most probably the cause of minute decomposition that occurred at peak **M2(1)**, implying peak **H2(2)**, may be the melting of the decomposed product/s. However the energy of this peak is so small (0.6 % of the melting peak) that it is not regarded as significant. The peak **M3(2)** (83.87 °C, -77000 J mol^{-1}) is the melting of **[22]**. Peak **C2(2)** (44.51 °C, 70300 J mol^{-1}) is the crystallisation of **[22]**, and is lower in temperature than **M3(2)**, because of super-cooling. The crystallisation peak is followed by a solid state transition, **C1(2)** (28.71 °C, 16000 J mol^{-1}).

Cycle 3, have four thermal events, all in the heating segment, with destructive decomposition at peak **D4(3)**. No thermal events are observed in the cooling segment, because of destructive decomposition in the heating segment. This cycle has temperature limits between -50 °C to 250 °C. The peaks **H1(3)** (41.70 °C, -17200 J mol^{-1}) and **H2(3)** (54.12 °C, -800 J mol^{-1}) is a solid state transition and a melting peak respectively. Peak **H1(3)** is the repositioning of the long aliphatic chains in the molecular structure of **[22]** and **H2(3)** may be the melting of very small quantities of decomposition products. The melting peak **M3(3)** (83.22 °C, -74700 J mol^{-1}), is followed by destructive decomposition at **D4(3)** (170.52 °C, 33400 J mol^{-1}).

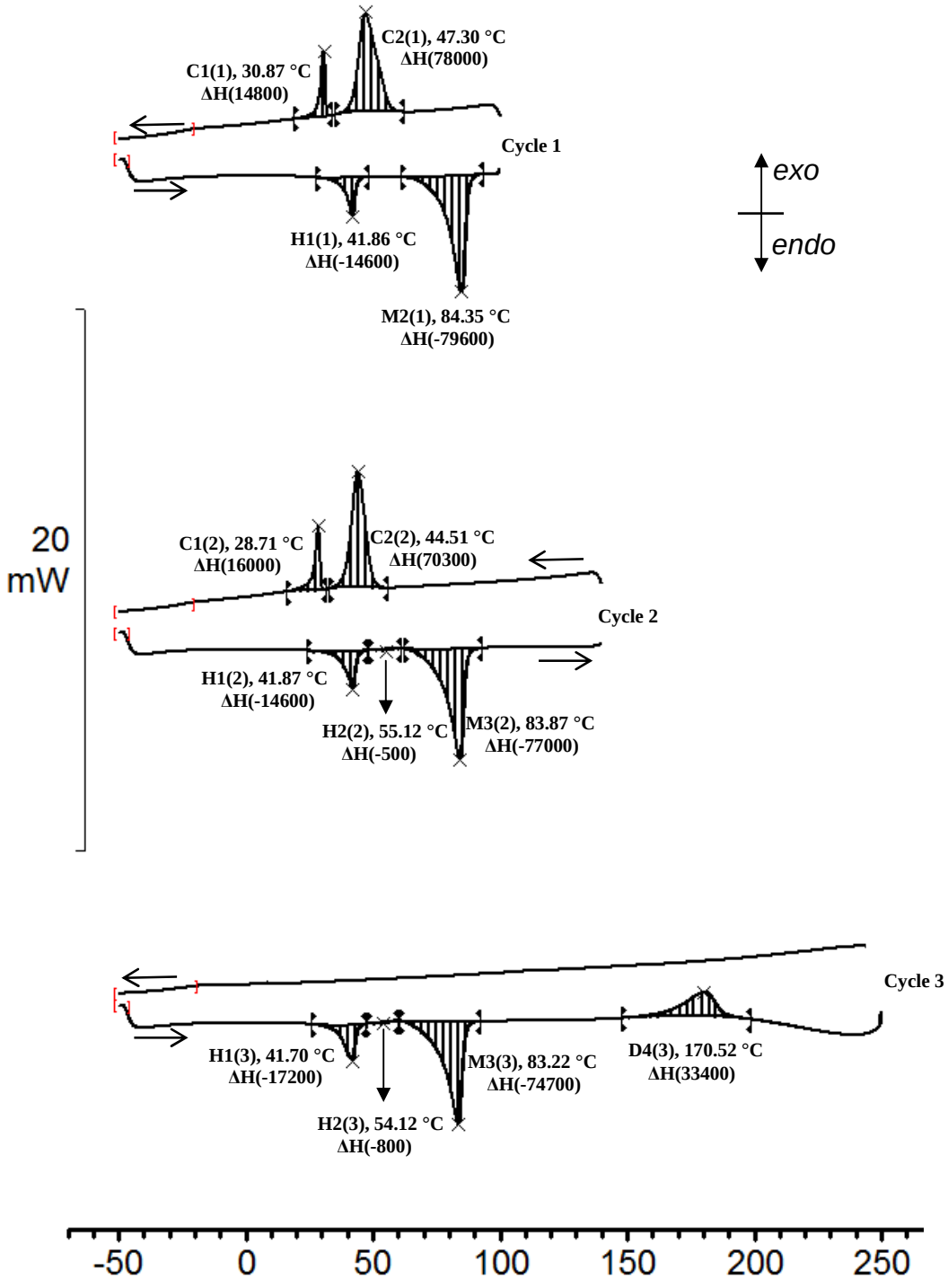

Figure 3.41: DSC of $PdCo(C_{12})_4$ **[22]** with a scan speed of 10 °C min^{-1} under nitrogen. The arrow pointing left indicates the cooling segment while the arrow pointing to the right indicates the heating segment. **H** and **C** denote heating and cooling respectively, while **M** is associated with melting. The number in brackets is the cycle number while the middle number is the peak number. For example **C1(2)** would indicate the first peak in the cooling segment of cycle 2. The temperatures (°C) are peak temperatures and the energies are enthalpies (ΔH) in J mol^{-1}.

Table 3.27: DSC data of $PdCo(C_{12})_4$, **[12]**, relating each thermal event with peak temperature (°C) and enthalpy change (J mol^{-1}).

Peak	**Temperature °C**	**ΔH J mol^{-1}**	**Peak**	**Temperature °C**	**ΔH J mol^{-1}**
Cycle 1			**Cycle 2**		
C1(1)	30.87	14800	**C1(2)**	28.71	16000
C2(1)	47.30	78000	**C2(2)**	44.51	70300
H1(1)	41.86	-14600	**H1(2)**	41.87	-14600
M2(1)	84.35	-79600	**H2(2)**	55.12	-500
-	-	-	**M3(2)**	83.87	-77000
Cycle 3			**-**	**-**	**-**
H1(3)	41.70	-17200	**-**	-	-
H2(3)	54.12	-800	**-**	-	-
M3(3)	83.22	-74700	**-**	-	-
D4(3)	170.52	33400	**-**	-	-

3.5.8.8. Variable Temperature Polarised Light Microscopic study of $[Pd^{II}Co^{II}(\mu\text{-}OOC(CH_2)_{10}CH_3)_4]$, [22]

Figure 3.42 exhibits the polarised light microscope photographs of $PdCo(C_{12})_4$, **[22]**, obtained at a heating rate of 10 °C min^{-1}, under atmospheric conditions at the indicated temperatures. The first image in the heating segment shows $PdCo(C_{12})_4$, **[22]**, as a crystalline diamond shaped solid. The next image labelled 91 °C, shows **[22]**, as an isotropic liquid. The images in the cooling segment shows the successive cooling of **[22]**, to a crystalline solid.

Heating

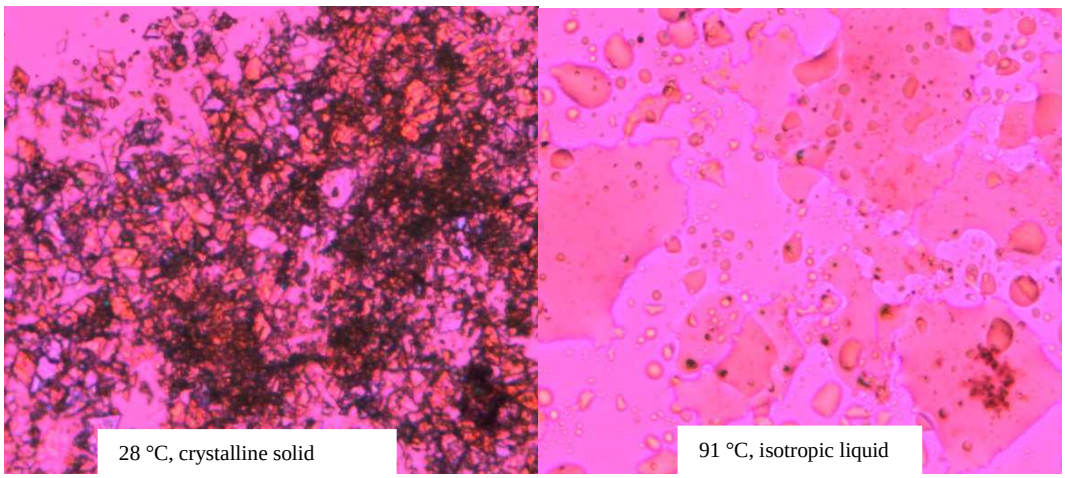

Cooling

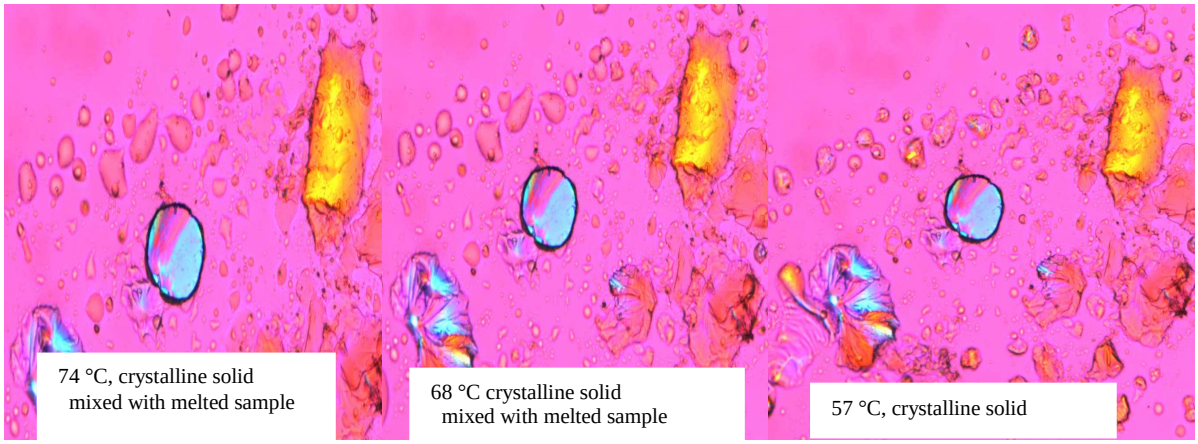

Figure 3.42: Polarised light microscope pictures of $PdCo(C_{12})_4$, **[22]**, at the indicated temperatures.

3.5.8.9. Thermal gravimetric analysis coupled with mass spectroscopy of $[Pd^{II}Co^{II}(\mu\text{-}OOC(CH_2)_nCH_3)_4]$, where is n = 4 for [19], 6 for [20], 8 for [21] or 10 for [22]

The TGA for $PdCo(C_8)_4$, **[20]**, is given in **Figure 3.43**. The decomposition data and the analysis of the gaseous products from the decomposition of **[19-22]** are tabulated in **Table 3.28** and **Table 3.29** respectively. Mass loss is initiated at 126.66 °C and proceeds through two separate steps up to 349.84 °C for **[20]**. The temperature range for each step, as well as the associated mass loss is tabulated in **Table 3.28**.

The mass loss in both decomposition steps one and two are 37 %, which coincides with the loss of two octanoatido ligands having a theoretical mass loss value of 38.80 %. The total mass lost during the thermal decomposition process of $PdCo(C_8)_4$, **[20]**, amounts to 74 %. The theoretical remaining mass values is calculated as 16.55 % for PdO and 10.16 % for CoO, thus for the formation of these two decomposition products the theoretical mass loss value will be 73.29 %. This corresponds very well with the experimentally determined value of 74%. Complexes **[19]**, **[21]** and **[22]** behaved similarly to the complex **[20]** when subjected to heat, results are summarised in **Table 3.28**.

Considering the onset decomposition temperatures of **[19-22]**, the previous DSC and variable temperature polarised light microscopic studies of **[1-4]** and **[19-22]** are further confirmed. The first decomposition step does coincide with the palladium coordinated moiety being melted and decomposed. The onset decomposition, temperatures, for the palladium cobalt tetracarboxylatido complexes **[19-22]** is between 118.35 °C to 130.26 °C.

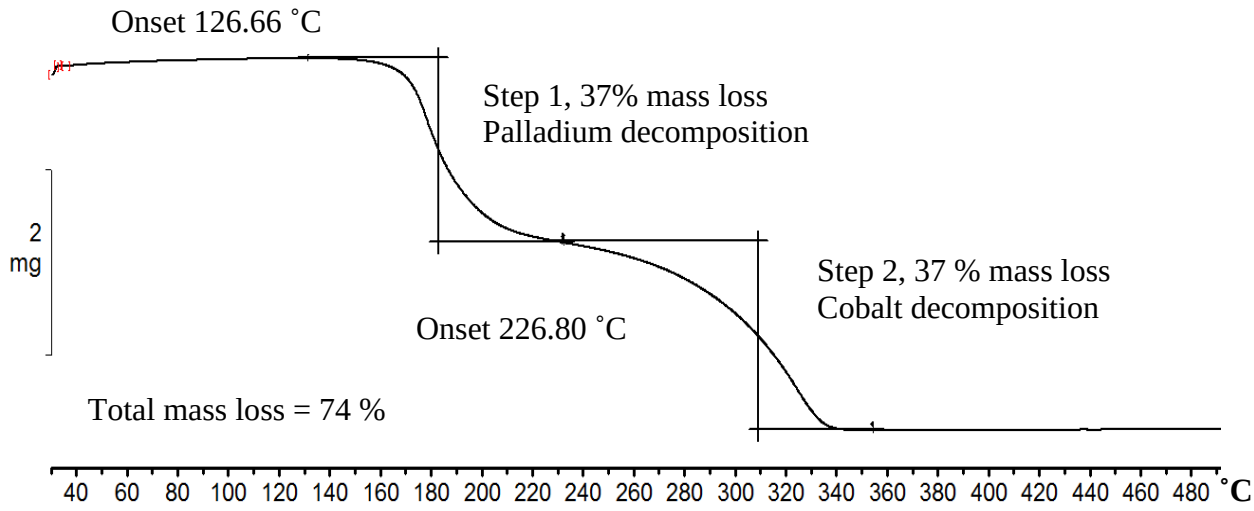

Figure 3.43: TGA of $PdCo(C_8)_4$, **[20]**, at a scan rate of 10 °C min^{-1} under argon.

Table 3.28 Depicts the decomposition temperature ranges of **[19-22]**, with **[19]** having three decomposition steps while **[20-22]** only have two decomposition steps.

Table 3.28: TGA data of $PdCo(C_m)_4$ **[19-22]**, which includes the decomposition temperature and mass loss (%).

$PdCo(C_m)_4$	**Step**	**Decomposition temperature range / °C**	**mass loss / %**
$PdCo(C_6)_4$, [19]	1	126.37 - 223.51	35
	2	223.51 – 324.32	25
	3	324.32 – 362.77	12
$PdCo(C_8)_4$, [20]	1	126.66 – 226.80	37
	2	226.80 – 349.84	37
$PdCo(C_{10})_4$, [21]	1	130.26 – 226.28	37
	2	226.28 – 358.99	37
$PdCo(C_{12})_4$, [22]	1	118.35 – 244.73	48
	2	244.73 – 363.00	32

The analysis of the gaseous products from pyrolytic decomposition for **[19-22]** are tabulated **Table 3.29**, showed that numerous mass fragments was released. These include oxygenated species such as water, carbon dioxide and carbon monoxide in addition to hydrocarbon fragments.

Table 3.29: Mass charge ratio and gaseous compounds detected while using mass spectroscopy coupled with TGA of $PdCo(C_m)_4$, **[19-22]**.

m/z	**$PdCo(C_6)_4$, [19]**	**$PdCo(C_8)_4$, [20]**	**$PdCo(C_{10})_4$, [21]**	**$PdCo(C_{12})_4$, [22]**
2	-	H_2	H_2	H_2
14	-	-	CH_2	CH_2
16	-	-	CH_4	CH_4
17	OH	OH	OH	OH
18	H_2O	H_2O	H_2O	H_2O
28	CO, C_2H_2	CO, C_2H_2	CO, C_2H_2	CO, C_2H_2
29	-	-	-	C_2H_5
30	-	-	-	C_2H_6, CH_2O
32	O_2, CH_2OH	O_2, CH_2OH	O_2, CH_2OH	O_2, CH_2OH
38	C_3H_2	C_3H_2	C_3H_2	C_3H_2
40	C_3H_4	C_3H_4	C_3H_4	C_3H_4
44	CO_2	CO_2	CO_2	CO_2

3.5.9. Thermal analysis of $[Pd^{II}Cd^{II}(\mu\text{-}OOC(CH_2)_8CH_3)_4]\cdot H_2O$, [34]

The thermal analysis of $PdCd(C_{10})_4$, **[34]**, will be discussed. Focusing on solid state transitions and polymorphism of $PdCd(C_{10})_4$, **[34]**, as well as the decomposition thereof.

3.5.9.1. Differential scanning calorimetry, (DSC)

Figure 3.44 depicts the DSC thermogram of the heating and cooling cycles for $PdCd(C_{10})_4$, **[34]**, at a heating rate of 10 °C min^{-1} under an inert nitrogen atmosphere. **Table 3.30** summarises the DSC data for $PdCd(C_{10})_4$, **[34]**.

Cycle 1 reveals six thermal events, four for the heating segment and two thermal events for the cooling segment. During the cooling of the sample a crystallisation peak **C2(1)** (15.80 °C, 10700 J mol^{-1}) is observed followed by a second exothermic peak **C1(1)** (-15.41 °C, 2200 J mol^{-1}), which may be interpreted as reordering of the crystal structure to form a low temperature polymorph. In the heating segment of cycle 1, peak **H1(1)** (-7.16 °C, -3400 J mol^{-1}) is the melting of the unstable low temperature polymorph, which immediately crystallises into the stable high temperature polymorph at peak **H2(1)** (1.89 °C, 3300 J mol^{-1}). Peak **H3(1)** (15.20 °C, -3600 J mol^{-1}) is the melting of this stable high temperature polymorph, followed by **H4(1)** (29.89 °C, -200 J mol^{-1}) which is assigned to a solid state transition of the long aliphatic chains, of the carboxylatido ligands, settling into different conformations. Peak **M5(1)** (51.32 °C, -16100 J mol^{-1}) is the melting of the highest temperature polymorph of the sample.

In cycle 2, eight thermal events are observed including the partial decomposition of the complex at **D6(2)** (166.04 °C, 40000 J mol^{-1}). During the second heating segment, **H1(2)** (-7.00 °C, -4500 J mol^{-1}) and **H2(2)** (1.89 °C, 4200 J mol^{-1}) is again assigned to the melting of the unstable polymorph and the immediate crystallisation to the stable polymorph respectively. Peak **H3(2)** (15.20 °C, -2600 J mol^{-1}) is the melting of the stable polymorph, **H4(2)** (30.38 °C, -700 J.mol^{-1}) is a solid state transition and **M5(2)** (51.31 °C, -15900 J mol^{-1}) is the melting of this polymorph. Peak **D6(2)** represents decomposition of **[34]**. In the cooling segment of cycle 2 the crystallisation peak **C2(2)** (57.10 °C, 50000 J mol^{-1}) is assigned as the crystallisation of the decomposed products generated at peak **D6(2)**. Peak **C1(2)** (3.09 °C, 6500 J mol^{-1}) is also related to the decomposed products of **[34]**.

Cycle 3 has only two thermal events both are in the heating segment, **H1(3)** (18.52 °C, -5500 J mol^{-1}) and **M2(3)** (87.52 °C, -49900 J mol^{-1}) followed by destructive decomposition.

Evidence of this is found in the cooling segment of cycle 3, which has no cooling thermal events. Both **H1(3)** and **M2(3)** are related to the decomposed products of **[34]**.

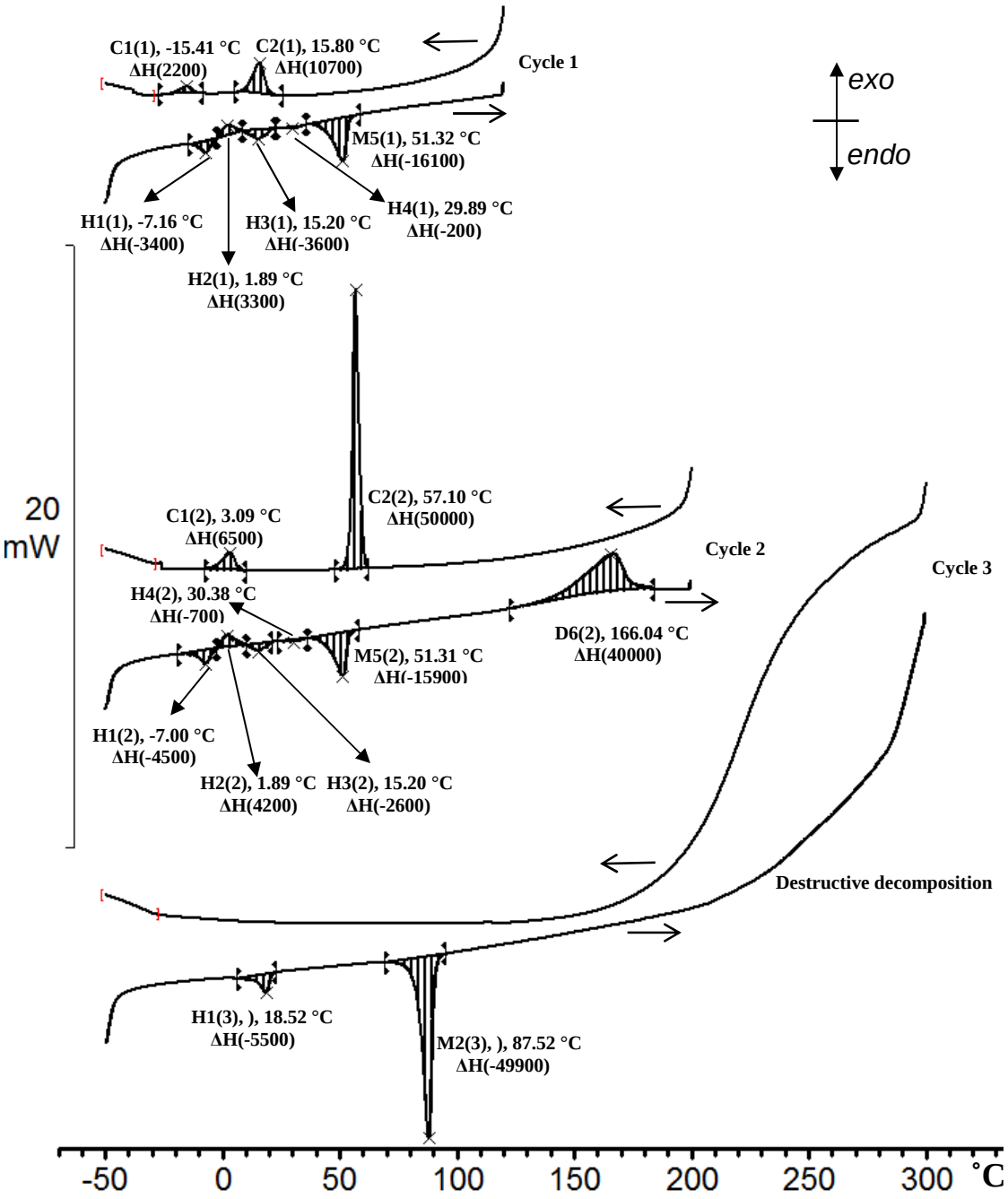

Figure 3.44: DSC of $PdCd(C_{10})_4$, **[34]**, with a scan speed of 10 °C min^{-1} under an inert atmosphere of nitrogen. The arrow pointing left indicates the cooling segment while the arrow pointing to the right indicates the heating segment. **H** and **C** denote heating and cooling respectively, while **M** is associated with melting. The number in brackets is the cycle number while the middle number is the peak number. For example **H2(1)** would indicate the second peak in the heating segment of cycle 1. The temperatures (°C) are peak temperatures and the energies are enthalpies (ΔH) in J mol^{-1}.

Table 3.30: DSC data of $PdCd(C_{10})_4$, **[34]**, which includes the peak, temperature (°C) and enthalpy change (J mol^{-1}) of each thermal event.

Peak	Temperature °C	ΔH J mol^{-1}	Peak	Temperature °C	ΔH J mol^{-1}	Peak	Temperature °C	ΔH J mol^{-1}
Cycle 1			**Cycle 2**			**Cycle 3**		
C1(1)	-15.41	2200	**C1(2)**	3.09	6500	**H1(3)**	18.52	-5500
C2(1)	15.80	10700	**C2(2)**	57.10	50000	**M2(3)**	87.52	-49900
H1(1)	-7.16	-3400	**H1(2)**	-7.00	-4500	-	-	-
H2(1)	1.89	3300	**H2(2)**	1.89	4200	-	-	-
H3(1)	15.20	-3600	**H3(2)**	15.20	-2600	-	-	-
H4(1)	29.89	-200	**H4(2)**	30.38	-700	-	-	-
M5(1)	51.32	-16100	**M5(2)**	51.31	-15900	-	-	-
-	-	-	**D6(2)**	166.04	40000	-	-	-

3.5.9.2. Variable temperature polarised light microscopy

Figure 3.45 shows some of the images obtained during the heating and cooling of $PdCd(C_{10})_4$, **[34]**. The series of pictures in the top row shows how $PdCd(C_{10})_4$, **[34]**, melts from a solid (17 ºC) to an isotropic liquid (88 ºC). The series of images at the bottom row shows super cooling, and that even at temperatures of -21.00 ºC, crystallisation has not yet set in, in the light beam of the microscope

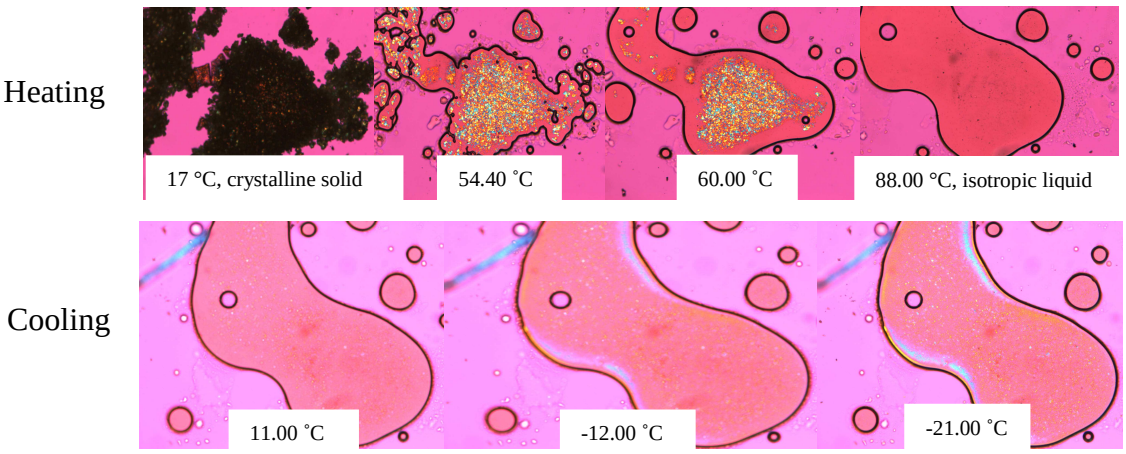

Figure 3.45: Polarised light microscope pictures of $PdCd(C_{10})_4$ **[34]** obtained while heating the sample at a rate of 10 °C min^{-1} under an open atmosphere. Top: heating of the sample from 17 °C to 88 °C and Bottom: cooling from 11.00 °C to -21.00 °C. No crystallisation was observed even at -21.00 °C while in the light beam of the microscope.

3.5.9.3. Thermal gravimetric analysis, (TGA)

The TGA curve for $PdCd(C_{10})_4$, **[34]**, obtained under an inert atmosphere of argon, and is shown in **Figure 3.46.** The decomposition of the **[34]** proceeds through five major steps, the first of which corresponds to loss of crystal water. A mass loss of 1.66 % is recorded for the dehydration step of **[34]** which is slightly less than the theoretical mass loss of 2.03 %. The total measured mass loss (including the water loss) is 69.18 %. The theoretical mass loss value to form the decomposition products PdO and CdO is 72.68 %. The calculated mass loss value correspond fairly well with the total experimental mass loss of 69.18 %, and it could thus be assumed that during the thermal decomposition of $PdCd(C_{10})_4$, **[34]**, PdO and CdO is formed, as non-volatile products.

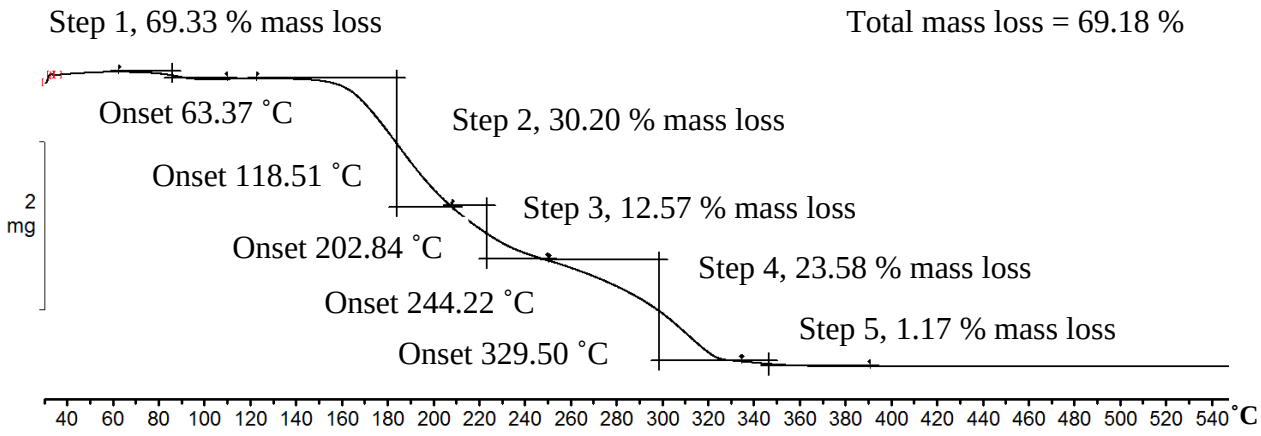

Figure 3.46: TGA of $PdCd(C_{10})_4$, **[34]**, obtained by using a scan rate of 10 °C min^{-1} under an inert argon atmosphere.

3.5.10. Thermal analysis of $[Pd^{II}Zn^{II}(\mu\text{-}OOC(CH_2)_8CH_3)_4]$, [36]

The thermal analysis of $PdZn(C_{10})_4$, **[36]**, will be discussed. Focusing on solid state transitions, the mesophase behaviour of $PdZn(C_{10})_4$, **[36]**, and also the decomposition of **[36]**.

3.5.10.1. Differential scanning calorimetry, (DSC)

Figure 3.47 represents the thermogram for heating and cooling of $PdZn(C_{10})_4$, **[36]**, at a heating rate of 10 °C min^{-1} under an inert atmosphere of nitrogen. **Table 3.31** summarises the DSC data for $PdZn(C_{10})_4$, **[36]**. The DSC study of **[36]**, is consistent with smectic liquid crystalline mesophase behaviour.[14] Cycle 1, has six thermal events, peak **H1(1)** (33.89 ˚C, -1300 J mol^{-1}) is assigned to a solid state transition and **H2(1)** (81.67 ˚C, -60200 J mol^{-1}) is the conversion of the crystalline solid into the smectic liquid crystalline mesophase and peak **M3(1)** (103.47 ˚C, -240 J mol^{-1}) is the melting of the smectic liquid crystalline mesophase into an isotropic liquid. Peak **C3(1)** (98.09 ˚C, 25 J mol^{-1}) is the exothermic conversion of the isotropic liquid into the smectic liquid crystalline mesophase, with **C2(1)** (59.88 ˚C, 67400 J mol^{-1}) being the crystallisation of the liquid crystalline mesophase into a crystalline solid. Peak **C1(1)** (11.38 ˚C, 2600 J mol^{-1}) is consistent with reordering of the long aliphatic chains into lower temperature conformations for the crystal. Peak **C2(1)** differs from **H2(1)** by 21.79 ˚C, this is due to super-cooling. Cycle 2, has seven thermal events, peak **H1(2)** (9.40 ˚C, -400 J mol^{-1}) and **H2(2)** (26.57 ˚C, -900 J mol^{-1}) are solid state transitions. Peak **H3(2)** (81.14 ˚C, -59700 J mol^{-1}) is the endothermic conversion of the crystalline solid into the smectic liquid crystalline mesophase. The peak **M4(2)** (106.61 ˚C, -60 J mol^{-1}) is the melting of the smectic liquid crystalline mesophase into an isotropic liquid. Peak **C3(2)** (98.08 ˚C, 44 J mol^{-1}) is the exothermic conversion of the isotropic liquid into the smectic liquid crystalline mesophase, with **C2(2)** (57.87 ˚C, 66100 J mol^{-1}) being the crystallisation of the liquid crystalline mesophase into a crystalline solid. Peak **C1(2)** (12.06 ˚C, 2500 J mol^{-1}) is consistent with reordering of the long aliphatic chains into lower temperature conformations for **[36]**. Cycle 3 has seven thermal events, peak **H1(3)** (9.06 ˚C, -400 J mol^{-1}) and **H2(3)** (26.73 ˚C, -1200 J mol^{-1}) are the same solid transitions as was observed in cycle 2 and **M3(3)** (80.97 ˚C, -60600 J mol^{-1}) is the melting of the crystallised complex. Peak **D4(3)** (178.91 ˚C, 34800 J mol^{-1}) represents the first decomposition stage of the complex. In the cooling segment, the crystallization peak **C3(3)** (93.46 ˚C, 52000 J mol^{-1}) is at a temperature higher than that of the crystallisation peaks observed for cycles 1 and 2. This implies that a new compound was generated at peak **D4(3)** and **C3(3)** represents the crystallisation of this compound. Peaks **C2(3)** (19.55 ˚C, 20600 J mol^{-1}) and **C1(3)** (5.22 ˚C, 2100 J mol^{-1}) is attributed to solid state transformations of the decomposed products. Cycle 4, has four thermal

events, however no significance is given to any of these peaks in terms of the original complex, **[36]**.

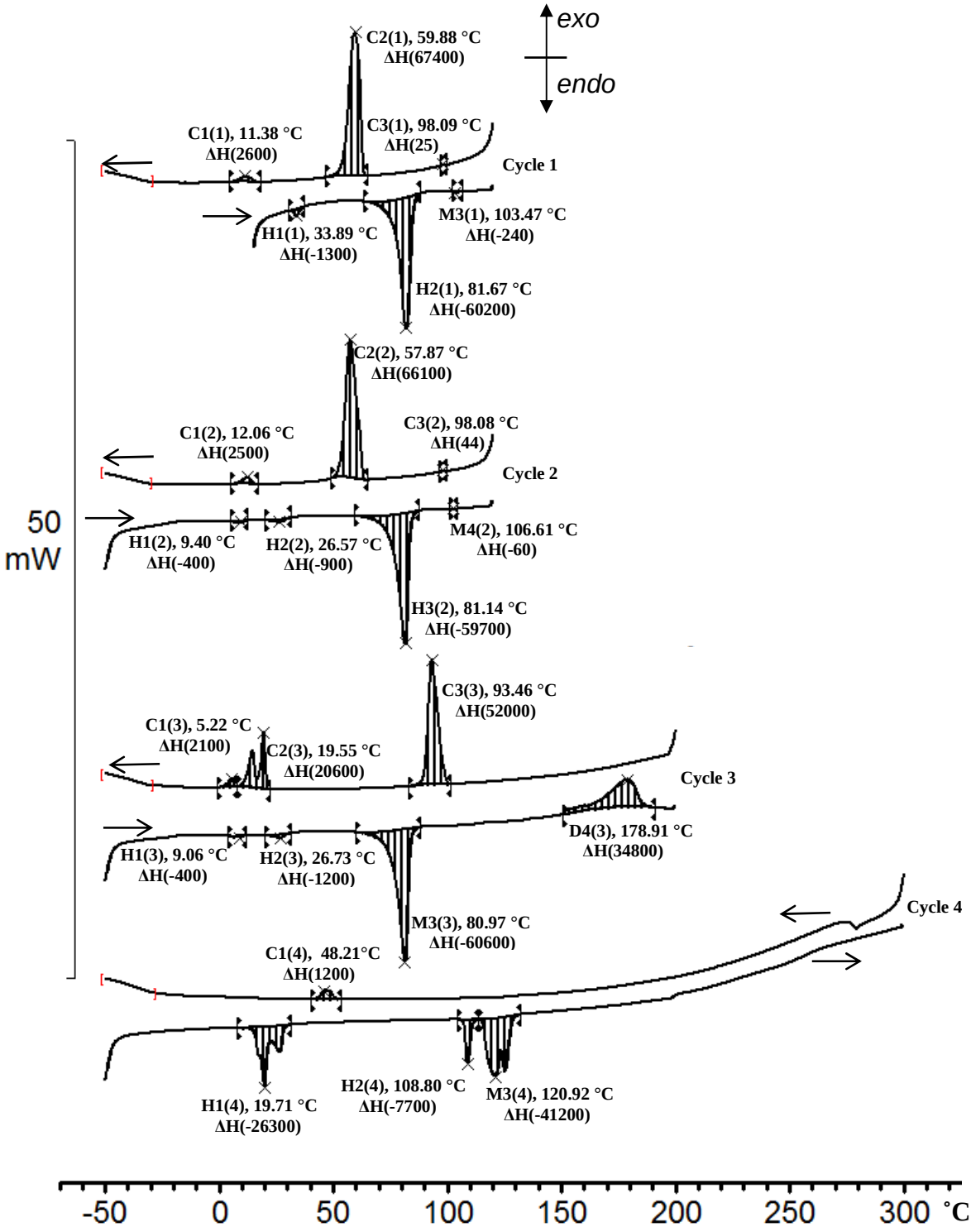

Figure 3.47: DSC of $PdZn(C_{10})_4$, **[36]**, with a scan speed of 10 °C min^{-1} under an inert atmosphere of nitrogen. The arrow pointing left indicates the cooling segment while the arrow pointing to the right indicates the heating segment. **H** and **C** denote heating and cooling respectively, while **M** is associated with melting. The number in brackets is the cycle number while the middle number is the peak number. For example **H2(1)** would indicate the second peak in the heating segment of cycle 1. The temperatures (°C) are peak temperatures and the energies are enthalpies (ΔH) in J mol^{-1}.

Table 3.31: DSC data of $PdZn(C_{10})_4$ **[36]**, which includes the temperature (˚C) and enthalpy change (J mol^{-1}) of each thermal event.

Peak	**Temperature °C**	**ΔH J mol^{-1}**	**Peak**	**Temperature °C**	**ΔH J mol^{-1}**
Cycle 1			**Cycle 2**		
C1(1)	11.38	2600	**C1(2)**	12.06	2500
C2(1)	59.88	67400	**C2(2)**	57.87	66100
C3(1)	98.09	25	**C3(2)**	98.08	44
H1(1)	33.89	-1300	**H1(2)**	9.40	-400
H2(1)	81.67	-60200	**H2(2)**	26.57	-900
M3(1)	103.47	-240	**H3(2)**	81.14	-59700
-	-	-	**M4(2)**	106.61	-60
Cycle 3			**Cycle 4**		
C1(3)	5.22	2100	**C1(4)**	48.21	1200
C2(3)	19.55	20600	**H1(4)**	19.71	-26300
C3(3)	93.46	52000	**H2(4)**	108.80	-7700
H1(3)	9.06	-400	**M3(4)**	120.92	-41200
H2(3)	26.73	-1200	-	-	-
M3(3)	80.97	-60600	-	-	-
D4(3)	178.91	34800	-	-	-

3.5.10.2. Variable Temperature Polarised Light Microscopy

Figure 3.48 shows some of the images obtained during the heating and cooling of $PdZn(C_{10})_4$, **[36]**, in atmospheric conditions. The heating series (top row) indicates the formation of the smectic liquid crystalline mesophase as observed in the DSC study. The cooling segment indicates the starting of the conversion of the isotropic liquid, 69 °C, to smectic liquid crystalline mesophase, 61 °C, to crystallisation, 55 °C, of $PdZn(C_{10})_4$, **[36]**.

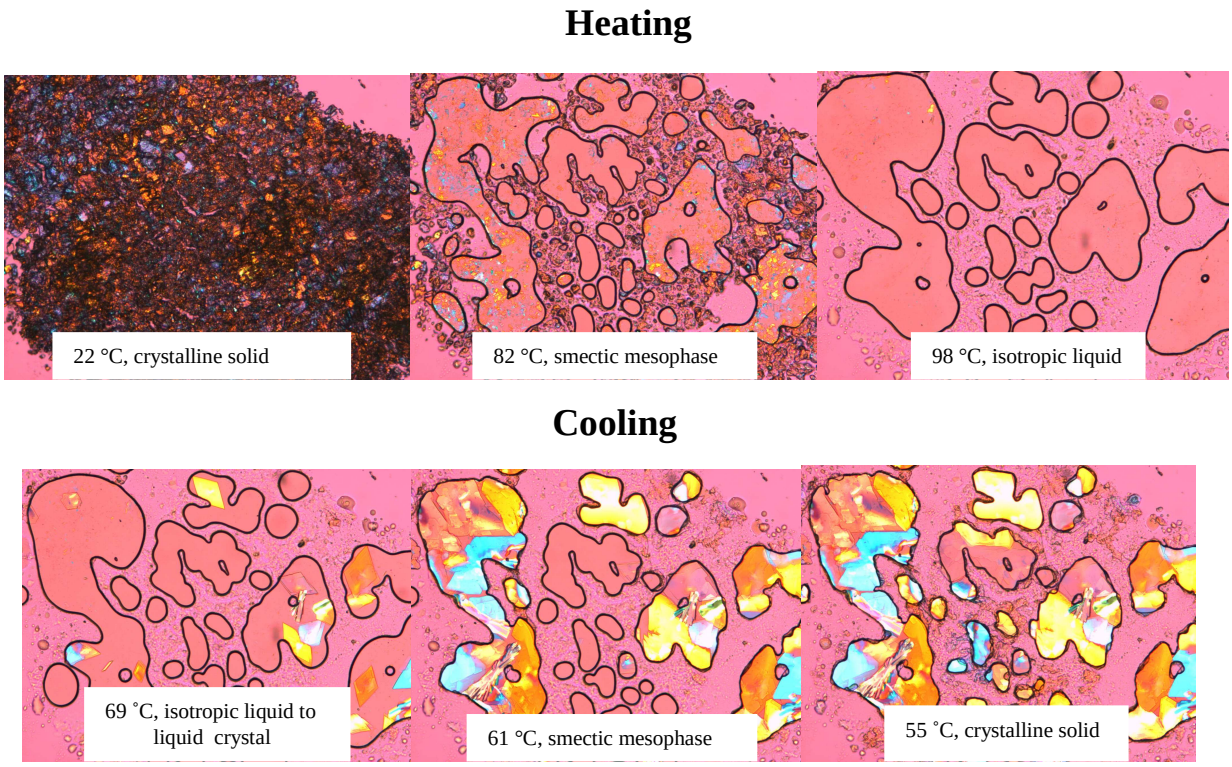

Figure 3.48: Polarised light microscope pictures of $PdZn(C_{10})_4$, **[36]**, with a heating rate of 10 °C.min^{-1} under atmospheric conditions. Top: heating of the sample from 22.00 °C to 98.00 °C and Bottom: cooling from 69.00 °C to 55.00 °C.

3.5.10.3. Thermal Gravimetric Analysis, (TGA)

Figure 3.49 depicts the decomposition of $PdZn(C_{10})_4$, **[36]**, under an atmosphere of argon utilising a heating rate of 10 ˚C min^{-1}. The decomposition proceeds via four main steps, consisting of two larger mass loss steps (37.13 and 20.40 %) and two smaller mass loss steps (4.58 and 13.00 %). The total measured mass loss is 75.11 %, which correspond well with the theoretical mass loss of 74.51 % if the decomposition products that formed are PdO_2 and ZnO.

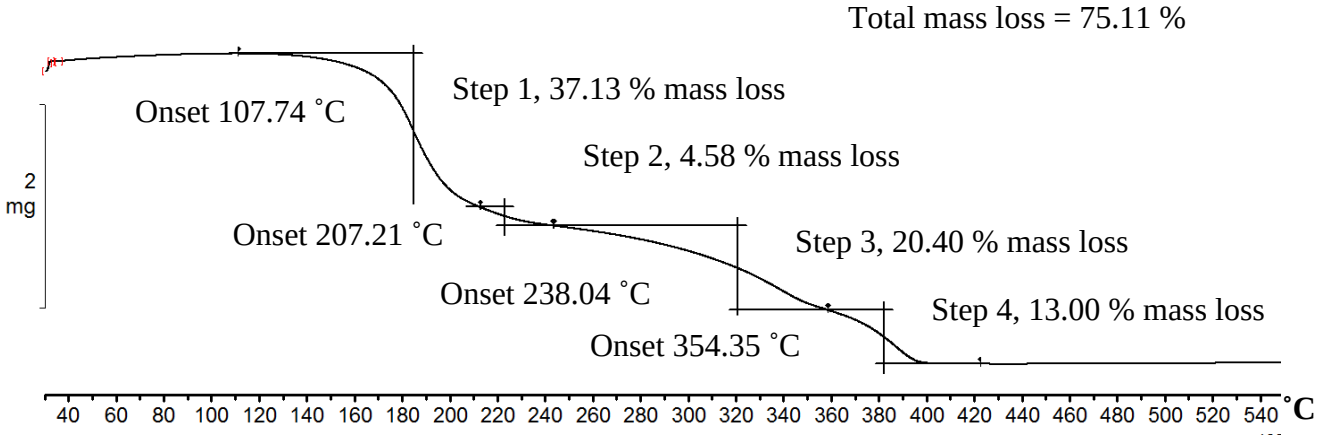

Figure 3.49: TGA of $PdZn(C_{10})_4$, **[36]**, utilising a scan rate of 10 °C min^{-1} under argon.

3.5.11. Thermal analysis of $[Pd^{II}Mn^{II}(\mu\text{-}OOC(CH_2)_8CH_3)_4]$, [39]

The thermal analysis of $PdMn(C_{10})_4$, **[39]**, will be discussed. Focusing on solid state transitions, polymorphism and also the decomposition thereof.

3.5.11.1. Differential scanning calorimetry, (DSC)

Figure 3.50 depicts the DSC thermogram for the heating and cooling of $PdMn(C_{10})_4$, **[39]**, utilising a heating rate of 10 °C min^{-1} under a nitrogen atmosphere. **Table 3.32** summarises the DSC data for $PdMn(C_{10})_4$, **[39]**.

Cycle 1, has four thermal events, two in the cooling segment and two in the heating segment. **H1(1)** (37.38 °C, -46500 J mol^{-1}) can be interpreted as a solid state transition while **M2(1)** (62.95 °C, -18100 J mol^{-1}) is the melting of the sample. In the cooling segment of cycle 1, **C2(1)** (9.90 °C, 31100 J mol^{-1}) represents crystallisation of the isotropic liquid. The difference between **M2(1)** and **C2(1)** is 53.05 °C, this is an indication of super-cooling. The second cooling peak **C1(1)** (-9.95 °C, 18900 J mol^{-1}) in cycle 1, can be interpreted as reordering of the long aliphatic chains of the complex, most probably into unstable polymorphs.

Cycle 2 has ten thermal events, two in the cooling segment and eight in the heating segment. However, the major transitions correspond to those absent in cycle 1. From the heating segment, it is evident that three low temperature polymorphs exist due to solid state transitions. Peaks **H1(2)** (-8.68 ˚C, -1600 J mol^{-1}) and **H2(2)** (2.00 ˚C, 500 J mol^{-1}) is considered to the first polymorph. Peaks **H3(2)** (10.99 ˚C, -1900 J mol^{-1}) and **H4(2)** (19.21 ˚C, 5000 J mol^{-1}) is considered to be the second polymorph. Peak **H5(2)** (30.76 ˚C, -43400 J mol^{-1}) is assigned to be the partial melting of the second polymorph, which also includes most of **[39]**. Peak **H6(2)** (59.47 ˚C, -8000 J mol^{-1}) is the melting of the last polymorph, while **H7(2)** (66.19 ˚C, 2500 J mol^{-1}) is the crystallisation of this polymorph. Peak **M8(2)** (77.67 ˚C, -2400 J mol^{-1}) is assigned to be the final melting of **[39]**. In the cooling segment of cycle 2, two thermal events are observed **C1(2)** (-10.10 ˚C, 20600 J.mol^{-1}) and **C2(2)** (8.67 ˚C, 30600 J mol^{-1}). Peak **C2(2)** is the crystallisation of the isotropic liquid and **C1(2)** is a solid state transition of the complex. The crystallisation peak **C2(2)** is observed at a much lower temperature than that of the melting peak, this is attributed to super-cooling. Cycle 3 has many, possibly eleven identifiable thermal events, ten in the heating segment and one in the cooling segment. In cycle 3 the creation of polymorphs is again evident from the heating segment with partial melting at peak **H5(3)** (30.75 ˚C, -77900 J mol^{-1}), this peak however has two shoulders to the left and to the right of the peak. These thermal events can be attributed to the partial melting of the polymorph created earlier in the heating segment. **D10(3)** (170.22 ˚C, 11900 J mol^{-1}) represents the partial decomposition of

the complex. During the cooling segment of cycle 3 one peak is observed which is attributed to the crystallisation of a mixture of isotropic liquids (including the partial decomposition products). It is not regarded as a representative, meaningful thermal event related to **[39]**. Cycle 4, **H1(4)** (31.59 ˚C, -17800 J mol^{-1}) is the melting of the residual portion of the remaining **[39]** after decomposition. Peaks **H2(4)** (60.60 ˚C, -7600 J mol^{-1}), **H3(4)** (68.32 ˚C, 2000 J mol^{-1}) and **M4(4)** (80.89 ˚C, -14200 J mol^{-1}) is identifiable as polymorphism and melting respectively even after partial decomposition occurred. No cooling thermal event is observed as the complex was completely decomposed at *ca.* 225 °C.

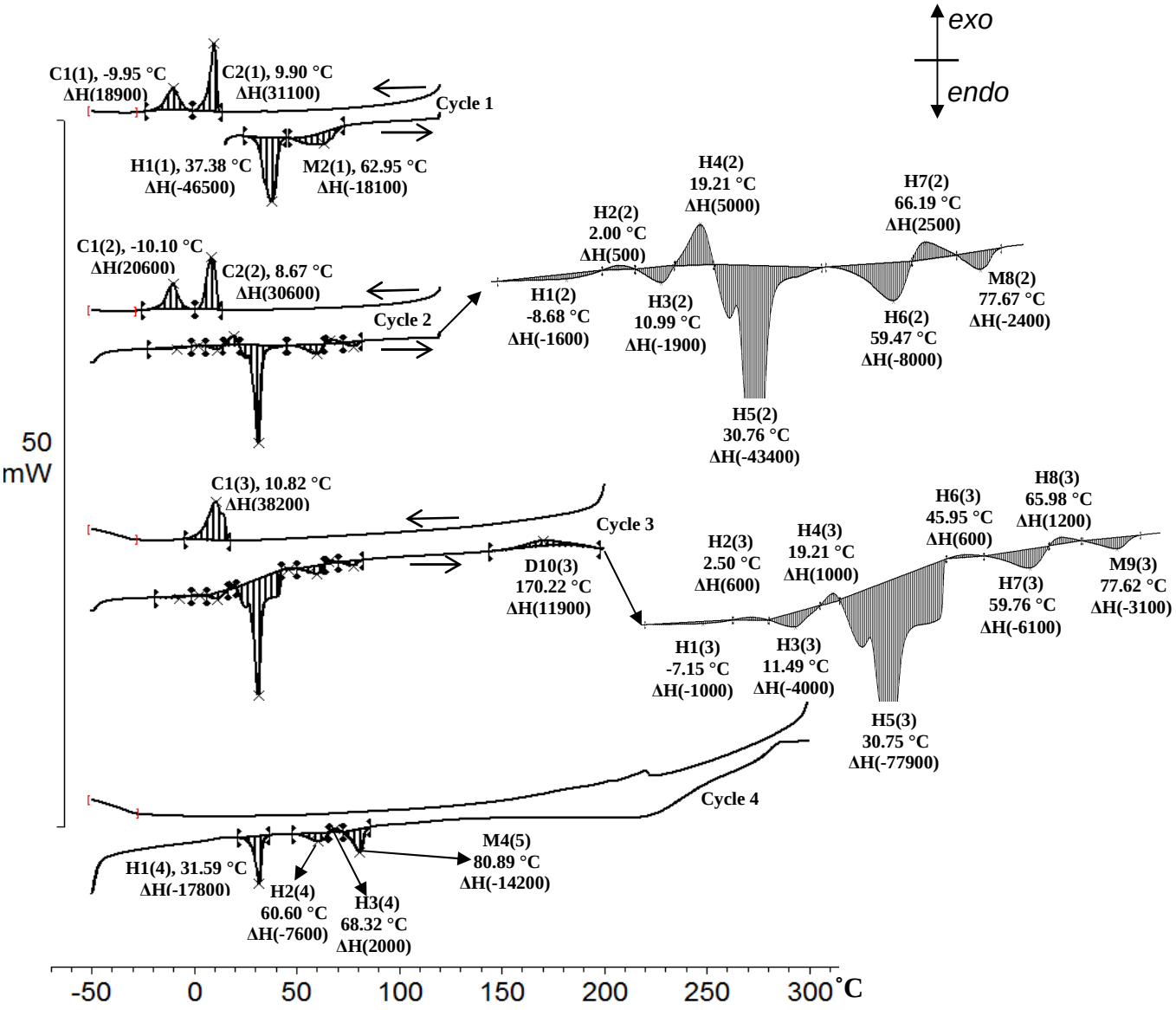

Figure 3.50: DSC of $PdMn(C_{10})_4$, **[39]**, with a scan speed of 10 °C min^{-1} under an inert atmosphere of nitrogen. The arrow pointing left indicates the cooling segment while the arrow pointing to the right indicates the heating segment. **H** and **C** denote heating and cooling respectively, while **M** is associated with melting. The number in brackets is the cycle number while the middle number is the peak number. For example **H6(3)** would indicate the sixth peak in the heating segment of cycle 3. The temperatures (°C) are peak temperatures and the energies are enthalpies (ΔH) in J mol^{-1}.

Table 3.32: DSC data of $PdMn(C_{10})_4$, **[39]**, which includes the temperature (˚C) and enthalpy change (J mol^{-1}) of each thermal event.

Peak	**Temperature °C**	**ΔH J mol^{-1}**	**Peak**	**Temperature °C**	**ΔH J mol^{-1}**
Cycle 1			**Cycle 2**		
C1(1)	-9.95	18900	**C1(2)**	-10.10	20600
C2(1)	9.90	31100	**C2(2)**	8.67	30600
H1(1)	37.38	-46500	**H1(2)**	-8.68	-1600
M2(1)	62.95	-18100	**H2(2)**	2.00	500
-	-	-	**H3(2)**	10.99	-1900
-	-	-	**H4(2)**	19.21	5000
-	-	-	**H5(2)**	30.76	-43400
-	-	-	**H6(2)**	59.47	-8000
-	-	-	**H7(2)**	66.19	2500
-	-	-	**M8(2)**	77.67	-2400
Cycle 3			**Cycle 4**		
C1(3)	10.82	38200	**H1(4)**	31.59	-17800
H1(3)	-7.51	-1000	**H2(4)**	60.60	-7600
H2(3)	2.50	600	**H3(4)**	68.32	2000
H3(3)	11.49	-4000	**M4(4)**	80.89	-14200
H4(3)	19.21	1036	-	-	-
H5(3)	30.75	-77900	-	-	-
H6(3)	45.95	600	-	-	-
H7(3)	59.76	-6100	-	-	-
H8(3)	65.98	1200	-	-	-
M9(3)	77.62	-3100	-	-	-
D10(3)	170.22	11900	-	-	-

3.5.11.2. Variable Temperature Polarised Light Microscopy

Figure 3.51 shows the heating and cooling of $PdMn(C_{10})_4$, **[39]**, the heating segment, cycle 1, illustrates the melting of the crystalline solid at 80 ˚C. The cooling segment, cycle 1, indicates the initial stages of crystallisation at 35 ˚C, of the isotropic liquid to the crystalline solid at 20 ˚C. The heating segment, cycle 2, confirms the polymorphism, observed in the DSC study, see **Figure 3.50**.

The image labelled 50 °C, confirms the partial melting of $PdMn(C_{10})_4$, **[39]**, at peak **H6(2)**. The images labelled 61 °C, 73 °C and 75 °C, confirms the peaks **H7(2)** (cold crystallisation) and **M8(2)** (melting to the isotropic liquid) see **Figure 3.50**.

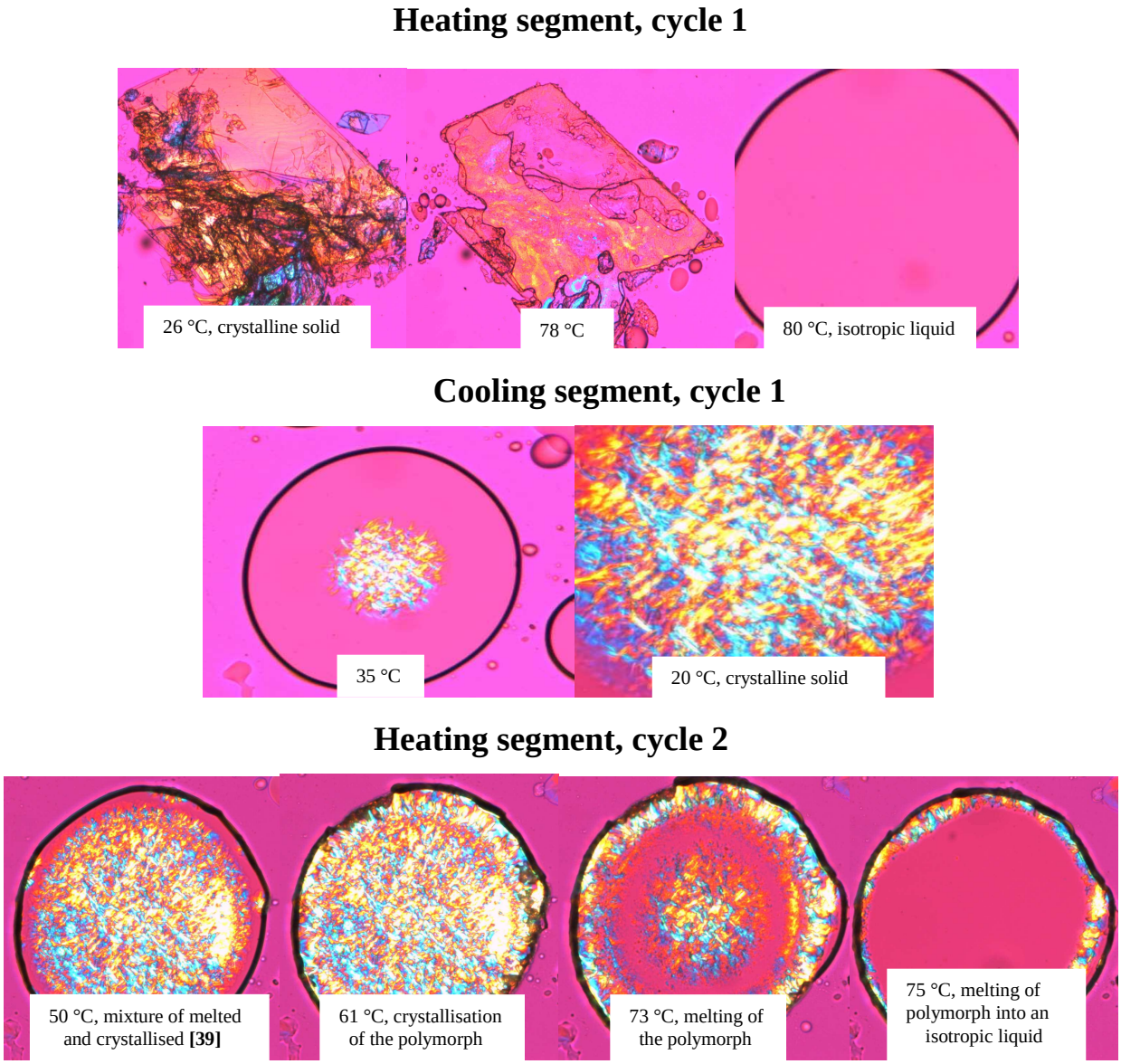

Figure 3.51: Polarised light microscope pictures of $PdMn(C_{10})_4$, **[39]**, with a heating rate of 10 °C min^{-1} under atmospheric conditions. The heating cycle 1, is the heating of the sample from 26 °C to 80 °C and cooling cycle 1, is the cooling from 35 °C to 20 °C. The heating segment cycle 2, confirms the polymorphism observed in the DSC study.

3.5.11.3. Thermal Gravimetric Analysis $Pd^{II}Mn^{II}(\mu\text{-}OOC(CH_2)_8CH_3)_4]$, [39]

Figure 3.52 shows the TGA thermogram of $PdMn(C_{10})_4$, **[39]**. Mass loss occurs in four steps. The total measured mass loss is 67.14 % which corresponds well with PdO and Mn_2O_3 as final decomposition products. Theoretically a mass loss of 66.88 %, would result exclusively in PdO and Mn_2O_3. The first step is the largest mass loss (38.17 %) while the other three are small mass losses of 9.06, 17.96 and 1.95 %, respectively.

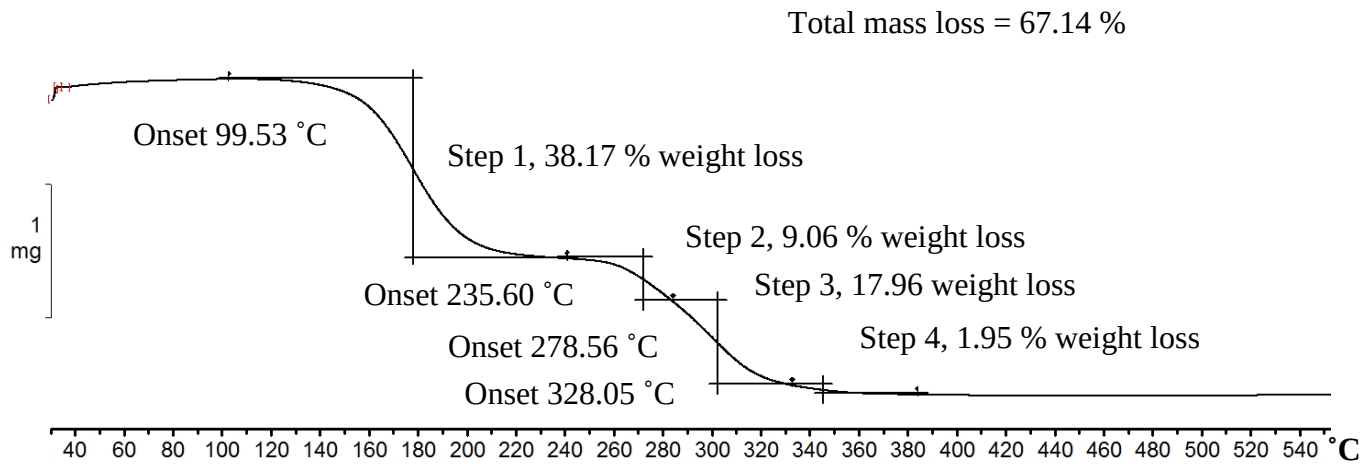

Figure 3.52: TGA of $PdMn(C_{10})_4$, **[39]**, utilising a scan rate of 10 °C min^{-1} under a argon atmosphere.

3.5.12. Thermal analysis of $[Pd^{II}Cu^{II}(\mu\text{-}OOC(CH_2)_8CH_3)_4]$, [40]

The thermal analysis of $PdCu(C_{10})_4$, **[40]**, will be discussed. Focusing on solid state transitions, polymorphism and also the decomposition of **[40]**.

3.5.12.1. Differential scanning calorimetry, (DSC)

Figure 3.53 represents the DSC thermogram for the heating and cooling of $PdCu(C_{10})_4$, **[40]**, utilising a heating rate of 10 °C min^{-1} under an inert nitrogen atmosphere. **Table 3.33** summarises the DSC data for $PdCu(C_{10})_4$, **[40]**.

Cycle 1 has two thermal events, one in the heating segment and one in the cooling segment. **M1(1)** (76.60 °C, -59300 J mol^{-1}) is the melting peak of **[40]** and shows a small shoulder to the right of the peak, peak **C1(1)** (45.62 °C, 27800 J mol^{-1}) is the crystallisation peak of the isotropic liquid to the crystalline solid state. The crystallisation peak is at a much lower temperature than the melting peak which indicates super-cooling.

Cycle 2, has five thermal vents. Peaks **H1(2)** (-25.47 °C, -1500 J mol^{-1}) and **H2(2)** (-7.43 °C, 2100 J mol^{-1}) indicating melting and crystallisation of a low temperature polymorph respectively. This thermal event is followed by a solid state reordering of the crystal prior to melting at peak **H3(2)** (12.39 °C, -6300 J mol^{-1}). During cycle 2, the melting peak **M4(2)** (93.42 ˚C, -25100 J mol^{-1}) is nearly half of **M1(1)**. This indicates less material was available for melting, but it is not necessarily due to decomposition. More likely it is due to the bulkiness of the original sample and large gas pockets between the original powdered particles. This view is supported when one observes that peak **M4(2)** of cycle 2 and peak **M4(3)** of cycle 3 exhibits almost the same energy absorption. The crystallisation of the isotropic liquid is observed at peak **C1(2)** (43.78 °C, 28200 J mol^{-1}).

Cycle 3 has six thermal events, with **H1(3)** (-25.46 °C, -2300 J mol^{-1}) and **H2(3)** (-5.60 °C, 4500 J mol^{-1}) indicating melting and crystallisation of a low temperature polymorph respectively. This event is followed by a solid state reordering of the crystal prior to melting **M4(3)** (93.41 °C, -25500 J mol^{-1}) indicated by **H3(3)** (12.38 °C, -4400 J mol^{-1}). The cooling segment of cycle 3 has two cooling events peak **C2(3)** (38.79 °C, 18600 J mol^{-1}) represents the crystallisation from the isotropic liquid to a crystalline solid and **C1(3)** (6.19 °C, 19100 J mol^{-1}) is an exothermic solid state transition.

Cycle 4 shows two thermal events in the heating segment at peak **H1(4)** (17.66 °C, -17900 J mol^{-1}) and **M2(4)** (94.40 °C, -9700 J mol^{-1}) followed by destructive decomposition of the complex

above 205 °C. No thermal event in the cooling segment is observed implying the complex was completely destroyed in the heating segment of cycle 4.

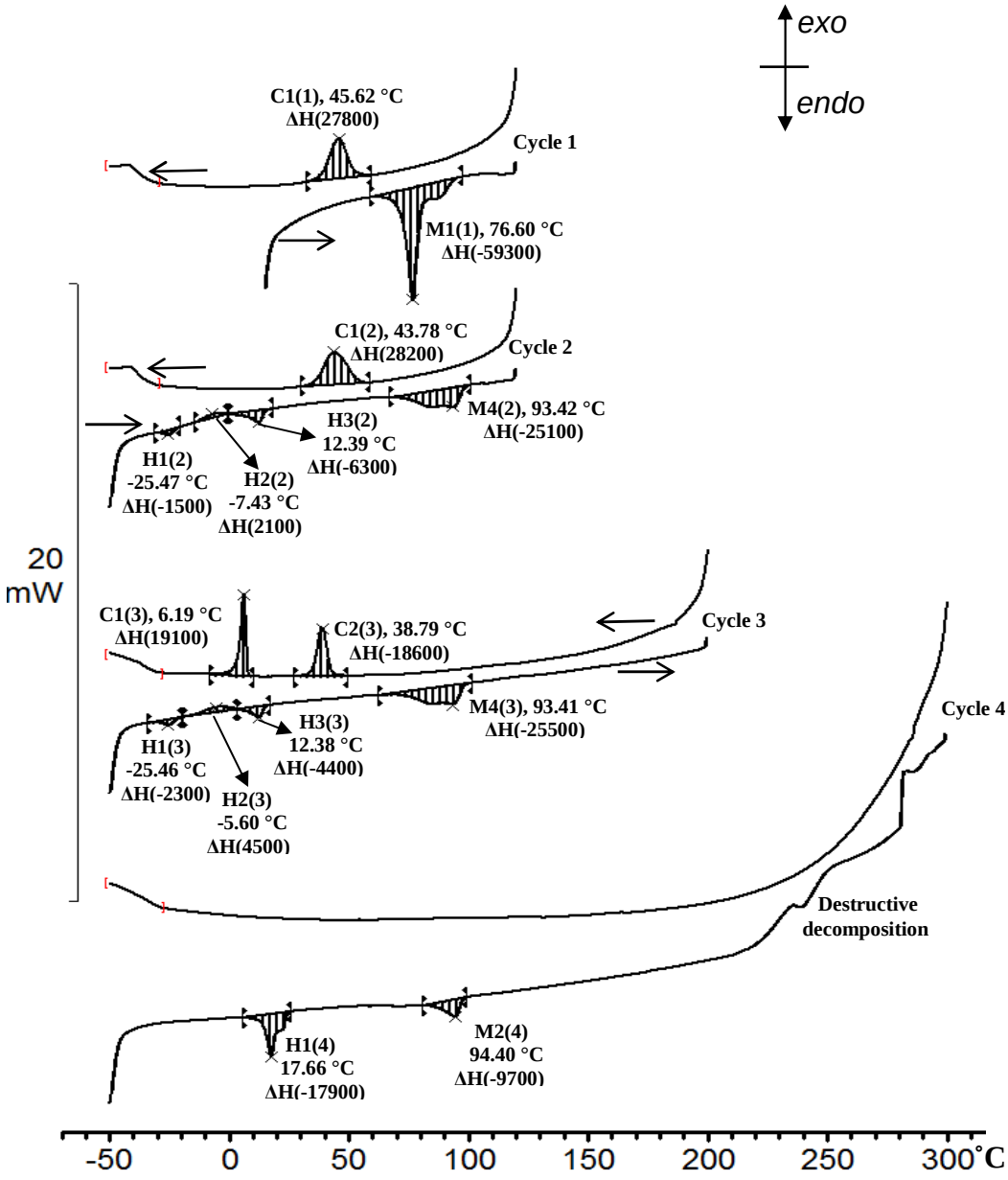

Figure 3.53: DSC of $PdCu(C_{10})_4$, **[40]**, utilising a scan speed of 10 °C min^{-1} under an inert atmosphere of nitrogen. The arrow pointing left indicates the cooling segment while the arrow pointing to the right indicates the heating segment. **H** and **C** denote heating and cooling respectively, while **M** is associated with melting. The number in brackets is the cycle number while the middle number is the peak number. For example **H2(3)** would indicate the second peak in the heating segment of cycle 3. The temperatures (°C) are peak temperatures and the energies are enthalpies (ΔH) in J mol^{-1}.

Table 3.33: DSC data of $PdCu(C_{10})_4$, **[40]**, which includes the temperature (˚C) and enthalpy change (J mol^{-1}) of each thermal event.

Peak	Temperature °C	ΔH J mol^{-1}	Peak	Temperature °C	ΔH J mol^{-1}
Cycle 1			**Cycle 2**		
C1(1)	45.62	27800	**C1(2)**	43.78	28200
M1(1)	76.60	-59300	**H1(2)**	-25.47	-1500
-	-	-	**H2(2)**	-7.43	2100
-	-	-	**H3(2)**	12.39	-6300
-	-	-	**M4(2)**	93.42	-25100
Cycle 3			**Cycle 4**		
C1(3)	6.19	19100	**H1(4)**	17.66	-17900
C2(3)	38.79	18600	**M2(4)**	94.40	-9700
H1(3)	-25.46	-2300	-	-	-
H2(3)	-5.60	4500	-	-	-
H3(3)	12.38	-4400	-	-	-
M4(3)	93.41	-25500	-	-	-

3.5.12.2. Variable Temperature Polarised Light Microscopy

Figure 3.54 showes the images of the heating and cooling of $PdCu(C_{10})_4$, **[40]**. The series at the top shows how $PdCu(C_{10})_4$, **[40]**, melts from a solid (21.00 ºC) to an isotropic liquid (98.00 ºC). The series of images at the bottom shows the cooling from an isotropic liquid to crystallisation at 61.00 ºC.

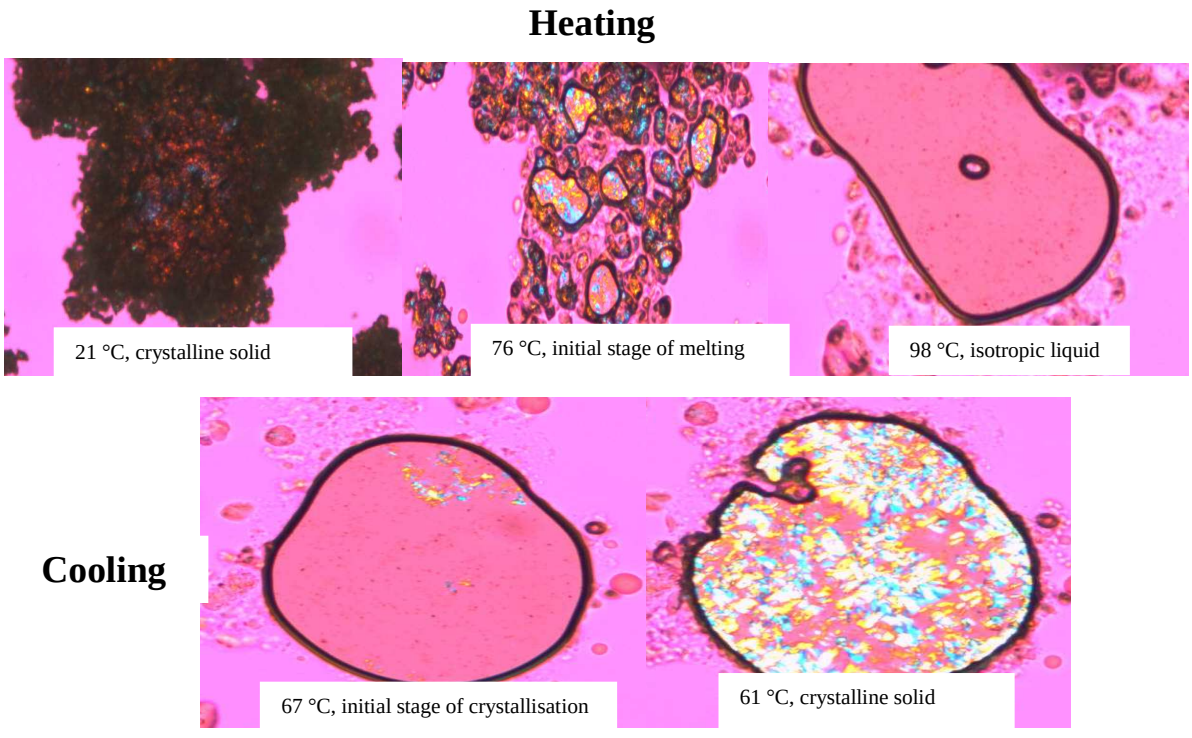

Figure 3.54: Polarised light microscope pictures of $PdCu(C_{10})_4$ **[40]** obtained by using a heating rate of 10 °C min^{-1} under open atmospheric conditions. Top: heating of the sample from 21 °C to 98 °C and Bottom: cooling from 67 °C to 61 °C.

3.5.12.3. Thermal Gravimetric Analysis

The TGA curve for $PdCu(C_{10})_4$, **[40]**, obtained under an argon atmosphere, is shown in **Figure 3.55.** The decomposition of **[40]** proceeds in one global pyrolytic process comprising of many overlapping steps. The total measured mass loss is 77.24 % and correlates well with the theoretical mass loss of 76.35% if only PdO and CuO are formed.

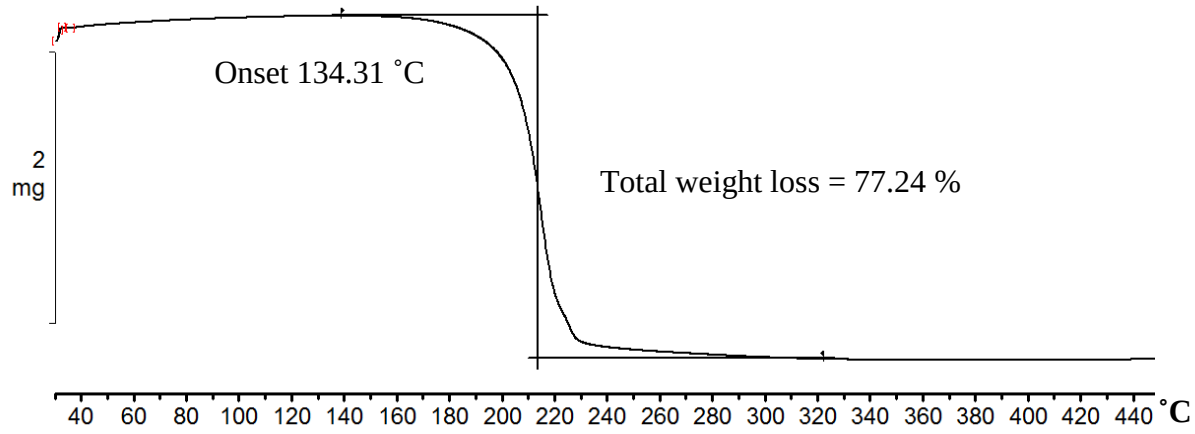

Figure 3.55: TGA of $PdCu(C_{10})_4$, **[40]**, with a scan rate of 10 °C min^{-1} under an argon atmosphere.

3.6. Electrochemistry

The oxidation and/or reduction potentials of all the redox active metal centres of the following selected synthesised mono- and mixed-metal carboxylatido complexes were explored **[1-4]**, **[19-22]**, **[23]**, **[29]**, **[30], [32]**, **[34]**, **[36]**, **[39]**, **[41]** and **[42]**. An attempt was then made to quantify the electronic influences of the different metals and chain lengths of the carboxylatido ligands on the oxidation and/or reduction potential of the redox active metal centres of these compounds.

3.6.1. Cyclic voltammetry of circular tripalladium hexa-carboxylatido complexes $Pd_3(C_6)_6$ [1], $Pd_3(C_8)_6$ [2], $Pd_3(C_{10})_6$ [3], $Pd_3(C_{12})_6$ [4] and $Pd_3(C_2)_6$ [42]

The cyclic voltammetry of all the circular tripalladium hexacarboxylatido complexes of **[1-4]** and **[42]** are shown in **Figure 3.56**. The CV data are summarised in **Table 3.34**.

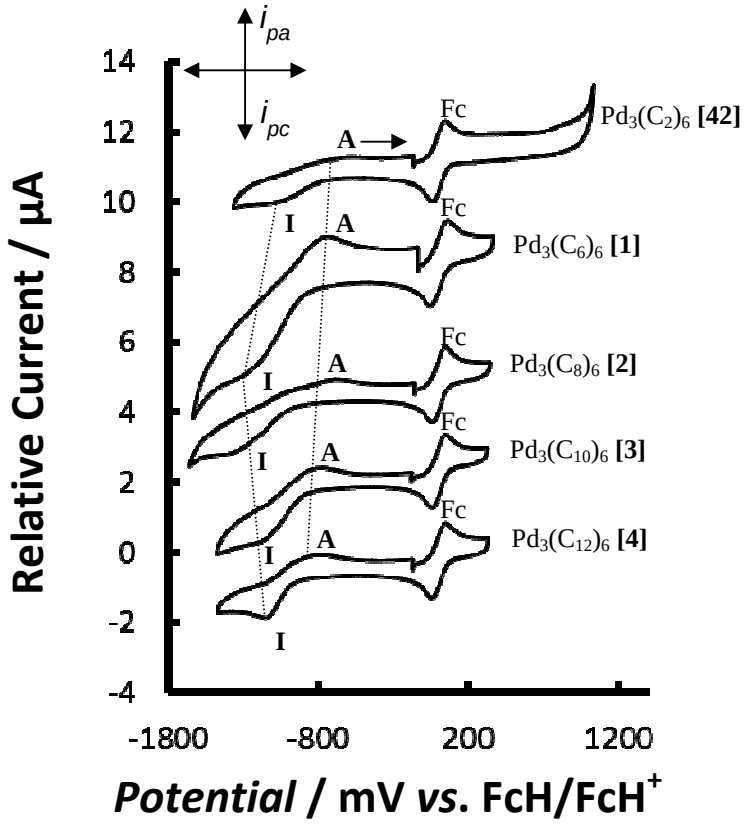

Figure 3.56: Comparative cyclic voltammograms of a 0.5 mmol dm^{-3} solution of **[1-4]** and **[42]** in DCM. With 0.1 mol dm^{-3} $[NBu_4][PF_6]$ as supporting electrolyte and using a glassy carbon working electrode at 25 ºC. Scan rate of 100 mV s^{-1} with ferrocene as internal standard. The oxidation wave is labelled as **A** and the reduction wave is labelled as **I**. Scan direction is indicated.

Cyclic voltammograms of **[1-4]** and **[42]** are shown in **Figure 3.56** with a scan rate of 100 mV s^{-1} of a 0.5 mmol dm^{-3} solution, at 25 ºC in DCM. With ferrocene as internal standard and 0.1 mol dm^{-3} supporting electrolyte, $[NBu_4][PF_6]$. Two redox processes are observed in the CV's of **Figure 3.56**, is associated with the redox centres of **[1-4]** and **[42]**, together with the internal standard FcH/FcH^+ couple. These are the cathodic waves labelled **I** at $-1.384 \leq E_{pc} \leq -1.063$ mV and the anodic wave labelled **A** at $-824 \leq E_{pa} \leq -578$ mV. Waves **I** and **A** are not associated with the carboxylatido reduction, these occur at far negative potentials (outside the solvent window of DCM). This leaves only the Pd(II) centre as the redox active species in **[1-4]** and **[42]**.[15] This leads us to assign **wave I** as the reduction of $Pd^{II} \rightarrow Pd^0$ and **wave A** as the oxidation of $Pd^0 \rightarrow Pd^{II}$. In all cases the redox process is chemically irreversible because $i_{pc}/i_{pa} < 0.48$ and electrochemically irreversible because $\Delta E_p = E_{pa} - E_{pc} > 327$ mV, for electrochemical reversibility the difference in peak potential has to be $59 \text{ mV} \leq \Delta E_p \leq 95$ mV.

The length of the aliphatic chain of the carboxylatido ligand clearly has an influence on the position of the oxidation and reduction peaks, see **Figure 3.56** and **Figure 3.57**. The general trend that was observed is that, as the chain length increases the oxidation potential, E_{pa}, goes to more negative values. This implies that a longer chain length makes oxidation of the palladium metal centre increasingly difficult. The reduction potential, E_{pc}, is more complex, and the correlation graph between the chain length and E_{pc}, is V-shaped. Up to a chain length of eight carbons the reduction potential of the palladium metal centre goes to more negative values and for ten and twelve carbon atom chain lengths, the reduction potential shifts to less negative values. Therefore **[42]**, **[1]** and **[2]** becomes increasingly difficult to be reduced, while **[3]** and **[4]** becomes easier to be reduced see **Figure 3.57**.

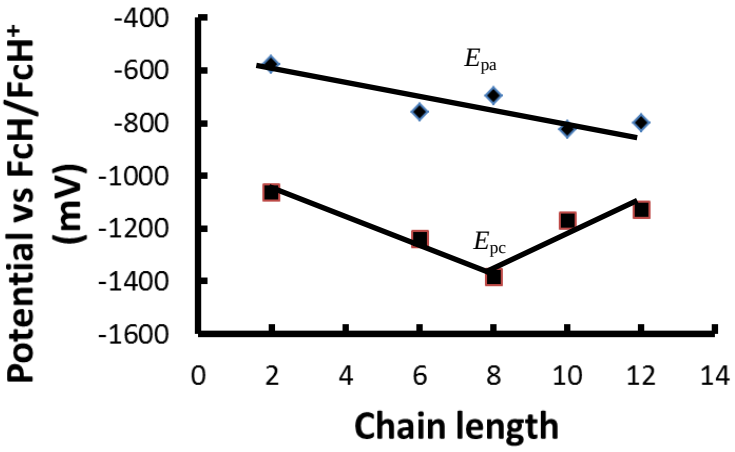

Figure 3.57: Correlation graph for the chain length of **[1-4]** and **[42]** against the oxidation and reduction potentials.

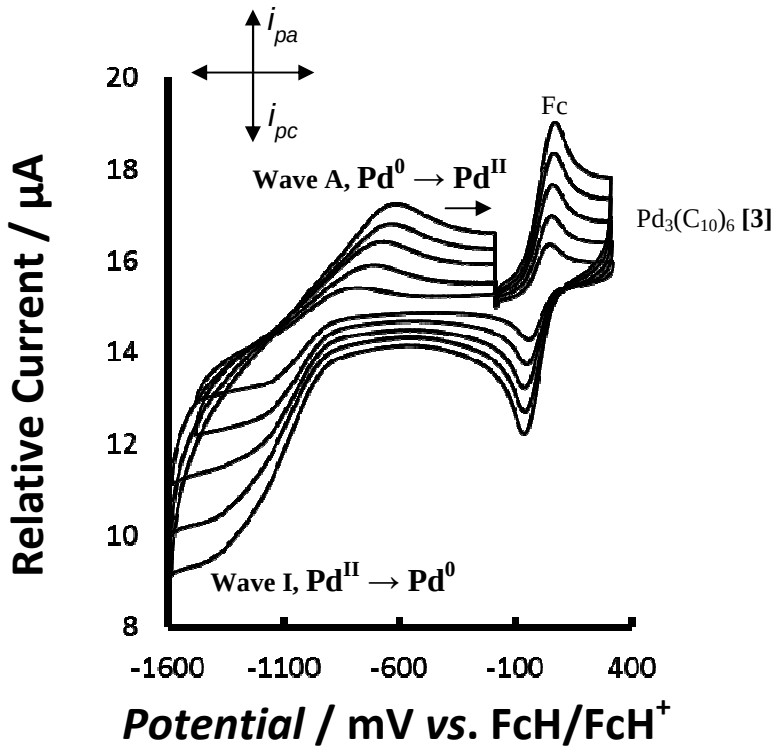

Figure 3.58: The cyclic voltammograms of a 0.5 mmol dm^{-3} solution of $Pd_3(C_{10})_6$, **[3]**, in DCM. With 0.1 mol dm^{-3} $[NBu_4][PF_6]$ as supporting electrolyte using a glassy carbon working electrode at 25ºC. Scan rates of 100, 200, 300, 400 and 500 mV s^{-1} with ferrocene as internal standard. The oxidation wave is labelled as **A** and the reduction wave is labelled as **I** and the scan direction is indicated.

It can be observed that varying the scan rate does not provide any extra information about the reduction and oxidation of palladium, see **Figure 3.58**.

[15] C. Amatore, E. Carré, A. Jutand and M. A. M' Barki, *Organometallics*, 1995, **14**, 1818

Table 3.34: CV data of the circular tripalladium hexacarboxylatido complexes **[1-4]** and **[42]** with scan rates of 100, 200, 300, 400 and 500 mV s^{-1}.

$Pd_3(C_6)_6$, [1]	**E_{pc} (mV), Wave I**	**E_{pa} (mV), Wave A**	**ΔE_p**	**$E^{0'}$(mV)**	**i_{pc} (µA)**	**i_{pa} (µA)**	**i_{pc}/i_{pa}**
100	-1241	-760	481	-1000	0.71	1.67	0.43
200	-1349	-726	623	-1038	0.68	2.24	0.30
300	-1423	-700	723	-1061	0.89	2.50	0.35
400	-1474	-666	807	-1070	0.83	2.71	0.31
500	-1513	-639	874	-1076	0.83	3.13	0.27
$Pd_3(C_8)_6$, [2]	**E_{pc} (mV), Wave I**	**E_{pa} (mV), Wave A**	**ΔE_p**	**$E^{0'}$(mV)**	**i_{pc} (µA)**	**i_{pa} (µA)**	**i_{pc}/i_{pa}**
100	-1384	-698	686	-1041	5	18.5	0.27
200	-1407	-632	775	-1020	6	26.8	0.22
300	-1466	-606	849	-1031	7.2	31	0.23
400	-1488	-582	906	-1035	6.2	35	0.18
500	-1531	-558	973	-1044	8.5	36	0.24
$Pd_3(C_{10})_6$, [3]	**E_{pc} (mV), Wave I**	**E_{pa} (mV), Wave A**	**ΔE_p**	**$E^{0'}$(mV)**	**i_{pc} (µA)**	**i_{pa} (µA)**	**i_{pc}/i_{pa}**
100	-1172	-824	348	-998	0.43	1.01	0.43
200	-1228	-759	469	-994	0.43	1.38	0.31
300	-1265	-711	554	-988	0.57	1.35	0.42
400	-1355	-661	694	-1008	0.57	2.33	0.24
500	-1431	-646	784	-1038	0.58	2.71	0.21
$Pd_3(C_{12})_6$, [4]	**E_{pc} (mV), Wave I**	**E_{pa} (mV), Wave A**	**ΔE_p**	**$E^{0'}$(mV)**	**i_{pc} (µA)**	**i_{pa} (µA)**	**i_{pc}/i_{pa}**
100	-1128	-801	327	-964	0.21	0.87	0.24
200	-1148	-739	409	-943	0.25	1.15	0.22
300	-1161	-711	450	-936	0.23	1.30	0.18
400	-1171	-689	482	-930	0.25	1.42	0.18
500	-1178	-668	512	-922	0.29	1.5	0.19
$Pd_3(C_2)_6$, [42]	**E_{pc} (mV), Wave I**	**E_{pa} (mV), Wave A**	**ΔE_p**	**$E^{0'}$(mV)**	**i_{pc} (µA)**	**i_{pa} (µA)**	**i_{pc}/i_{pa}**
100	-1063	-578	484	-820	0.22	0.45	0.48
200	-1107	-503	604	-805	0.17	0.41	0.41
300	-1149	-470	679	-809	0.16	0.77	0.21
400	-1234	-430	804	-832	0.21	0.8	0.27
500	-1296	-388	908	-842	0.19	0.95	0.20

3.6.2. Cyclic voltammetry of mixed-metal palladium cobalt paddlewheel complexes

The cyclic voltammetry of all the mixed-metal palladium cobalt paddlewheel carboxylatido complexes **[19-22]** and **[29]** are shown in **Figure 3.59** and the corresponding data are shown in **Table 3.35**.

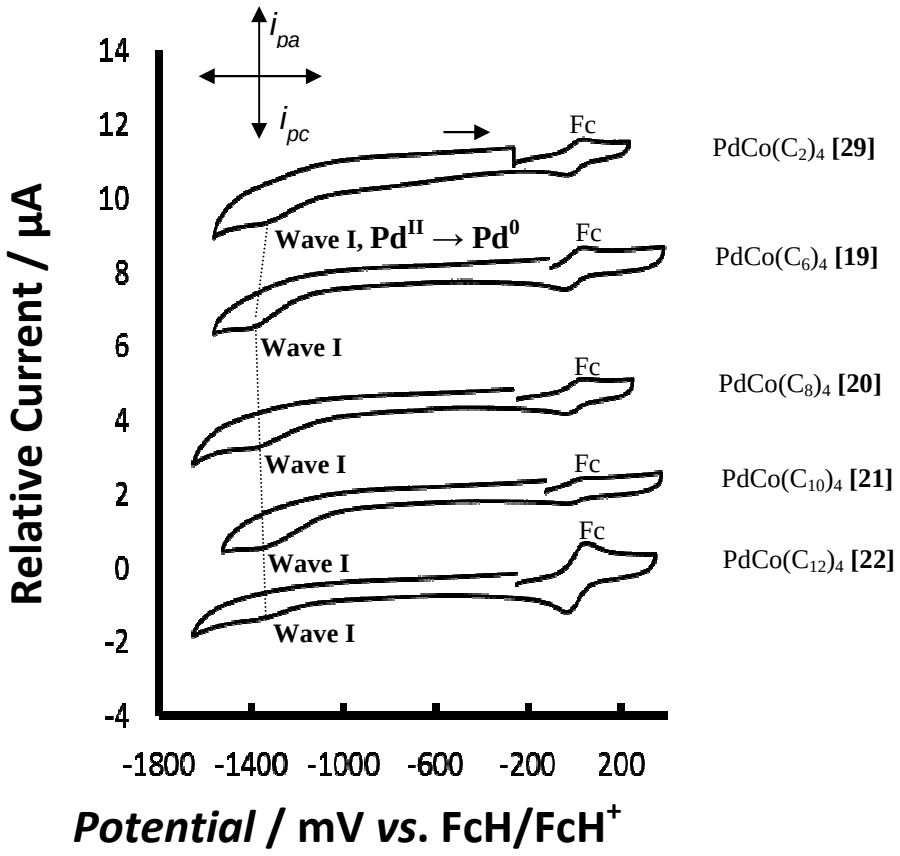

Figure 3.59: The comparative cyclic voltammograms of a 0.5 mmol dm^{-3} solution of **[19-22]** and **[29]** in DCM. With 0.1 mol dm^{-3} $[NBu_4][PF_6]$ as supporting electrolyte using a glassy carbon working electrode at 25 °C. Scan rate 100 mV s^{-1} with ferrocene as internal standard. The reduction wave is labelled as **I**. Scan direction is indicated.

In all the cyclic voltammograms of **[19-22]** and **[29]** only one reduction wave was observed labelled as **wave I**. No oxidation peak is observed implying the redox process is chemically and electrochemically irreversible. This reduction wave is assigned, in accordance with the data obtained from the palladium electrochemistry discussed in paragraph 3.6.1, to the $Pd^{II} \rightarrow Pd^0$ reduction process. Values for the reduction of $Pd^{II} \rightarrow Pd^0$, were found to be -1396 mV $\leq E_{pa} \leq$ -1329 mV.

No peaks could be identified for the oxidation and reduction of the cobalt.[16] In general, the reduction potential of the palladium in **[19-22]**, shifts to more negative values when it is complexed with cobalt, see **Table 3.34** and **Table 3.35** for comparison.

[16] P. Bhyrapa and V. Krishnan, *Inorganic Chemistry*, 1991, **30**, 239

The influence of the cobalt in $[Pd^{II}Co^{II}(\mu\text{-}OOC(CH_2)_{10}CH_3)_4]$ **[22]** on the oxidation potential of the palladium is evident from the shift to more negative values for the complexes, E_{pa} $[Pd_3(\mu\text{-}OOC(CH_2)_{10}CH_3)_6]$ = **-1128 mV** while, E_{pa} $[Pd^{II}Co^{II}(\mu\text{-}OOC(CH_2)_{10}CH_3)_4]$ = **-1338 mV**. The increased electron density on the palladium atom due to the cobalt atom shifts the reduction wave to more negative values. This shows that there is good electronic communication between the two metals through the carboxylatido ligands.

Also the presence of the cobalt within the complexes **[19-22]** decreases the electron density on the palladium atom. As the carbon chain length increases the reduction potentials shifts to less negative values making the palladium atom easier to be reduced see **Figure 3.61**. The cyclic voltammograms of $PdCo(C_{10})_4$, **[21]**, are shown in **Figure 3.60**, at scan rates of 100, 200, 300, 400 and 500 mV s^{-1}. No extra information could be obtained from these faster scan rates.

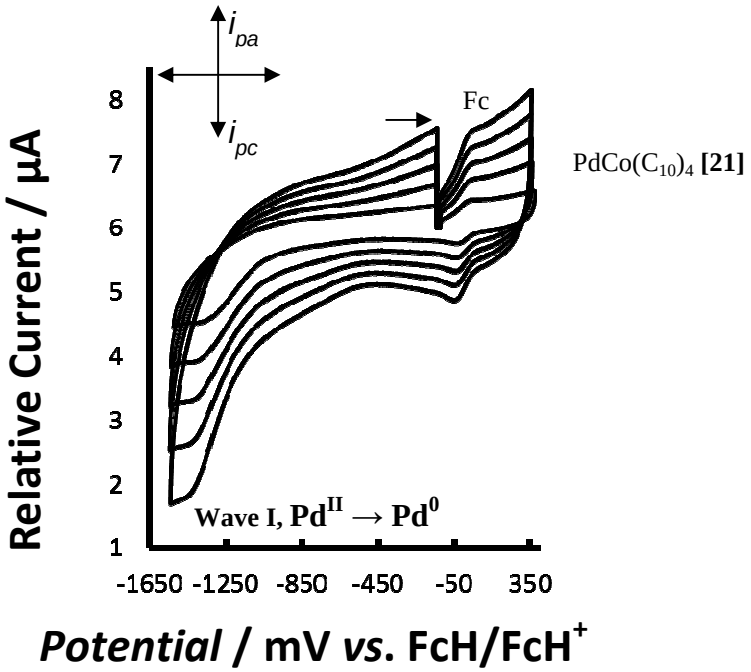

Figure 3.60: The cyclic voltammograms of a 0.5 mmol.dm^{-3} solution of $PdCo(C_{10})_4$, **[21]**, of in DCM. With 0.1 mol.dm^{-3} $[NBu_4][PF_6]$ as supporting electrolyte with a glassy carbon electrode at 25 ºC. Scan rates of 100, 200, 300, 400 and 500 mV s^{-1} with ferrocene as internal standard. The reduction wave is labelled as **I**. Scan direction is indicated.

The general trend is a decrease in the negative reduction potential of $Pd^{II} \rightarrow Pd^0$ as the aliphatic chain length of the carboxylatido ligand increases, see **Figure 3.62**.

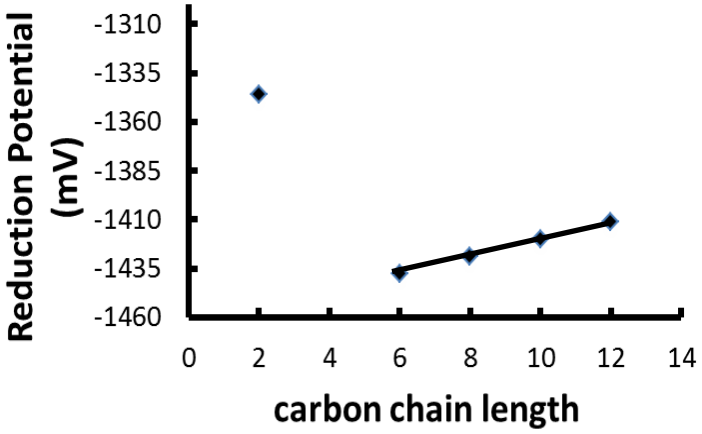

Figure 3.61: The correlation graph of the chain length of $[PdCo(\mu\text{-}OOC(CH_2)_nCH_3)_4]$ where n = 0, 4, 6, 8 and 10 against the reduction potentials of the palladium atom for the 500 mV s^{-1} scan rate.

Table 3.35: CV data of palladium cobalt mixed-metal paddlewheel carboxylatido complexes, **[19-22]** and **[29]** at scan rates of 100, 200, 300, 400, 500 mV s^{-1}.

$PdCo(C_6)_4$, [19]	**E_{pc} (mV), Wave I**	**i_{pc} (µA)**
100	-1396	0.63
200	-1408	0.82
300	-1418	1.00
400	-1430	1.16
500	-1438	1.28
$PdCo(C_8)_4$, [20]	**E_{pc} (mV), Wave I**	**i_{pc} (µA)**
100	-1376	0.43
200	-1383	0.45
300	-1403	0.52
400	-1421	0.66
500	-1429	0.73
$PdCo(C_{10})_4$, [21]	**E_{pc} (mV), Wave I**	**i_{pc} (µA)**
100	-1329	0.54
200	-1373	0.60
300	-1362	0.73
400	-1409	0.85
500	-1420	1.27
$PdCo(C_{12})_4$, [22]	**E_{pc} (mV), Wave I**	**i_{pc} (µA)**
100	-1338	0.24
200	-1354	0.29
300	-1381	0.33
400	-1392	0.36
500	-1411	0.49
$PdCo(C_2)_4$, [29]	**E_{pc} (mV), Wave I**	**i_{pc} (µA)**
100	-1323	0.31
200	-1329	0.76
300	-1344	0.33
400	-1353	1.20
500	-1346	1.58

3.6.3. Cyclic voltammetry of short-chain mixed-metal paddlewheel acetatido complexes

The cyclic voltammetry of the mixed-metal paddlewheel acetatido complexes $PdZn(C_2)_4$, **[23]**, $PdMn(C_2)_4$ **[30]** and $PdCe(C_2)_4^+$ **[32]**, will be discussed in this section. The CV data are summarised in **Table 3.36**.

3.6.3.1. Cyclic voltammetry of $[Pd^{II}Zn^{II}(\mu\text{-}OOCCH_3)_4]$, [23]

Cyclic voltammograms of $PdZn(C_2)_4$, **[23]**, are depicted in **Figure 3.62**. The complex was dissolved in DCM having a concentration of 0.5 mmol dm^{-3} at 25 ºC. Ferrocene was used as internal standard and 0.1 mol dm^{-3} supporting electrolyte, $[NBu_4][PF_6]$. Utilising a scan rate of 100, 200, 300, 400 and 500 mV s^{-1}.

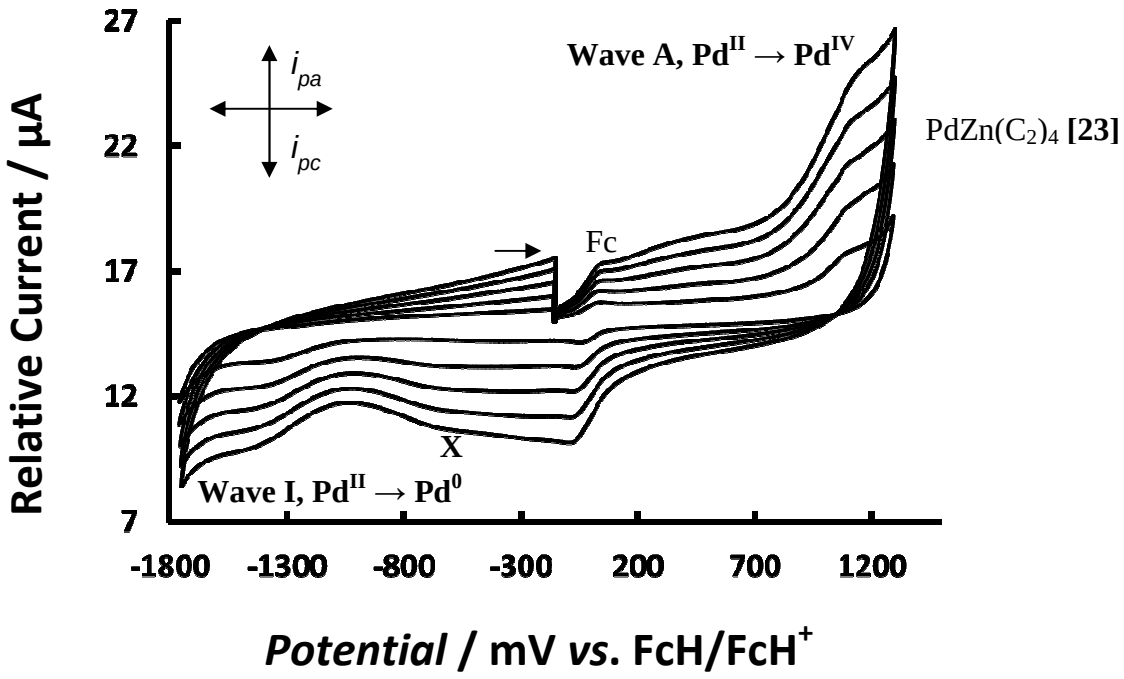

Figure 3.62: Comparative cyclic voltammograms of a 0.5 mmol dm^{-3} solution of $PdZn(C_2)_4$, **[23]**, in DCM. With 0.1 mol dm^{-3} $[NBu_4][PF_6]$ as supporting electrolyte and a glassy carbon working electrode at 25 ºC. Scan rate of 100, 200, 300, 400 and 500 mV s^{-1} and ferrocene as internal standard. The reduction wave is labelled as a bold roman numeral and the oxidation wave is labelled as a bold capital letter. Scan direction is indicated.

From **Figure 3.62**, it can be observed that $PdZn(C_2)_4$, **[23]**, has two redox waves, one oxidation wave labelled **A (1080 mV)**, and one reduction wave labelled **I (-1330 mV)**.

The oxidation **wave A** can only be the oxidation of $Pd^{II} \rightarrow Pd^{IV}$.[17] This is because, Zn(II) does not have any oxidation number higher than +2.[18] The reduction **wave I** can be assigned to $Pd^{II} \rightarrow Pd^{0}$ reduction. Following the $Pd^{II} \rightarrow Pd^{IV}$ oxidation at **wave A**, all the Pd(IV) species that was produced, diffuses away from the electrode. This only allows for $Pd^{II} \rightarrow Pd^{0}$ reduction at **wave I**. The redox process for $PdZn(C_2)_4$, **[23]**, is chemically and electrochemically irreversible. No reduction half waves was observed for **wave A** and no oxidation half waves was observed for **wave I**. The wave marked **X** is not a redox process, and was confirmed by Oster young square wave voltammetry.

3.6.3.2. Cyclic voltammetry of $[Pd^{II}Mn^{II}(\mu\text{-}OOCCH_3)_4]$, [30]

Cyclic voltammograms of $PdMn(C_2)_4$, **[30]**, are illustrated in **Figure 3.63**. The complex was dissolved in DCM having a concentration of 0.5 mmol dm^{-3} at 25 ºC. Ferrocene was used as internal standard and 0.1 mol dm^{-3} supporting electrolyte, $[NBu_4][PF_6]$. Utilising a scan rate of 100, 200, 300, 400 and 500 mV s^{-1}.

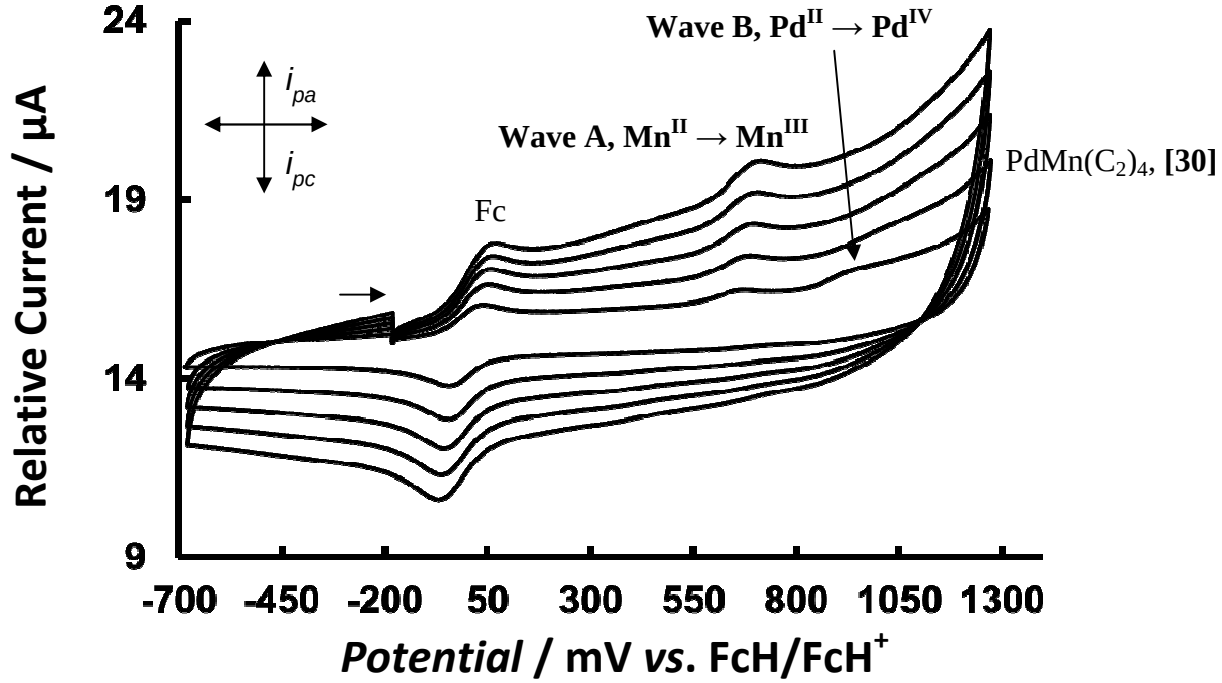

Figure 3.63: Comparative cyclic voltammograms of a 0.5 mmol.dm^{-3} solution of $PdMn(C_2)_4$, **[30]**, in DCM. With 0.1 mol dm^{-3} $[NBu_4][PF_6]$ as supporting electrolyte and a glassy carbon working electrode at 25 ºC. Scan rate 100, 200, 300, 400 and 500 mV s^{-1} with ferrocene as internal standard. The oxidation waves are labelled as bold capital letters. Scan direction is indicated.

---

[17] D. B. Nicholas, J. F. Kampf and M. S. Sanford, *J. Am. Chem. Soc.* 2010, **132**, 2878

[18] F.A. Cotton, G. Wilkinson and P.L. Gaus, *Basic Inorganic Chemistry*, John Wiley and sons, inc, 1995, 3rd, 494.

The complex, $PdMn(C_2)_4$, **[30]**, exhibits two oxidation waves **A** (**695 mV**) and **B** (**935 mV**). Conradie and Freitag[19] reported, $Mn^{II} \rightarrow Mn^{III}$ oxidation at a potential of **520 mV**, for the $Mn(CH_3COCHCOCF_3)_3$ complex. The redox process for $PdMn(C_2)_4$, **[30]**, is chemically and electrochemically irreversible, as no reduction half waves are observed for waves **A** and **B**. **Wave A** is assigned to the $Mn^{II} \rightarrow Mn^{III}$ oxidation, while **wave B** is assigned to the $Pd^{II} \rightarrow Pd^{IV}$ oxidation. Wave **B** (**935 mV**) is only clearly observed for the 100, 200 and 300 mV s^{-1} scan rate, see **Table 3.36**. No Pd^{II} reduction was observed at large negative potentials within the potential range that DCM as solvent allows.

3.6.3.3. Cyclic voltammetry of $[Pd^{II}Ce^{III}(\mu\text{-}OOCCH_3)_4]^+$, [32]

Cyclic voltammograms of $PdCe(C_2)_4{}^+$, **[32]**, are depicted in **Figure 3.64**. The complex was dissolved in DCM having a concentration of 0.5 mmol dm^{-3} at 25 ºC. Decamethyl ferrocene (Fc*) was used as internal standard and 0.1 mol dm^{-3} supporting electrolyte, $[NBu_4][PF_6]$. Utilising a scan rate of 100, 200, 300, 400 and 500 mV s^{-1}.

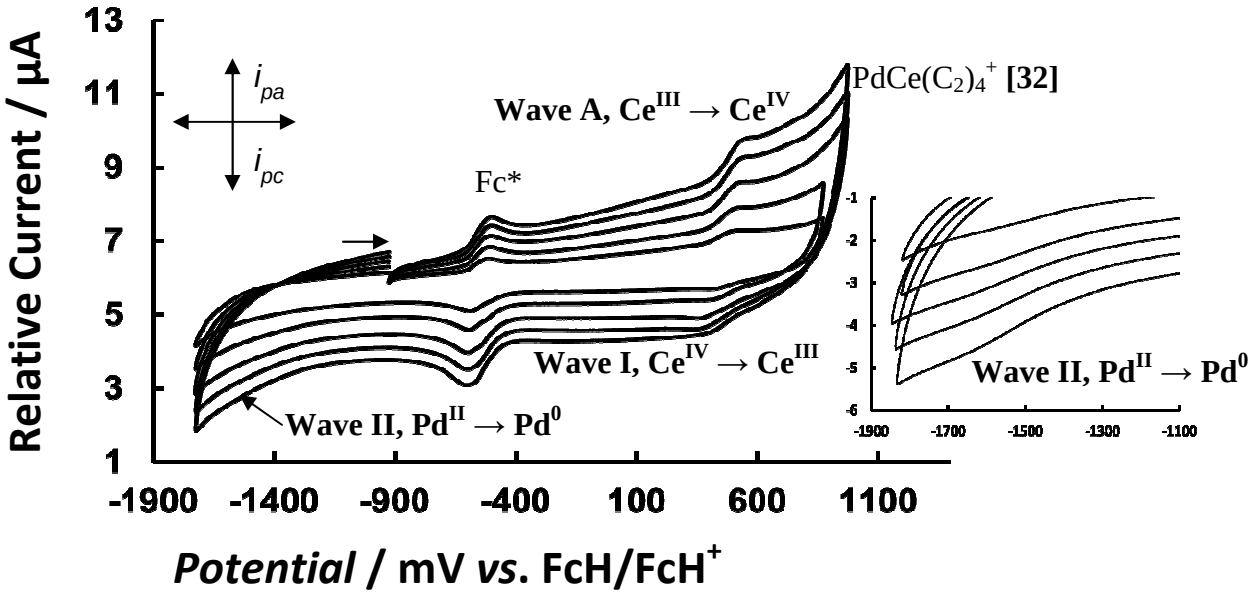

Figure 3.64: The cyclic voltammograms of a 0.5 mmol dm^{-3} solution of $PdCe(C_2)_4{}^+$, **[32]**, of in DCM. With 0.1 mol.dm^{-3} $[NBu_4][PF_6]$ as supporting electrolyte and a glassy carbon electrode at 25 ºC. Scan rates of 100, 200, 300, 400 500 mV s^{-1} with decamethyl ferrocene as internal standard. The reduction waves are labelled as bold roman numerals and the oxidation wave is labelled as a bold capital letter. Scan direction is indicated. Insert, (right) illustrating the weak reduction **wave II**.

The complex, $PdCe(C_2)_4{}^+$, **[32]**, shows an electrochemically reversible but chemically irreversible redox process at about **470 mV**.

Oxidation and reduction half waves are labelled **A (514 mV)** and **I (424 mV)**, with **ΔE = 90 mV** and $\mathbf{i_{pc}/i_{pa}}$ **= 0.48** at 100 mVs^{-1} scan rate for the complex. The oxidation **wave A** is assigned to the $Ce^{III} \rightarrow Ce^{IV}$ oxidation and **wave I**, is assigned to the reduction of $Ce^{IV} \rightarrow Ce^{III}$ in accordance with published data.[20] Although not visible in the scan with the decamethyl ferrocene as reference a weak broad reduction **wave II (-1555,** estimated**)** is observed in the scan without the reference if the y-axis is enlarged. This redox process is assigned to the reduction of $Pd^{II} \rightarrow Pd^{0}$.

Table 3.36: CV data of the mixed-metal paddlewheel acetatido complexes $PdZn(C_2)_4$ **[23]**, $PdMn(C_2)_4$ **[30]** and $PdCe(C_2)_4^+$ **[32]** utilising scan rate of 100, 200, 300, 400, 500 mV s^{-1} are shown.

$PdZn(C_2)_4$, [23]	**E_{pa} (mV), Wave A**	**i_{pa} (µA)**	**E_{pc} (mV), Wave I**	**i_{pc} (µA)**	-	-	-
100	1080	1.45	-1330	0.73	-	-	-
200	1085	2.78	-1355	0.59	-	-	-
300	1112	3.56	-1394	0.66	-	-	-
400	1120	4.35	-1390	0.79	-	-	-
500	1138	5.28	-1369	0.86	-	-	-
$PdMn(C_2)_4$, [30]	**E_{pa} (mV), Wave A**	**i_{pa} (µA)**	**E_{pa} (mV), Wave B**	**i_{pa} (µA)**	-	-	-
100	664	0.28	935	0.29	-	-	-
200	672	0.49	950*	0.12*	-	-	-
300	683	0.57	962*	0.05*	-	-	-
400	690	0.68	-	-	-	-	-
500	692	0.69	-	-	-	-	-
$PdCe(C_2)_4^+$, [32]	**E_{pa} (mV), Wave A**	**E_{pc} (mV), Wave I**	**ΔE**	**$E^{0'}$(mV)**	**i_{pa} (µA)**	**i_{pc} (µA)**	**i_{pc}/i_{pa}**
100	514	424	90	469	0.27	0.13	0.48
200	518	425	93	472	0.42	0.17	0.40
300	524	370	154	447	0.54	0.13	0.24
400	540	379	162	460	0.67	0.17	0.25
500	546	385	162	465	0.79	0.18	0.23
$PdCe(C_2)_4^+$, [32]	**E_{pc} (mV), Wave II**	-	-	-	-	-	-
100	-1555*	-	-	-	-	-	-
200	-1588*	-	-	-	-	-	-
300	-1613*	-	-	-	-	-	-
400	-1636*	-	-	-	-	-	-
500	-1663*	-	-	-	-	-	-

*Estimated values

[19] R. Freitag and J. Conradie, *Electrochimica Acta*, 2015, **158**, 418.
[20] A. Paulenova, S. E. Creager, J. D. Navratil and Y. Wei, *Journal of Power Sources*, 2002, **109**, 431

3.6.4. Cyclic voltammetry of aliphatic long-chain mixed-metal paddlewheel carboxylatido complexes

The cyclic voltammetry of mixed metal paddlewheel carboxylatido complexes $PdCd(C_{10})_4$ **[34]**, $PdZn(C_{10})_4$) **[36]**, $PdMn(C_{10})_4$ **[39]** and $PdCe(C_{10})_4^+$ **[41]** will be discussed, and the CV data are tabulated in **Table 3.37**.

3.6.4.1. Cyclic voltammetry of $[Pd^{II}Cd^{II}(\mu\text{-}OOC(CH_2)_8CH_3)_4]$, [34]

Cyclic voltammograms of $PdCd(C_{10})_4$, **[34]**, are depicted in **Figure 3.65**. The complex was dissolved in DCM having a concentration of 0.5 mmol dm^{-3} at 25 ºC. Decamethyl ferrocene (Fc*) was used as internal standard and 0.1 mol dm^{-3} supporting electrolyte, $[NBu_4][PF_6]$. Utilising a scan rate of 100, 200, 300, 400 and 500 mV s^{-1}.

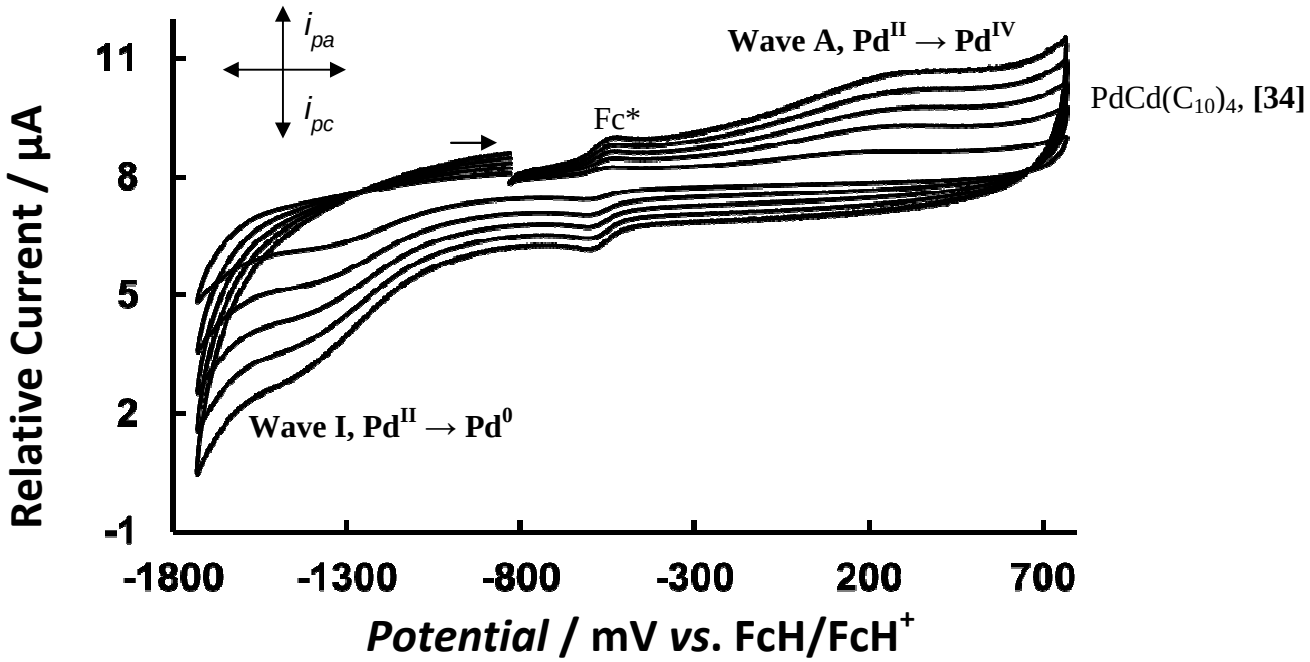

Figure 3.65: The cyclic voltammograms of a 0.5 mmol dm^{-3} solution of $PdCd(C_{10})_4$, **[34]**, in DCM. With 0.1 mol dm^{-3} $[NBu_4][PF_6]$ as supporting electrolyte and a glassy carbon working electrode at 25 ºC. Scan rates of 100, 200, 300, 400 and 500 mV s^{-1} with decamethyl ferrocene (Fc*) as internal standard. The reduction wave is labelled as a bold roman numeral and the oxidation wave is labelled as a bold capital letter. Scan direction is indicated.

For the $PdCd(C_{10})_4$, **[34]**, complex, one irreversible oxidation and one irreversible reduction wave was observed. The oxidation **wave A (226 mV)** is assigned to the oxidation of $Pd^{II} \rightarrow Pd^{IV}$. This is because, the highest oxidation number of Cd is +2.[18]

The reduction **wave I (-1339 mV)** is assigned to the $Pd^{II} \rightarrow Pd^{0}$ reduction similar to previous assignments. After the $Pd^{II} \rightarrow Pd^{IV}$ oxidation at **wave A**, all the Pd(IV) species that was produced diffuses away from the electrode. This only allows for the $Pd^{II} \rightarrow Pd^{0}$ reduction process at **wave I**. For the $PdZn(C_2)_4$, **[23]**, the oxidation of $Pd^{II} \rightarrow Pd^{IV}$ was assigned, **1080 mV**, while the oxidation of $Pd^{II} \rightarrow Pd^{IV}$ for $PdCd(C_{10})_4$, **[34]**, was assigned as **226 mV**. The cadmium atom, together with the electron donating property of the aliphatic long-chains decreased the $Pd^{II} \rightarrow Pd^{IV}$ oxidation potential by **854 mV**, confirming communication between the palladium and cadmium atoms.

3.6.4.2. Cyclic voltammetry of $[Pd^{II}Zn^{II}(\mu\text{-}OOC(CH_2)_8CH_3)_4]$, [36]

Cyclic voltammograms of $PdZn(C_{10})_4$, **[36]**, are depicted in **Figure 3.66**. The complex was dissolved in DCM having a concentration of 0.5 mmol dm^{-3} at 25 ºC. Ferrocene was used as internal standard and 0.1 mol dm^{-3} supporting electrolyte, $[NBu_4][PF_6]$. Utilising a scan rate of 100, 200, 300, 400 and 500 mV s^{-1}.

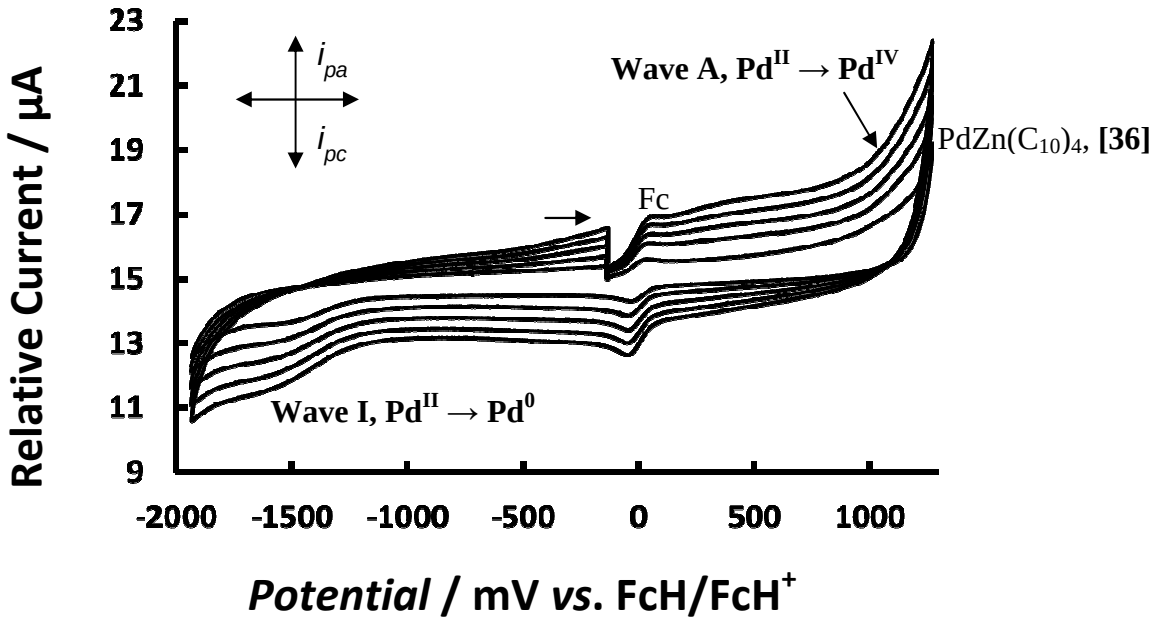

Figure 3.66: The cyclic voltammograms of a 0.5 mmol dm^{-3} solution of $PdZn(C_{10})_4$, **[36]**, in DCM. With 0.1 mol dm^{-3} $[NBu_4][PF_6]$ as supporting electrolyte and a glassy carbon working electrode at 25 ºC. Scan rates of 100, 200, 300, 400 and 500 mV s^{-1} with ferrocene (Fc) as internal standard. The reduction wave is labelled as a bold roman numeral and the oxidation wave is labelled as a bold capital letter. Scan direction is indicated.

Electrochemical studies of $PdZn(C_{10})_4$, **[36]**, illustrates one irreversible oxidation and one irreversible reduction wave. Two redox processes, an oxidation wave labelled **A (1066 mV)**, and one reduction wave labelled **I (-1460 mV)**. Oxidation wave **A** can only be the oxidation of

$Pd^{II} \rightarrow Pd^{IV}$. [21] This is because Zn(II) does not have any oxidation number higher than +2.[18] The reduction **wave I** is assigned to the $Pd^{II} \rightarrow Pd^{0}$ reduction. Following the $Pd^{II} \rightarrow Pd^{IV}$ oxidation at **wave A**, all the Pd(IV) species that was produced, diffuses away from the electrode. This only allows the $Pd^{II} \rightarrow Pd^{0}$ reduction process. Redox process for $PdZn(C_{10})_4$, **[36]**, is chemically and electrochemically irreversible because in both redox processes no reduction half wave was observed for **wave A** and no oxidation half wave was observed for **wave I**. Comparing the reduction potential of $Pd^{II} \rightarrow Pd^{0}$, of $PdZn(C_2)_4$, **[23] (-1330 mV)** and $PdZn(C_{10})_4$, **[36]**, **(-1460 mV)** the reduction potential shifts to more negative values, confirming the electron donating property of the decanoatido aliphatic chain.

3.6.4.3. Cyclic voltammetry of $[Pd^{II}Mn^{II}(\mu\text{-}OOC(CH_2)_8CH_3)_4]$, [39]

Cyclic voltammograms of $PdMn(C_{10})_4$, **[39]**, are depicted in **Figure 3.67**. The complex was dissolved in DCM having a concentration of 0.5 mmol dm^{-3} at 25 ºC. Ferrocene was used as internal standard and 0.1 mol dm^{-3} supporting electrolyte, $[NBu_4][PF_6]$. Utilising a scan rate of 100, 200, 300, 400 and 500 mV s^{-1}.

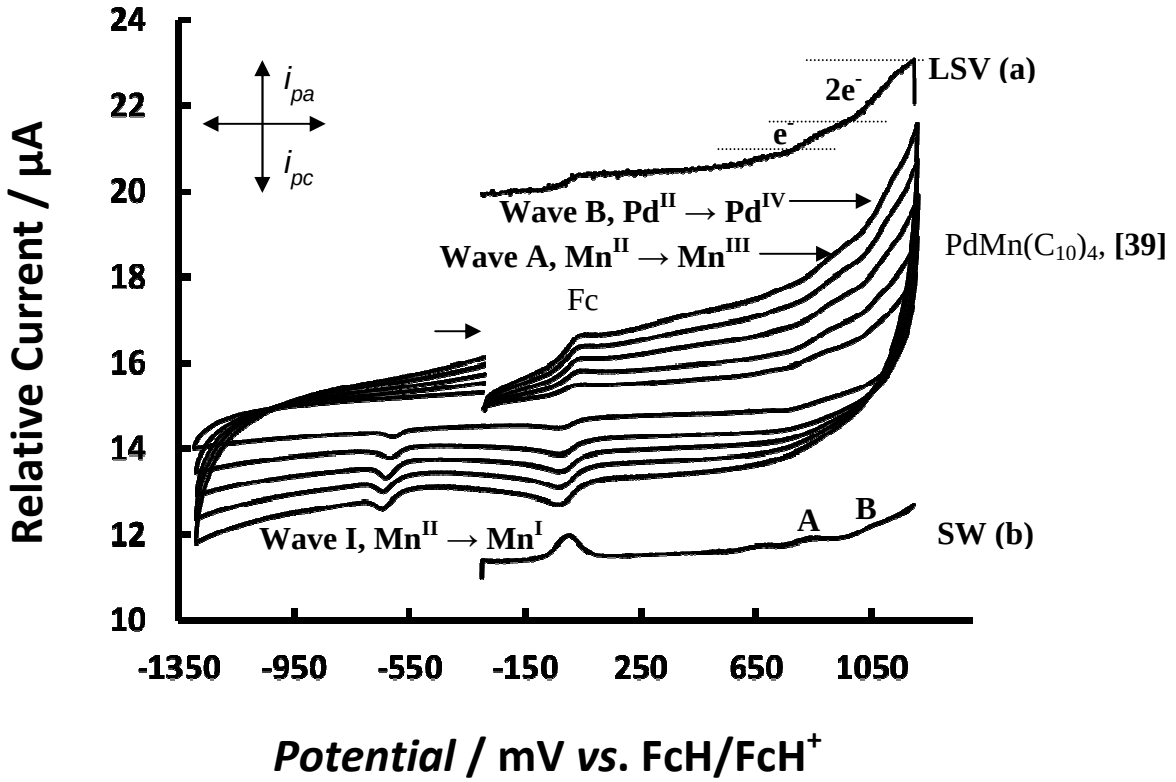

Figure 3.67: The cyclic voltammograms of a 0.5 mmol.dm^{-3} solution of $PdMn(C_{10})_4$, **[39]** of in DCM. With 0.1 mol dm^{-3} $[NBu_4][PF_6]$ as supporting electrolyte and a glassy carbon working electrode at 25ºC. Scan rates of 100, 200, 300, 400 500 mV s^{-1} with ferrocene as internal standard. The oxidation waves are labelled as bold capital letters and the reduction wave is labelled as a bold roman numeral. Scan direction is indicated. (a) Linear sweep voltammetry performed at 2 mV s^{-1} and (b) Oster Young square wave voltammetry performed at 60 Hz.

[21] D. B. Nicholas, J. F. Kampf and M. S. Sanford, *J. Am. Chem. Soc.* 2010, **132**, 2878

The $PdMn(C_{10})_4$, **[39]**, exhibits two oxidation waves. The oxidation **waves A (853 mV)** and **B (1058 mV)** are assigned to the oxidation of $Mn^{II} \rightarrow Mn^{III}$ and $Pd^{II} \rightarrow Pd^{IV}$ respectively. These assignments are based upon the LSV and SW data collected see **Figure 3.67**. This illustrates a one and two electron oxidation for **wave A** and **wave B** respectively. Lastly, $Mn^{II} \rightarrow Mn^{I}$ reduction at **wave I**, is observed at **-650 mV**. All redox processes are chemically and electrochemically irreversible, as no reduction half waves are observed for **waves A** and **B** while no oxidation half wave was observed for **wave I**.

3.6.4.4. Cyclic voltammetry of $[Pd^{II}Ce^{III}(\mu\text{-}OOC(CH_2)_8CH_3)_4]^+$, [41]

Cyclic voltammograms of $PdCe(C_{10})_4^+$, **[41]**, are depicted in **Figure 3.68**. The complex was dissolved in DCM having a concentration of 0.5 mmol dm^{-3} at 25 ºC. Decamethyl ferrocene (Fc*) was used as internal standard and 0.1 mol dm^{-3} supporting electrolyte, $[NBu_4][PF_6]$. Utilising a scan rate of 100, 200, 300, 400 and 500 mV s^{-1}.

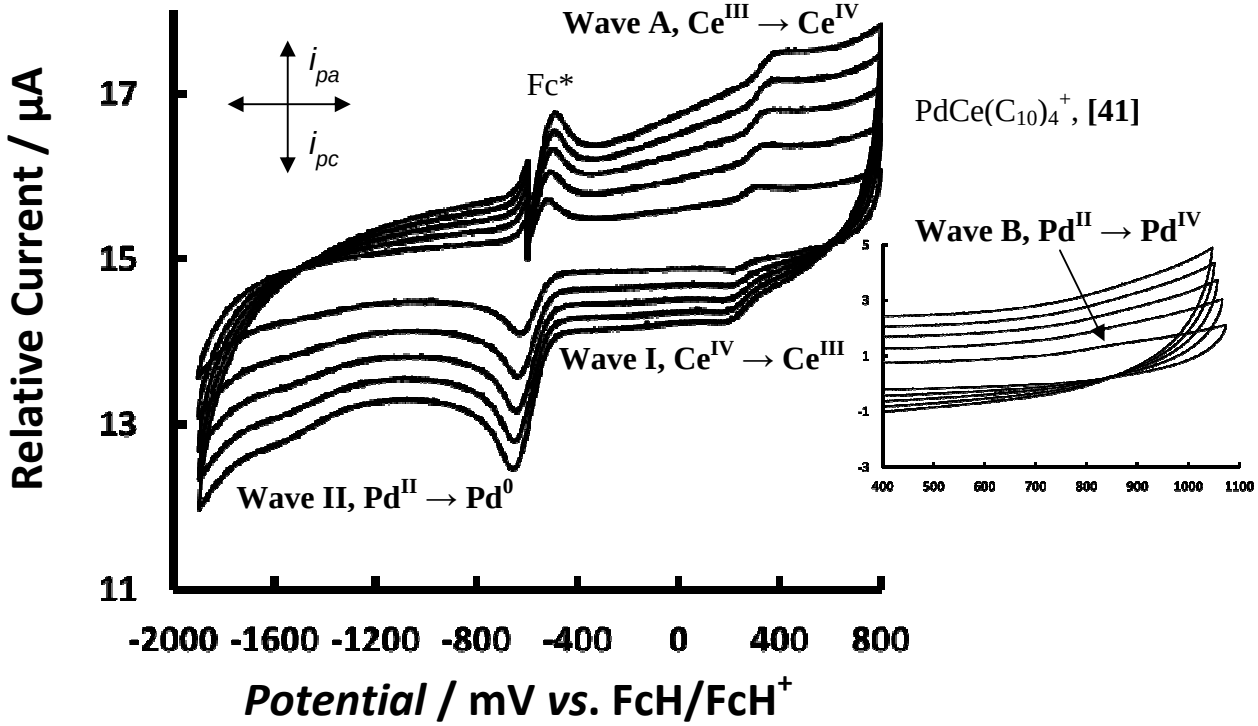

Figure 3.68: The cyclic voltammograms of a 0.5 mmol.dm^{-3} solution of $PdCe(C_{10})_4$, **[41]** of in DCM. With 0.1 mol dm^{-3} $[NBu_4][PF_6]$ as supporting electrolyte and a glassy carbon working electrode at 25ºC. Scan rates of 100, 200, 300, 400 500 mV s^{-1} with decamethyl ferrocene (Fc*) as internal standard. The oxidation waves are labelled as bold capital letters and the reduction waves are labelled as bold roman numerals. Scan direction is indicated. The insert illustrates a weak $Pd^{II} \rightarrow Pd^{IV}$ oxidation at **wave B**, in the scan without decamethyl ferrocene as internal standard.

Oxidation of $Ce^{III} \rightarrow Ce^{IV}$ is observed at **A (297 mV)** and the reduction, $Ce^{IV} \rightarrow Ce^{III}$ is observed at **I (229 mV)**. Similar to the acetatido complex, $PdCe(C_2)_4^+$, **[32]**, $PdCe(C_{10})_4^+$ **[41]**, exhibits a chemically irreversible **(i_{pc}/i_{pa} = 0.62)** and electrochemically reversible **(ΔE = 69 mV)** redox process at about **263 mV** for 100 m s^{-1} scan rate. Increasing the carboxylatido carbon chain length from two to ten, the E_{pa} decreased from **514 mV** for $PdCe(C_2)_4^+$ **[32]** to **297 mV** for $PdCe(C_{10})_4^+$ **[41]**. This implies that a longer chain length causes the oxidation of the cerium to be easier, and therefore an increase in the electron density of cerium. A weak $Pd^{II} \rightarrow Pd^{IV}$ oxidation wave is observed in the scan without the decamethyl ferrocene as internal standard at **wave B (881 mV)**, see insert in **Figure 3.68**. The reduction of $Pd^{II} \rightarrow Pd^0$ is observed at **wave II (-1430 mV)**. The redox processes of the $Pd^{II} \rightarrow Pd^{IV}$ oxidation and the $Pd^{II} \rightarrow Pd^0$ reduction are chemically and electrochemically irreversible.

Table 3.37: CV data of aliphatic long-chain mixed-metal paddlewheel carboxylatido complexes $PdCd(C_{10})_4$ **[34]**, $PdZn(C_{10})_4$) **[36]**, $PdMn(C_{10})_4$ **[39]** and $PdCe(C_{10})_4^+$ **[41]** at a scan rate of 100, 200, 300, 400, 500 mV s^{-1}.

$PdCd(C_{10})_4$, [34]	**E_{pa} (mV), Wave A**	**i_{pa} (µA)**	**E_{pc} (mV), Wave I**	**i_{pc} (µA)**	-	-	-
100	226	0.68	-1339	0.20	-	-	-
200	246	0.81	-1357	0.32	-	-	-
300	267	1.13	-1371	0.24	-	-	-
400	270	1.23	-1393	0.28	-	-	-
500	275	1.39	-1426	0.44	-	-	-
$PdZn(C_{10})_4$, [36]	**E_{pa} (mV), Wave A**	**i_{pa} (µA)**	**E_{pc} (mV), Wave I**	**i_{pc} (µA)**	-	-	-
100	1066	0.42	-1460	0.06	-	-	-
200	1082	0.32	-1475	0.07	-	-	-
300	1093	0.21	-1490	0.08	-	-	-
400	1098	0.11	-1523	0.08	-	-	-
500	1104	0.05	-1560	0.09	-	-	-
$PdMn(C_{10})_4$, [39]	**E_{pa} (mV), Wave A**	**i_{pa} (µA)**	**E_{pa} (mV), Wave B**	**i_{pa} (µA)**	**E_{pc} (mV) Wave I**	**i_{pc} (µA)**	-
100	853	0.70	1058	0.40	-650	0.10	-
200	888	1.0	1076	0.44	-640	0.11	-
300	911	1.20	1085	0.44	-626	0.21	-
400	912	1.58	1087	0.50	-612	0.27	-
500	912	1.94	1091	0.53	-598	0.45	-
$PdCe(C_{10})_4^+$, [41]	**E_{pa} (mV), Wave A**	**E_{pc} (mV), Wave I**	**ΔE**	**$E^{0'}$(mV)**	**i_{pa} (µA)**	**i_{pc} (µA)**	**i_{pc}/i_{pa}**
100	297	229	69	263	0.13	0.08	0.62
200	302	222	80	262	0.17	0.09	0.53
300	308	212	95	260	0.21	0.10	0.44
400	314	208	106	261	0.23	0.12	0.53
500	321	208	113	264	0.26	0.13	0.52
$PdCe(C_{10})_4^+$, [41]	**E_{pa} (mV), Wave B**	**E_{pc} (mV), Wave II**	-	-	-	-	-
100	881*	-1430*	-	-	-	-	-
200	895*	-1450*	-	-	-	-	-
300	923*	-1470*	-	-	-	-	-
400	951*	-1490*	-	-	-	-	-
500	980*	-1510*	-	-	-	-	-

*Estimated values

3.7. Surface Chemistry

The short- and long-chain aliphatic mixed-metal paddlewheel complexes **[19-25]**, **[27-30]** and **[33-41]** were coated onto hydroxylated silicon wafers and tested for catalytic activity for the aerobic oxidation of 1-octadecanol to 1-octadecanoic acid as model reactant.

3.7.1. Wafer preparation and coating of complexes

Supported mixed-metal catalysts were prepared on modified flat two-dimensional supports as potential catalysts for the solvent-free aerobic oxidation of long-chain aliphatic alcohols.

Single sided polished silicon wafers, with a diameter of 120 mm, was calcined at 750 °C for 24 h in oxygen. This resulted in the formation of an amorphous -O-Si-O- layer on the silicon surface, 90 nm thick. The amorphous -O-Si-O- layer was then cleaned with H_2O_2 and NH_4OH. Furthermore the wafers were boiled in double distilled water which resulted in the formation of hydrophilic silanol groups -Si-OH on the wafer surface. Selected complexes in this study were coated onto the -Si-OH prepared wafer surface using spin-coating see **Scheme 3.12**.[22]

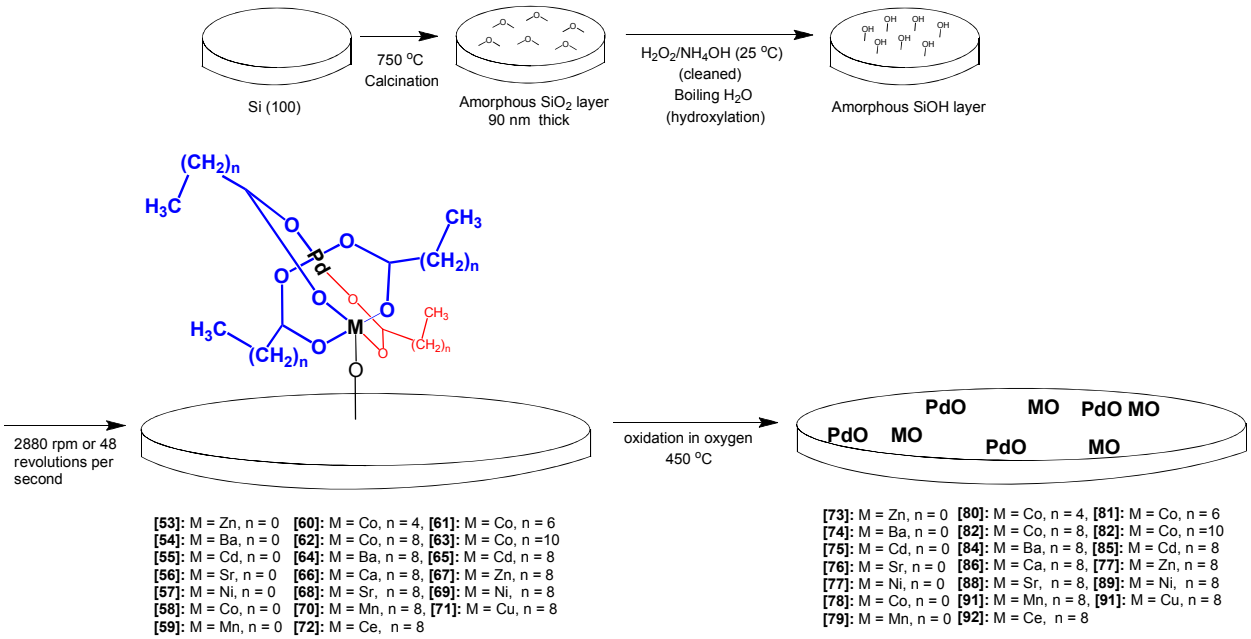

[53]: M = Zn, n = 0 **[60]:** M = Co, n = 4, **[61]:** M = Co, n = 6
[54]: M = Ba, n = 0 **[62]:** M = Co, n = 8, **[63]:** M = Co, n =10
[55]: M = Cd, n = 0 **[64]:** M = Ba, n = 8, **[65]:** M = Cd, n = 8
[56]: M = Sr, n = 0 **[66]:** M = Ca, n = 8, **[67]:** M = Zn, n = 8
[57]: M = Ni, n = 0 **[68]:** M = Sr, n = 8, **[69]:** M = Ni, n = 8
[58]: M = Co, n = 0 **[70]:** M = Mn, n = 8, **[71]:** M = Cu, n = 8
[59]: M = Mn, n = 0 **[72]:** M = Ce, n = 8

[73]: M = Zn, n = 0 **[80]:** M = Co, n = 4, **[81]:** M = Co, n = 6
[74]: M = Ba, n = 0 **[82]:** M = Co, n = 8, **[82]:** M = Co, n =10
[75]: M = Cd, n = 0 **[84]:** M = Ba, n = 8, **[85]:** M = Cd, n = 8
[76]: M = Sr, n = 0 **[86]:** M = Ca, n = 8, **[77]:** M = Zn, n = 8
[77]: M = Ni, n = 0 **[88]:** M = Sr, n = 8, **[89]:** M = Ni, n = 8
[78]: M = Co, n = 0 **[91]:** M = Mn, n = 8, **[91]:** M = Cu, n = 8
[79]: M = Mn, n = 0 **[92]:** M = Ce, n = 8

Scheme 3.12: The above scheme demonstrates the preparation of silicon wafers by calcination and hydroxylation (top) as well as the coating of the complexes utilising spin-coating and oxidation of the pre-catalyst (bottom).

Spin-coating is the two-dimensional equivalent of wet incipient impregnation for three dimensional systems. Modified wafers of approximate sise 4 x 5 mm^2 were spin-coated at 2880 rpm (48 revolutions per second). A 5 mM solution of the mixed-metal complex was added at a constant rate to the rotating wafer.

The appearance of Newton rings is an indication that all the excess solvent has been spun off from the hydroxylated wafer leaving the dissolved complex coated onto the modified wafer surface. The amount of moles coated onto the hydroxylated wafer can be calculated by using the following equation:[23,24]

$$m = 1.35 \times C_0 \sqrt{\frac{n}{\rho \omega^2 t_{evp}}} \qquad (1)$$

In equation 1, m is the amount of moles coated onto the –Si-OH functionalised surface of the silicon wafer, C_0 is the concentration of the catalyst precursor in the bulk solution (mol m^{-3}), n is the viscosity and ρ is the density of the solvent, here acetone (n = 0.000316 kg m^{-1} s^{-1}, ρ = 791 kg m^{-3}) and DCM (n = 0.00041 kg m^{-1} s^{-1}, ρ = 1330 kg m^{-3}), ω is the rotation speed 2880 rpm (48 revolutions per second), and t_{evp} (one second for DCM and two seconds for acetone) is the evaporation time.

3.7.2. Catalytic studies on the modified wafers (-Si-OH)

The goal of this part of the research project is to serve as a proof of concept that by increasing the number of carbons in the carboxylatido backbone (replacing the acetatido ligand with either a hexanoatido, octanoatido, decanoatido or dodecanoatido ligand) of the mixed-metal carboxylatido complexes, the catalytic activity of this catalyst would improve. By increasing the number of carbons in the carboxylatido backbone, the metals are less likely to aggregate and form big clusters on the surface of the modified wafer, which could cause a decrease in catalytic activity. The long chains would in essence keep the mixed-metal carboxylatido complexes further apart from each other, thereby minimising aggregation of the metallic centres upon further treatment such as calcining (high temperature oxidation).

---

[22] E. Erasmus, P. C. Thüne , M.W.G.M. (Tiny) Verhoeven, J.W. (Hans) Niemantsverdriet, J. C. Swarts, *Cat Comm*, 2012, **27**, 193

[23] J. W. Niemantsverdriet, A. F. P. Engelen, A. M. de Jong, W. Wieldraaijer, G. J. Kramer, *Appl. Surf. Sci*, 1999, **144**, 366

[24] P. J. L. Gunter, J. W. Niemantsverdriet, F. H. Ribeiro, G. A. Somorjai, *Catal. Rev. Sci. Eng.* 1997, **39**, 77

After preparation of the modified silicon wafers and coating of the surface with the desired carboxylatido complex by means of spin-coating, the pre-catalyst was oxidised (calcined at 450 ˚C) in oxygen where the organic fragments (the carboxylatido ligands) were burned off and metal oxides was deposited on the surface PdO and MO (metal oxides). To test the activated PdO and MO (metal oxide) catalysts in a model reaction, the aerobic solvent-free oxidation of 1-octadecanol to 1-octadecanoic acid was chosen. The reaction is shown in **Scheme 3.13**.

The catalytic reactions for the various catalysts were monitored by ATR-FTIR, see **Figure 3.69**, by following the appearance of the carbonyl stretching frequencies at 1730 and 1710 cm^{-1}.

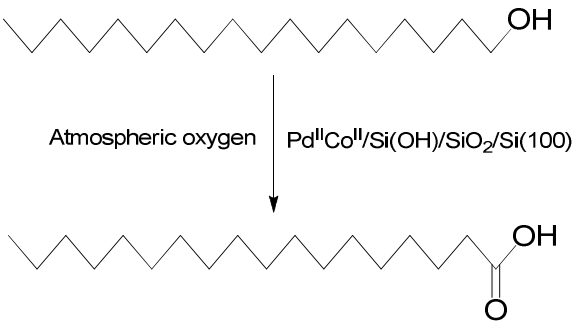

Scheme 3.13: Aerobic oxidation (open to air) of 1-octadecanol to 1-octadecanoic acid, using (as an example) the $Pd^{II}Co^{II}$/Si(OH)/SiO2/Si(100) catalyst.

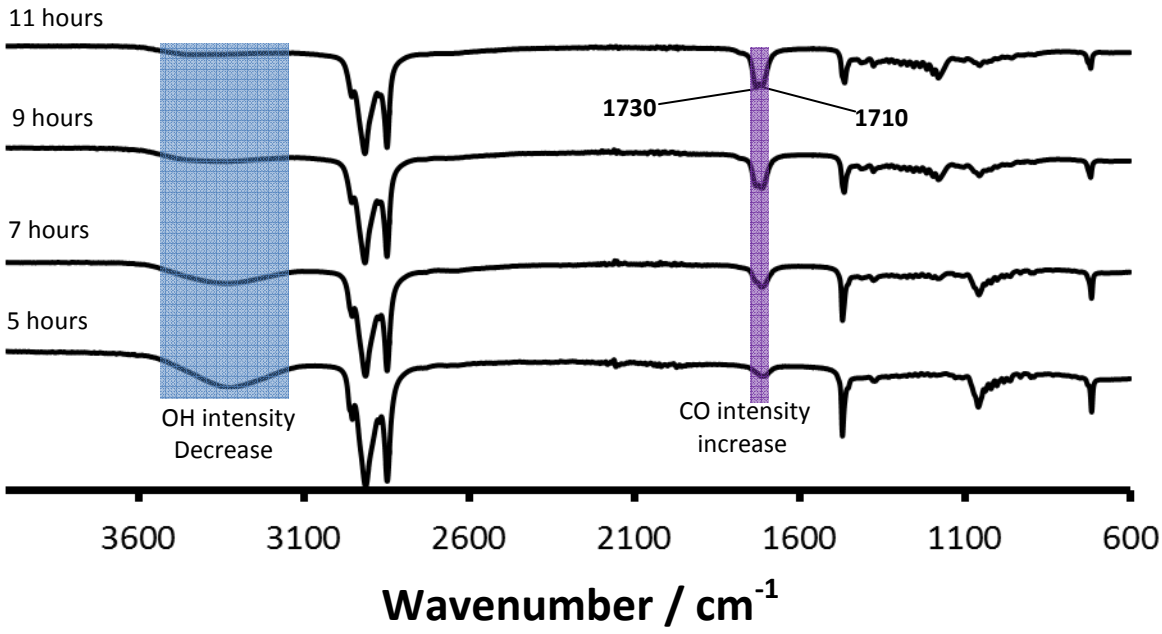

Figure 3.69: ATR-FTIR spectra showing the oxidation of 1-octadecanol to 1-octadecanoic acid, on the surface of $Pd^{II}Co^{II}$/Si(OH)/SiO2/Si(100). Note the decrease in OH signal intensity at 3350 cm^{-1} and the increase in intensity of C=O stretching frequencies at 1730 and 1710 cm^{-1} as the reaction proceeds.

Turn over frequency (TOF) of a catalyst is a good indication of how active the catalyst is. To determine the TOF of a catalyst requires both equations (1) and (2) see below. The total amount of active sites deposited on the modified Si-wafer was determined to be 7.76 x 10^{-5} mol m^{-2} using equation (1).

$$m = 1.35 \times C_0 \sqrt{\frac{n}{\rho\omega^2 t_{evp}}} \qquad (1)$$

$$m = 1.35 \times 5 \frac{mol}{m^3} \sqrt{\frac{0.00041 \ \frac{kg}{ms}}{1330 \ \frac{kg}{m^3} \ (48s^{-1})^2 \ 1s}}$$

$$m = 7.76 \times 10^{-5} \ \frac{mol}{m^2}$$

The quantity, *m*, may be converted into the amount of active sites, which was calculated to be 47 molecules nm^{-2}. This can then be further manipulated to obtain the amount of molecules mm^{-2}. For this example a modified wafer with an average surface area of 20 mm^2, was found to have $9.4x10^{14}$ molecules mm^{-2} (active sites). Equation (2), may be used to obtain the TOF (turn over frequency) for each catalyst prepared. If 0.1 g of 1-octadecanol (2.1 x 10^{20} molecules) was fully oxidised to the carboxylic acid in 14 hours (50400 s), with the catalyst having $9.4x10^{14}$ active sites, a TOF of 5 molecules s^{-1} is calculated. The TOF's for all the catalysts prepared in this study are summarised in **Table 3.38**.

$$TOF \ (Turn \ over \ frequency) = \frac{\frac{amount \ of \ molecules \ converted}{amount \ of \ active \ sites}}{time \ in \ seconds} \qquad (2)$$

$$TOF = \frac{\frac{2.1x10^{20} \ molecules}{9.4x10^{14} \ active \ sites}}{50400 \ s}$$

$$TOF = 5 \text{ molecules } s^{-1}$$

Table 3.38: Contains the time in hours (conversion of 1-octadecanol to 1-octadecanoic acid) and turnover frequency (TOF) in seconds of the tested modified wafer catalysts.

Catalysts prepared from short-chain complexes			**Catalysts prepared from long-chain complexes**		
Catalyst (Oxidised)	**Time (hrs)**	**TOF (molecules s^{-1})**	**Catalyst (Oxidised)**	**Time (hrs)**	**TOF (molecules s^{-1})**
$Pd^{II}Zn^{II}/Si(OH)/SiO_2/Si(100)$ **[73]**, from $PdZn(C_2)_4$	84	1	$Pd^{II}Co^{II}/Si(OH)/SiO_2/Si(100)$ **[80]**, from $PdCo(C_6)_4$	11	6
$Pd^{II}Ba^{II}/Si(OH)/SiO_2/Si(100)$ **[74]**, from $PdBa(C_2)_4$	60	1	$Pd^{II}Co^{II}/Si(OH)/SiO_2/Si(100)$ **[81]**, from $PdCo(C_8)_4$	11	6
$Pd^{II}Cd^{II}/Si(OH)/SiO_2/Si(100)$ **[75]**, from $PdCd(C_2)_4$	36	2	$Pd^{II}Co^{II}/Si(OH)/SiO_2/Si(100)$ **[82]**, from $PdCo(C_{10})_4$	13	5
$Pd^{II}Sr^{II}/Si(OH)/SiO_2/Si(100)$ **[76]**, from $PdSr(C_2)_4$	69	1	$Pd^{II}Co^{II}/Si(OH)/SiO_2/Si(100)$ **[83]**, from $PdCo(C_{12})_4$	13	5
$Pd^{II}Ni^{II}/Si(OH)/SiO_2/Si(100)$ **[77]**, from $PdNi(C_2)_4$	60	1	$Pd^{II}Ba^{II}/Si(OH)/SiO_2/Si(100)$ **[84]**, from $PdBa(C_{10})_4$	16	4
$Pd^{II}Co^{II}/Si(OH)/SiO_2/Si(100)$ **[78]**, from $PdCo(C_2)_4$	72	1	$Pd^{II}Ca^{II}/Si(OH)/SiO_2/Si(100)$ **[85]**, from $PdCa(C_{10})_4$	14	5
$Pd^{II}Mn^{II}/Si(OH)/SiO_2/Si(100)$ **[79]**, from $PdMn(C_2)_4$	93	0.8	$Pd^{II}Cd^{II}/Si(OH)/SiO_2/Si(100)$ **[86]**, from $PdCd(C_{10})_4$	11	6
-	-	-	$Pd^{II}Ce^{III}/Si(OH)/SiO_2/Si(100)$ **[87]**, from $PdCe(C_{10})_4$	12	6
-	-	-	$Pd^{II}Cu^{II}/Si(OH)/SiO_2/Si(100)$ **[88]**, from $PdCu(C_{10})_4$	11	6
-	-	-	$Pd^{II}Mn^{II}/Si(OH)/SiO_2/Si(100)$ **[89]**, from $PdMn(C_{10})_4$	14	5
-	-	-	$Pd^{II}Ni^{II}/Si(OH)/SiO_2/Si(100)$ **[90]**, from $PdNi(C_{10})_4$	13	5
-	-	-	$Pd^{II}Sr^{II}/Si(OH)/SiO_2/Si(100)$ **[91]**, from $PdSr(C_{10})_4$	13	5
-	-	-	$Pd^{II}Zn^{II}/Si(OH)/SiO_2/Si(100)$ **[92]**, from $PdZn(C_{10})_4$	9	7

Data in **Table 3.38** confirms the hypothesis that an increase of the aliphatic chains of the mixed-metal paddlewheel complexes will lead to an increase in catalytic activity of the prepared catalysts, see chapter 1. Catalysts prepared from **[26]**, **[31]** and **[32]** showed no activity. Modified silicon wafer catalysts **[73-79]**, with a TOF of 0.8 molecules s^{-1} to 2 molecules s^{-1} prepared from the short-chain mixed-metal complexes **[23-25]** and **[27-30]** have an average conversion time (1-octadecanol to 1-octadecanoic acid) of 60 hours.

The catalysts **[80-92]** prepared from long-chain mixed-metal complexes **[19-22]** and **[33-41]** have an average conversion time (1-octadecanol to 1-octadecanoic acid) of 12 hours with an average TOF of 6 molecules s^{-1}. Therefore a definite increase in catalytic activity was observed. From the results, catalysts prepared from the aliphatic long-chain mixed-metal complexes have a higher surface area i.e. less aggregation of the metals compared to the short-chain mixed-metal catalysts. This follows from the fact that the $Pd^{II}O$-$Co^{II}O$, catalysts, **[80-81]** and **[82-83]**, are five to six times more catalytically active than **[78]**. However, **[82]** and **[83]**, showed an increase in conversion time and a decrease in turn over frequency. This implies that the further away the active sites are from each other, results in a decrease in catalytic activity. Therefore the catalysts prepared from the $PdCo(C_6)_4$ and $PdCo(C_8)_4$ complexes are optimal for the Pd and Co atoms to oxidise 1-octadecanol to 1-octadecanoic acid.

Figure 3.69, shows the relationship between ionic radius (pm) versus TOF for the metals of **[21]** and **[33-41]** except for palladium. The relationship illustrates that a decrease in ionic radius leads to an increase in catalytic activity. Period 4, metals show the same TOF, while an increase in TOF is observed for copper and zinc. Copper and zinc has an ionic radius close to that of nickel and cobalt. However, copper and zinc has a higher synergy with palladium, than cobalt and nickel, thereby increasing the catalytic behaviour of the catalysts.

Regarding the metals from period 5 and 6, an increase in catalytic activity is observed as the ionic radius of the metals decreases. Barium has an ionic radius of 149 pm compared to that of palladium which is 137 pm. Therefore the catalytic activity of the catalyst decreases, because 1-octadecanol cannot optimally coordinate to the palladium. This results in a decrease of catalytic activity.

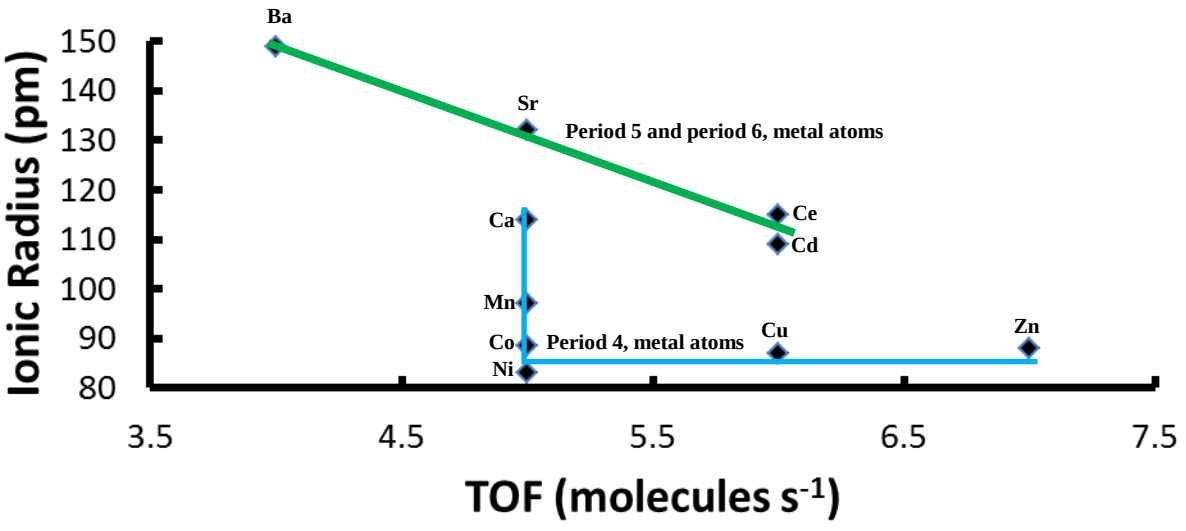

Figure 3.70: Comparison of ionic radius (pm) for PdM (M = Ba, Sr, Ce, Cd, Ca, Mn, Co, Ni, Cu, Zn) vs the TOF (molecules s^{-1}) obtained for the solvent free aerobic oxidation of 1-octadecanol to 1-octadecanoic acid.

3.7.3. XPS

XPS was used to characterise the surfaces of the hydroxylated silicon wafers coated with selected mixed-metal complexes. The XPS measurements collected was of the calcined catalysts having PdO and MO (metal oxide) on the modified surface (i.e. the organic ligand fragments, the carboxylatido ligands, were burned off).

3.7.3.1. XPS data of the activated PdO and MO (metal oxide) catalysts [73], [82], [84], [86], [89] and [90]

Figure 3.71, illustrates the XPS spectra of zinc oxide, nickel oxide, cobalt oxide, manganese dioxide, cadmium oxide, palladium oxide and barium oxide. The XPS data are summarised in **Table 3.39**. In general the $Pd^{II}O$ $3d_{5/2}$ peak was observed at *ca.* **337.15 eV** for all six catalysts. This corresponds well with the reported binding energies of **337.10 eV** for $Pd^{II}O$.[25] The $Co^{II}O$ $2p_{3/2}$ peak was observed at **782.04 eV**, which is within range of **779.3-781.80 eV** reported for oxidised $Co^{II}O/SiO_2$. The shake-up peak of the $Co^{II}O$ was observed at **4.72 eV** higher than the photoelectron lines of the $2p_{3/2}$ and $2p_{1/2}$ peaks.[26] $Zn^{II}O$ $2p_{3/2}$ was observed at **1022.43 eV**, which is within experimental error of the reported value of **1022.10 eV** for $Zn^{II}O$.[27] $Ni^{II}O$ $2p_{3/2}$ was observed at **857.90 eV**, which is within experimental error of the reported value of **857.20 eV** for $Ni^{II}O$.[28] $Mn^{IV}O_2$ $2p_{1/2}$ was observed at **653.93 eV**, which correlates very well with the reported value of **653.90 eV** for $Mn^{IV}O_2$.[29] $Cd^{II}O$ $3d_{5/2}$ was observed at **406.02 eV**, which is within experimental error of the reported values of **404.60-407.38 eV** for $Cd^{II}O$.[30,31] $Ba^{II}O$ $4d_{5/2}$ was observed at **90.07 eV**, which corresponds very well with the reported value of **89.90 eV** for $Ba^{II}O$.[32] $Pd^{II}O/Ba^{II}O$ and $Pd^{II}O/Zn^{II}O$ have a 1:1 metal ratio, while $Pd^{II}O/Co^{II}O$, $Pd^{II}O/Cd^{II}O$ and $Pd^{II}O/Ni^{II}O$ have a 1:1.5 metal ratio. However $Pd^{II}O/Mn^{IV}O_2$ has a ratio of 2.7:0.8. The palladium atoms aggregate to form larger particles on the modified silicon wafer surface after oxidation of the pre-catalyst.

---

[25] T.H. Fleisch, G.W. Zaiac, J.O. Schreiner and G.J. Mains, *Appl. Surf. Sci.*, 1986, **26**, 488

[26] Y. Okamoto, K. Nagata, T. Adachi, T. Imanaka, K. Inamura and T. Takyu, *J. Phys. Chem.* 1991, **95**, 310.

[27] G. Deroubaix and P. Marcus, *Surf. Interface Anal.*, 1992, **18**, 39

[28] S.O. Grim, L.J. Matienzo and W.E. Swartz, *J. Am. Chem. Soc*., 1972, **94**, 5116

[29] B.J. Tan, K.J. Klabunde and P.M.A. Sherwood, *J. Am. Chem. Soc.*, 1991, **113**, 855

[30] F. Golestani-Fard, T. Hashemi, K.J.D. Mackenzie, C.A. Hogarth, *J. Mater. Sci.*, 1983, **18**, 3679

[31] M.S. Setty, A.P.B. Sinha, *Thin Solid Films*, 1986, **144**, 7

[32] H. Van Doveren and J.H.Th. Verhoeven, *J. Electron Spectrosc. Relat. Phenom.* 1980, **21**, 265

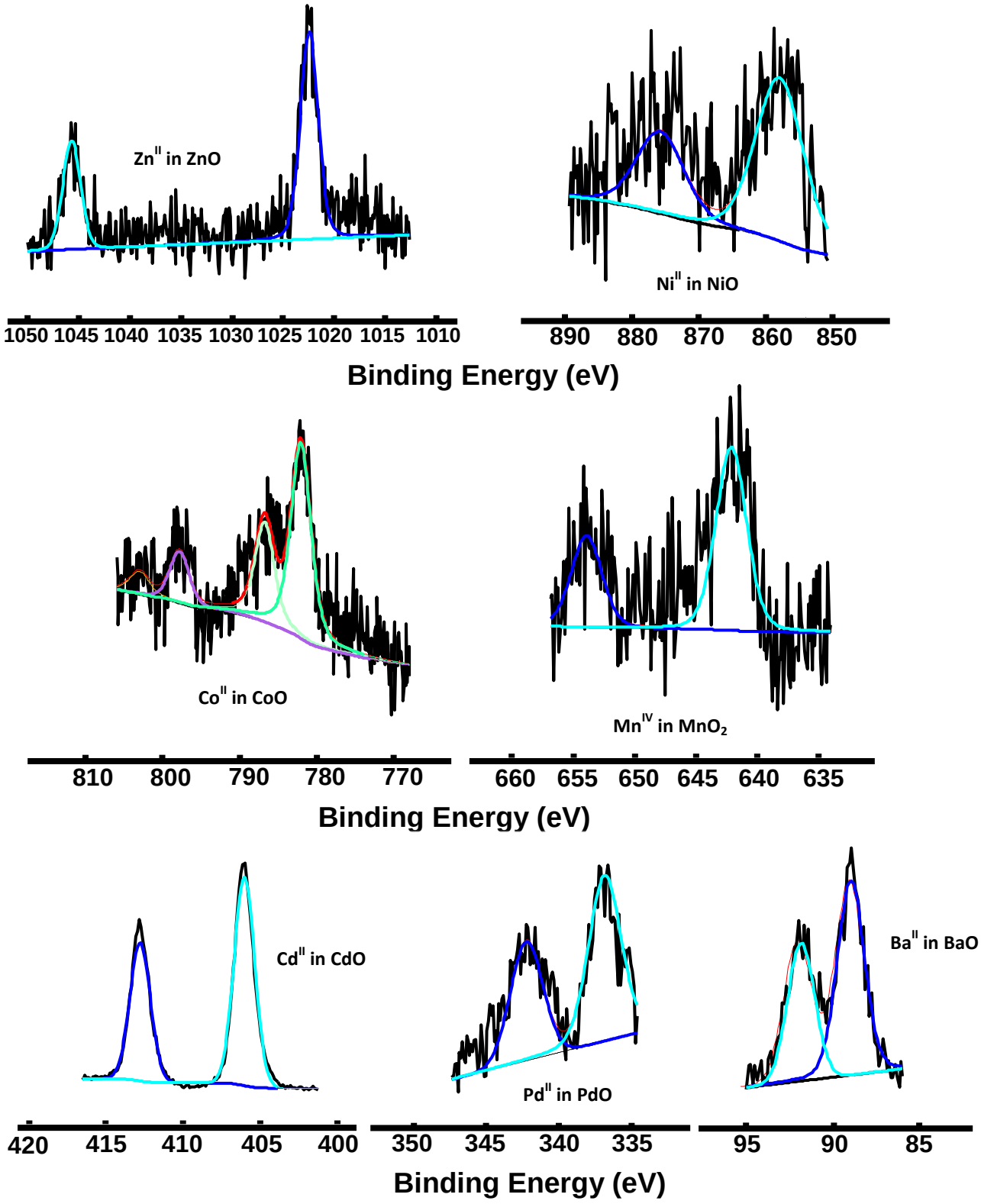

Figure 3.71: XPS spectra of $Pd^{II}O$, $Co^{II}O$, $Zn^{II}O$, $Ba^{II}O$, $Cd^{II}O$, $Ni^{II}O$, $Mn^{IV}O_2$, on the modified wafer.

Table 3.39: XPS data of $Pd^{II}O$, $Co^{II}O$, $Zn^{II}O$, $Ba^{II}O$, $Cd^{II}O$, $Ni^{II}O$, $Mn^{IV}O_2$, on the modified wafer.

Pd^{II}			**Co^{II}**		
Peak	**Binding energy (eV)**	**Atomic %**	**Peak**	**Binding energy (eV)**	**Atomic %**
$3d_{5/2}$	337.19	1.2	$2p_{3/2}$	782.04	1.9
$3d_{3/2}$	342.54		$2p_{3/2}$ Shake-up peak	786.76	
-	-	-	$2p_{1/2}$	797.75	
-	-	-	$2p_{1/2}$ Shake-up peak	802.92	
Pd^{II}			**Zn^{II}**		
$3d_{5/2}$	337.19	0.8	$2p_{1/2}$	1045.68	0.6
$3d_{3/2}$	342.54		$2p_{3/2}$	1022.43	
Pd^{II}			**Ba^{II}**		
$3d_{5/2}$	337.23	0.6	$4d_{5/2}$	90.07	0.6
$3d_{3/2}$	342.30		$4d_{3/2}$	92.59	
Pd^{II}			**Cd^{II}**		
$3d_{5/2}$	337.21	1.1	$3d_{5/2}$	406.02	1.8
$3d_{3/2}$	342.46		$3d_{3/2}$	412.78	
Pd^{II}			**Ni^{II}**		
$3d_{5/2}$	337.07	1.2	$2p_{3/2}$	857.90	0.7
$3d_{3/2}$	342.20		$2p_{1/2}$	875.74	
Pd^{II}			**Mn^{IV}**		
$3d_{5/2}$	337.03	2.7	$2p_{3/2}$	642.14	0.8
$3d_{3/2}$	342.30		$2p_{1/2}$	653.93	

This concludes the discussion on the results obtained from this study as outlined in chapter 1. All objectives have been met.

4. Experimental

4.1 Introduction

Experimental procedures, reaction conditions and techniques used during the course of this investigation are reported in this chapter.

4.2. Synthesis

4.2.1. Synthesis of $[Pd_3^{II}(\mu\text{-}OOC(CH_2)_nCH_3)_6]$, where n = 4 for [1], 6 for [2], 8 for [3] or 10 for [4]

Synthesis of long-chain circular aliphatic hexacarboxylatidotripalladium(II) complexes $[Pd_3^{II}(\mu\text{-}OOC(CH_2)_nCH_3)_6]$, where n = 4 for **[1]**, 6 for **[2]**, 8 for **[3]** or 10 for **[4]**, according to the Schemes below each section, utilizing the same general procedure. This procedure will be outlined for hexakis(hexanoatido)tripalladium(II), while only the characterisation data will be given for the rest. These four novel complexes were synthesised by using a modified procedure from Stephenson *et al*.[1]

4.2.1.1. Synthesis of circular hexakis(hexanoatido)tripalladium(II), $[Pd_3^{II}(\mu\text{-}OOC(CH_2)_4CH_3)_6]$, [1]

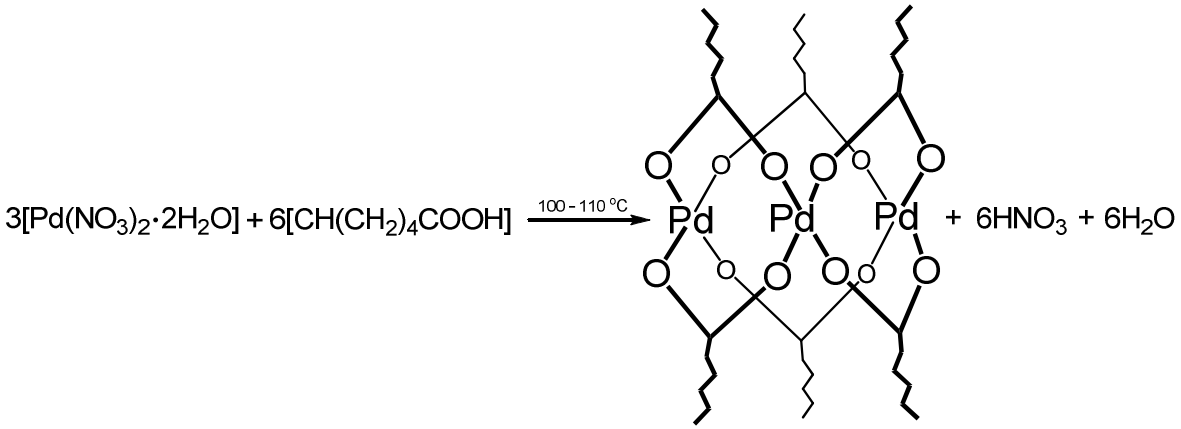

1

$Pd(NO_3)_2 \cdot 2H_2O$ (0.4 g, 1.5012 mmol) was suspended in hexanoic acid (4 ml) in a three necked round bottom flask (50 ml). The resulting mixture was heated to 100 - 110 ºC in an oil bath. The acid was removed by passing compressed air over the reaction until no more acid was present. The condensed acid was collected in a beaker (200ml), depending on the chain length this may take 5 hours to 1 day. When all the acid has been removed, analytically pure $[Pd(II)_3(\mu\text{-}OOC(CH_2)_4CH_3)_6]$ was obtained. Yield: 0.4 g, 0.3919 mmol, 78 %, m.p. decomposes above 200

[1] T. A. Stephenson, S. M. Morehouse, A. R. Powell, J. P. Heffer, and G. Wilkinson, *J. Chem. Soc.*, 1965, 3632

˚C, Elemental Analysis: calc. C: 42.80 %; H: 6.59 %, found: C: 43.29 %; H: 6.73 %. δ_H (300 MHz, $CDCl_3$)/ppm: 0.73 – 0.96 (18 H, t, 6 x C<u>H</u>$_3$), 0.96 – 1.15 (12 H, m, 6 x C<u>H</u>$_2$), 1.14 – 1.29 (12 H, m, 6 x C<u>H</u>$_2$), 1.31 – 1.51 (12 H, m, 6 x C<u>H</u>$_2$), 2.04 – 2.31 (12 H, m, 6 x C<u>H</u>$_2$), FTIR (cm^{-1}): 2955, 2928, 2859, 1602, 1559, 1500, 1411, 1378, 1344 and 1319.

4.2.1.2. Characterisation data of circular hexaoctanoatidotripalladium(II), $[Pd_3^{II}(\mu\text{-}OOC(CH_2)_6CH_3)_6]$, [2]

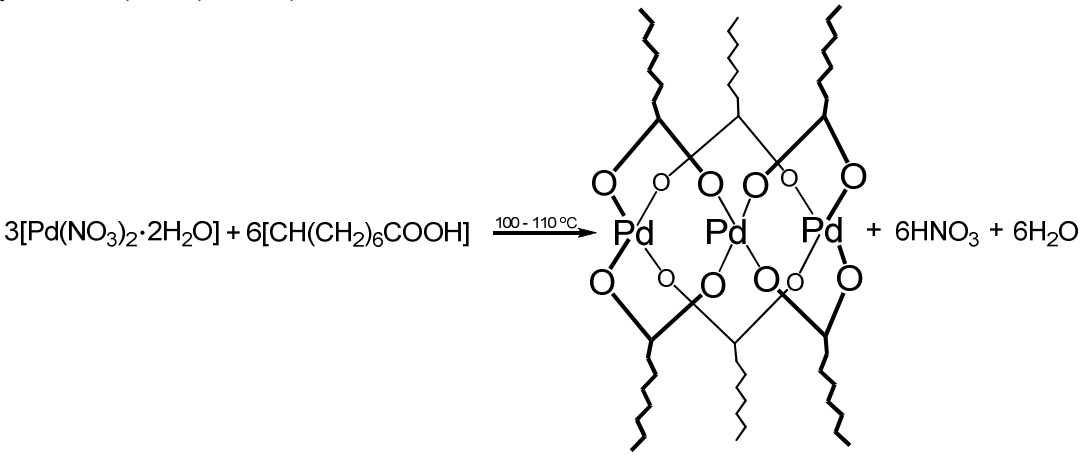

2

Yield: 0.4 g, 0.35 mmol, 70 %, m.p. decomposes above 200 ˚C, Elemental Analysis: calc. C: 49.72 %; H: 8.08 %, found: C: 49.87 %; H: 7.91 %. δ_H (300 MHz, $CDCl_3$)/ppm: 0.75 – 0.95 (18 H, t, 6 x C<u>H</u>$_3$), 0.97 – 1.55 (60 H, m, 30 x C<u>H</u>$_2$), 2.01 – 2.32 (12 H, m, 6 x C<u>H</u>$_2$), FTIR (cm^{-1}): 2954, 2924, 2854, 1604, 1559, 1499, 1411, 1378 and 1317.

4.2.1.3. Charaterisation data of hexadecanoatidotripalladium(II), $[Pd_3^{II}(\mu\text{-}OOC(CH_2)_8CH_3)_6]$, [3]

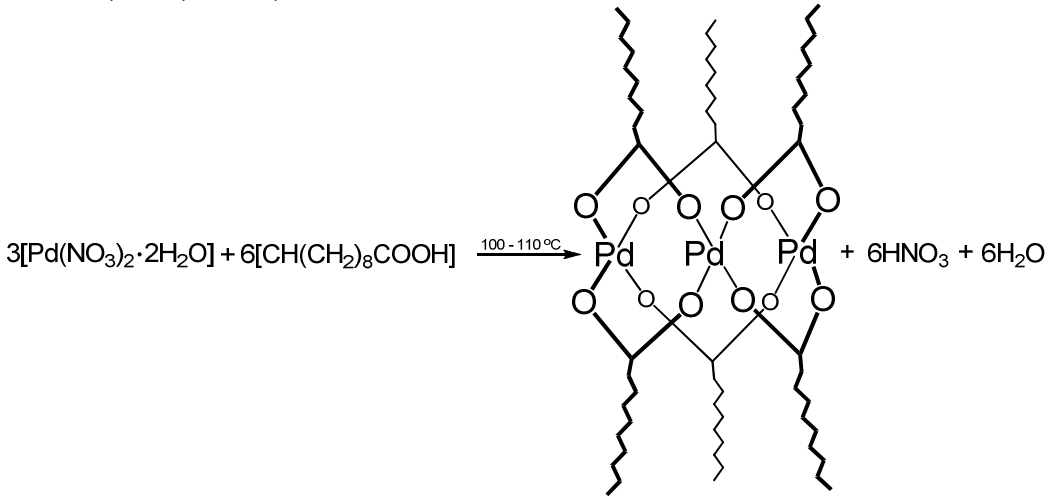

3

Yield: 0.5 g, 0.3911 mmol, 78 %, m.p. 22-23 ˚C, Elemental Analysis: calc. C: 53.27 %; H: 8.94 %, found: C: 53.12 %; H: 8.52 %. δ_H (300 MHz, $CDCl_3$)/ppm: 0.77 – 0.97 (18 H, t, 6 x C<u>H</u>$_3$), 0.97 –

1.55 (84 H, m, 42 x C<u>H</u>$_2$), 2.04 – 2.41 (12 H, m, 6 x C<u>H</u>$_2$), FTIR (cm^{-1}): 2954, 2921, 2852, 1604, 1560, 1500, 1412, 1377 and 1318.

4.2.1.4. Characterisation data of hexadodecanoatidotripalladium(II), [Pd_3^{II}(μ-$OOC(CH_2)_{10}CH_3)_6$], [4]

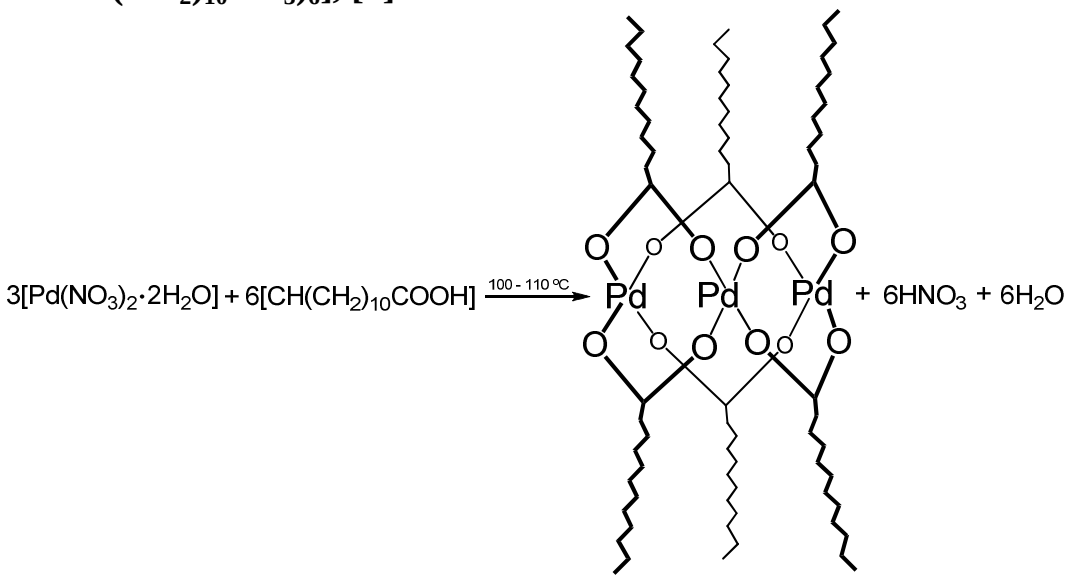

4

Yield: 0.5 g, 0.3911 mmol, 78 %, m.p. 42-43 ˚C, Elemental Analysis: calc. C: 57.08 %; H: 9.18 %, found: C: 57.52 %; H: 9.71 %. δ_H (300 MHz, $CDCl_3$)/ppm: 0.79 – 0.98 (18 H, t, 6 x C<u>H</u>$_3$), 0.98 – 1.55 (108 H, m, 54 x C<u>H</u>$_2$), 2.04 – 2.42 (12 H, m, 6 x C<u>H</u>$_2$), FTIR (cm^{-1}): 2955, 2916, 2849, 1596, 1500, 1489, 1467, 1414, 1378 and 1318.

4.2.2. Synthesis of [$K(OOC(CH_2)_nCH_3)$], where n = 4 for [5], 6 for [6], 8 for [7] or 10 for [8]*

The known long-chain aliphatic potassium carboxylates, [$K(OOC(CH_2)_nCH_3)$], where n = 4 for **[5]**, 6 for **[6]**, 8 for **[7]**, 10 for **[8]** were synthesised according to the Schemes below , utilizing Ishioka *et al.'s* [2] general procedure. This procedure will be outlined for potassium hexanoate while only the characterisation data will be given for the rest.

[2] T. Ishioka, H. Wakisaka, T. Saito and I. Kanesaka, *J. Phys. Chem. B*, 1998, **102**, 5239

* According to IUPAC, the term "carboxylate" implies that the anionic carboxylate ligand is ionically bound (i.e. electrostatically) to the K^+ cation, e.g. $K[OOC(CH_2)_4CH_3]$. The term "carboxylatido" implies that the anionic ligand is coordinatively (covalently) bound to a metal, e.g. [Pd_3^{II}(μ-$OOC(CH_2)_4CH_3)_6$].

4.2.2.1. Synthesis of potassium hexanoate, $K[OOC(CH_2)_4CH_3]$, [5]

$$CH_3(CH_2)_4COOH + KOH_{(aq)} \longrightarrow K[OOC(CH_2)_4CH_3] + H_2O$$

5

A slight excess of KOH(*aq*) (60 ml, 44 mmol) was added dropwise to hexanoic acid (4 g, 43 mmol) in a 500 ml beaker, this resulted in a basic solution. The solution was dried under reduced pressure to yield the crude product. The solid was then dissolved in 100 ml warm, methanol (*ca.* 60 °C) and the excess KOH was removed by decantation. The alcohol solution was then dried under reduced pressure to yield: 5 g, 33 mmol, 77 %, of pure potassium hexanoate, m.p. 312-313 ˚C, characterisation,[3,4] FTIR (cm^{-1}): 2954, 2927, 2872, 1561, 1466, 1455, 1428, 1403, 1381 and 1340.

4.2.2.2. Characterisation data of potassium octanoate, $K[OOC(CH_2)_6CH_3]$, [6]

$$CH_3(CH_2)_6COOH + KOH_{(aq)} \longrightarrow K[OOC(CH_2)_6CH_3] + H_2O$$

6

Yield: 5 g, 29 mmol, 84 %, m.p. 292-294 ˚C, Charaterisation.[3] FTIR (cm^{-1}): 2952, 2924, 2853, 1561, 1535, 1466, 1459, 1431, 1407, 1384 and 1372.

4.2.2.3. Characterisation data of potassium decanoate, $K[OOC(CH_2)_8CH_3]$, [7]

$$CH_3(CH_2)_8COOH + KOH_{(aq)} \longrightarrow K[OOC(CH_2)_8CH_3] + H_2O$$

7

Yield: 11 g, 45 mmol, 52 %, m.p. 280-283 ˚C, Charaterisation.[3] FTIR (cm^{-1}): 2954, 2923, 2849, 1561, 1465, 1456, 1429, 1411, 1382 and 1339.

4.2.2.4. Characterisation data of potassium dodecanoate, $K[OOC(CH_2)_{10}CH_3]$,[8]

$$CH_3(CH_2)_{10}COOH + KOH_{(aq)} \longrightarrow K[OOC(CH_2)_{10}CH_3] + H_2O$$

8

Yield: 11 g, 45 mmol, 90 %, m.p. 272-273 ˚C, Charaterisation.[3] FTIR (cm^{-1}): 2952, 2917, 2848, 1562, 1463, 1432, 1412, 1383, 1338 and 1328.

---

[3] All these long-chain potassium carboxylates are previously known. As in the original publications, elemental analysis could not be obtained within satisfactory limits (within 0.4% of the theoretical). Hence the original papers characterised these compounds by FTIR and powder X-ray diffraction only. This is perfectly normal in almost all long chain carboxylate or carboxylatido complexes. In this study, where elemental analysis gave satisfactory results, they were included. If not, it was omitted. For the potassium carboxylates, our FTIR results were fairly close to those of the original publications and we did not characterise them any further.

[4] T. R. Lomer *Acta Cryst.*, 1952, **5**, 11

4.2.3. Synthesis of $[Co^{II}(OOC(CH_2)_nCH_3)_2]\cdot 4H_2O$, where n = 4 for [9], 6 for [10], 8 for [11] or 10 for [12]

Synthesis of previously unknown long-chain aliphatic cobalt carboxylatido complexes $[Co^{II}(OOC(CH_2)_nCH_3)_2]\cdot 4H_2O$ where n = 4 for **[9]**, 6 for **[10]**, 8 for **[11]**, 10 for **[12]** were synthesised according to the Schemes below each section, utilizing the same general procedure. This procedure will be outlined for dihexanoatidocobalt(II) tetrahydrate while only the characterisation data will be given for the rest. These complexes were synthesised by following a modified procedure from Pereira *at el*.[5] Due to the paramagnetic property of cobalt no NMR study could be performed.

4.2.3.1. Synthesis of dihexanoatidocobalt(II) tetrahydrate, $[Co^{II}(OOC(CH_2)_4CH_3)_2]\cdot 4H_2O$, [9]

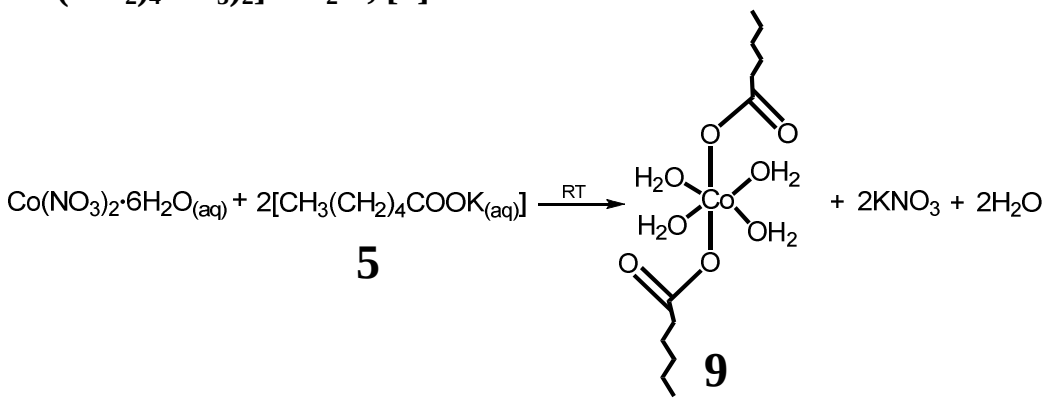

Potassium hexanoate (0.5 g, 3.24 mmol) was dissolved in minimum amount of water. An aqueous solution of $Co(NO_3)_2\cdot 6H_2O$ (0.47 g, 1.62 mmol) was prepared and added drop wise to the Potassium hexanoate solution. The solution was then stirred for 30 minutes, and the solid filtered. The purple solid that resulted was washed with a water/ethanol mixture and the product was dried in an oven at 60 ºC overnight to yield: 0.077 g, 0.2134 mmol, 13.17 % m.p. decomposes at *c.a.* 200 ˚C of pure dihexanoatidocobalt(II) tetra hydrate, FTIR (cm^{-1}): 2956, 2929, 2859, 1552, 1406, 1376, 1363 and 1319.

[5] R. F. P. Pereira, A. J. M. Valente, M. Fernandes and H. D. Burrows. *Phys. Chem. Chem. Phys.*, 2012, **14**, 7517

4.2.3.2. Charaterization data of dioctanoatidocobalt(II) tetrahydrate, $[Co^{II}(OOC(CH_2)_6CH_3)_2]\cdot 4H_2O$, [10]

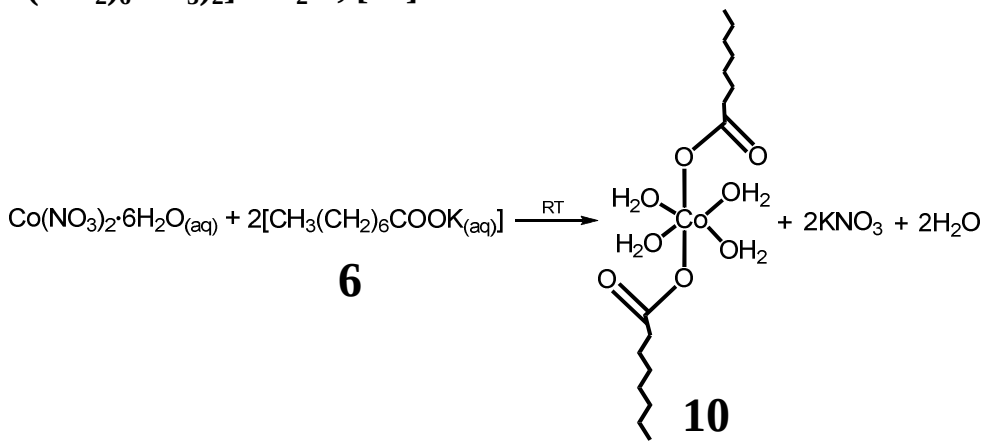

Yield: 0.27 g, 0.66 mmol, 48 %, m.p. decomposes at *c.a.* 160 ˚C, FTIR (cm^{-1}): 2955, 2923, 2853, 1547, 1406 and 1378.

4.2.3.3. Characterisation data of didecanoatidocobalt(II) tetrahydrate, $[Co^{II}(OOC(CH_2)_8CH_3)_2]\cdot 4H_2O$, [11]

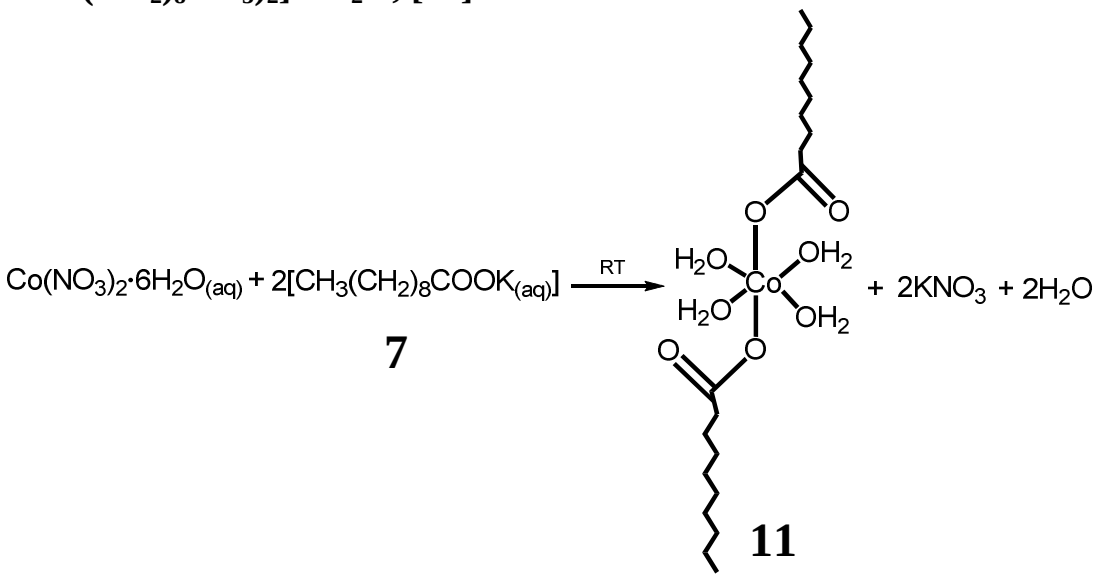

Yield: 0.2 g, 0.4 mmol, 34 %, m.p. decomposes at *c.a.* 200 ˚C, FTIR (cm^{-1}): 2955, 2920, 2851, 1551, 1407 and 1310.

4.2.3.4. Characterisation data of didodecanoatidocobalt(II) tetrahydrate $[Co^{II}(OOC(CH_2)_{10}CH_3)_2]\cdot 4H_2O$ [12]

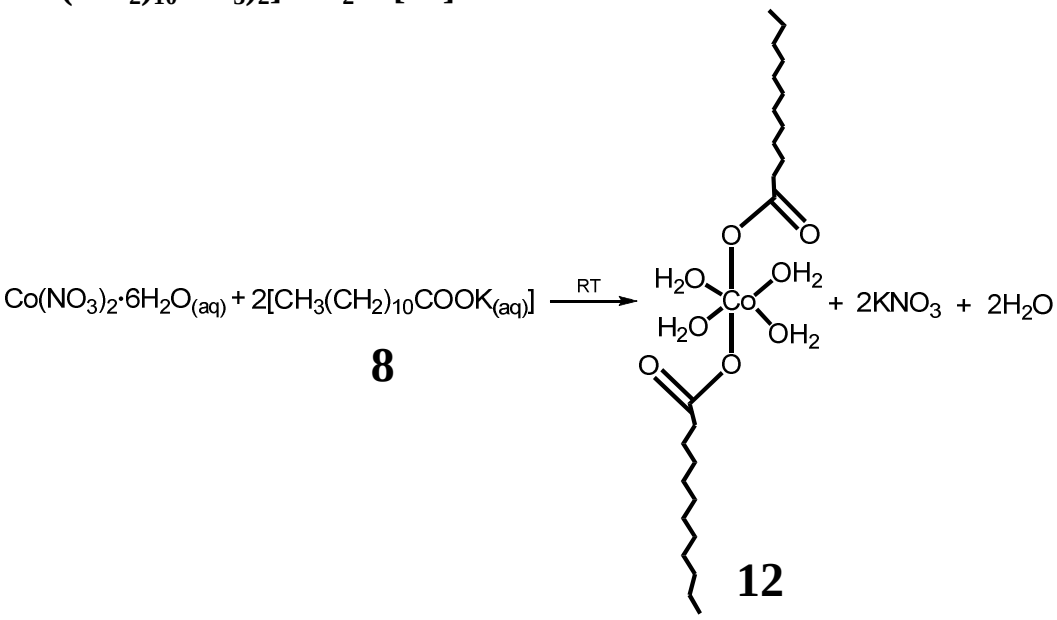

Yield: 0.15 g, 0.3 mmol, 27 %, m.p. decomposes at *c.a.* 160 ˚C, FTIR (cm^{-1}): 2955, 2919, 2850, 1623, 1588, 1545, 1466, 1408 and 1312.

4.2.4. Synthesis of $[M^{II}(OOC(CH_2)_8CH_3)_2]\cdot xH_2O$, where M = Ni for [13], Mn for [14], Zn [15], Ca for [16] or Sr for [17], x = 0-4, as well as $[Ce^{III}(OOC(CH_2)_8CH_3)_3]$, [18]

Synthesis of known long-chain aliphatic metal dicarboxylatido complexes $[M^{II}(OOC(CH_2)_8CH_3)_2]\cdot xH_2O$ where M = Ni for **[13]**, Mn for **[14]**, Zn **[15]**, Ca for **[16]** or Sr for **[17]** as well as $[Ce^{III}(OOC(CH_2)_8CH_3)_3]$ were synthesised, according to the Schemes below each section, utilizing the same general procedure. This procedure will be outlined for didecanoatidonickel(II) tetra hydrate while only the characterisation data will be given for the rest. These known complexes were synthesised, following a modified procedure from Pereira *at el.*[5] Due to the insolubility of the complexes no NMR study could be performed.

4.2.4.1. Synthesis of didecanoatidonickel(II) tetrahydrate, $[Ni^{II}(OOC(CH_2)_8CH_3)_2]\cdot 4H_2O$, [13]

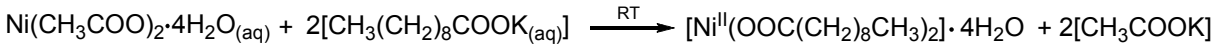

7 **13**

Potassium decanoate (0.40 g, 1.9 mmol) was dissolved in minimum amount of water. An aqueous solution of $Ni(OOCCH_3)_2\cdot 4H_2O$ (0.24 g, 0.95 mmol) was prepared and added drop wise to the Potassium decanoate solution. The solution was then stirred for 30 minutes, and the solid filtered. The green solid that resulted was washed with a water/ethanol mixture and the product was dried in an oven at 60 ºC overnight to Yield: 0.7 g, 1.6 mmol, 54 %, m.p. decomposes at *c.a.* 250-251 ˚C, FTIR (cm^{-1}): 2958, 2916, 2847, 1695, 1544, 1464, 1405, 1335, 1304, 1269, 1241, 1204, 1112 and 722.

4.2.4.2. Characterisation data of didecanoatidomanganese(II), $[Mn^{II}(OOC(CH_2)_8CH_3)_2]$, [14]

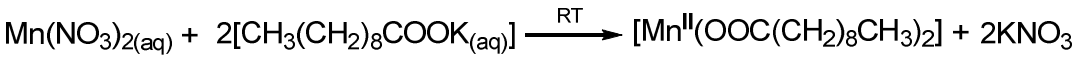

7 **14**

Yield: 0.9 g, 2 mmol, 86 %, m.p. 168-169 ˚C, FTIR (cm^{-1}): 3341, 3193, 2954, 2918, 2872, 2849, 1678, 1562, 1467, 1460, 1413, 1370, 1356, 1334, 1405, 1269, 1236, 1200, 1074 and 696.

4.2.4.3. Characterisation data of didecanoatidozinc(II), $[Zn^{II}(OOC(CH_2)_8CH_3)_2]$, [15]

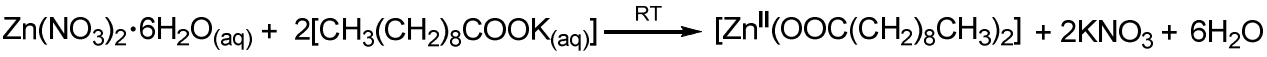

7 **15**

Yield: 0.9 g, 2 mmol, 82 %, m.p. 136-137 ˚C, Elemental Analysis: calc. C: 59.08 %; H: 9.43 %, found: C: 58.75 %; H: 9.05 %, FTIR (cm^{-1}): 2952, 2914, 2849, 1534, 1455, 1396, 1341, 1317, 1279, 1243, 1204, 1079 and 741

4.2.4.4. Characterisation data of didecanoatidocalcium(II) monohydrate, $[Ca^{II}(OOC(CH_2)_8CH_3)_2]\cdot H_2O$, [16]

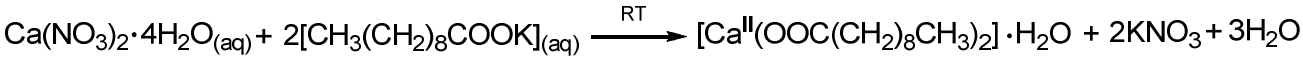

7 **16**

Yield: 0.8 g, 1.9 mmol, 80 %, m.p. 220-221 ˚C, Elemental Analysis: calc. C: 62.79 %; H: 10.02 %, found: C: 62.70 %; H: 9.84 %, FTIR (cm^{-1}): 3570, 3368, 2957, 2919, 2847, 1627, 1576, 1537, 1466, 1431, 1415, 1334, 1308, 1116, 723.

4.2.4.5. Characterisation data of didecanoatidostrontium(II), $[Sr^{II}(OOC(CH_2)_8CH_3)_2]$, [17]

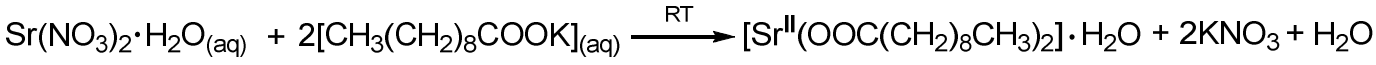

7 **17**

Yield: 0.8 g, 1.9 mmol, 40 %, m.p. 169-170 ˚C, FTIR (cm^{-1}): 2957, 2925, 2846, 1510, 1458, 1448, 1442, 1406, 1334, 1310, 1289, 1197, 1118 and 723.

4.2.4.6. Characterisation data of tridecanoatidocerium(III), $[Ce^{III}(OOC(CH_2)_8CH_3)_3]$, [18]

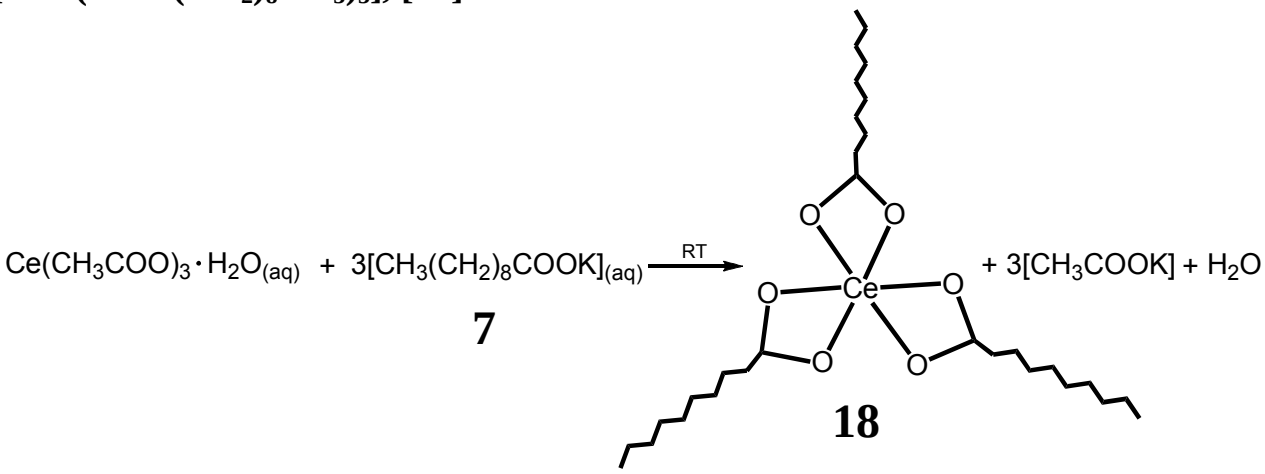

7 **18**

Yield: 0.9 g, 1.4 mmol, 87 %, m.p. 149-150 ˚C, Elemental Analysis: calc. C: 55.10 %; H: 8.79 %, found: C: 53.81 %; H: 8.66 %, FTIR (cm^{-1}): 2956, 2919, 2850, 1561, 1534, 1411, 1433 and 1309.

4.2.5. Synthesis of $[Pd^{II}Co^{II}(\mu\text{-}OOC(CH_2)_nCH_3)_4]\cdot H_2O$, where n = 4 for [19], 6 for [20], 8 for [21] or 10 for [22], utilising Method 1

Synthesis of new long-chain aliphatic tertracarboxylatidopalladium(II)cobalt(II) monohydrate complexes $[Pd^{II}Co^{II}(\mu\text{-}OOC(CH_2)_nCH_3)_4]\cdot H_2O$, where n = 4 for **[19]**, 6 for **[20]**, 8 for **[21]** and 10 for **[22]**. The complexes were synthesised according to the Schemes below each section, utilizing the same general procedure. This procedure will be outlined for tetrahexanoatidopalladium(II)cobalt(II) mono hydrate while only the characterisation data will be given for the rest. These four novel complexes were synthesised by following a modified procedure from Kozitsyna, *et al.*[6] and Akhmadullina, *et al.*[7] Due to the paramagnetic properties of cobalt no NMR studies could be performed.

4.2.5.1. Synthesis of tetrahexanoatidopalladium(II)cobalt(II) monohydrate, $[Pd^{II}Co^{II}(\mu\text{-}OOC(CH_2)_4CH_3)_4]\cdot H_2O$, [19]

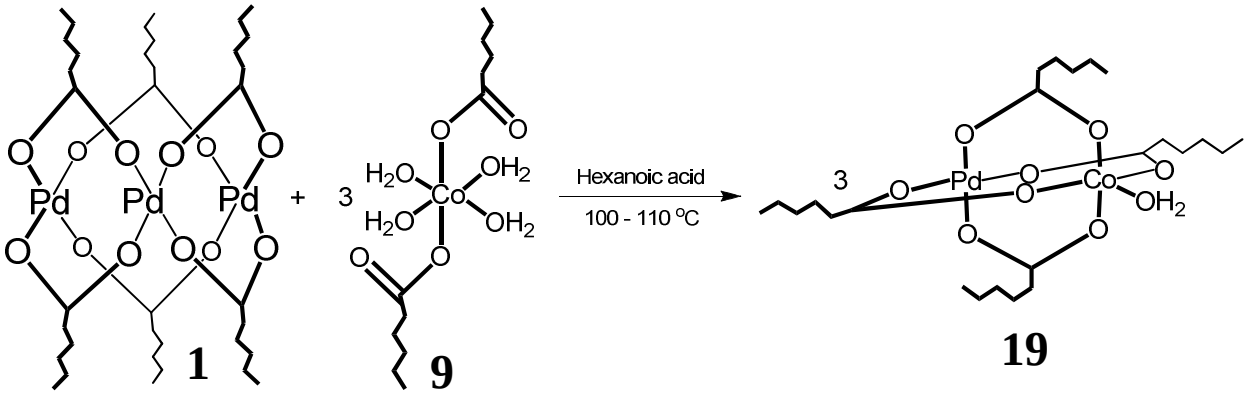

Dihexanoatidocobalt(II) tetrahydrate (0.1 g, 0.28 mmol) was added to a suspension of hexakis(hexanoatido)tripalladium(II) (0.1 g, 0.1 mmol) in hexanoic acid (minimum amount) in a three necked round bottom flask (50 ml). This mixture was heated to 100 - 110 ºC while stirring. Through one of the necks of the flask compressed air was passed over the reaction. This caused the excess acid to evaporate from the reaction mixture and through the other neck of the flask the acid crystallised in a collection beaker, this may take 5 hours to 1 day, depending in the chain length. The resulting yield (based on cobalt) 0.12 g, 0.186 mmol, pure tetrahexanoatidopalladium(II)cobalt(II) mono hydrate (71 %), m.p. 52-53 ˚C, Elemental Analysis: calc. C: 43.54 %; H: 7.31 %. found: C: 43.87 %; H: 7.24 % FTIR (cm^{-1}): 3370, 2954, 2929, 2870, 1589, 1534, 1440, 1400, 1341, 1308, 1229, 1190, 1111, 722.

[6] N. Y. Kozitsyna, S. E. Nefedov, F. M. Dolgushin, N. V. Cherkashina, M. N. Vergaftik and I. I. Moiseev, *Inorg. Chim. Acta*, 2006, **359**, 2072

[7] N. S. Akhmadullina, N. V. Cherkashina, N. Kozisyna, I. P. Stolarov, E. V. Perova, A. E. Gekhman, S. E. Nefedov, M. N. Vargaftik, I. I. Moiseev, *Inorg. Chim. Acta*, 2009, **362**, 1943

4.2.5.2. Characterisation data of tetraoctanoatidopalladium(II)cobalt(II) mono hydrate, $[Pd^{II}Co^{II}(\mu\text{-}OOC(CH_2)_6CH_3)_4]\cdot H_2O$, [20]

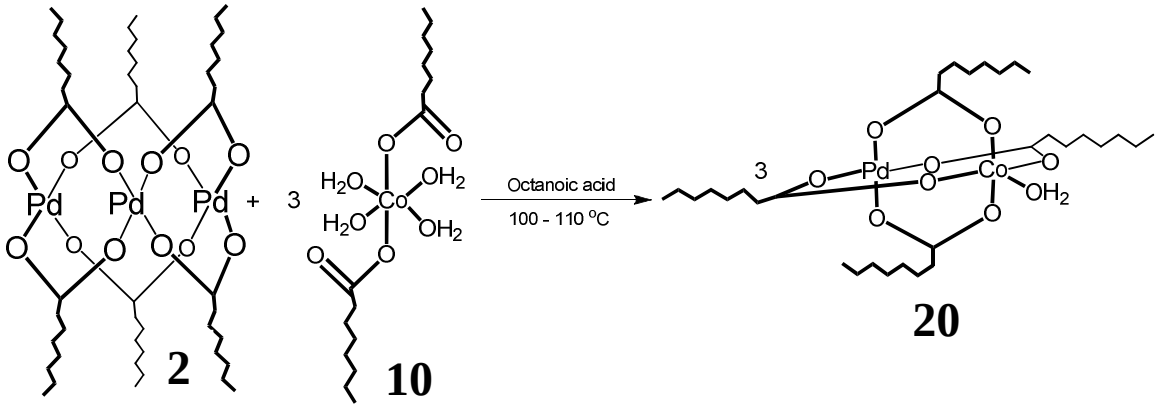

2 **10** **20**

Yield (based on cobalt): 0.16 g, 0.222 mmol, 89 %, m.p. 76-77 ˚C, Elemental Analysis: calc. C: 50.83 %; H: 8.26 %. found: C: 51.10 %; H: 8.41 %, FTIR (cm^{-1}): 2955, 2919, 2851, 1709, 1590, 1515, 1465, 1420, 1405, 1312, 1113, 719.

4.2.5.3. Characterisation data of tetradecanoatidopalladium(II)cobalt(II) mono hydrate, $[Pd^{II}Co^{II}(\mu\text{-}OOC(CH_2)_8CH_3)_4]\cdot H_2O$, [21]

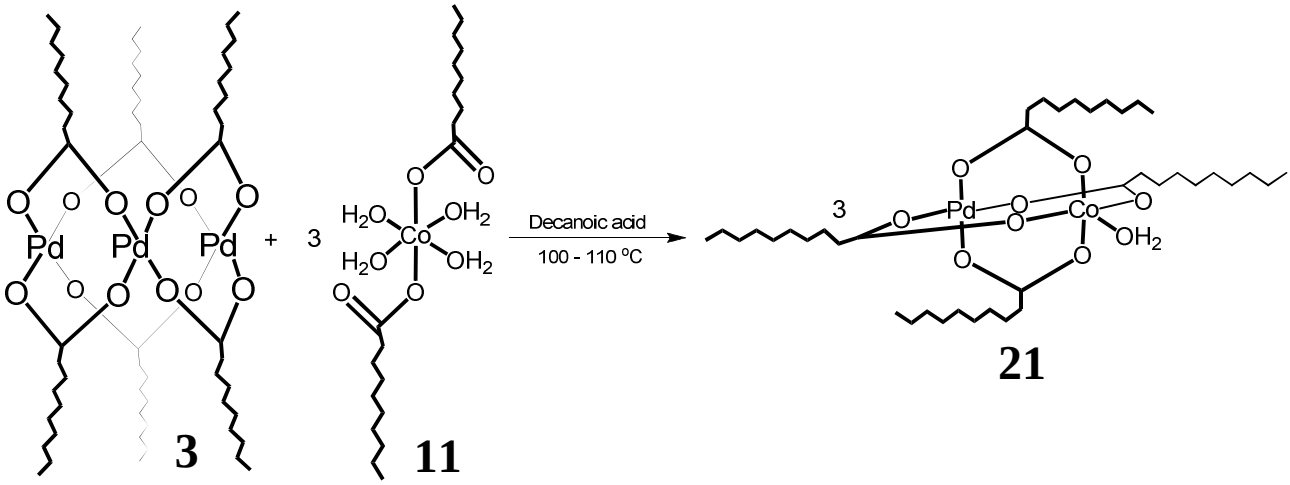

3 **11** **21**

This compound can be crystallised by dissolving the powder in DCM, and overlayed with n-Hexane in a test tube covered with parrafilm with a few holes poked inside it. After 5 days crystals suitable for X-ray crystallography may be obtained. Yield (based on cobalt): 0.12 g, 0.1382 mmol, 62 %, m.p. 83-84 ˚C, Elemental Analysis: calc. C: 54.20 %; H: 9.10 %. found, C: 54.24 %; H: 9.13 %, FTIR (cm^{-1}): 2955, 2915, 2849, 1589, 1517, 1464, 1420, 1404, 1314, 1113, 720.

4.2.5.4. Characterisation data of tetradodecanoatidopalladium(II)cobalt(II) mono hydrate, $[Pd^{II}Co^{II}(\mu\text{-}OOC(CH_2)_{10}CH_3)_4]\cdot H_2O$, [22]

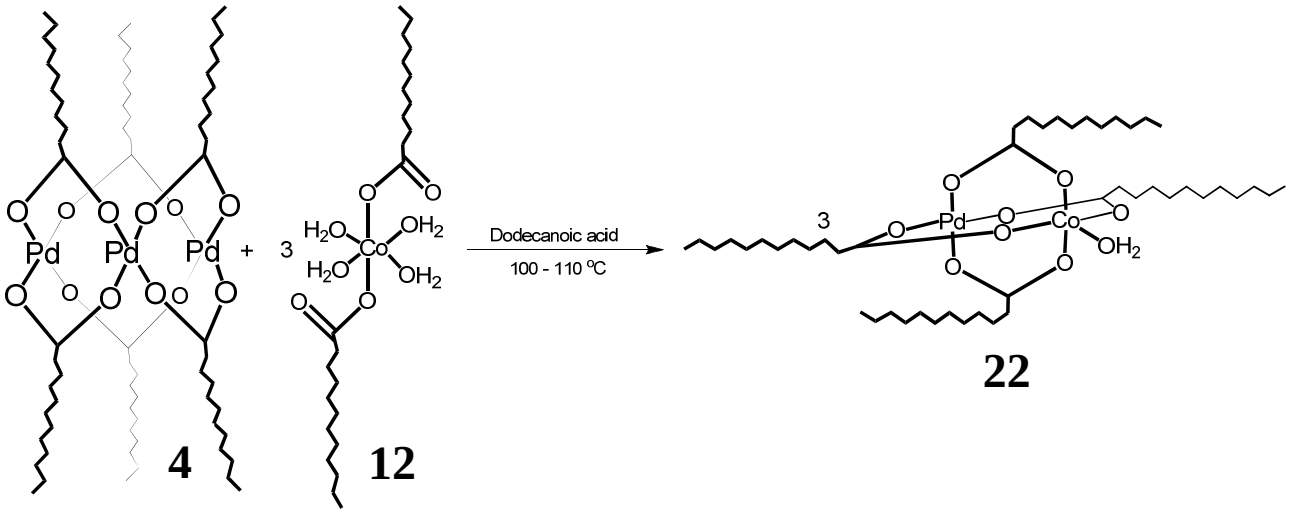

Yield (based on cobalt): 0.12 g, 0.122 mmol, 62 %, m.p. 84-85 ˚C, Elemental Analysis: calc. C: 61.40 %; H: 10.20 %. found: C: 61.52 %; H: 9.85 %, FTIR (cm^{-1}): 2916, 2850, 1590, 1560, 1516, 1466, 1420, 1406, 1316, 1114, 719

4.2.6. Synthesis of $[Pd^{II}M^{II}(\mu\text{-}OOCCH_3)_4]\cdot H_2O$, where M = Zn for [23], Ba for[24], Cd for [25], Ca for [26], Sr for [27], Ni for [28], Co for [29], Mn for [30] or Cu for [31] as well as $[Pd^{II}Ce^{III}(\mu\text{-}OOCCH_3)_4]\cdot H_2O$ [32], utilising Method 1

Synthesis of the known short-chain tetracarboxylatidopalladium(II)metal(II) complexes, $[Pd^{II}M^{II}(\mu\text{-}OOCCH_3)_4]\cdot H_2O$, where M = Zn for **[23]**, Ba for **[24]**, Cd for **[25]**, Ca for **[26]**, Sr for **[27]**, Ni for **[28]**, Co for **[29]**, Mn for **[30]** or Cu for **[31]** as well as $[Pd^{II}Ce^{III}(\mu\text{-}OOCCH_3)_4]\cdot H_2O$ **[32]**, utilising Method 1. The complexes were synthesised according to the Schemes below each section, utilizing the same general procedure. This procedure will be outlined for tetraacetatidopalladium(II)zinc(II) while only the characterisation data will be given for the rest. These published complexes were synthesised by following a modified procedure from Kozitsyna, *et al.*[6] and Akhmadullina, *et al.*[7]

4.2.6.1. Synthesis of tetraacetatidopalladium(II)zinc(II) mono hydrate, $[Pd^{II}Zn^{II}(\mu\text{-}OOCCH_3)_4]\cdot H_2O$, [23]

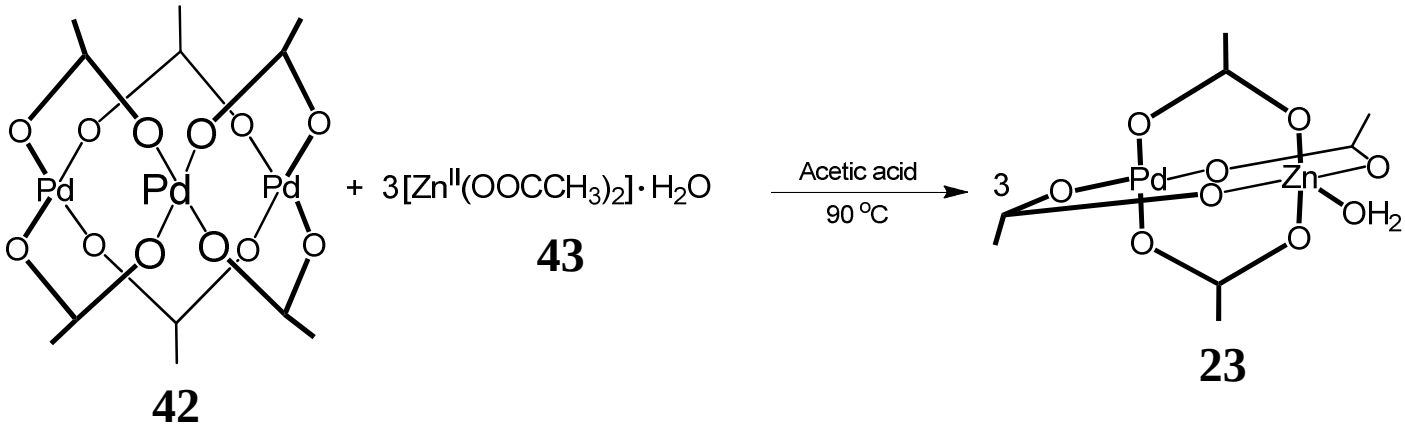

42 **43** **23**

Hexaacetatidotripalladium(II) (0.1 g, 0.4454 mmol) and diacetatidozinc(II) (0.082 g, 0.4454 mmol) was added to acetic acid (2 mL). The solution was gently refluxed for 3 hours and let to cool overnight in the reaction vessel. The precipitate was filtered and washed with cold n-Hexane and Benzene. The solid obtained was dried in an oven at 60 ˚C. Yield: 0.16 g, 0.382 mmol, 86 %, m.p.: Decomposes before melting, above 170 ˚C, Elemental Analysis: calc. C: 26.39 %; H: 4.06 %. found, C: 26.67 %; H: 4.28 %, δ_H (300 MHz, $CDCl_3$)/ppm: 2.37 (12 H, s, 4 x C<u>H</u>$_3$), FTIR (cm^{-1}): 3201, 3024, 2986, 2938, 1587, 1537, 1409, 1394, 1348, 1051, 697.

4.2.6.2. Characterisation data of tetraacetatidopalladium(II)barium(II) mono hydrate, $[Pd^{II}Ba^{II}(\mu\text{-}OOCCH_3)_4]\cdot H_2O$, [24]

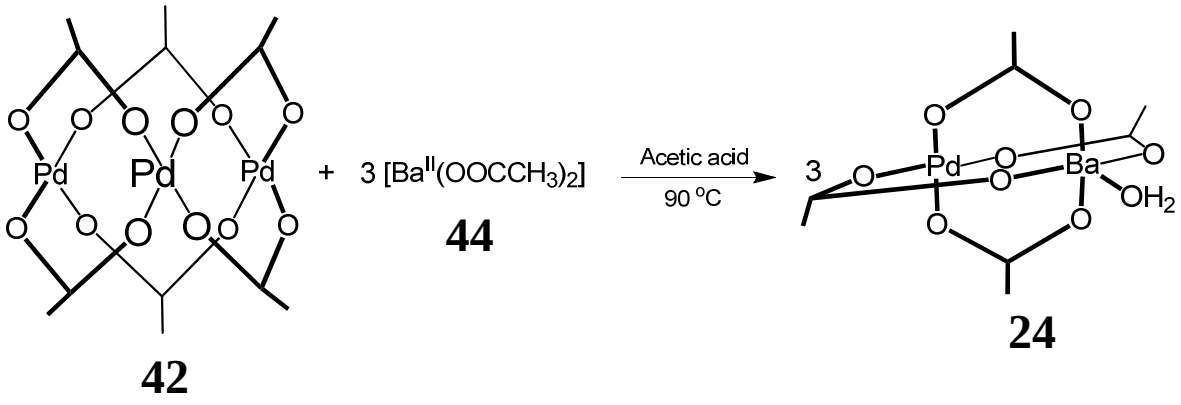

42 **44** **24**

Yield: 0.16 g, 0.34 mmol, 76 %, m.p.: Decomposes before melting, above 170 ˚C, Elemental Analysis: calc. C: 19.28 %; H: 2.83 %. found, C: 19.10 %; H: 2.67 %, δ_H (300 MHz, $CDCl_3$)/ppm: not soluble, FTIR (cm^{-1}): 3399, 3011, 2984, 2933, 1630, 1600, 1551, 1420, 1375, 1320, 1022, 685.

4.2.6.3. Characterisation data of tetraacetatidopalladium(II)cadmium(II), mono hydrate, $[Pd^{II}Cd^{II}(\mu\text{-}OOCCH_3)_4]\cdot 2CH_3COOH\cdot H_2O$, [25]

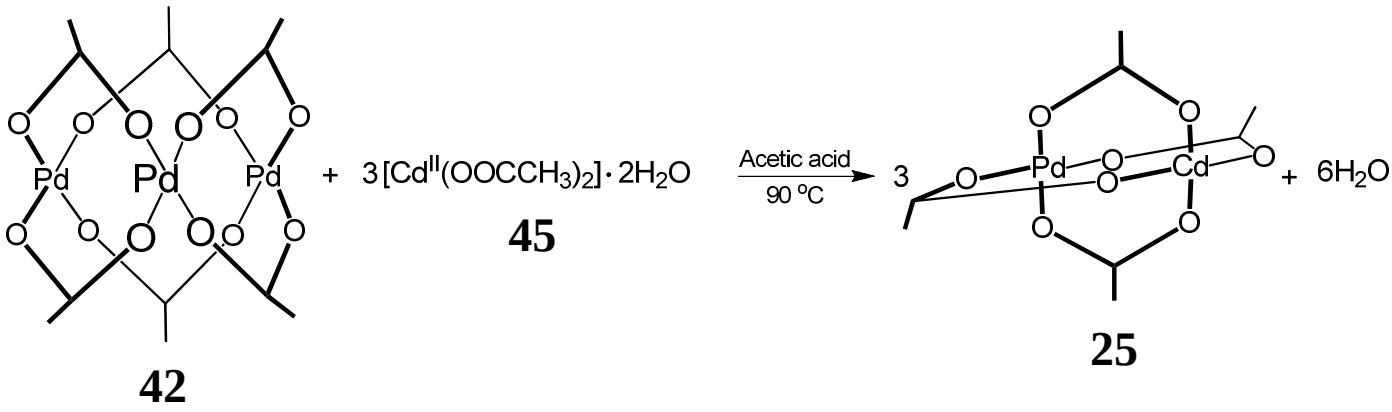

42 **25**

Yield: 0.14 g, 0.23 mmol, 51 %, m.p.: Decomposes before melting, above 170 ˚C, Elemental Analysis: calc. C: 20.26 %; H: 2.98 %. found, C: 19.94 %; H: 2.84 %, δ_H (300 MHz, $CDCl_3$)/ppm: c.a. 1.50 (water), 2.26 (3 H, s, 1 x $C\underline{H}_3$), FTIR (cm^{-1}): 3402, 3013, 2985, 2941, 1731, 1616, 1537, 1518, 1404, 1374, 1339, 1235, 1029, 696.

4.2.6.4. Characterisation data of tetraacetatidopalladium(II)calcium(II) mono hydrate, $[Pd^{II}Ca^{II}(\mu\text{-}OOCCH_3)_4]\cdot H_2O$, [26]

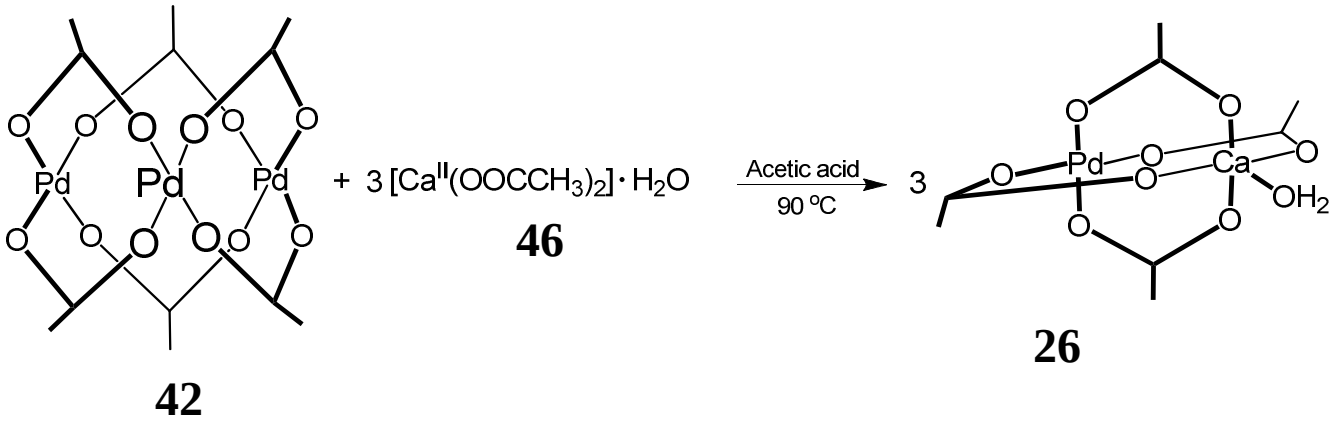

42 **26**

Yield: 0.12 g, 0.24 mmol, 54 %, m.p.: Decomposes before melting, above 170 ˚C, Elemental Analysis: calc. C: 24.00 %; H: 3.53 %. found, C: 23.62 %; H: 3.48 %, δ_H (300 MHz, $CDCl_3$)/ppm: *c.a.* 1.50 (water), 2.13 (12 H, s, 4 x $C\underline{H}_3$), FTIR (cm^{-1}): 3398, 3016, 2972, 2937, 1708, 1630, 1564, 1437, 1400, 1375, 1335, 1029, 691.

4.2.6.5. Characterisation data of tetracetatidopalladium(II)strontium(II) mono hydrate, $[Pd^{II}Sr^{II}(\mu\text{-}OOCCH_3)_4]\cdot H_2O$, [27]

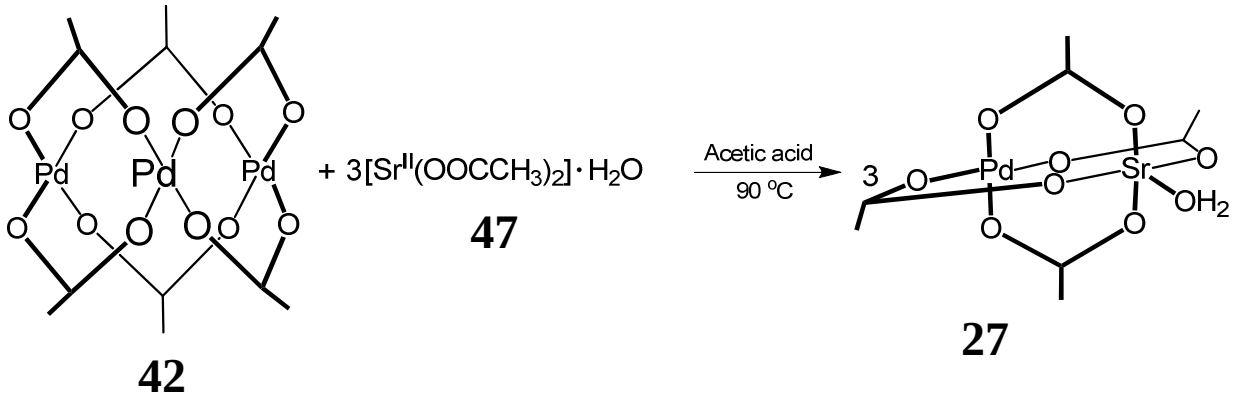

42 **27**

Yield: 0.13 g, 0.298 mmol, 67 %, m.p.: Decomposes before melting, above 170 ˚C, Elemental Analysis: calc. C: 21.43 %; H: 3.15 %. found, C: 21.12 %; H: 3.02 %, δ_H (300 MHz, $CDCl_3$)/ppm: *c.a.* 1.50 (water), 2.13 (12 H, s, 4 x C<u>H</u>$_3$), FTIR (cm^{-1}): 3390, 3012, 2932, 2853, 1698, 1637, 1602, 1564, 1429, 1407, 1369, 1348, 1289, 1020, 690.

4.2.6.6. Characterisation data of tetraacetatidopalladium(II)nickel(II) mono hydrate, $[Pd^{II}Ni^{II}(\mu\text{-}OOCCH_3)_4]\cdot H_2O$, [28]

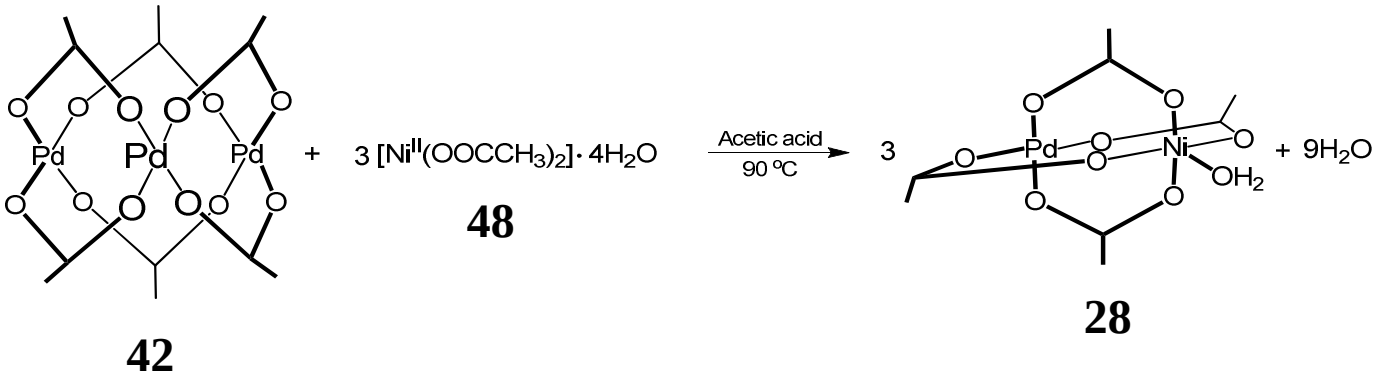

42 **28**

Yield: 0.19 g, 0.35 mmol, 79 %, m.p.: Decomposes before melting, above 170 ˚C, Elemental Analysis: calc. C: 27.15 %; H: 3.42 %. found, C: 27.26 %; H: 3.50 %, δ_H (300 MHz, $CDCl_3$)/ppm: *c.a.* 1.50 (water), 1.90 (12 H, s, 4 x C<u>H</u>$_3$), FTIR (cm^{-1}): 3251, 1706, 1596, 1524, 1451, 1431, 1395, 1379, 1340, 1251, 1019, 699.

4.2.6.7. Characterisation data of tetraacetatidopalladium(II)cobalt(II) diacetic acid mono hydrate, $[Pd^{II}Co^{II}(\mu\text{-}OOCCH_3)_4]\cdot 2CH_3COOH\cdot H_2O$, [29]

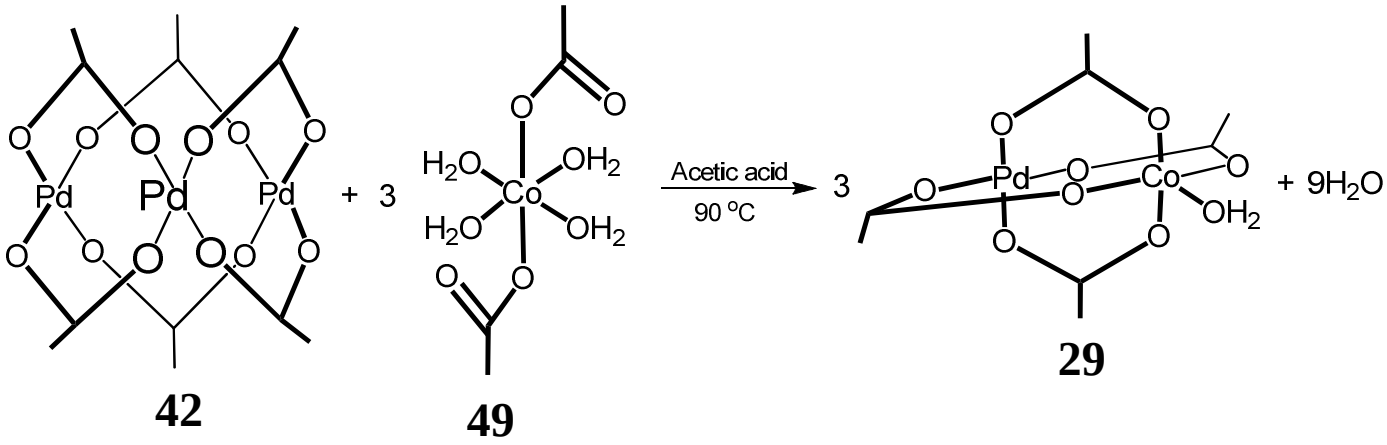

Yield: 1.071 g, 1.995 mmol, 90 %, m.p.: Decomposes before melting, above 170 ˚C, Elemental Analysis: calc. C: 27.14 %; H: 3.42 %. found, C: 27.34 %; H: 3.49 %, δ_H (300 MHz, $CDCl_3$)/ppm: paramagnetic, FTIR (cm^{-1}): 3229, 3021, 1703, 1634, 1619, 1600, 1394, 1375, 1344, 1326, 1258, 1022, 693.

4.2.6.8. Characterisation data of tetraacetatidopalladium(II)managanese(II), mono hydrate $[Pd^{II}Mn^{II}(\mu\text{-}OOCCH_3)_4]\cdot H_2O$, [30]

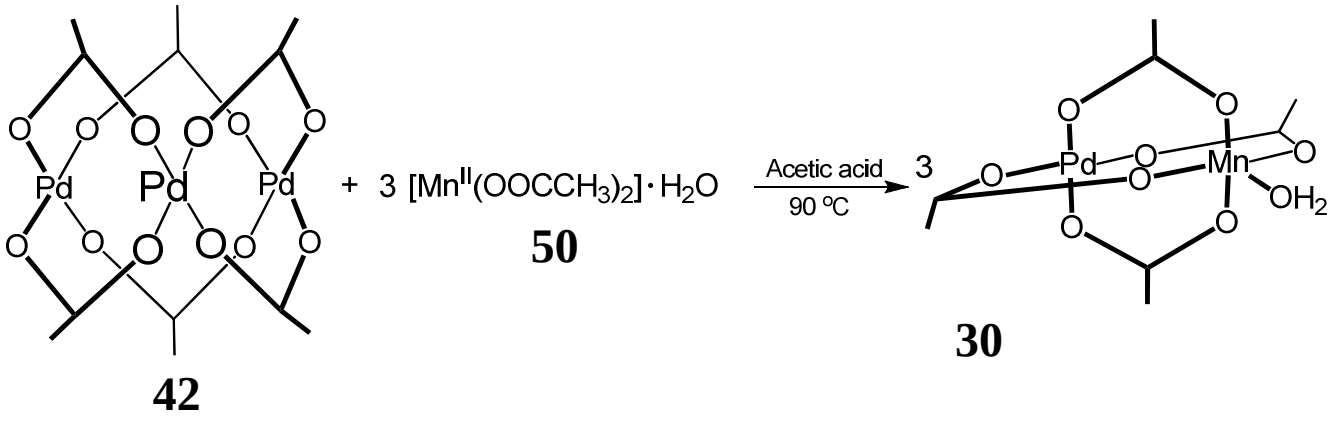

Yield: 0.143 g, 0.344 mmol, 77 %, m.p.: Decomposes before melting, above 170 ˚C, Elemental Analysis: calc. C: 29.57 %; H: 4.55 %. found, C: 28.96 %; H: 4.59 %, δ_H (300 MHz, $CDCl_3$)/ppm: paramagnetic, FTIR (cm^{-1}): 3294, 3252, 3169, 1622, 1601, 1540, 1494, 1471, 1400, 1339, 1119, 1026, 691.

4.2.6.9. Characterisation data of tetraacetatidopalladium(II)copper(II), $[Pd^{II}Cu^{II}(\mu\text{-}OOCCH_3)_4]$, [31]

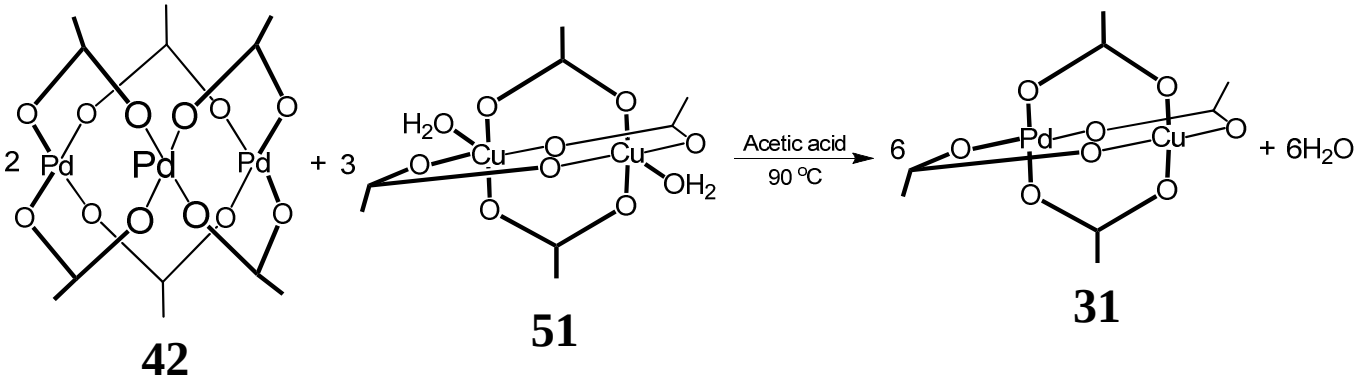

42 **51** **31**

Yield: 0.112 g, 0.277 mmol, 62 %, m.p.: Decomposes before melting, above 170 ˚C, Elemental Analysis: calc. C: 26.48 %; H: 4.07 %. found, C: 27.02 %; H: 4.31 %, δ_H (300 MHz, $CDCl_3$)/ppm: *c.a.* 1.50 (water), 1.91 (12 H, s, 4 x C<u>H</u>$_3$), FTIR (cm^{-1}): 3013, 2989, 2938, 1572, 1524, 1426, 1402, 1348, 1051, 689.

4.2.6.10. Characterisation data of tetraacetatidopalladium(II)cerium(III) mono hydrate, $[Pd^{II}Ce^{III}(\mu\text{-}OOCCH_3)_4]\cdot H_2O$, [32]

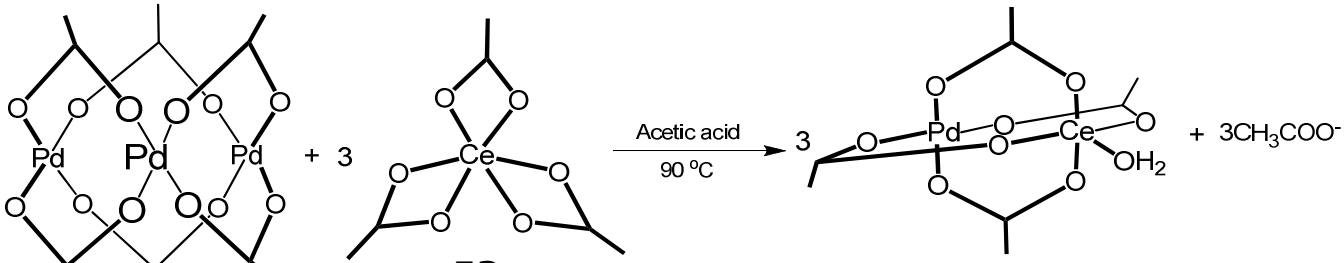

42 **52** **32**

Yield: 0.17 g, 0.28 mmol, 71 %, m.p.: Decomposes before melting, above 170 ˚C, Elemental Analysis: calc. C: 27.74 %; H: 3.97 %. found, C: 27.69 %; H: 3.95 %, δ_H (300 MHz, $CDCl_3$)/ppm: *c.a.* 1.50 (water), 1.90 (12 H, s, 4 x C<u>H</u>$_3$), FTIR (cm^{-1}): 3388, 3016, 2983, 2936, 1701, 1619, 1608, 1536, 1402, 1377, 1340, 1025, 688.

4.2.7. Synthesis of $[Pd^{II}M^{II}(\mu\text{-}OOC(CH_2)_8CH_3)_4]$, where M = Ca for [35], Zn for [36], Sr for [37], Ni for [38] or Mn for [39] as well as $[Pd^{II}Ce^{III}(\mu\text{-}OOC(CH_2)_8CH_3)_4]\cdot H_2O$ [41], utilising Method 1

Synthesis of previously unknown long-chain aliphatic tertracarboxylatidopalladium(II)metal(II) complexes, M = Ca for **[35]**, Zn for **[36]**, Sr for **[37]**, Ni for **[38]** or Mn for **[39]** as well as $[Pd^{II}Ce^{III}(\mu\text{-}OOC(CH_2)_8CH_3)_4]$ **[41]**, utilising Method 1. The complexes were synthesised according to the Schemes below each section, utilizing the same general procedure. This procedure will be outlined for tetradecanoatidopalladium(II)calcium(II) while only the characterisation data will be given for the rest. These six novel complexes were synthesised by following a modified procedure from Kozitsyna, *et al.*[6] and Akhmadullina, *et al.*[7]

4.2.7.1. Characterisation data of tetradecanoatidopalladium(II)calcium(II), $[Pd^{II}Ca^{II}(\mu\text{-}OOC(CH_2)_8CH_3)_4]$, [35]

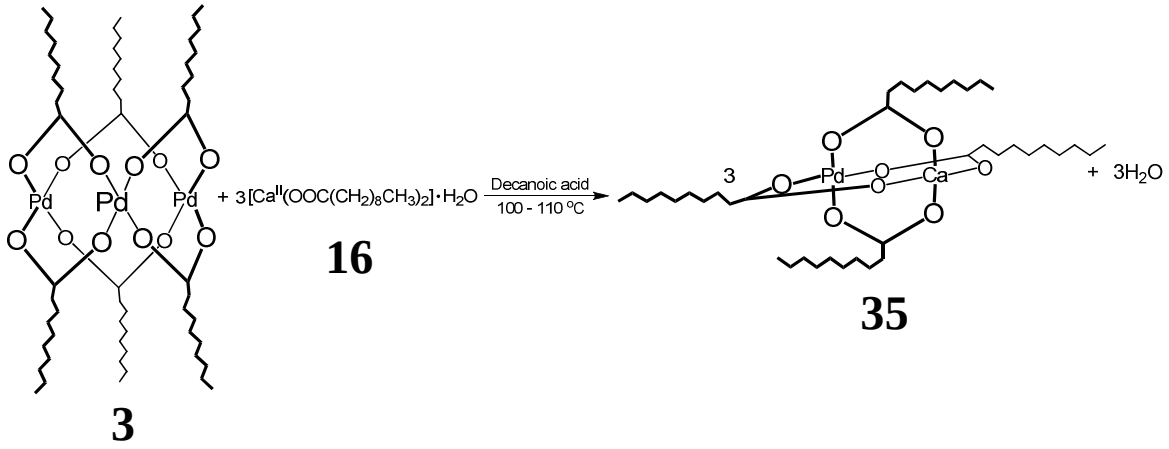

3 **16** **35**

Didecanoatidocalcium(II) mono hydrate (0.05 g, 0.111 mmol) was added to a suspension of hexadecanoatidotripalladium(II) (0.052 g, 0.037 mmol) in decanoic acid (minimum amount) in a three necked round bottom flask (50 ml). This mixture was heated to 100 - 110 ºC while stirring. Through one of the necks of the flask compressed air was passed over the reaction. This caused the excess acid to evaporate from the reaction mixture and through the other neck of the flask the acid crystallised in a collection beaker. This may take about 1 day, for decanoic acid. Yield (based on Calcium): 0.15 g, 0.18 mmol, 58 %, m.p. 78-79 ˚C, Elemental Analysis: calc. C: 56.58 %; H: 9.27 %. found: C: 57.03 %; H: 9.44 %, δ_H (300 MHz, $CDCl_3$)/ppm: 0.81 – 0.99 (12 H, t, 4 x C$\underline{H}_3$), 1.05 – 1.49 (52 H, m, 26 x C$\underline{H}_2$), 1.57 – 1.75 (4 H, m, 2 x C$\underline{H}_2$), 2.03 – 2.18 (4 H, t, 2 x C$\underline{H}_2$), 2.30 – 2.44 (4 H, t, C$\underline{H}_2$), FTIR (cm^{-1}): 3366, 2919, 2853, 1708, 1621, 1606, 1568, 1542, 1457, 1400, 1112, 721.

4.2.7.2. Characterisation data of tetradecanoatidopalladium(II)zinc(II), $[Pd^{II}Zn^{II}(\mu\text{-}OOC(CH_2)_8CH_3)_4]$, [36]

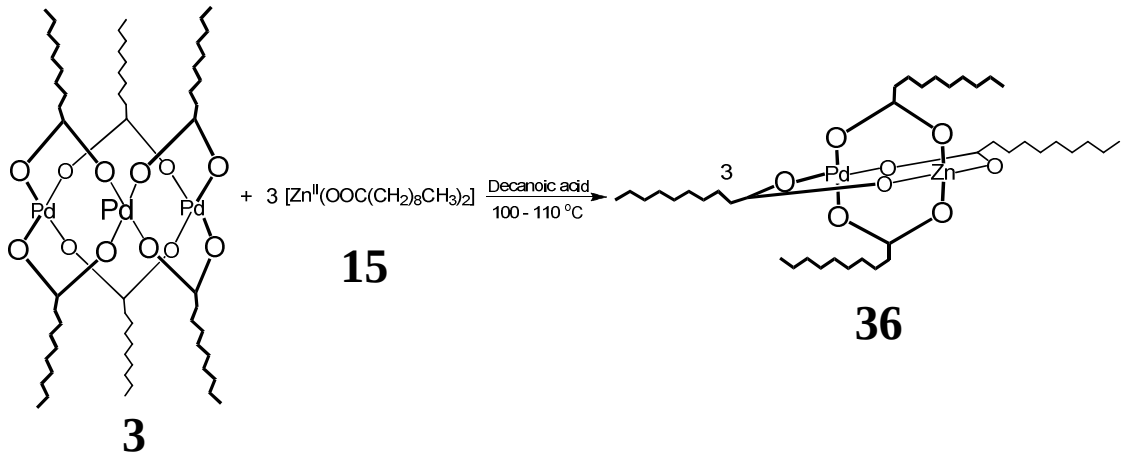

3 **15** **36**

This compound was crystallised by dissolving the powder in DCM, and overlayed with n-Hexane in a test tube covered with parrafilm with a few holes poked inside it. After 5 days crystals suitable for X-ray crystallography may be obtained. Yield (based on zinc): 0.14 g, 0.16 mmol, 56 %, m.p. 103-104 ˚C, Elemental Analysis: calc. C: 56.18 %; H: 8.96 %. found: C: 55.90 %; H 9.00 %, δ_H (300 MHz, $CDCl_3$)/ppm: 0.79 – 0.96 (12 H, t, 4 x C<u>H</u>$_3$), 1.03 – 1.40 (48 H, m, 24 x C<u>H</u>$_2$), 1.44 – 1.82 (8 H, m, 4 x C<u>H</u>$_2$), 2.13 – 2.58 (8 H, m, 4 x C<u>H</u>$_2$), FTIR (cm^{-1}): 2916, 2849, 1712, 1608, 1593, 1547, 1523, 1465, 1458, 1422, 1407, 1398, 1315, 1117, 720.

4.2.7.3. Characterisation data of tetradecanoatidopalladium(II)strontium(II), $[Pd^{II}Sr^{II}(\mu\text{-}OOC(CH_2)_8CH_3)_4]\cdot H_2O$, [37]

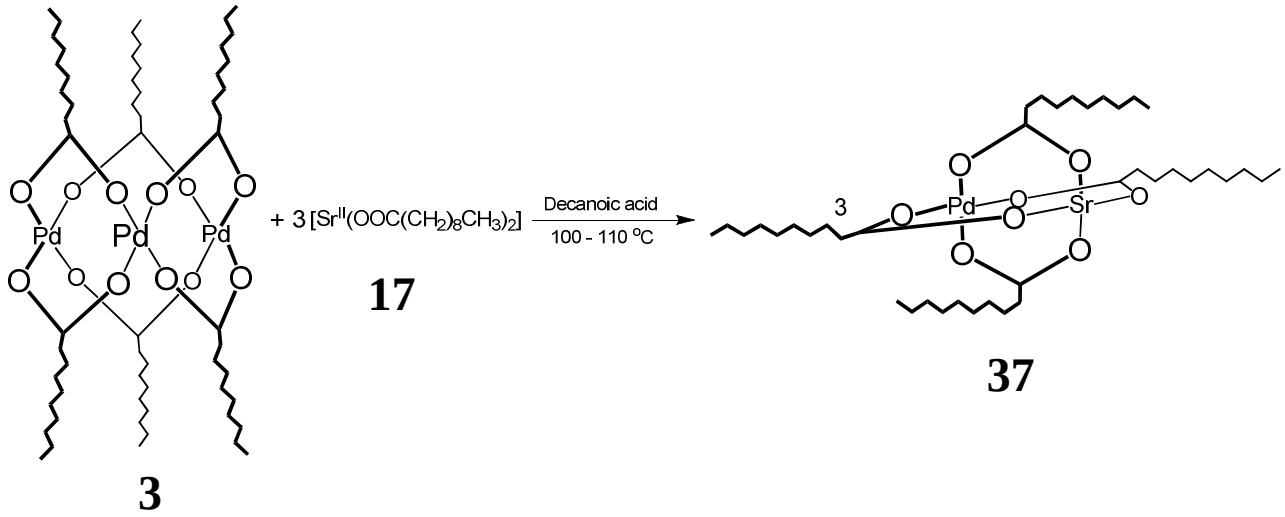

3 **17** **37**

Yield (based on strontium): 0.19 g, 0.21 mmol, 95 %, m.p. 63-64 ˚C, Elemental Analysis: calc. C: 54.65 %; H: 8.72 %. found: C: 55.23 %; H: 8.64 %, δ_H (300 MHz, $CDCl_3$)/ppm: 0.78 – 0.98 (12 H, t, 3 x C<u>H</u>$_3$), 0.99 – 1.55 (52 H, m, 26 x C<u>H</u>$_2$), 1.58 – 1.74 (4 H, m, 2 x C<u>H</u>$_2$), 1.99 – 2.22 (4 H, m, 2

x C<u>H</u>$_2$), 2.26 – 2.70 (4 H, m, 2 x C<u>H</u>$_2$), FTIR (cm^{-1}): 2919, 2850, 1706, 1628, 1608, 1540, 1459, 1444, 1395, 1297, 1110, 720.

4.2.7.4. Characterisation data of tetradecanoatidopalladium(II)nickel(II), [Pd^{II}Ni^{II}(μ-OOC(CH$_2$)$_8$CH$_3$)$_4$], [38]

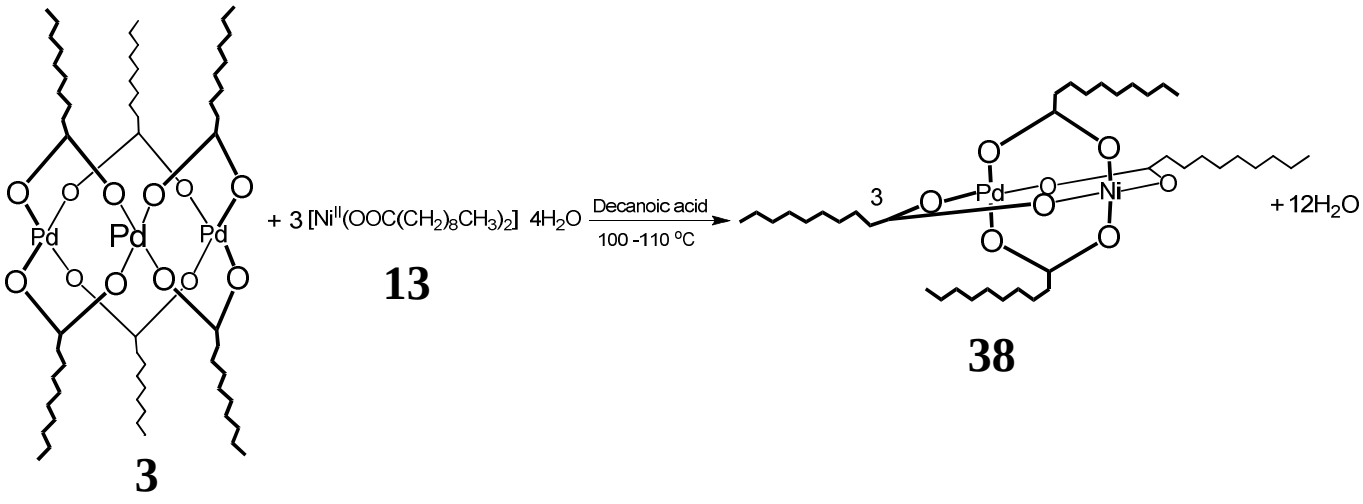

3 **13** **38**

This compound can be crystallised by dissolving the powder in DCM, and overlayed with n-Hexane in a test tube covered with parrafilm with a few holes poked inside it. After 5 days crystals suitable for X-ray crystallography may be obtained. Yield (based on nickel): 0.33 g, 0.38 mmol, 90 %, m.p. 94-95 ˚C, Elemental Analysis: calc. C: 58.03 %; H: 9.62 %. found: C: 57.53 %; H 9.48 %, δ_H (300 MHz, $CDCl_3$)/ppm: 0.73 – 1.13 (12 H, t, 4 x C<u>H</u>$_3$), 1.13 – 4.15 (64 H, m, 32 x C<u>H</u>$_2$), FTIR (cm^{-1}): 2915, 2848, 1588, 1538, 1515, 1468, 1440, 1405, 1307, 1119, 721.

4.2.7.5. Characterisation data of tertadecanoatidopalladium(II)manganese(II), [Pd^{II}Mn^{II}(μ-OOC(CH$_2$)$_8$CH$_3$)$_4$], [39]

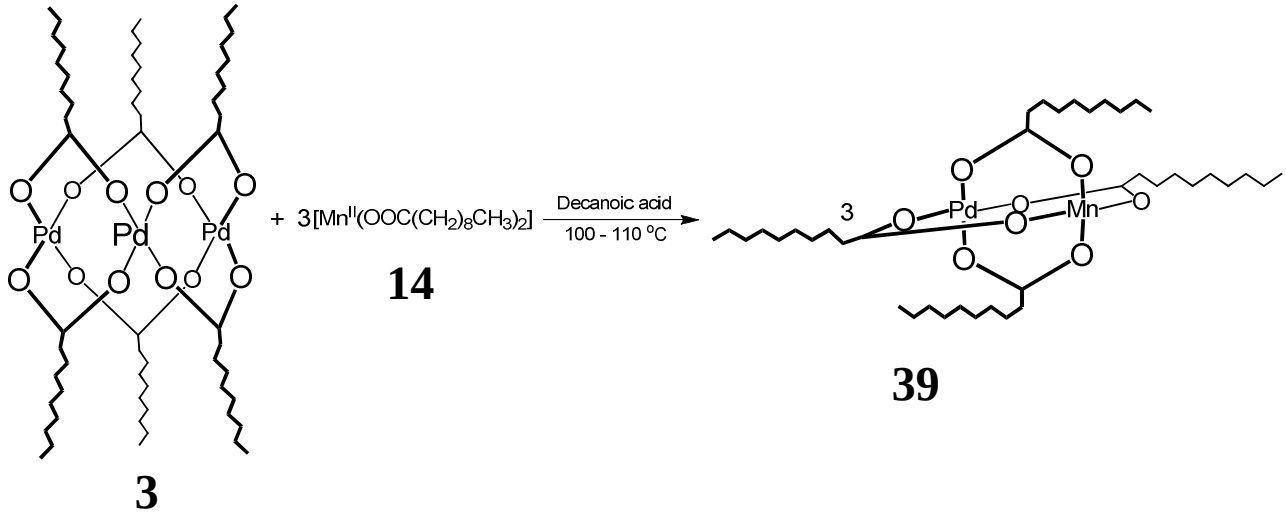

3 **14** **39**

Yield (based on manganese): 0.16 g, 0.19 mmol, 86 %, m.p. 77-78 ˚C, Elemental Analysis: calc. C: 56.78 %; H: 9.06 %. found: C: 56.77 %; H 9.05 %, δ_H (300 MHz, $CDCl_3$)/ppm: 0.15 – 2.49 (76 H,

m, 4 x C<u>H</u>$_3$, 32 x C<u>H</u>$_2$), FTIR (cm^{-1}): 3324, 2919, 2851, 1688, 1594, 1559, 1458, 1406, 1317, 1115, 723.

4.2.7.6. Characterisation data of tetradecanoatidopalladium(II)cerium(III), $[Pd^{II}Ce^{III}(\mu\text{-}OOC(CH_2)_8CH_3)_4]^+$, [41]

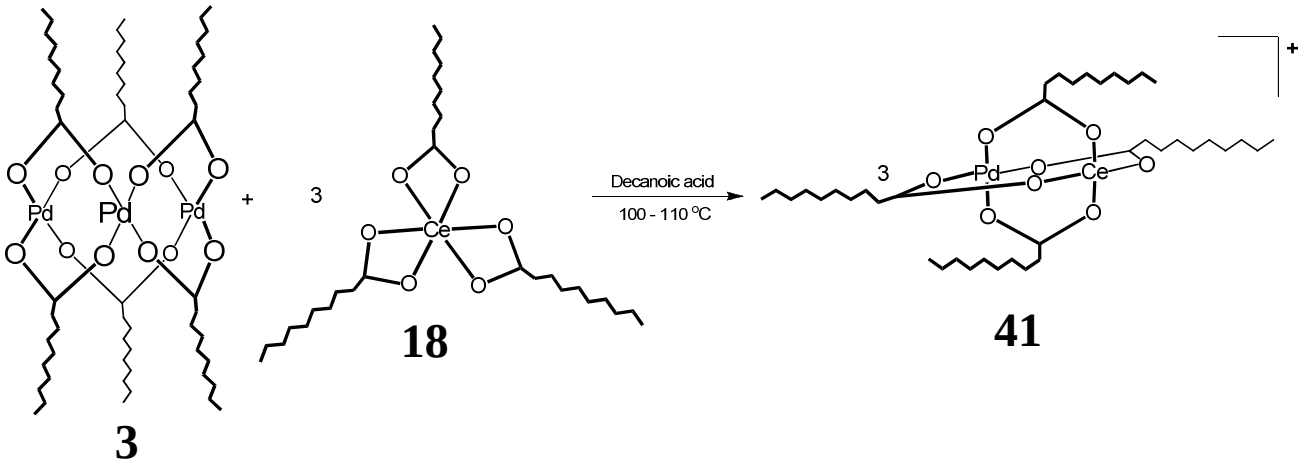

3 **18** **41**

Yield (based on cerium): 0.15 g, 0.16 mmol, 72 %, m.p. 54-55 ˚C, Elemental Analysis: calc. C: 52.74 %; H: 8.75 %. found: C: 53.33 %; H 8.20 %, δ_H (300 MHz, $CDCl_3$)/ppm: 0.73 – 0.95 (12 H, t, 4 x C<u>H</u>$_3$), 0.96 – 1.90 (64 H, m, 32 x C<u>H</u>$_2$), FTIR (cm^{-1}): 3382, 2922, 2853, 1701, 1618, 1591, 1556, 1453, 1408, 1309, 1115, 723.

4.2.6. Synthesis of $[Pd^{II}Co^{II}(\mu\text{-}OOC(CH_2)_nCH_3)_4]\cdot H_2O$, where for n = 4 for [19], 6 for [20], 8 for [21] or 10 for [22], utilising method 2

Synthesis of previously unknown long-chain aliphatic paddlewheel tertracarboxylatidopalladium(II)cobalt(II) mono hydrate complexes $[Pd^{II}Co^{II}(\mu\text{-}OOC(CH_2)_nCH_3)_4]\cdot H_2O$, where n = 4 for **[19]**, 6 for **[20]**, 8 for **[21]** and 10 for **[22]**. The complexes were synthesised according to the Schemes below each section, utilizing the same general procedure. This procedure will be outlined for tetrahexanoatidopalladium(II)cobalt(II) mono hydrate while only the characterisation data will be given for the rest. These four novel complexes were synthesised by following a ligand exchange reaction. Due to the paramagnetic properties of Cobalt no NMR studies could be performed.

4.2.6.1. Synthesis of tetrahexanoatidopalladium(II)cobalt(II) mono hydrate, $[Pd^{II}Co^{II}(\mu\text{-}OOC(CH_2)_4CH_3)_4]\cdot H_2O$, [19]

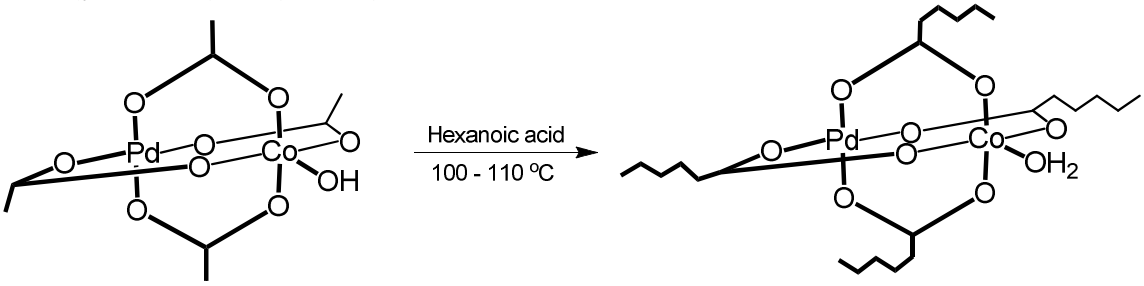

29 **19**

Tetraacetatidopalladium(II)cobalt(II) (0.1 g, 0.209 mmol) was suspended in hexanoic acid (minimum amount). The solution was heated to 100 - 110 ˚C, under compressed air flow until all excess acid was removed depending on the chain length this may take 5 hours to 1 day. Yield: 0.13 g, 0.207 mmol, 99 %, m.p. 52-53 ˚C, Elemental Analysis: calc. C: 44.78 %; H: 7.21 %. found, C: 44.27 %; H 7.07 %, FTIR (cm^{-1}): 3370, 2954, 2929, 2870, 1589, 1534, 1440, 1400, 1341, 1308, 1229, 1190, 1111, 722.

4.2.6.2. Characterisation data of tetraoctanoatidopalladium(II)cobalt(II) mono hydrate, $[Pd^{II}Co^{II}(\mu\text{-}OOC(CH_2)_6CH_3)_4]\cdot H_2O$, [20]

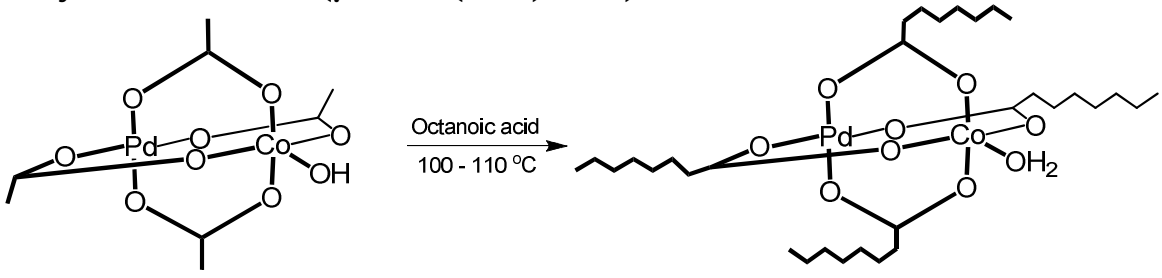

29 **20**

Yield: 0.13 g, 0.17 mmol, 81 %, m.p. 76-77 ˚C, Elemental Analysis: calc. C: 52.08 %; H: 8.20 %. found: C: 52.17 %; H 7.82 %, FTIR (cm^{-1}): 2955, 2919, 2851, 1709, 1590, 1515, 1465, 1420, 1405, 1312, 1113, 719

4.2.6.3. Characterisation data of tetradecanoatidopalladium(II)cobalt(II) mono hydrate, $[Pd^{II}Co^{II}(\mu\text{-}OOC(CH_2)_8CH_3)_4]\cdot H_2O$, [21]

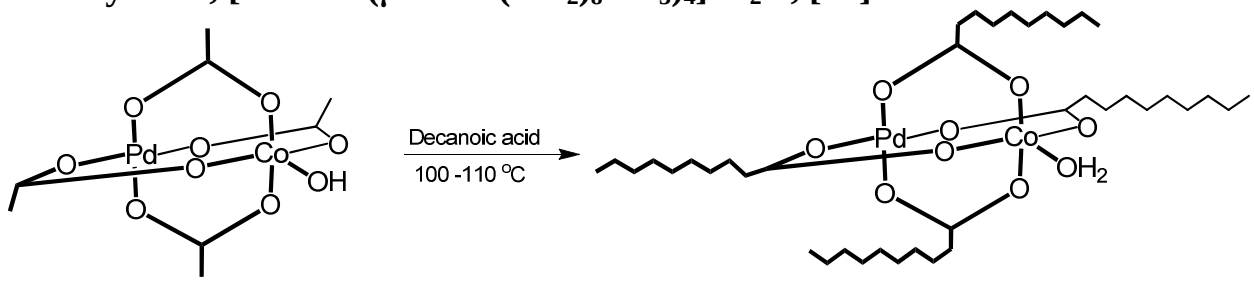

29 **21**

Yield: 0.12 g, 0.139 mmol, 66 %, m.p. 83-84 ˚C, Elemental Analysis: calc. C: 55.34 %; H: 9.06 %. found, C: 55.04 %; H 8.61 %, FTIR (cm^{-1}): 2955, 2915, 2849, 1589, 1517, 1464, 1420, 1404, 1314, 1113, 720.

4.2.6.4. Characterisation data of tetradodecanoatidopalladium(II)cobalt(II) mono hydrate, $[Pd^{II}Co^{II}(\mu\text{-}OOC(CH_2)_{10}CH_3)_4]\cdot H_2O$, [22]

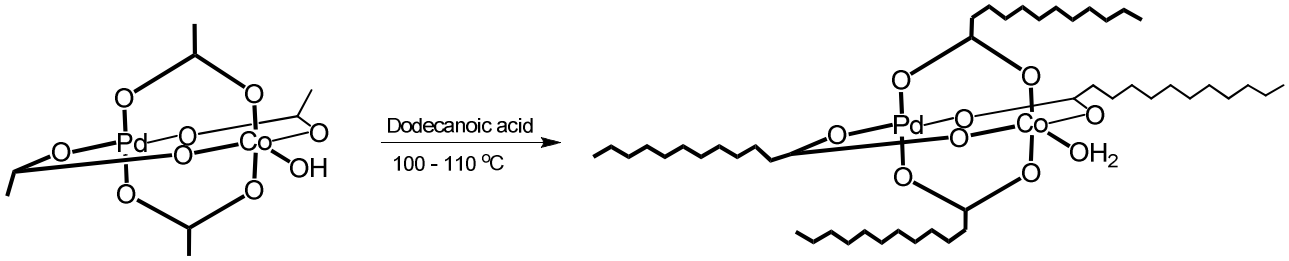

29 **22**

Yield: 0.14 g, 0.22 mmol, 88 %, m.p. 84-85 ˚C, Elemental Analysis: calc. C: 59.91 %; H: 9.64 %. found: C: 59.96 %; H 10.83 %, FTIR (cm^{-1}): 2916, 2850, 1590, 1560, 1516, 1466, 1420, 1406, 1316, 1114, 719

4.2.7. Synthesis of $[Pd^{II}M^{II}(\mu\text{-}OOC(CH_2)_8CH_3)_4]$, where M = Ba for [33], Cd for [34], Ca for [35], Zn for [36], Sr for [37], Ni for [38] or Mn for [39], Cu for [40] as well as $[Pd^{II}Ce^{III}(\mu\text{-}OOC(CH_2)_8CH_3)_4]$, [41], utilising Method 2

Synthesis of previously unknown long-chain aliphatic tetracarboxylatidopalladium(II)metal(II) complexes The complexes were synthesised according to the Schemes below each section, utilizing the same general procedure. This procedure will be outlined for tetradecanoatidopalladium(II)barium(II) while only the characterisation data will be given for the rest. These nine novel complexes were synthesised by following a ligand exchange reaction.

4.2.7.1. Synthesis of tetradecanoatidopalladium(II)barium(II), $[Pd^{II}Ba^{II}(\mu\text{-}OOC(CH)_8CH_3)_4]$, [33]

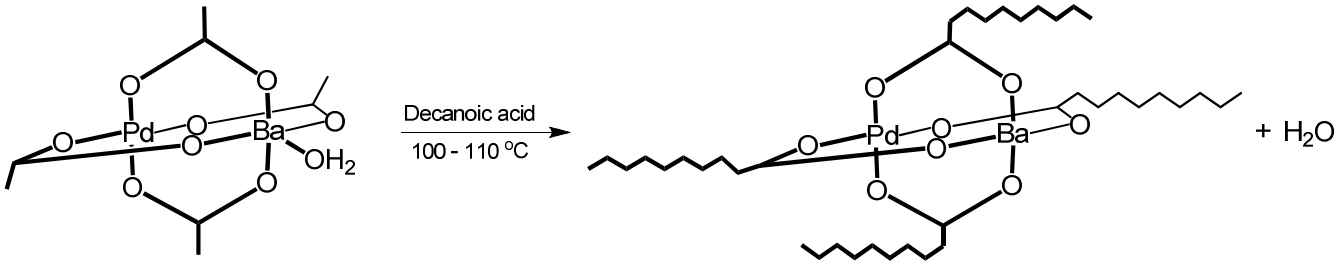

24 **33**

Tetraacetatidopalladium(II)barium(II) (0.1 g, 0.2008 mmol) was suspended in decanoic acid (minimum amount). The solution was stirred, and heated to 100 - 110 ˚C, under compressed air flow until all excess acid was removed. For decanoic acid this may take 1 day. Yield: 0.143 g, 0.151 mmol, 75 %, m.p. 55-56 ˚C, Elemental Analysis: calc. C: 52.88 %; H: 8.76 %. found, C: 52.44 %; H 8.95 %, δ_H (300 MHz, $CDCl_3$)/ppm: 0.81 – 0.96 (12 H, t, 4 x C<u>H</u>$_3$), 1.03 – 1.50 (52 H, m, 26 x C<u>H</u>$_2$), 1.51 – 2.45 (12 H, m, 6 x C<u>H</u>$_2$), FTIR (cm^{-1}): 2920, 2851, 1703, 1645, 1629, 1573, 1548, 1467, 1441, 1387, 1301, 1113, 720.

4.2.7.2. Characterisation data of tetradecanoatidopalladium(II)cadmium(II), $[Pd^{II}Cd^{II}(\mu\text{-}OOC(CH)_8CH_3)_4]$, [34]

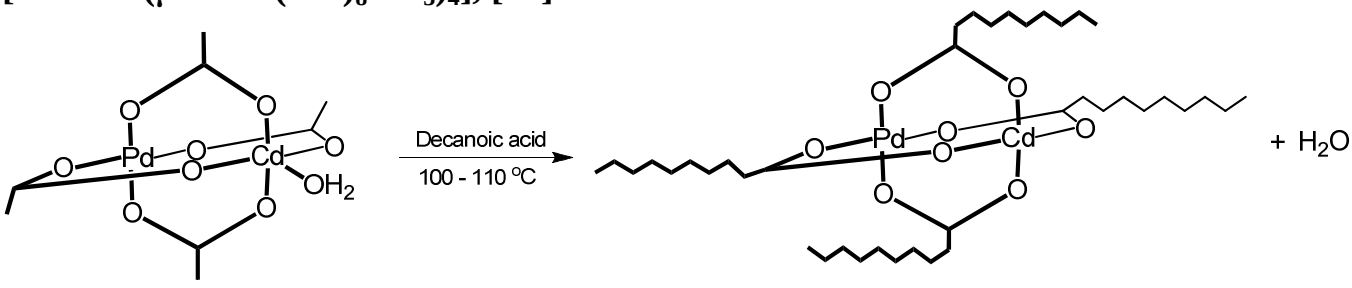

25 **34**

Yield: 0.138 g, 0.149 mmol, 88 %, m.p. 51-52 ˚C, Elemental Analysis: calc. C: 52.04 %; H: 8.52 %, found: C: 51.49 %; H 8.85 %, δ_H (300 MHz, $CDCl_3$)/ppm: 0.84 – 0.93 (12 H, t, 4 x C<u>H</u>$_3$), 1.01 – 1.35 (48 H, m, 24 x C<u>H</u>$_2$), 1.36 – 1.58 (8 H, m, 4 x C<u>H</u>$_2$), 2.03 – 2.17 (8 H, m, 4 x C<u>H</u>$_2$), FTIR (cm^{-1}): 3339, 2922, 2851, 1686, 1600, 1564, 1526, 1456, 1400, 1316, 1114, 721.

4.2.7.3. Characterisation data of tetradecanoatidopalladium(II)calcium(II), $[Pd^{II}Ca^{II}(\mu\text{-}OOC(CH)_8CH_3)_4]$, [35]

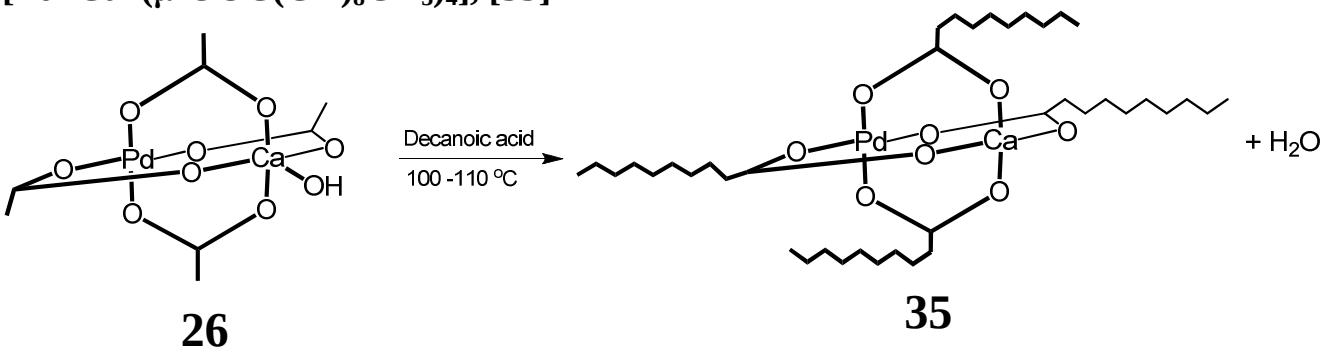

26 **35**

Yield: 0.12 g, 0.136 mmol, 71 %, m.p. 78-79 ˚C, Elemental Analysis: calc. C: .56.58 %; H: 9.27 %, found: C: 56.93 %; H: 9.33 %, δ_H (300 MHz, $CDCl_3$)/ppm: 0.81 – 0.99 (12 H, t, 4 x C<u>H</u>$_3$), 1.05 – 1.49 (52 H, m, 26 x C<u>H</u>$_2$), 1.57 – 1.75 (4 H, m, 2 x C<u>H</u>$_2$), 2.03 – 2.18 (4 H, t, 2 x C<u>H</u>$_2$), 2.30 – 2.44 (4 H, t, C<u>H</u>$_2$),FTIR (cm^{-1}): 3366, 2919, 2853, 1708, 1621, 1606, 1568, 1542, 1457, 1400, 1112, 721.

4.2.7.4. Characterisation data of tetradecanoatidopalladium(II)zinc(II), $[Pd^{II}Zn^{II}(\mu\text{-}OOC(CH)_8CH_3)_4]$, [36]

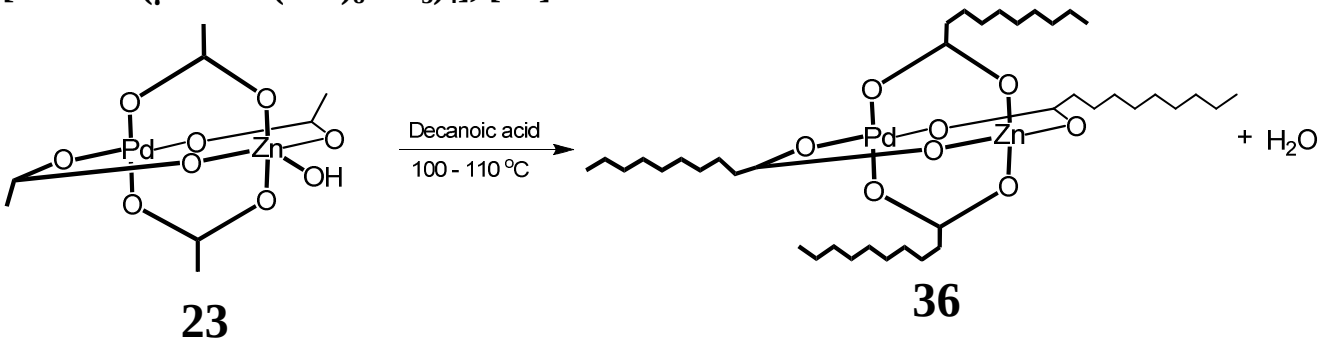

23 **36**

Yield: 0.15 g, 0.175 mmol, 95 %, m.p. 103-104 ˚C, Elemental Analysis: calc. C: 57.56 %; H: 9.56 %, found: C: 57.15 %; H 9.08 %, δ_H (300 MHz, $CDCl_3$)/ppm: 0.79 – 0.96 (12 H, t, 4 x C<u>H</u>$_3$), 1.03 – 1.40 (48 H, m, 24 x C<u>H</u>$_2$), 1.44 – 1.82 (8 H, m, 4 x C<u>H</u>$_2$), 2.13 – 2.58 (8 H, m, 4 x C<u>H</u>$_2$), FTIR (cm^{-1}): 2916, 2849, 1712, 1608, 1593, 1547, 1523, 1465, 1458, 1422, 1407, 1398, 1315, 1117, 720.

4.2.7.5. Characterisation data of tetradecanoatidopalladium(II)strontium(II) $[Pd^{II}Sr^{II}(\mu\text{-}OOC(CH)_8CH_3)_4]$, [37]

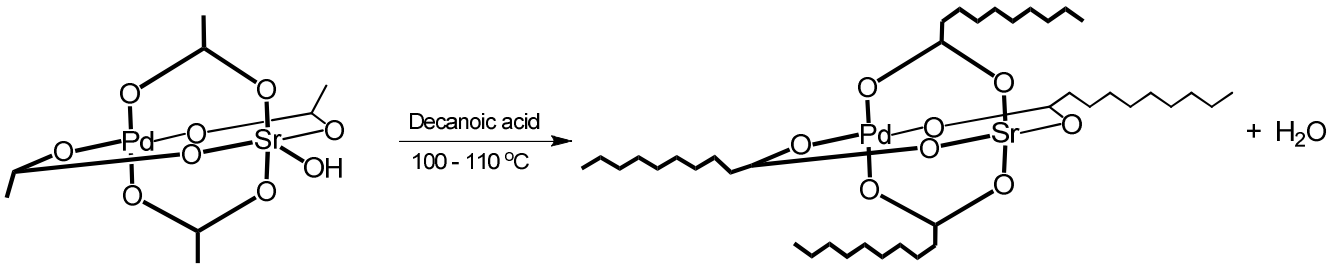

27 **37**

Yield: 0.081 g, 0.0909 mmol, 81 %, m.p. 63-64 ˚C, Elemental Analysis: calc. C: 54.85 %; H: 9.32 %, found: C: 55.25 %; H: 9.04 %, δ_H (300 MHz, $CDCl_3$)/ppm: 0.78 – 0.98 (12 H, t, 3 x C<u>H</u>$_3$), 0.99 – 1.55 (52 H, m, 26 x C<u>H</u>$_2$), 1.58 – 1.74 (4 H, m, 2 x C<u>H</u>$_2$), 1.99 – 2.22 (4 H, m, 2 x C<u>H</u>$_2$), 2.26 – 2.70 (4 H, m, 2 x C<u>H</u>$_2$), FTIR (cm^{-1}): 2919, 2850, 1706, 1628, 1608, 1540, 1459, 1444, 1395, 1297, 1110, 720.

4.2.7.6. Characterisation data of tetradecanaotidopalladium(II)nickel(II) $[Pd^{II}Ni^{II}(\mu\text{-}OOC(CH)_8CH_3)_4]$, [38]

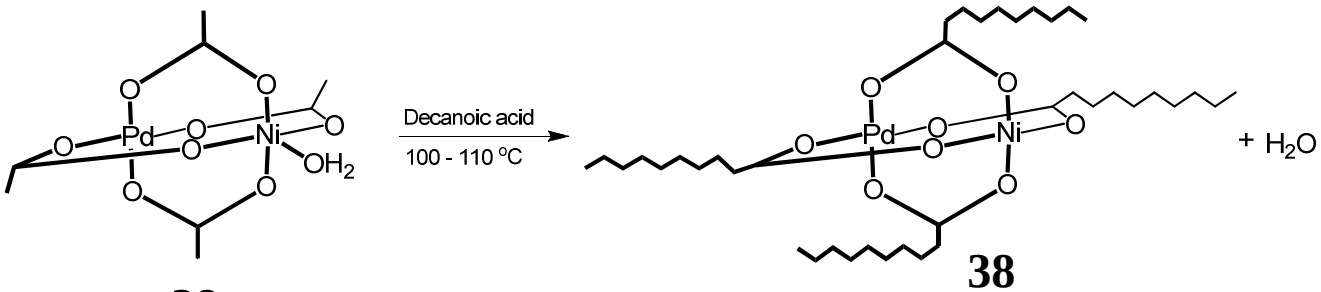

28 **38**

Yield: 0.15 g, 0.175 mmol, 95 %, m.p. 94-96 ˚C, Elemental Analysis: calc. C: 58.03 %; H: 9.62 %, found: C: 57.50 %; H: 9.24 %, δ_H (300 MHz, $CDCl_3$)/ppm: 0.73 – 1.13 (12 H, t, 4 x C<u>H</u>$_3$), 1.13 – 4.15 (64 H, m, 32 x C<u>H</u>$_2$), FTIR (cm^{-1}): 2915, 2848, 1588, 1538, 1515, 1468, 1440, 1405, 1307, 1119, 721.

4.2.7.7. Characterisation data of tetradecanaotidopalladium(II)manganese(II) $[Pd^{II}Mn^{II}(\mu\text{-}OOC(CH)_8CH_3)_4]$, [39]

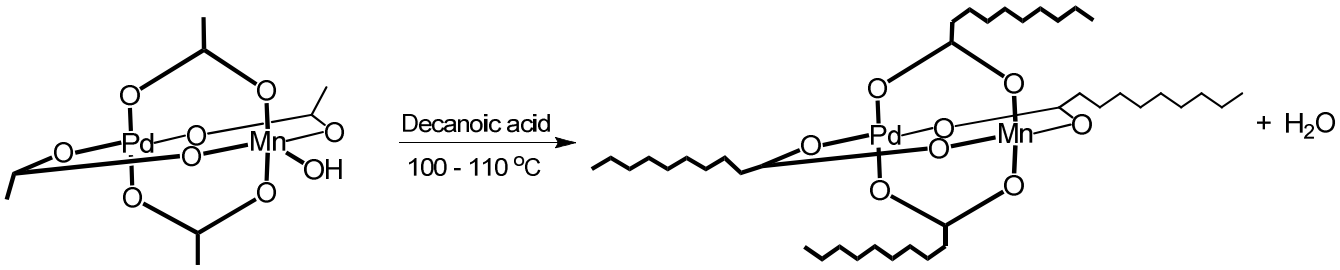

30 **39**

Yield: 0.15 g, 0.178 mmol, 71 %, m.p. 77-79 ˚C, Elemental Analysis: calc. C: 58.31 %; H: 9.66 %, found: C: 57.83 %; H 9.20 %, δ_H (300 MHz, $CDCl_3$)/ppm: 0.15 – 2.49 (76 H, m, 4 x C<u>H</u>$_3$, 32 x C<u>H</u>$_2$), FTIR (cm^{-1}): 3324, 2919, 2851, 1688, 1594, 1559, 1458, 1406, 1317, 1115, 723.

4.2.7.8. Characterisation data of tetradecanoatidopalladium(II)copper(II), $[Pd^{II}Cu^{II}(\mu\text{-}OOC(CH)_8CH_3)_4]$, [40]

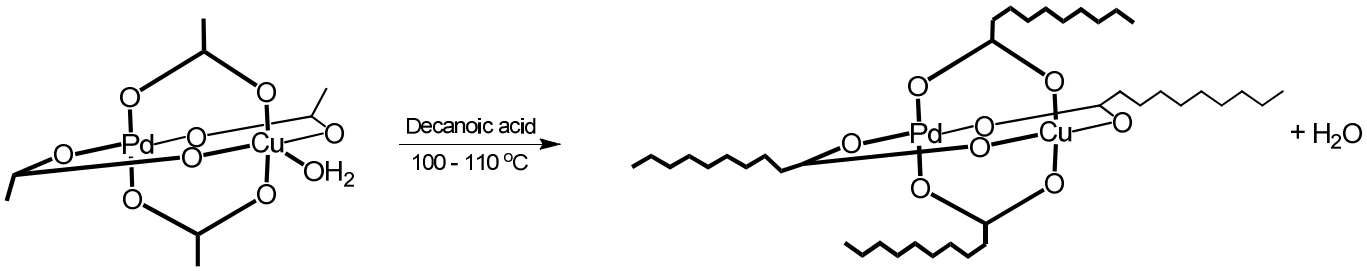

31 **40**

Yield: 0.17 g, 0.199 mmol, 84 %, m.p. 93-94 ˚C, Elemental Analysis: calc. C: 56.25 %; H: 8.98 %, found: C: 55.99 %; H 9.34 %, δ_H (300 MHz, $CDCl_3$)/ppm: 0.39 – 1.56 (76 H, m, 4 x C<u>H</u>$_3$, 32 x C<u>H</u>$_2$), FTIR (cm^{-1}): 2920, 2851, 1608, 1580, 1465, 1428, 1416, 1403, 1313, 1116, 721.

4.2.7.9. Characterisation data of tetradecanoatidopalladium(II)cerium(III) $[Pd^{II}Ce^{III}(\mu\text{-}OOC(CH)_8CH_3)_4]^+$, [41]

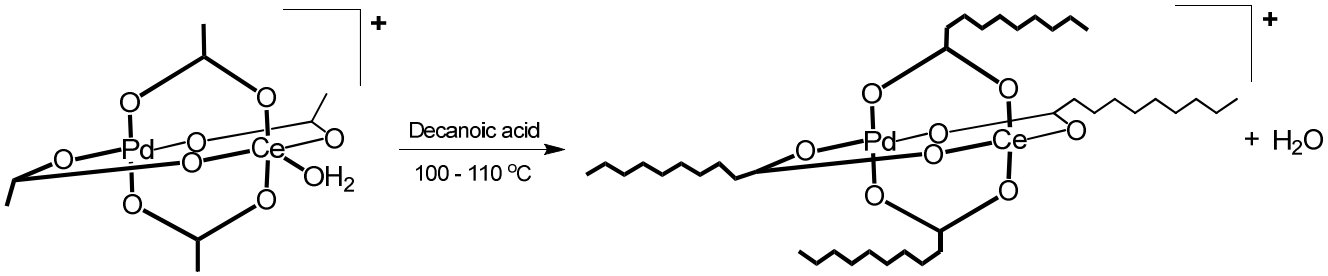

32 **41**

Yield: 0.12 g, 0.128 mmol, 79 %, m.p. 54-55 ˚C, Elemental Analysis: calc. C: 52.72 %; H: 8.73 %, found: C: 53.29 %; H: 8.67 %, δ_H (300 MHz, $CDCl_3$)/ppm: 0.73 – 0.95 (12 H, t, 4 x C<u>H</u>$_3$), 0.96 – 1.90 (64 H, m, 32 x C<u>H</u>$_2$), FTIR (cm^{-1}): 3382, 2922, 2853, 1701, 1618, 1591, 1556, 1453, 1408, 1309, 11115, 723.

4.2.8. Silicon wafer preparation, spin-coating, grafting and calcination (activation) thereof

4.2.8.1. Preparation of silicon wafers having a hydroxylated (Si-OH) surface

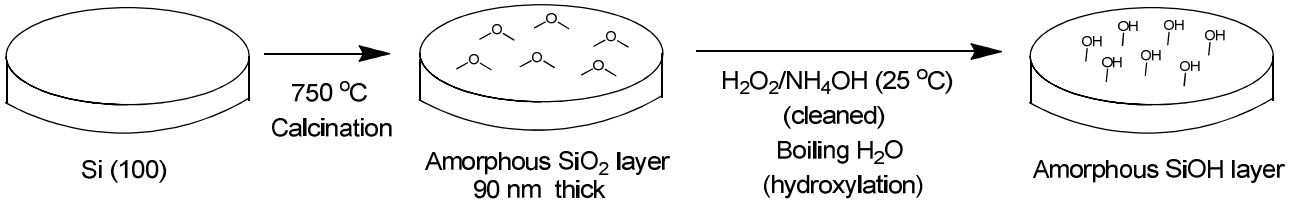

Silicon wafers were calcined in oxygen at 750 °C for 24 hours to form an amorphous SiO_2 layer and then cleaned/etched by allowing it to stand in a mixture of 1/1 (v/v) of H_2O_2 (25% solution) and NH_4OH (35% solution) at room temperature for 10 minutes. The Si-wafers were then hydroxylated to form Si-OH bonds on the surface of the wafer, by boiling the wafers in double distilled water for 1 h and dried at room temperature under a flow of nitrogen.

4.2.8.2. Spin-coating of the complexes were accomplished as follow, [53-72]

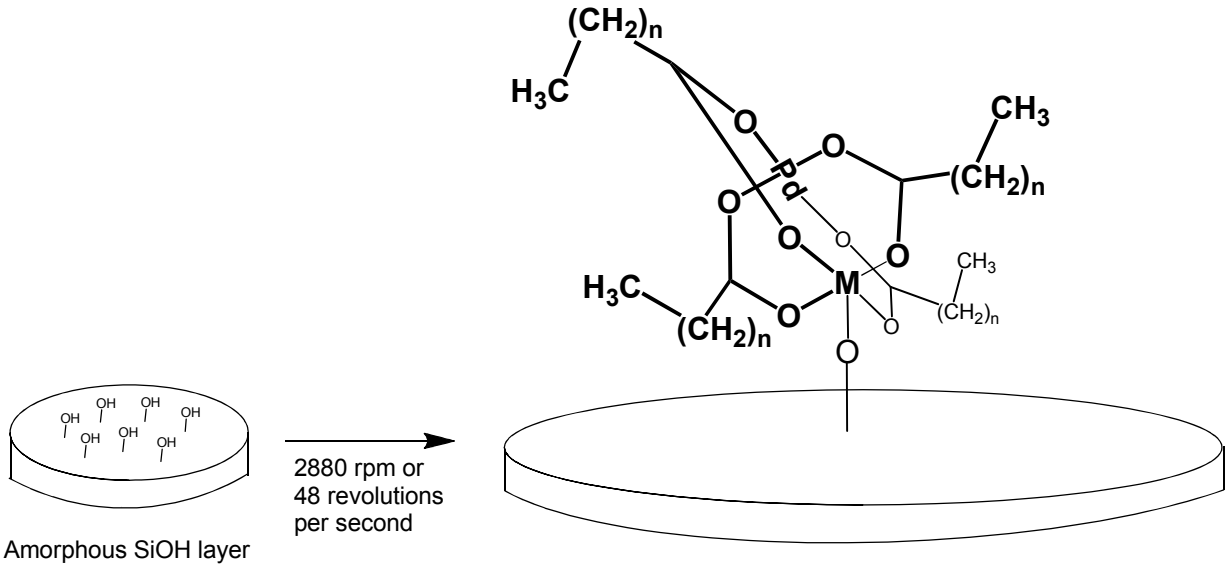

[53]: M = Zn, n = 0 **[60]:** M = Co, n = 4, **[61]:** M = Co, n = 6
[54]: M = Ba, n = 0 **[62]:** M = Co, n = 8, **[63]:** M = Co, n =10
[55]: M = Cd, n = 0 **[64]:** M = Ba, n = 8, **[65]:** M = Cd, n = 8
[56]: M = Sr, n = 0 **[66]:** M = Ca, n = 8, **[67]:** M = Zn, n = 8
[57]: M = Ni, n = 0 **[68]:** M = Sr, n = 8, **[69]:** M = Ni, n = 8
[58]: M = Co, n = 0 **[70]:** M = Mn, n = 8, **[71]:** M = Cu, n = 8
[59]: M = Mn, n = 0 **[72]:** M = Ce, n = 8

The hydroxylated wafer was cut to the appropriate size for the spin coater (4 x 5 mm). The hydroxylated wafer was then first washed with clean solvent DCM or acetone depending in which solvent the complexes were dissolved and spun dried using the spin coater. This cleaned wafer was then spun at 2880 rpm (or 48 revolutions per second). A solution of 5 mM (0.2 mL) of the specific complex **[23-25]** and **[27-30]** as well as **[19-41]** was added dropwise to the revolving waver. The wafer with the anchored complex was then dried by spinning the wafer for an additional 1 minute.

4.2.8.3. Activation (Oxidation) of the spin coated complexes on functionalised Si-OH wafers were accomplished as follow [73-92]

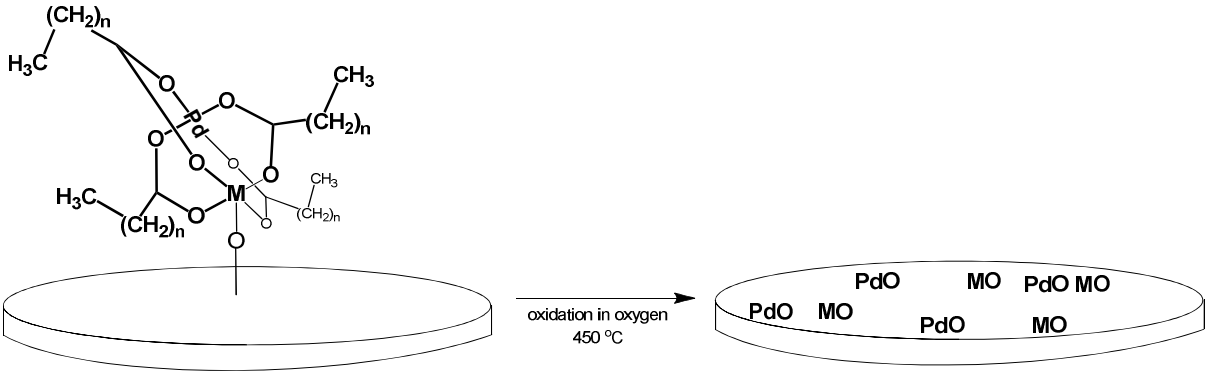

[53]: M = Zn, n = 0 **[60]:** M = Co, n = 4, **[61]:** M = Co, n = 6
[54]: M = Ba, n = 0 **[62]:** M = Co, n = 8, **[63]:** M = Co, n =10
[55]: M = Cd, n = 0 **[64]:** M = Ba, n = 8, **[65]:** M = Cd, n = 8
[56]: M = Sr, n = 0 **[66]:** M = Ca, n = 8, **[67]:** M = Zn, n = 8
[57]: M = Ni, n = 0 **[68]:** M = Sr, n = 8, **[69]:** M = Ni, n = 8
[58]: M = Co, n = 0 **[70]:** M = Mn, n = 8, **[71]:** M = Cu, n = 8
[59]: M = Mn, n = 0 **[72]:** M = Ce, n = 8

[73]: M = Zn, n = 0 **[80]:** M = Co, n = 4, **[81]:** M = Co, n = 6
[74]: M = Ba, n = 0 **[82]:** M = Co, n = 8, **[82]:** M = Co, n =10
[75]: M = Cd, n = 0 **[84]:** M = Ba, n = 8, **[85]:** M = Cd, n = 8
[76]: M = Sr, n = 0 **[86]:** M = Ca, n = 8, **[77]:** M = Zn, n = 8
[77]: M = Ni, n = 0 **[88]:** M = Sr, n = 8, **[89]:** M = Ni, n = 8
[78]: M = Co, n = 0 **[91]:** M = Mn, n = 8, **[91]:** M = Cu, n = 8
[79]: M = Mn, n = 0 **[92]:** M = Ce, n = 8

The Si-OH wavers that were coated with the complexes were all activated, in a calcination oven at 450 ˚C under a stream of oxygen for four hours. This resulted in PdO (palladium oxide) and MO (metal oxide) being deposited on the modified wafer surface.

4.2.8.4. Catalyst testing of the activated PdO and MO (metal oxide) wafers, here, using $Pd^{II}Co^{II}/Si(OH)/SiO_2/Si(100)$ as an example

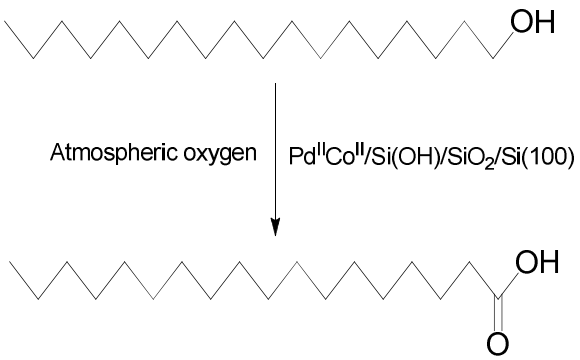

The catalysts were tested using 1-octadecanol as model catalyst in an aerobic solvent-free reaction. In this reaction, 1-octadecanol was oxidised to 1-octadecanoic acid. A 5 mL pill tube was used as a reaction vessel. 1-octadecanol (0.1 g) was weighed and placed inside the pill tube; the activated catalyst was placed on top of the pellets of 1-octadecanol. The temperature was raised to 105 °C and kept constant until the reaction was complete. The reaction was followed using ATR-FTIR until completed.

4.3. Materials

Solid and liquid reagents were purchased from Sigma-Aldrich, and used without further purification. UniLAB grade solvents were purchased from Merck. Double-distilled water was used where necessary.

4.4. Spectroscopic measurements

Nuclear magnetic resonance ^{1}H spectra were recorded on a 300 MHz Bruker Avance DPX NMR spectrometer, at 298 K. Chemical shifts are reported relative to $SiMe_4$ (0 ppm). Spectral processing was done by means of the MestReNova v. 5.3.0.4469 NMR software for Windows. Melting points (uncorrected) of products were determined with an Olympus BX51 polarised microscope, fitted with a LINKAM THRM 600 heating stage. The upper temperature limit of this instrument is 300 °C. Infrared measurements were taken using a Nicolet iS50 ATR Fourier transform spectrometer.

4.5. Electrochemistry

Cyclic voltammetry (CV), linear-sweep voltammetry (LSV) and square wave voltammetry (SW) were performed using a Princeton Applied Research PARSTAT 2273 Voltammographs were recorded using Powersuite (version 2.58). A platinum wire was used as an auxiliary electrode and a silver wire as reference electrode. A glassy carbon electrode was used as the working electrode, with surface area 3.14 mm^2. The working electrode was polished on a Buhler polishing mat, utilising 1 micron and then ¼ micron diamond paste. Solutions contained 0.5 mM of analyte, 0.5 mM of decamethylferrocene or ferrocene as internal standard and 0.1 M tetrabutylammonium tetrakis(pentafluorophenyl)borate as the supporting electrolyte. All complexes were dissolved in 1 cm^3 anhydrous dichloromethane as solvent. Temperatures were kept constant to within 0.5 °C. Experimental potentials were referenced against ferrocene (FcH/FcH^+ $E° = 0.00V$) as an internal standard, according to internationally accepted IUPAC standards. To achieve this, each experiment was performed first in the absence of ferrocene and then repeated in the presence of < 1 mM ferrocene. Data was manipulated on a Microsoft Excel worksheet to set the formal reduction potentials of FcH/FcH^+ couple at 0 V.

4.6. Thermal gravimetric analysis with coupled mass spectrometry (TGA-MS)

TGA experiments were performed on a TGA/SDTA851^{e} coupled to a ThermoStar^{TM} Pfeifer vacuum mass spectrometer. Instruments were initialised and purged with argon gas 24 hours in advance of experimentation. Successive blank curves (no sample) were run on empty 60 µl aluminium oxide crucible until reproducible curves were obtained. Samples sizes for all tested compounds were 2 - 8 mg and were weighed on a five decimal Mettler **XS205** dualrange elecrobalance. Samples were heated at a rate of 10 °C min^{-1} in the temperature range 30 °C < T < 700 °C. A constant flow of argon was maintained over all experiments, unless stated otherwise. a TGA experiment synchronised with an analog mass spectrometry scan is run to identify *m/z* values of evolved gasses.

4.7. Differential Scanning Calorimetry (DSC)

Differential scanning calorimetry (DSC) measurements were performed on a METTLER DSC822^{e} differential scanning calorimeter with FRS5 detector and robotic auto-sampler. The maximum temperature range for the instrument is -50 °C < T < 500 °C. Samples sizes for all tested compounds were 2 - 8 mg and were weighed on a five decimal Mettler **XS205** dualrange elecrobalance, then sealed in standard 40 µl aluminium crucibles. The aluminium cap was perforated with a needle creating a hole of ~ 1 mm in diameter to allow any gasses evolved during potential decomposition to escape without deformation of the crucible. All experiments were performed under nitrogen. The scan rate was in all cases (unless specifically mentioned otherwise) was 10 °C min^{-1} for both heating and cooling. Isothermal segments of one minute prior to and at the final temperature between dynamic heating and cooling segments were included to allow for instrumental overshot and setting. Curve analyses were performed using STAR^{e} SW 8.10$^{®}$ software.

5. Summary, Conclusions and Future Perspectives

5.1. Summary and Conclusions

The circular long-chain palladium carboxylatido complexes **[1-4]** were synthesised by reacting palladium nitrate with the appropriate long chain carboxylic acid, in this case hexanoic, octanoic, decanoic or dodecanoic acid. Ionic potassium carboxylates **[5-8]** were synthesised using a neutralisation reaction between KOH and the appropriate long chain carboxylic acid. The mono-metal carboxylatido complexes **[9-12]** and **[13-18]** were prepared by a metathesis reaction between the desired aqueous ionic potassium carboxylate and the selected aqueous metal salt. The mixed-metal palladium metal tetraacetatido complexes **[23-32]** were synthesised by reacting one equivalent of palladium acetatido complex with three equivalents of the appropriate metal acetatido complex in acetic acid. Synthesis of the long-chain mixed-metal palladium metal tetracarboxylatido complexes **[19-22]** and **[33-41]** were achieved using two methods. The first method involves the reaction of one equivalent of a palladium long-chain hexacarboxylatido complex with three equivalents of the relevant metal long-chain carboxylatido complex, with yields between 56 and 95 %. The second method involves a ligand exchange type of reaction where the palladium metal paddlewheel tetraacetatido complex is reacted with the desired long chain carboxylic acid. This results in the desired long-chain paddlewheel palladium metal tetracarboxylatido complexes, with yields between 66 and 99 %. Method two gave higher yields and more pure products than method one.

NMR analysis showed that the length of the long-chain carboxylatido complexes has an influence on the resonance position of the proton peaks. As the carbon chain becomes longer, the CH_2 groups start to overlap. The CH_3 is located at *ca.* 0.75-0.95 ppm and get shifted to higher ppm values as the carbon chain length increases.

Synthesis of the long-chain circular tripalladium hexacarboxylatido and long-chain mixed-metal paddlewheel tetracarboxylatido complexes was monitored using ATR-FTIR. Also the disappearance of the peak at *ca.* 1700 cm^{-1} indicated the consumption of the free acid. While the appearance of the stretching frequencies at *ca.* 1600 cm^{-1} and 1400 cm^{-1} for the long-chain circular tripalladium hexacarboxylatido complexes and long-chain mixed-metal paddlewheel tetracarboxylatido complexes confirmed the formation of the target complexes.

The long-chain mono- and mixed-metal carboxylatido complexes showed mixed binding modes which could be identified as unidentate, bidentate, tridendate, bridging (*syn-syn*) binding mode and ionic binding mode. These conclusions were made from the following frequencies observed: For a $\Delta_{Difference} > 200$ cm^{-1}, the carboxylatido binding mode to the metal is considered to be unidentate. For a $\Delta_{Difference} < 120$ cm^{-1}, the binding mode is considered to be bidentate. When a series of symmetric and anti-symmetric stretching frequencies are observed that results in a $\Delta_{Difference} = 120 - 200$ cm^{-1}, the binding mode is considered to be bridging. For a $\Delta_{Difference} = 150 - 200$ cm^{-1}, (mostly close to 150 cm^{-1} only) the binding mode is considered to be ionic.

The single crystal X-ray structures of $[Pd^{II}Co^{II}(\mu\text{-}OOC(CH_2)_8CH_3)_4]$ **[21]** (Z = 2, space group $P2_1/c$), $[Pd^{II}Zn^{II}(\mu\text{-}OOC(CH_2)_8CH_3)_4]$ **[36]** (Z = 4, space group $P2_1/c$), and $[Pd^{II}Ni^{II}(\mu\text{-}OOC(CH_2)_8CH_3)_4]$ **[38]** (Z = 2, space group *P*-1) were solved and confirmed the binding modes observed in the ATR-FTIR studies. All three complexes have the same bridging structure, with four carboxylatido ligands around the Pd-Ni, Pd-Co and Pd-Zn metals. All three complexes are dimers.

Thermal studies in the form of DSC and TGA-MS were conducted on selected compounds to determine temperature dependent physical properties. The long-chain circular palladium complexes **[1]** and **[2]** are oils even at -50 °C and it decomposes at 212.74 °C and 229.68 °C respectively. Due to super-cooling, **[3]** has a cold crystallisation peak at -12.43 °C and has a melting point at 20.80 °C while **[4]** crystallises at 23.26 °C with a melting point at 40.89 °C. Variable temperature polarized light microscopic studies confirmed the observations made by DSC thermal studies.

TGA-MS studies showed that the decomposition of the long-chain circular palladium carboxylatido complexes all proceed in one step. Percentage mass loss for **[1]**, **[2]**, **[3]** and **[4]** are 63.70 %, 67.71 %, 71.43 % and 74.23 % respectively. The formation of Pd, PdO and PdO_2 during pyrolysis as the final non-volatile decomposition products. The TGA-MS studies showed different volatile products are liberated during the decomposition of **[1-4]**. These include methane, hydroxide ions, water, carbon monoxide, oxygen, methanol, propyne, carbon dioxide and other products.

The long-chain mono-metal carboxylatido complexes **[15]** and **[16]** showed solid state transitions with melting points at 136.26 °C and 220.35 °C respectively. The variable temperature polarized light microscopic studies showed that **[15]** and **[16]** melts without any prior thermal activity before melting.

Complex **[15]** does not show a step for a loss of water but does show two decomposition steps with a total mass loss of 79.08 %. Non-volatile ZnO and CaO are the final decomposition products. Both these complexes decompose through two steps, **[16]** has a loss of water for the first step while the second step is the decomposition of the complex with 69.33 % total mass loss. The long-chain mixed-metal carboxylatido complexes that showed mesophase behaviour were **[20]**, **[21]** and **[36]**. The smectic mesophase was observed over a temperature range of 8.61 °C for **[20]** and 21.80 °C for **[36]**. However no liquid crystal mesophase behaviour was observed for **[21]** in the DSC thermogram, but was confirmed by variable temperature polarised light microscopic study. Melting point of 76.24 °C for **[20]**, and a melting point of 103.47 °C for **[36]** was obtained. The smectic mesophase behaviour was confirmed for **[20]** and **[36]** using variable temperature polarized light microscopic studies. Complex **[20]** and **[36]** goes through a two-step and four-step decomposition process with a total mass loss of 73% and 75%. The formation of PdO and CoO as well as PdO_2 and ZnO as the final non-volatile decomposition products. The volatile gases observed for **[20]** were found to be hydrogen, hydroxide ions, water, carbon monoxide, ethyne, oxygen, methanol, cyclopropenylidene, propyne and carbon dioxide.

The long-chain mixed-metal carboxylatido complexes **[34]**, **[39]** and **[40]** had melting points of 51.32 °C, 77.67 °C and 76.60 °C and respectively. Complex **[39]** has the most solid state transitions and also shows polymorphism compared to the other complexes. Complex **[34]**, has five decomposition steps (total mass loss 69.18 %). With the formation of PdO and CdO, as the final decomposition products. The complex **[39]** has four steps (total mass loss 67.14 %) and PdO and Mn_2O_3 as the final decomposition products. Complex **[40]** has one decomposition step (total mass loss 77.24 %) and PdO and CuO as the final decomposition products.

From the electrochemistry of the circular tripalladium hexacarboxylatido complexes, one oxidation and one reduction wave was observed. The reduction wave was assigned to $Pd^{II} \rightarrow Pd^{0}$ while the oxidation wave was assigned to $Pd^{0} \rightarrow Pd^{II}$. The complexes however do not disintegrate, the complexes stays intact with the oxidation and reduction process.

The electrochemical study of **[1-4]** revealed that the carboxylatido ligand chain length influence the position of the reduction peak. The general trend observed, as the chain length increases the oxidation potential, E_{pa}, goes to a more negative values, implying that a longer chain length makes oxidation more difficult.

The influence of the cobalt in $[Pd^{II}Co^{II}(\mu\text{-}OOC(CH_2)_{10}CH_3)_6]$ **[22]** on the oxidation potential of the palladium is evident from the shift to more negative values for the complexes, E_{pa} $[Pd_3(\mu\text{-}OOC(CH_2)_{10}CH_3)_6]$ = **-1128 mV** while, E_{pa} $[Pd^{II}Co^{II}(\mu\text{-}OOC(CH_2)_{10}CH_3)_4]$ = **-1338 mV**. The increased electron density due to the cobalt, shifts the reduction wave to a more negative values. The length of the carbon chain had an influence on the position of the oxidation wave of the palladium cerium carboxylatido complexes. Increasing the carboxylatido carbon chain length from two to ten, the E_{pa} decreased from **514 mV** for $[Pd^{II}Ce^{III}(\mu\text{-}OOCCH_3)_4]^+$ **[32]** to **297 mV** for $[Pd^{II}Ce^{III}(\mu\text{-}OOC(CH_2)_8CH_3)_4]^+$ **[41]** making oxidation easier.

Silicon wafers were modified to have Si-OH sites on the surface to provide a suitable anchoring site for the complexes. Selected mixed-metal carboxylatido complexes were coated onto the hydroxylated wafers using spin coating. The pre-catalysts were activated under a stream of oxygen at 450 °C. This allowed for PdO and MO (metal oxide) to be deposited on the modified silicon surface. The solvent-free aerobic oxidation of 1-octadecanol to 1-octadecanoic acid was used as model reaction to test the catalytic activity of the two dimensional supported model catalysts. The catalytic reactions were followed using ATR-FTIR by observing the appearance of the carbonyl stretching frequencies at 1730 cm^{-1} and 1710 cm^{-1} as the reaction progressed. A turnover frequency (TOF) of 0.8 to 2 molecules s^{-1} was obtained from the catalysts prepared from the short-chain mixed-metal acetatido complexes. The catalysts prepared from the long-chain mixed-metal carboxylatido complexes had a TOF of 4 to 7 molecules s^{-1}. Comparison of the obtained TOF with the ionic radius of the second metal showed that the larger ionic radius is accompanied by a decrease in the turnover frequency; this implies that larger atoms tend to be more sluggish in catalytically oxidising 1-octadecanol to 1-octadecanoic acid.

XPS characterisation studies of the activated catalysts revealed that the ratio of palladium to cobalt on the surface is 1.2:1.9. The $Pd^{II}O$ $3d_{5/2}$ peak at **337.19 eV** is well within range of reported binding energy of with an average value of $Pd^{II}O$ **(337.10 eV)**. The Co $2p_{3/2}$ peak at **782.04 eV**, is within the range of **779.3-781.8 eV** reported for oxidised Co/SiO_2. It also relates closely with the reported value of **781.1 eV** of the oxidised palladium cobalt tetraacetatido spin coated onto the hydroxylated silicon wafer.

It is clear that all objectives described in Chapter 1was achieved during the course of this study.

5.2. Future Perspectives

The present research program can further be expanded by varying the axial ligand for example with THF and acetonitrile or even long chain aliphatic ligands. The aliphatic chains can be replaced with unsaturated long chains and even with substituted long chains. Metallocenoic acids (metal = iron, ruthenium or osmium) can be used to replace the long chain carboxylatido ligands thereby introducing a third metal to the complex. The chain length of the metallocenoic acid can also be varied to get different chain lengths.

The palladium metal carboxylatido complexes prepared in this study can also be anchored onto three dimensional supports and a wide variety of catalytic reactions can be tested. The catalysts can also be reduced to have the metals on the surface.

This concludes the study by the author on long-chain mono- and mixed-metal carboxylatido complexes as outlined in the objectives described in chapter 1.

Declaration

I, Ebrahiem Botha, declare that the dissertation/thesis hereby handed in for the qualification Philosophiae Doctor in Chemistry at the University of the Free State is my own independent work and that I have not previously submitted the same work for a qualification at/in another university/faculty. I furthermore cede copyright of the thesis in favour of the University of the Free State.

Signed Date

.....

19/10/15